From Craton to Present Mountains
–
The Scandinavian Lithosphere Imaged by Rayleigh Surface Waves and Ambient Noise

Alexandra Carina Mauerberger

GFZ
Helmholtz-Zentrum
POTSDAM

Dissertation
zur Erlangung des akademischen Grades
Doktor der Naturwissenschaften (Dr. rer. nat.)

Freie Universität Berlin

vorgelegt im Fachbereich Geowissenschaften
Freie Universität Berlin
Berlin, 2021

Dissertation eingereicht am: 23. Juli 2021
Disputation am: 29. Oktober 2021

Prüfungskommission:
Prof. Dr. Serge Shapiro (Vorsitz)
Prof. Dr. Timm John
Prof. Dr. Frederik Tilmann
Prof. Dr. Valérie Maupin
Dr. Jörn Kummerow

Erstgutachter: Prof. Dr. Frederik Tilmann (FU Berlin und GFZ Potsdam)

Zweitgutachterin: Prof. Dr. Valérie Maupin (Univ. Oslo)

To Jonas and Melinda. May you be proud of your mom.

Zusammenfassung

Skandinavien bildet mit seinem bis zu 2,500 m hohem Gebirge (den Skanden) am westlichen Rand des Baltischen Kratons eine außergewöhnliche Struktur. Die ursprüngliche Gebirgsbildung war bereits vor 420 Ma abgeschlossen und anschließend wurden die Caledoniden weitgehend erodiert. Da die Region keinen aktiven tektonischen Kompressionskräften unterliegt, fehlt eine umfassende Erklärung für die Topographie der Skanden, die sowohl in ihrer Höhe als auch in ihrer Ost-West Ausdehnung variieren. In meiner Dissertation analysiere ich die Struktur von Kruste und Erdmantel mittels Oberflächenwellen von Erdbeben und Umgebungsrauschen mit dem primären Ziel neue Erkenntnisse zur Aufrechterhaltung der Topographie zu liefern. Im Vordergrund steht zudem die Erkundung von strukturellen Unterschieden zwischen den verschiedenen tektonischen Einheiten. Ich benutze hierbei die seismischen Aufzeichnungen des ScanArray Netzwerkes, dass zusammen mit permanenten und weiteren temporären Stationen die gesamte Fläche von Skandinavien abdeckt.

Beamforming von Erdbebenoberflächenwellen ermöglicht die Analyse von durchschnittlichen Phasengeschwindigkeiten im gesamten Untersuchungsgebiet und Teilen davon. Dabei zeigt sich eine ungewöhnliche azimuthale 360° bzw. $\sin(1\theta)$ Variation der Phasengeschwindigkeiten im nördlichen Untersuchungsgebiet sowie in Südnorwegen/ Südschweden, die jedoch nicht im zentralen Untersuchungsgebiet auftritt. Für Perioden >35 s ergibt sich eine maximale Varianz von 5% zwischen den gemessenen Phasengeschwindigkeiten für entgegengesetzte Rückazimuthe von 120° und 300°. Eine solche Variation ist inkompatibel mit der intrinsischen azimuthalen Anisotropie und widerspricht zudem der path average approximation, die in der Tomographie angewandt wird. Ich zeige, dass starke vertikale und horizontale Geschwindigkeitskontraste an der Lithosphären-Asthenosphären-Grenze (LAB), die perpendikular zur Richtung der extremen Phasengeschwindigkeiten verlaufen, für diesen 1θ Effekt verantwortlich sind. Zur Evaluierung führe ich eine 2D full-waveform Modellierung durch, in der die Rayleigh-Wellenausbreitung in einem Model mit steilen LAB Gradienten und stark reduzierten Scherwellengeschwindigkeiten unterhalb der LAB analysiert wird. Tatsächlich ergeben sich höhere Phasengeschwindigkeiten für Wellen die sich in Richtung der sich verdünnenden Lithosphäre ausbreiten, und geringere Phasengeschwindigkeiten für Wellen die zur mächtiger werdenden Lithosphäre propagieren. Eine Interferenz der am steilen LAB Gradienten reflektierten Oberflächenwelle mit der vorwärtspropagierenden Fundamentalmode ist wahrscheinlich für diesen Effekt verantwortlich.

Die gemeinsame Inversion von teleseismischen Oberflächenwellen und Umgebungsrauschen ermöglicht mir die strukturelle Abbildung bis 250 km Tiefe. Aus meinem Geschwindigkeitsmodell leite ich ein neues Krustenmodell ab, aus dem sich Karten der Moho Tiefe sowie der vermutlich hochdichten unteren Krustenschicht (LCL) ergeben. Ich beobachte eine Krustenverdickung von West nach Ost unter den präkambrischen Gebieten mit niedriger Topographie, die hauptsächlich eine Folge der Verdickung des LCL nach Osten ist. Im Gegensatz zu den südlichen Skanden mit der höchsten Topographie (2,500 m), zeigt sich eine krustale Wurzel unterhalb der nördlichen Skanden (max. 2,100 m), die hin zu den zentralen Skanden (max. 1,000 m) verschwindet. Generell wird die Lithosphäre unterhalb der Skanden nach Osten mächtiger. Die signifikanten Geschwindigkeitskontraste und steilen LAB Gradienten sowohl im Süden (90–120 km LAB Tiefe mit 5.5% V_{SV} Kontrast) als auch im Norden (150 km LAB Tiefe mit 9% V_{SV} Kontrast) korrelieren überraschenderweise mit der Gebirgsfront der Caledoniden. Im Bereich der zentralen Skanden lassen sich gleichmäßigere Strukturen abbilden

(150–170 km LAB Tiefe mit 4% V_{SV} Kontrast). Die Korrelation der Lithosphärenverdickung mit der Gebirgsfront könnte mit Metasomatismus als Folge der Orogenese und/oder der Bildung des passiven Kontinentalrandes zusammenhängen. Im präkambrischen Skandinavien werden unter dem Karelia-Kraton in Nordfinnland Strukturen mit niedrigen Geschwindigkeiten unterhalb von 150 km Tiefe beobachtet. Der paläoproterozoische Norrbotten-Kraton kann in der Mantel-Lithosphäre vom Karelia-Kraton, den Caledoniden und dem paläoproterozoischen Svecofennium getrennt werden, möglicherweise durch unterschiedliche Metasomatismus-Effekte.

Aufgrund der strukturellen Unterschiede vermute ich verschiedene Mechanismen, die für die Kompensation der Topographie verantwortlich sind. Gesteine mit niedriger Geschwindigkeit/Dichte in der flachen Kruste (<15 km Tiefe) und eine Schicht mit hoher Geschwindigkeit/Dichte in der tiefen Kruste (>10 km LCL Mächtigkeit) ergeben zusammen mit der Gebirgswurzel eine Airy-Pratt Isostasie der nördlichen Skanden. Die stark reduzierten Geschwindigkeiten unterhalb der LAB implizieren zusätzlich einen dynamischen Auftrieb durch den Oberen Mantel. Da die genannten krustalen Attribute in den südlichen Skanden fehlen, findet der isostasische Ausgleich hier vermutlich ausschließlich durch den Mantel statt. Sowohl für die südlichen als auch für die nördlichen Skanden vermute ich zudem eine Wechselwirkung mit kleinräumigen edge-driven Konvektionen (EDC), die sich neben den steilen LAB Gradienten ausbilden können. Dabei wird heißes und weniger dichtes Material der Asthenospähre nach oben konvektiert, dass wiederum zu einem dynamischen Auftrieb der Lithosphäre und damit der Oberflächentopographie führt. Die Topographieunterschiede in Ost-West Richtung entlang der Skanden können mit unterschiedlich großen EDC Zellen ebenfalls erklärt werden. In erster Linie kompensiert die Pratt-Isostasie die niedrigere Topographie der zentralen Skanden, aber ein geringer Beitrag durch dynamische Unterstützung könnte ebenso stattfinden.

Letztlich sehe ich die starken LAB Gradienten im Süden und im Norden als Ursache für die beobachteten 1θ Variation der Phasengeschwindigkeiten. Wohingegen die geringeren Geschwindigkeitskontraste im zentralen Bereich das Fehlen des 1θ Effektes erklären.

Summary

The Scandes mountain range along the western rim of the Archean Baltic craton with elevation up to 2500 m forms an exceptional setting as the orogeny terminated 420 Ma ago and the Caledonides were deeply eroded afterwards. Since this region lacks recent compressional tectonic forces, a comprehensive explanation for the topography, which shows north-south and lateral variations along the Scandes, is missing. In my dissertation, I use earthquake surface waves and ambient noise to image the crustal and mantle structure aiming to provide new clues about the topography's origin. The focus is also on exploring structural differences between the various tectonic domains. Here, I benefit from the seismic recordings by the ScanArray network supplemented by permanent and previous projects, distributed over entire Scandinavia.

First, I performed a beamforming of Rayleigh surface waves which yielded average phase velocities for the study region and several of its sub-regions. An unusual 360° or $\sin(1\theta)$ phase velocity variation with propagation azimuth is observed in northern Scandinavia and southern Norway/Sweden but not in the central area. For periods >35 s, a 5% variation between the maximum and minimum velocities was measured for opposite backazimuths of 120° and 300°, respectively. Such a variation is incompatible with the intrinsic azimuthal anisotropy and the path average approximation made in tomography. I assumed an eastward dipping lithosphere-asthenosphere boundary (LAB) to be the causing structure, inspired by some preliminary velocity models and observations made in previous studies. To test this hypothesis, I carried out 2D full-waveform modeling of the Rayleigh wave propagation. The models include a steep gradient at the LAB in combination with a pronounced reduction in the shear velocity below the LAB. The synthetic results are consistent with the observations: Faster phase velocities are obtained for propagation towards the thinning lithosphere, and slower ones for propagation in the direction of deepening LAB. The interference of reflected surface wave energy at the steep LAB with the forward propagating fundamental mode probably causes this peculiar effect.

Second, the joint inversion of Rayleigh surface waves and ambient noise provides structural imaging down to 250 km depth. Resultant from my velocity model, I derive a new crustal model from which maps of the Moho depth as well as of the high-density lower crustal layer (LCL) are obtained. I observe crustal thickening from west to east below the Precambrian low-topography terranes, which is mainly a consequence of eastward thickening of the LCL. In contrast to the southern Scandes, with the overall highest topography (2,500 m), a crustal root below the northern Scandes (max. 2,100 m) is seen which diminish towards the central Scandes (max. 1,000 m). The LAB below the Scandes is deepening from west to east. The sharp steps in the LAB and strong velocity reductions both in the south (90–120 km LAB depth with 5.5% V_{SV} contrast) and the north (150 km LAB depth with 9% V_{SV} contrast) surprisingly correlate with the Caledonian mountain front. Whereas smoother laterally varying structures (150–170 km LAB depth with 4% V_{SV} contrast) are found below the central Scandes. The correlation of the lithosphere thickening with the Caledonian front might be related to metasomatism as result of the orogeny and/or the passive margin rifting. In Precambrian Scandinavia, low-velocity areas below 150 km depth are observed beneath the Archean Karelia craton in northern Finland. At mantle depth, the Paleoproterozoic Norrbotten craton can be separated from the Karelia craton, Caledonides and Paleoproterozic Svecofennian likely due to different degrees of metasomatism.

Based on the structural differences, I conclude that different mechanisms are responsible

for the compensation of the topography. The northern Scandes are likely compensated by a combined Airy-Pratt isostasy as implied by low-density rocks in the shallow crust (<15 km depth), a high-density layer in the deep crust (>10 km LCL thickness) and the mountain root. The strongly reduced velocities at sub-lithospheric depth additionally suggest an uplift contribution from the upper mantle. Since the southern Scandes lacks these crustal attributes, they experience mainly mantle-driven buoyancy. In both cases, however, I assume the influence of small-scale edge-driven convections (EDC) that can arise at sharp LAB gradients. EDC emplaces thereby low-density material at sub-lithospheric depths by the upwelling of hot asthenosphere which implies additional buoyancy of the lithosphere. Moreover, the lateral topography differences along the Scandes can be explained by varying EDC cell dimensions. Primarily, Pratt isostasy compensates the low topography central Scandes, but a contribution from dynamic support could act as well.

Ultimately, I see the strong gradients at the LAB below the southern and northern Scandes as the cause of the observed 1θ phase velocity variation. While the smoother velocity structure in the central study area explains the absence of the 1θ effect.

Declaration

Hiermit versichere ich, dass ich die vorliegende Dissertation ohne unzulässige Hilfe Dritter und ohne Benutzung anderer als der angegebenen Literatur angefertigt wurde. Die Stellen der Arbeit, die anderen Werken wörtlich oder inhaltlich entnommen sind, wurden durch entsprechende Angaben der Quellen kenntlich gemacht. Diese Arbeit hat in gleicher oder ähnlicher Form noch keiner Prüfungsbehörde vorgelegen.

I hereby declare that except where specific reference is made to the work of others, the contents of this dissertation are original and have not been submitted in whole or in part for consideration for any other degree or qualification in this, or any other university. This dissertation is my own work and contains nothing which is the outcome of work done in collaboration with others, except as declared specified in the text.

Alexandra Carina Mauerberger
Potsdam, 23 July 2021

Contents

Zusammenfassung i

Summary iii

1 Introduction 1
- 1.1 Motivation . . . 1
- 1.2 Thesis contributions . . . 2
- 1.3 LITHOS-CAPP instrumentation . . . 4

2 Tectonic context 7
- 2.1 The Lithosphere . . . 7
  - 2.1.1 Definition and Concept . . . 7
  - 2.1.2 Evolution of the Lithosphere . . . 8
- 2.2 Tectonic evolution of Scandinavia . . . 12
- 2.3 The Caledonian orogeny . . . 16
- 2.4 The Progression of the Scandes mountain range . . . 17
- 2.5 Results from previous studies . . . 21
  - 2.5.1 The Scandes . . . 21
  - 2.5.2 Svecofennian domains . . . 24
  - 2.5.3 Archean and Paleoproterozoic domains . . . 25

3 Theory & methods 27
- 3.1 Surface waves . . . 27
  - 3.1.1 Surface wave tomography . . . 29
  - 3.1.2 Limitations of surface wave tomography . . . 31
  - 3.1.3 Phase velocity inversion with TPW . . . 32
  - 3.1.4 Inversion with transdimensional McMC . . . 32
- 3.2 Ambient noise . . . 35

4 Anomalous azimuthal variations with 360° periodicity of Rayleigh phase velocities observed in Scandinavia 39
- 4.1 Summary . . . 39
- 4.2 Introduction . . . 39
- 4.3 Tectonic setting . . . 41
- 4.4 Data . . . 44
- 4.5 Beamforming processing . . . 44
  - 4.5.1 Method . . . 44
  - 4.5.2 Results . . . 46
- 4.6 2D surface wave modeling . . . 53
  - 4.6.1 Method . . . 53
  - 4.6.2 Results . . . 54
- 4.7 Discussion . . . 60
  - 4.7.1 Theoretical considerations . . . 60

4.7.2 Observations in other regions and tectonic implications 64
4.8 Conclusion 66

5 A shear-wave velocity model for the Scandinavian lithosphere from Rayleigh waves and ambient noise - Implications for the origin of the topography of the Scandes mountain range 67
5.1 Abstract 67
5.2 Introduction 68
5.3 Tectonic history 72
5.4 Data 74
5.5 Ambient noise tomography 74
5.5.1 Computation of ambient noise cross-correlation functions 74
5.5.2 Dispersion curve measurement 75
5.5.3 2D ambient noise inversion 76
5.6 2D teleseismic surface wave inversion 79
5.6.1 Method 79
5.6.2 Inversion 80
5.6.3 Bootstrap testing: assessing the influence of backazimuthal distribution . 82
5.6.4 Phase velocity maps 84
5.7 Shear velocity inversion 86
5.7.1 Dispersion curves 86
5.7.2 Depth inversion 87
5.8 Shear velocity results 89
5.8.1 Crust 89
5.8.2 Mantle structures 93
5.9 Discussion 100
5.9.1 Why are the Norrbotten and Karelia cratons distinct at mantle depth? . . 100
5.9.2 The deep lithospheric keel below Svecofennian south-central Finland . . . 101
5.9.3 The Knaften anomaly in Svecofennian Sweden 102
5.9.4 How is the topography of the Scandes sustained 102
5.10 Conclusion 111

6 Conclusion & outlook 113

A Data 137
A.1 Data availability 137
A.2 ScanArray Core station information 139

B Supplementary for chapter 4 141
B.1 Supplementary material to paper I 141
B.2 Cross-validation of beamforming 142

C Supplementary for chapter 5 147
C.1 Supplementary material to paper II 147
C.2 Ambient noise data 159
C.3 Ambient noise phase velocity inversion 163

C.4 V_S-depth inversion with DLS noise results 165
C.5 1D Airy isostasy modeling 165

D Impact of local inhomogeneities on Eikonal and Helmholtz tomography 169
D.1 Introduction 169
D.2 Method and data processing 170
D.3 Eikonal tomography 175
D.4 Helmholtz tomography 178
D.5 Discussion and conclusion 181
D.5.1 Comparison of the 2D phase velocity inversions 181
D.5.2 Difficulties with the Eikonal and Helmholtz tomography 181

Chapter 1

Introduction

1.1 Motivation

This thesis examines the lithospheric structure of entire Scandinavia by teleseismic Rayleigh surface waves and ambient noise. Scandinavia is of particular interest because it allows the study of the Paleozoic Caledonian mountain range (the Scandes) that overthrusts the western edge of the Precambrian Baltic Shield. Today, a passive margin shapes the western Scandinavian coast. The present surface topography is conspicuously high in the absence of recent active tectonic forces and intense denudation by deep erosion in the past. Thereby, the elevation varies along the Scandes with the highest topography in southern Norway (2,500 m). The northern Scandes have a peak elevation of 2,100 m where the central Scandes are characterized by a maximum elevation of 1,000 m. Moreover, the east-west extent of the Scandes varies between the north and the south with dimensions of ∼250 km and ∼400 km, respectively. The low-topography central Scandes show a maximum east-west extent of 150 km (Fig. 1.1).

Scandinavia has been investigated for several decades by numerous passive and active seismic studies, on land and offshore, respectively (e.g., Guggisberg et al., 1991; Janik et al., 2009; Stratford et al., 2009; Breivik et al., 2017). Mainly southern Norway and Sweden, the Lofoten region and Finland have been imaged. The most relevant passive onshore studies to date are summarized in section 2.5. Beneath the high-topography southern Scandes in southern Norway a surprisingly shallow crust and lithosphere-asthenosphere boundary (LAB) have been found (e.g., Maupin et al., 2013; Kolstrup et al., 2015). A clear crustal mountain root is thereby absent. The lower topographic regions of the Baltic Shield in the east, however, reveal a thicker crust which is in contrast to the principles of Airy isostasy. Lower seismic velocities than expected for a tectonically stable region have been imaged below southern Norway with a sharp transition to higher velocities beneath southern Sweden. Scandinavia therefore provides a great opportunity to study the geodynamic evolution of the lithospheric structure at a present-day passive continental margin as well as its implications on the surface topography.

This thesis, as part of the international ScanArray project (Thybo et al., 2012, 2021), is now the connecting piece between previous studies and the unexplored northern and central areas. The ScanArray initiative consists of a consortium including NORSAR, NGU (both Norway) and the Universities of Copenhagen, Oslo, Uppsala, Bergen, Aarhus and Oulu which operated the temporary ScanArray Core network with 72 stations between 2012–2017. The German contribution is the LITHOspheric Structure of Caledonian, Archaean and Proterozoic Provinces (LITHOS-CAPP) project, funded by the DFG and accomplished by GFZ and KIT[1]. All ScanArray partners have access to the restricted Swedish permanent network SNSN (SNSN, 1904) between 2012–2016, kindly provided by the Uppsala University. To make this data set available, I archived the recordings of the SNSN network (78 stations) at the GEOFON data center. My results presented here mainly benefit from the analysis of seismic

[1]Karlsruhe Institute of Technology

data acquired by the ScanArray Core network and the SNSN network. Additional permanent and temporary stations (see Fig. 1.1 and Table 4.1) offer the possibility to jointly resolve all tectonic domains of Scandinavia.

Seismological methods (chapter 3) allow new insight into the deep structure beneath Scandinavia. Teleseismic earthquake surface waves, jointly analyzed with regional ambient noise measurements, provide the tool to understand major processes within the crust and the uppermost mantle. With the resultant shear-wave velocity model, I can examine the current state of the lithosphere and draw conclusions about its evolution in time (chapter 5). I focus hereby on the upper mantle rather than on the crust. In particular, lithospheric differences along the Scandes and differences among the Proterozoic and Archean provinces are of interest: What compensates the present high topography along a passive continental margin? Are similar crustal and mantle characteristics seen in the north as obtained for southern Norway and Sweden? Can we image the different Archean and Proterozoic domains on crustal and mantle depths?

Initially, one objective was also to investigate the intrinsic azimuthal anisotropy with a focus on spatial variations between the tectonic domains. However, during my research I found an unexpected and anomalous azimuthal pattern of the surface waves (chapter 4). Aiming to understand this peculiar azimuthal variation, which has been rarely studied in the past, this finding triggered further data analysis and modeling.

1.2 Thesis contributions

In the following, I clarify the content of this thesis as well as the contributions made to the papers. Chapters 4 and 5 form the core of this thesis.

- A summary of the German LITHOS-CAPP instrumentation is provided in section 1.3.
- Chapter 2 contains an introductory section about the lithosphere. It also includes details on the tectonic history of Scandinavia and the evolution of the mountain range.
- Chapter 3 deals with the seismological theory and methods used for the analysis of ambient noise and Rayleigh surface waves.
- Chapter 4 contains the published paper I (Mauerberger et al., 2021a):

  Mauerberger, A., Maupin, V., Gudmundsson, O. and Tilmann, F. *Anomalous Azimuthal Variations with 360° Periodicity of Rayleigh Phase Velocities Observed in Scandinavia.* Published on 13 November 2020 in Geophys. J. Int., doi:10.1093/gji/ggaa553

  I processed the data with the code of my co-author and second supervisor V. Maupin. The 2D forward modeling has been conducted by myself where my colleague Felix Schneider kindly shared the software package *Salvus* (Afanasiev et al., 2019) with me. I wrote the manuscript with contributions from my co-authors and prepared all figures.

- Chapter 5 contains the submitted version of paper II:

  Mauerberger, A., Sadeghisorkhani, H., Maupin, V., Gudmundsson, O. and Tilmann, F. *A shear-wave velocity model for the Scandinavian lithosphere from Rayleigh waves and ambient noise - Implications for the origin of the topography of the Scandes mountain range.* The manuscript has been submitted to Tectonophysics on 25 June 2021.

I processed and analyzed the surface wave data and calculated the ambient noise cross-correlations. My co-author H. Sadeghisorkhani carried out the fully automatic picking of the noise dispersion curves. Thereby, he used a modified version of his software package *GSpecDisp* (Sadeghisorkhani et al., 2018). My supervisor F. Tilmann applied these noise dispersion curves to his inversion method (Tilmann et al., 2020) from which the 2D noise phase velocities resulted. I performed the 2D Rayleigh phase velocity inversion and the final 1D velocity-depth inversion based on the merged dispersion curves. For the V_{SV} model, I used the open-source software *BayHunter* (Dreiling & Tilmann, 2019) which was implemented by my colleague J. Dreiling and slightly modified by me. I interpreted the velocity model and prepared all figures except for Fig. C.4. I wrote the manuscript with contributions from my co-authors.

- The appendix consists of several chapters including the supplementary materials of my papers. Additionally, in chapter D the results of an Eikonal tomography are presented which I conducted in the beginning of my doctoral research.

There are some publications I have contributed to, but they are not included in this thesis:

- Detailed information on the LITHOS-CAPP project can be found in the technical report:

  Grund, M., **Mauerberger, A.**, Ritter, J., and Tilmann, F., 2017. *Broadband Recordings for LITHOS-CAPP: LITHOspheric Structure of Caledonian, Archaean and Proterozoic Provinces, Sep. 2014 - Oct. 2016, Sweden and Finland.* Scientific Technical Report STR - Data; 17/02. GIPP Experiment and Data Archive.
  http://doi.org/10.2312/GFZ.b103-17029

  Together with M. Grund (former PhD candidate at KIT in the LITHOS-CAPP project) and W. Scherer (former technician at KIT) I have undertaken two service trips in 2015 to the GFZ and KIT seismic stations in Finland and Sweden (Fig. 1.1). These maintenance trips were mainly organized by me with the support of our local project partners in Oulu and Uppsala. I prepared the raw seismic data including the metadata files (log and GPS data) from the entire ScanArray Core network (72 stations) in order to archive them at the GFZ GEOFON data center. Michael and I wrote this technical report and prepared the figures. Some technical problems occurred at our stations which are described in the report. The supplementary material to this report contains the log and GPS data files for each station.

- The methodology of the noise tomography that I applied in chapter 5 is described in

  Tilmann. F, Sadeghisorkhani, H. and **Mauerberger, A.** *Another look at the treatment of data uncertainty in Markov chain Monte Carlo inversion and other probabilistic methods.* Published on 6 May 2020 in Geophys. J. Int., doi:10.1093/gji/ggaa168

  For this paper, I processed the ambient noise data and calculated the cross-correlations where a subset was used as test case here. I reviewed the manuscript, in particular the introduction. The procedure of the ambient noise data processing is described in section 3.2 and some examples are shown in the appendix.

- A summary of the ScanArray project including some seismological results obtained by the project partners is published as

Thybo, H., N. Bulut, M. Grund, **A. Mauerberger**, A. Makushkina, I. M. Artemieva, N. Balling, O. Gudmundsson, V. Maupin, L. Ottemøller, et al. (2021). ScanArray - A Broadband Seismological Experiment in the Baltic Shield, Seismol. Res. Lett., 1–13, http://doi.org/10.1785/0220210015

Along a north-south profile across the tectonic provinces in the Baltic Shield, the results from receiver functions, body wave tomography and SKS splitting are discussed together with my shear-wave velocity model from chapter 5. I have provided the corresponding figures and reviewed the manuscript.

1.3 LITHOS-CAPP instrumentation

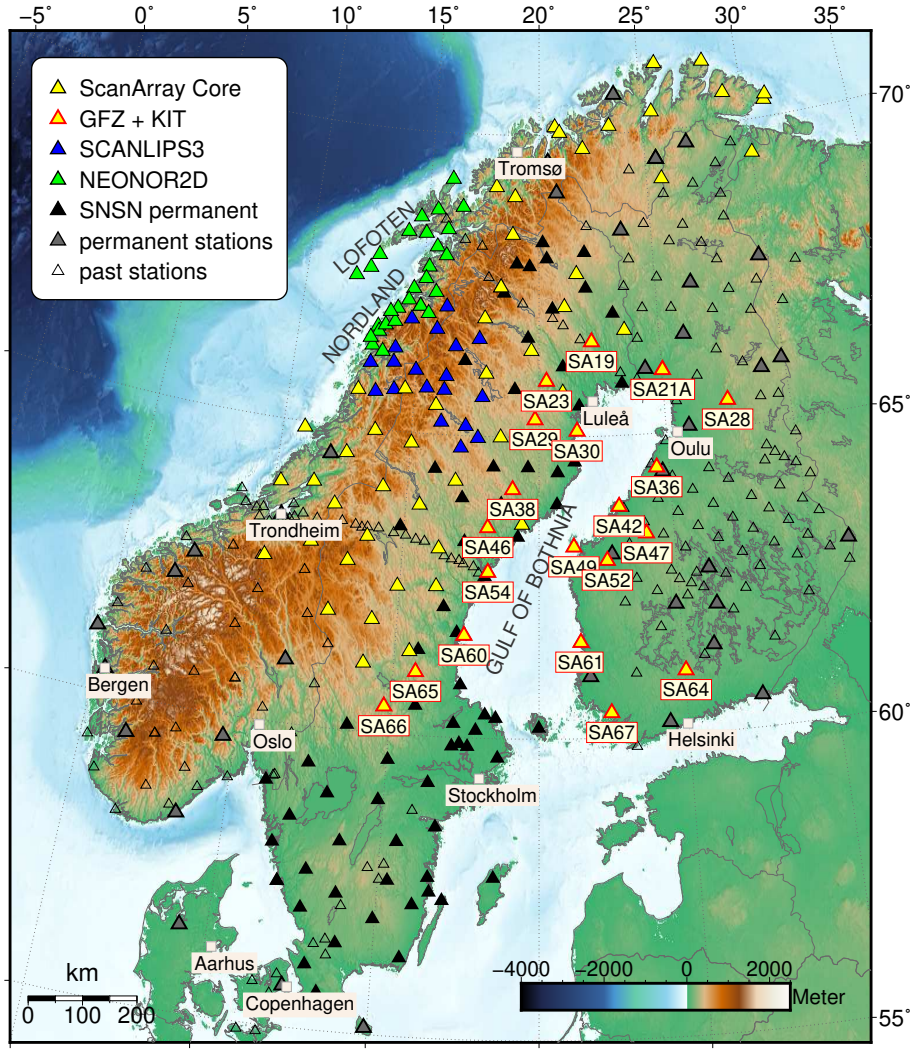

Fig. 1.1: Map of the study region with the stations of the ScanArray Core network as well as stations from other temporary and permanent networks used for the analyses. In total, 228 stations are used in this thesis. The 20 stations deployed by GFZ and KIT for the LITHOS-CAPP project are highlighted as yellow triangles with red edges. The NEONOR2D network (green triangles, 28 stations) was operated by the University of Bergen and NORSAR, the SCANLIPS3D network (blue triangles, 20 stations) by the University of Leicester. The SNSN Swedish National Seismic Network (filled black triangles) is a permanent network operated by the Uppsala University.

The ScanArray Core network (Thybo et al., 2012, 2021) is a regional array of 72 broadband seismic stations (labeled as SAxx where the number xx increases with decreasing latitude) with

an average inter-station distance of 70 km. From September 2014 to October 2016, 20 out of the 72 seismic stations were operated by GFZ and KIT within the LITHOS-CAPP project. All of the LITHOS-CAPP stations have been provided by the GFZ Geophysical Instrument Pool Potsdam (GIPP). The technical report by Grund et al. (2017) describes the details of the instrumentation and the technical problems encountered. Fig. 1.1 displays the stations used in this thesis with the ScanArray Core network as yellow triangles and the LITHOS-CAPP stations as red-edged yellow triangles, mainly located around the Gulf of Bothnia in Finland and central Sweden.

In May and September 2015 two service trips were undertaken to check the seismometers, data loggers and GPS signals. Our LITHOS-CAPP stations have been deployed, either on private or local governmental sites, in indoor cellars or traditional vaults, outside close to the main building. All sensors have been installed on bedrock, concrete floors or concrete plates. They recorded continuously, within the operational time period (see Fig. A.1 for an overview), at a sampling rate of 100 Hz. The seismic stations have been equipped with different sensor types and corner periods: 10 Guralp of 60 s, 5 Trillium of 120 s and 5 Trillium of 240 s (Fig. A.2). At site SA21, the instruments have been flooded in spring 2015 and had to be replaced with station SA21A during the second service trip in September 2015. Station SA36 experienced serious technical problems and only 5 months of recordings are available. Three large misorientations occurred at stations SA21A, SA36 and SA52 with deviations >5°.

I converted the raw data logger mseed files to standard mseed to make them consistent with the GFZ GEOFON archive requirements. The raw data have been stored in daily files. After conversion, the channels have been renamed to HH[ZNE] for the three recorded components, respectively. The measured misorientations are indicated in the metadata files. The same procedure has been applied to the remaining ScanArray Core data.

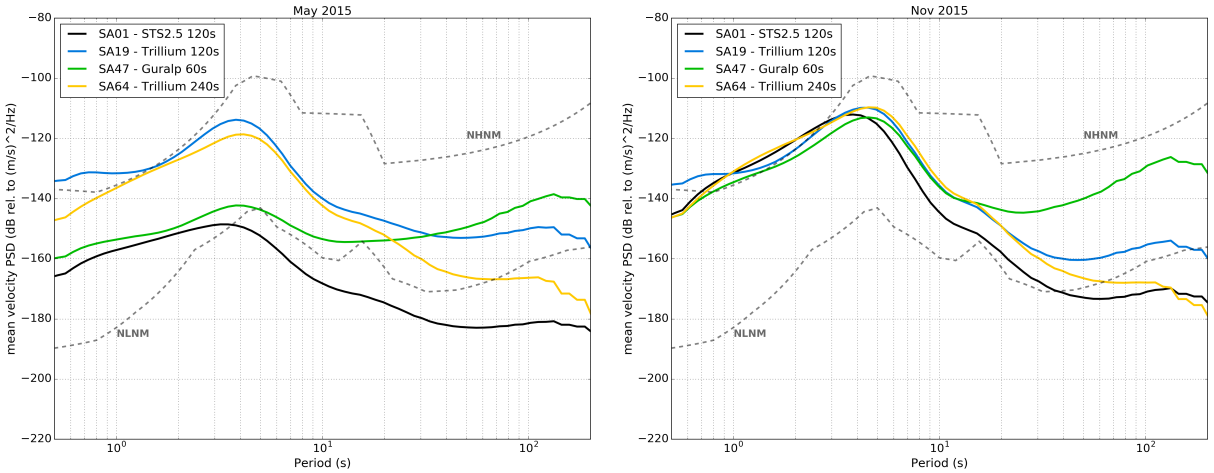

Fig. 1.2: Mean noise power spectral density plots for the vertical component of four ScanArray stations calculated for May 2015 (left) and November 2015 (right). The NLNM and NHNM labeled grey lines indicate the reference low-noise level and the high-noise level, respectively, after Peterson (1993).

Fig. 1.2 compares the noise level of three LITHOS-CAPP stations SA19, SA47 and SA64 as well as station SA01 deployed by the University of Oslo. Similar spectra can be observed for the other ScanArray stations which are equipped with 120 s or 240 s sensors. I calculated the probabilistic power spectral density (PPSD) after deconvolving the instrument response and removal of the mean and the trend of the daily time series. Prior to the deconvolution the

signals have been filtered between 0.5–200 s, a period range relevant for the analysis in this thesis. Finally, the mean of the stacked PPSD is taken. The major peak around 5 s corresponds to the secondary oceanic microseism whereas the primary microseism around 15 s is less pronounced or even undetectable. For periods <3 s the overall signal-to-noise ratio (SNR) in winter times is fairly low reaching or even exceeding the reference New High-Noise Model (NHNM) (Peterson, 1993). For periods >5 s the noise level is significantly decreasing, approaching the level of the New Low-Noise Model (NHLM). Interestingly, the seasonal noise variations of the Trillium sensors (SA19 and SA64) are insignificant compared with the variations of the STS-2.5 (SA01) and Guralp (SA47) seismometers. The coastal station SA01 has a much lower noise level in May (partly lower than the NHLM) compared with the other stations which are located far inland and away from the Atlantic coast. Also the SNR of the Guralp sensor (SA47) is better in summer times but the increased noise level for longer periods reflects the corner period of 60 s. To sum up, the LITHOS-CAPP and ScanArray instrumentation creates the prerequisites to obtain high-quality short-period noise measurements as well as long-period Rayleigh surface waves.

Chapter 2

Tectonic context

2.1 The Lithosphere

In this section, I summarize the various definitions of the lithosphere and explain some terms and mechanisms relevant for the discussion in this thesis. Unless otherwise stated, I hereby refer to the comprehensive textbook by Artemieva (2011).

2.1.1 Definition and Concept

The lithosphere consists of the Earth's crust and the non-convecting uppermost mantle and is regarded as the outer rigid shell. At its base, the lithosphere-asthenosphere boundary (LAB) marks the transition to the less viscous (more deformable) asthenosphere with reduced seismic velocities. The lithosphere is therefore the core concept for the plate tectonic theory.

For historical reasons, several definitions of the lithosphere exist where most of them are based on rapidly changes of temperature-dependent physical properties (e.g. density, elastic moduli and electrical conductivity) of the upper mantle. These sharp gradients are related to the transition from the conductive (rheologically strong) to the convective (rheologically weak) upper mantle. However, most of the upper mantle physical and chemical properties change only gradually with depth. Thus, constraining the LAB is non-trivial as a gradual change of a property occurs rather than an abrupt change. Five major definitions of the lithosphere exists - *seismic*, *thermal*, *elastic* (flexural), *electric* and *petrologic* lithosphere - potentially resulting in significant thickness discrepancies.

The most important geophysical definitions of the lithospheric base are illustrated in Fig. 2.1 together with some other relations. The thermal boundary layer (TBL) is the layer with dominating conductive heat transfer above the convective mantle and constrains the *thermal* lithosphere. The base of the TBL is between depths Z_1 and Z_3 in Fig. 2.1 and often defined by a depth-dependent isotherm of e.g. 1300°C. Imaged by tomography, the *seismic* LAB, points to depth Z_3 and is the base of the seismic lid. It extends more likely over some tens of kilometers due to the hotter, low-velocity regime below the LAB. This low-velocity zone (LVZ) probably originates from partial melting within the asthenosphere rather than high-temperature relaxation or contrasts in volatile content or in grain size. *Thermal* (or TBL) and *seismic* lithospheric thicknesses can differ by the order of tens of kilometers where the TBL is estimated shallower. Due to the presumed partial melt below the colder lithosphere, the LAB acts also as a *rheological* boundary (RBL). The base of the *chemical* boundary layer (CBL) is similar to the RBL and shallower than the TBL. It marks the top of the convective sublayer estimated by mantle-derived xenoliths, i.e. the CBL corresponds to the transition of the degree of depletion. Alternatively, the CBL can be regarded as the boundary between perisphere and tectosphere.

The lithospheric thermal thickness can be estimated by e.g. exhumed mantle xenoliths (xenolith P-T diagrams), surface heat flow measurements or velocity-to-temperature

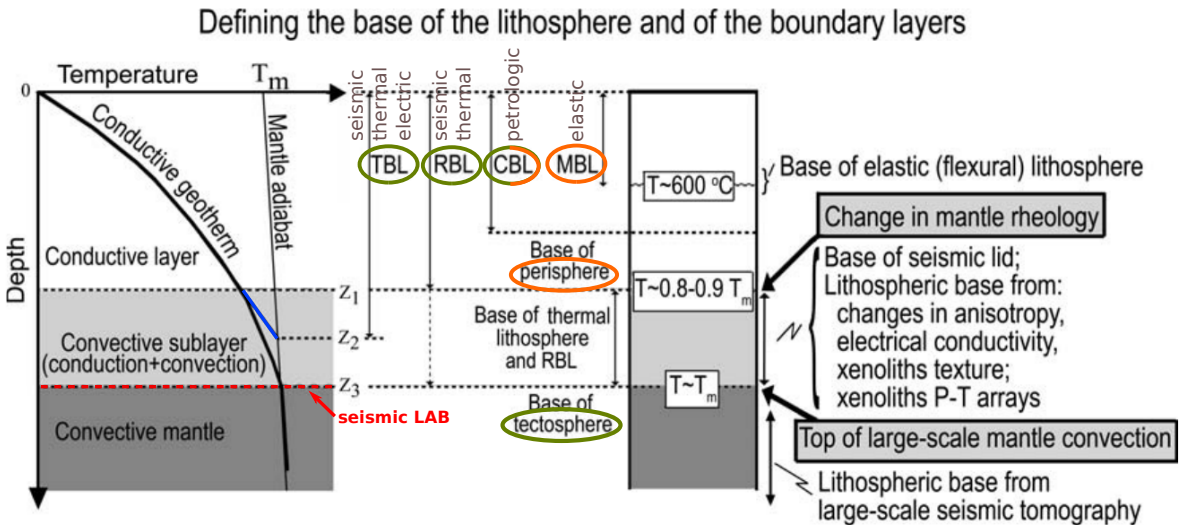

Fig. 2.1: Overview of the different definitions of the lithospheric base as well as the relations between the conductive boundary layer (= TBL) and the convective mantle. TBL, RBL, CBL, MBL are the thermal, rheological, chemical and mechanical boundary layers, respectively. The base of the TBL is between depths Z_1 and Z_3. Z_2 corresponds to the depth where a linear downward continuation of the geotherm intersects with mantle adiabat T_m (blue line) that is representative of the convective mantle temperature profile. Thermal models commonly estimate Z_2, while large-scale seismic tomography images Z_3. The difference between Z_2 and Z_3 can be as large as 50 km. Correspondence between lithosphere and boundary layer definitions (brown text) are also shown as well as other relations (green and orange ellipses). Modified from Artemieva (2011).

conversions. However, xenolith and heat flow methods do not necessarily constrain the corresponding lithospheric thickness (or LAB depth), i.e. the LAB as inferred from xenolith data (*petrologic* lithosphere) does not necessarily correspond to any of the TBL, CBL or RBL bases.

Finally, it should be noted that none of these definitions and methods, applied to measure the lithosphere base, gain a better depth resolution than 50 km.

2.1.2 Evolution of the Lithosphere

After the basic understanding, the lithospheric mantle has the same age as the overlying crust. A LAB is usually formed by mantle depletion and conductive cooling over time. Cooling of the TBL formed the initial cratonic lithosphere with a thickness of several hundreds of kilometers, but with time the lithosphere evolved. The often used tectono-thermal age is the age of the last major tectono-thermal event. One of the oldest continental lithosphere is found in northern Finland as part of the Baltic Shield. Isotopic analyses of exhumed xenolith and crustal samples indicate same ages for crust and the underlying mantle. Therefore, a tectonic stacking of Precambrian terranes is more plausible than gradual (horizontally) lithospheric growth from below.

The upper mantle mainly consists of peridotite. These are ultramafic rocks with olivine as major mineral, ranging from lherzolites (olivine + orthopyroxene + clinopyroxene (+ garnet + spinel)) to dunites (olivine) and harzburgites (olivine + orthopyroxene). This compositional range depends on the degree of depletion as well as pressure and temperature conditions. A *depleted* mantle results from chemical differentiation due to mantle melt reduction. Accordingly, the amount of specific elements as Mg, Ca, Al, Na and K as well as light rare earth elements (LREE, e.g. Sm, Nd, Sc) is reduced (depleted). Undifferentiated portions of the mantle are

called primitive or enriched. A depleted mantle is typical found in low-temperature Precambrian lithospheric keels, while primitive composition is found only in oceanic hot spot regions which are presumably fed by lowermost mantle material. Rocks which are rich in LREE composition are classified as *fertile*. A fertile continental mantle ranges between a primitive convective mantle and a depleted cratonic mantle, e.g. in terms of the Mg content. The degree of depletion is thus a degree of melt extraction (from fertile mantle), often quantified by the iron content in mantle olivine. Higher seismic velocities but reduced density characterize a depleted mantle. A geochemical *refertilization* of the depleted mantle may occur if fertile or less depleted material (e.g. eclogite) is mixing with the already depleted reservoir. *Metasomatism* is a change in the chemical composition with depletion as its major process. On the other side, a melt-related metasomatism is opposite to the depletion process and results in lower seismic velocities and higher density (by iron increase). Melt-metasomatism after Griffin et al. (2005) may alter the chemical composition of the cratonic mantle (refertilization) even several hundreds of kilometers away from the magmatic event.

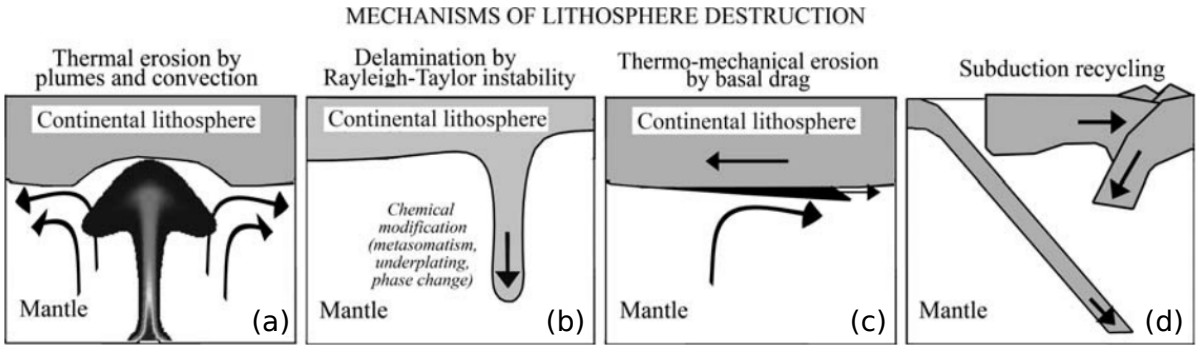

Fig. 2.2: Major mechanisms of lithosphere destruction from Artemieva (2011). (a) Thermal-convective erosion by hot mantle upwelling. (b)-(d) Different thermal-mechanical erosion mechanisms.

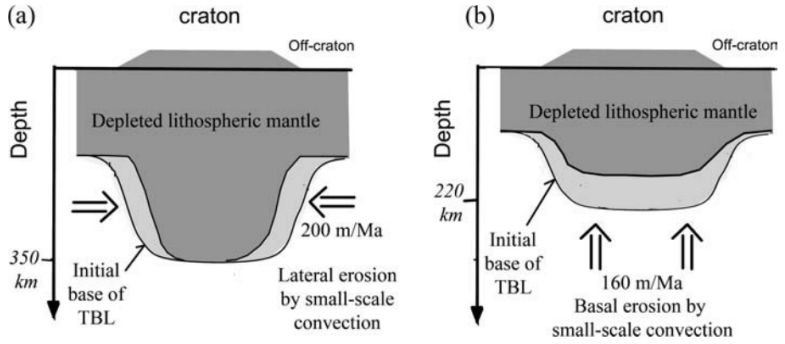

Fig. 2.3: Bimodal erosion of depleted cratonic lithosphere by small-scale sub-lithospheric convection. (a) An initially thick (∼350 km) lithosphere is eroded laterally. (b) A thinner (∼220 km) lithosphere is eroded vertically. Note that lithospheric thermal thickness is regarded here (depth Z_2 in Fig. 2.1). From Artemieva (2011).

The thickness and lateral extent of the lithosphere undergo alteration and destruction due to individual tectonic events (Fig. 2.2) and continuous evolution with time (Fig. 2.3). Plume impingement or any form of asthenospheric upwelling may cause *thermal thinning* by conduction due to an increase of mantle heat flow at the lithosphere base (Fig. 2.2a). *Mechanical thinning* can occur due to delamination as a result of gravitational Rayleigh-Taylor instability (Fig. 2.2b)

in the lower lithosphere (e.g. Rohrman & van der Beek, 1996; Korja et al., 2006). Rayleigh-Taylor instabilities are rather associated with younger lithosphere of low viscosity. Due to the temperature increase in the lower lithosphere (at the TBL) by hot mantle upwellings, convective erosion takes place removing the basal lithosphere layers. Lithosphere thinning results from these convective removal potentially leading to a dome-like surface uplift (e.g. southern Norway (Rohrman & van der Beek, 1996)). While in stable, cold cratonic regions (e.g. southern Finland), thermo-mechanical erosion is less effective due to the large viscosity contrast between the low viscosities of the cratonic root and the convective asthenospheric mantle. However, the resistance of the cratonic lithosphere depends on the degree of melt and hydrogen depletion, where a high degree of depletion does not favor thermo-mechanical erosion. After Doin et al. (1997) bimodal lithosphere thickness stages exist for Archean/Paleoproterozoic cratons yielding to secondary sub-lithospheric convection at their cratonic margins (Fig. 2.3). A thick (∼350 km) depleted lithosphere is in a stable (thermal) equilibrium and eroded laterally where the initial thickness is preserved. The lateral erosion continues until a critical lateral dimension is reached. A thinner lithosphere of ∼220 km is in disequilibrium and eroded vertically. The lithosphere is thinned until a stable balance is reached which can result in a very thin lithosphere < 150 km. Another mechanism for thermo-mechanical erosion is basal drag caused by localized mantle convection related to relative plate motion (Fig. 2.2c). The velocity of the plates seems thereby decisive for the order of basal erosion rates. Basal drag likely reduces the thickness also in case of melt and hydrogen depleted cratonic lithosphere. Today, this destruction type may be neglected as the Baltic Shield is about 2,000 km away from active plate boundaries. Subduction represents the third type of thermal-mechanical lithosphere destruction (Fig. 2.2d) where the oceanic lithosphere is recycled into the mantle. It is important to note that interactions of these erosion mechanisms likely occur along with chemical modifications as metasomatism and crustal underplating.

A zoom into the gravitational Rayleigh-Taylor instability and subsequent lithosphere delamination is illustrated in Fig. 2.4. Such an instability emerges if less dense material underlies denser material (density inversion) as resultant from hot mantle upwelling or lithosphere thickening due to orogeny. In the latter case (Fig. 2.4a-d), a dense mantle lithosphere root can develop (Fig. 2.4e) which leads to a lateral temperature gradient and thermal instability with the surrounding asthenosphere. Convective flow removes the dense root of the mantle lithosphere. The delaminated root descends as a block (Fig. 2.4g). After the delamination isostatic uplift occurs to compensate the mass imbalance. Less dense asthenospheric material replaces the lithospheric root, triggering partial melting and possibly terminating in crustal mafic underplating (Fig. 2.4h).

Another important geodynamic process is a small-scale edge-driven convection (EDC) (King & Anderson, 1998) illustrated in Fig. 2.5. An EDC mechanism can develop if two conditions are met: a sharp step in the lithospheric thickness (>100 km) and a significant lateral thermal gradient in the mantle between the thick and thinner lithosphere. Such a regime can be found at cratonic margins, continent-ocean boundaries or suture zones where terranes of different age adjoin. A sufficient large cratonic lithosphere can cause a thermal insulating effect leading to a temperature increase with respect to the thinner lithosphere. This setting will introduce a long-wavelength convection in the sub-lithospheric mantle (Fig. 2.5 left). At the sharp lithospheric steps, the long-wavelength convection triggers the small-scale EDC. Depending on the thermal anomaly and the time, the EDC can overwhelm

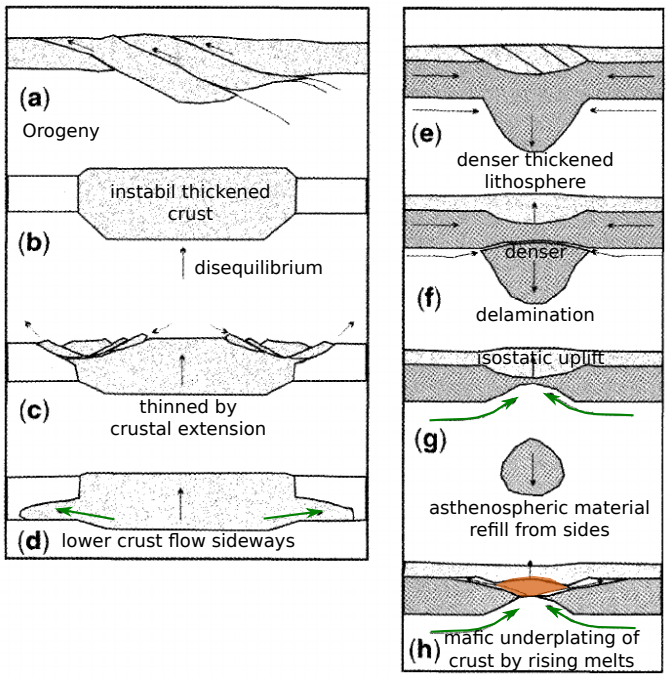

Fig. 2.4: Sketch illustrating lithospheric instabilities modified after Korja et al. (2006). (a)-(d) Due to orogeny the thickened crust is in gravitational disequilibrium. Post-orogenic collapse occurs and the crust is thinned by either upper crustal extension (c) or the lower crust flows sideways (d). (e)-(f) Thinning of the initially thickened lithospheric mantle by Rayleigh–Taylor instability if the mantle lithosphere is denser than the surrounding sub-lithospheric material. Finally, mantle delamination occurs. (g) After the delamination isostatic uplift occurs due to the thinned lithosphere. Asthenospheric material from the sides refills the delaminated lithospheric mantle. The asthenospheric material may initiate partial melting of the upper mantle. Rising melts may cause mafic underplating of the crust (red shaded area).

the long-wavelength convection. If the lateral temperature difference between the thick and thin lithosphere is <0.1-1% the small-scale convection will dominate (King & Anderson, 1998). Initially, the EDC was adduced as alternative explanation for flood basalts of large igneous provinces (King & Anderson, 1995) as they occur at the edges of cratons. But recently, also localized strong low-velocity anomalies have been attributed to this small-scale convection type

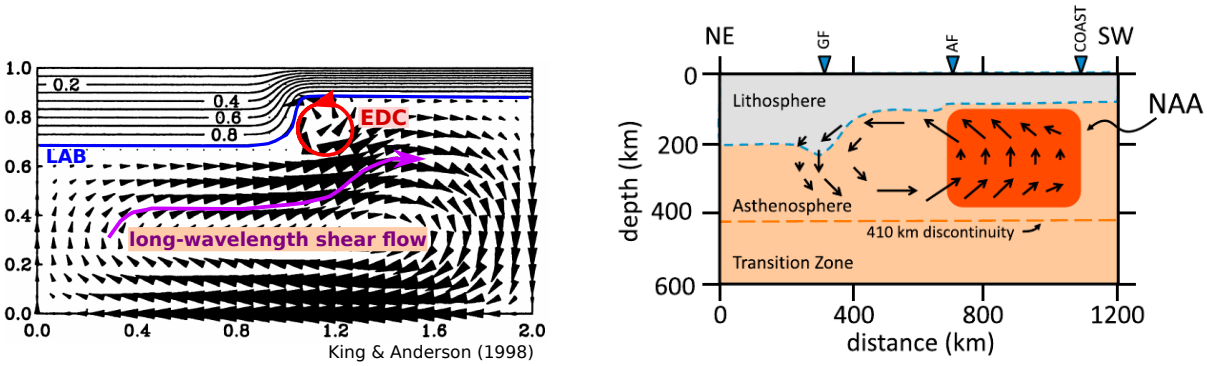

Fig. 2.5: Left: Small-scale edge-driven convection (EDC) modified after King & Anderson (1998). The long-wavelength convection in the sub-lithospheric mantle arise from a thermal anomaly of 1% of the background mantle temperature. An EDC cell is formed at the LAB step. Right: Concept of EDC applied to northeastern U.S. after Menke et al. (2016). NAA is the low-velocity North Appalachian Anomaly which results from upwelling of hot asthenospheric material due to the small-scale convection.

(Menke et al., 2016) (Fig. 2.5 right). Till et al. (2010) modeled that a minimum temperature

of 1350°C and water content are necessary to generate the observed 5-10% V_S drop across the LAB as imaged by tomography studies (e.g. van der Lee, 2002). Such conditions would lead to melt volumes next to the LAB step. Otherwise, Córdoba & Ballmer (2020) have recently shown in a 2D modeling that EDC cells can exist over long time scales without producing melts.

2.2 Tectonic evolution of Scandinavia

A geological map with the major fault zones and tectonic units is displayed in Fig. 2.6. Northeastern Scandinavia consists of one of the oldest terranes on Earth with rocks more than 3 Ga old exposed on the surface. This Archean domain is part of the Baltic Shield (or Fennoscandian Shield) as well as Precambrian terranes from the Early Proterozoic (Paleoproterozoic) in southern Finland and eastern Sweden, known as the Svecofennian domain (2.0-1.75 Ga). Since the shield expands to Russia including the Kola peninsula it is also referred to as the Kola-Karelia Shield. Towards southwestern Scandinavia, younger microcontinents and island arcs have been amalgamated. The south-western part of Scandinavia is dominated by the Proterozoic Sveconorwegian Province (1.2-0.9 Ga) and the Paleozoic Caledonian (500-400 Ma) mountain range along the Norwegian coast. Between these two major tectonic blocks, the Transscandinavian Igneous Belt (TIB) from the Middle Proterozoic (1.8-1.65 Ga) is located (Högdahl et al., 2004; Lahtinen et al., 2009). All of these provinces have been created by multiple episodes of orogeny, extension and rifting starting from about 2.9 Ga ago to the last major event about 60 Ma ago when the North Atlantic Ocean started to open. In the following, I summarize the most important tectonic episodes.

During the Saamian orogeny 3.1-2.9 Ga ago, the Karelia craton has been formed, the oldest Archean crust of the shield, which is still preserved at some spots (Gaal & Gorbatschev, 1987). A long phase of rifting (2.5-2.1 Ga) culminated in continental breakup of the Karelia craton ∼2.06 Ga ago. Subsequently, subduction and back-arc rifting acted on the Archean Karelia and Kola continents (Lapland-Kola area) as well as on the Keitele and Norrbotten microcontinents but the number, dating and orientation of the (multiple) subductions has been often revised during the past decades (e.g., Gaal & Gorbatschev, 1987; Lahtinen et al., 2005; Lahtinen & Huhma, 2019). The subsequent Paleoproterozoic Svecofennian orogenic evolution (Nironen, 1997) (2.0-1.75 Ga) can be divided into five stages (1.92–1.79 Ga after Lahtinen et al. (2005)) where the key stages are the microcontinent amalgamation and the ensuing continent-continent collisions that contribute to the Baltic Shield. The other three stages describe the continental extension, orogenic collapse (∼1.87 Ga) and, finally, the tectonic stabilization. The first stage begins with the collision of the Kola and Karelia cratons (Lapland-Kola orogeny, peak ∼1.91 Ga ago (Lahtinen & Huhma, 2019)) after a southwestward subduction of the Kola below the Archean Karelia continent which led to magmatic intrusions within the Karelia craton in Lapland. Partly overlapping in time, the Karelia craton collided with both the Norrbotten craton and the Keitele microcontinent (∼1.9 Ga) where the western boundary of the Karelia craton has been reworked (Berthelsen & Marker, 1986; Lahtinen et al., 2005). Ongoing collision episodes resulted in the accretion of the Knaften arc (cf. Fig. 5.2) and the Bothnia microcontinent to the Norrbotten craton as well as the docking of the Bergslagen to the Keitele microcontinent (∼1.89 Ga). The latter two microcontinents formed the present south-central Finland which consists of the Central Finnish Granite Massif.

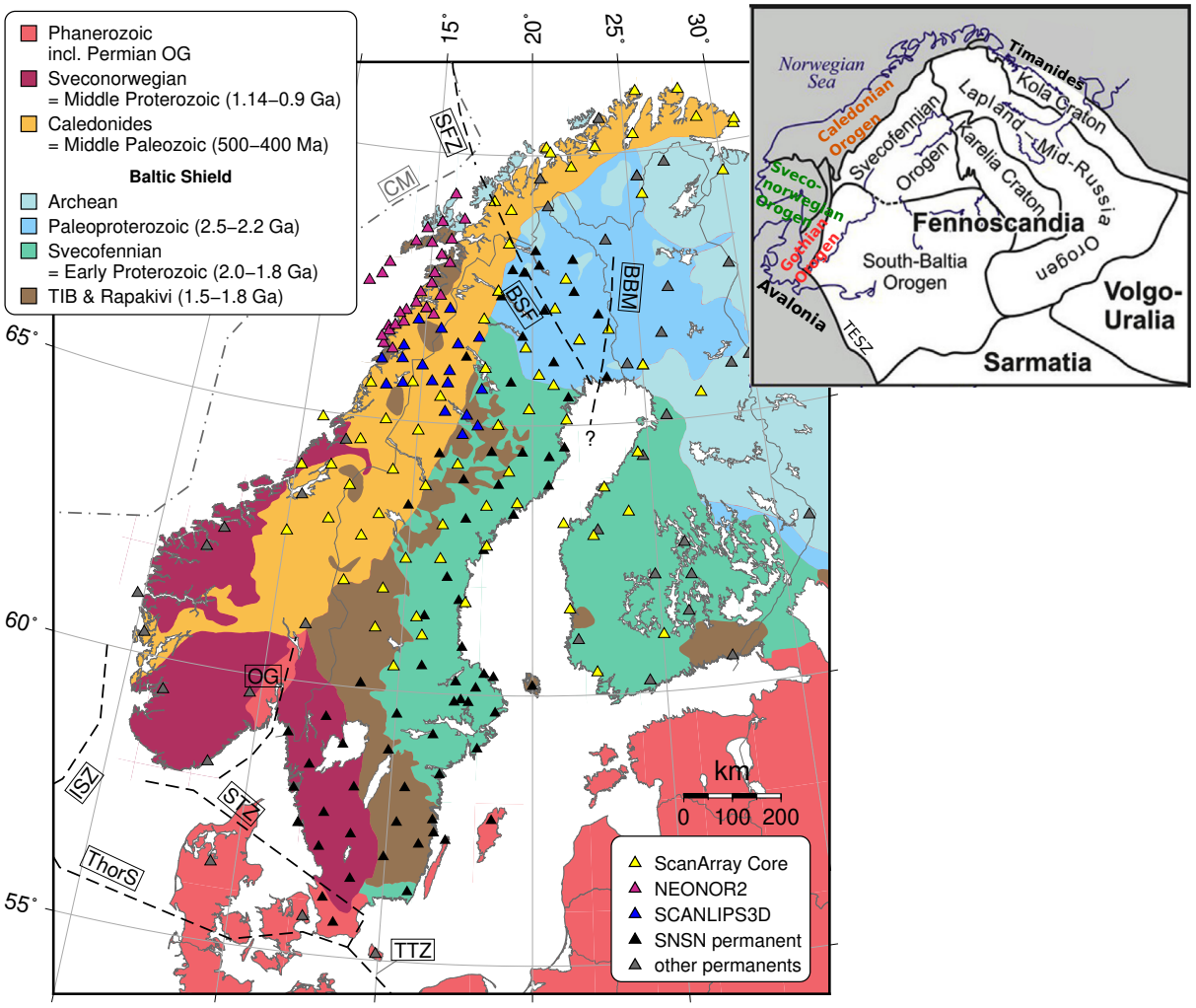

Fig. 2.6: Geological map of the major tectonic units, suture and fault zones as well as station distribution. The age statements in the legend refer to the time of tectonic evolutions. OG = Oslo Rift Graben. ISZ is the potential Iapetus-Suture-Zone; ThorS = Thor suture; CM = Continental Margin. The Sorgenfrei-Tornquist Zone (STZ) is the northern extension of the Teisseyre-Tornquist-Zone (TTZ) which belongs to the >2000 km long Trans-European Suture Zone (TESZ). SFZ = Senja Fracture Zone; BSF = Bothnian-Senja Fault complex. BBM = Baltic-Bothnian megashear. Stations and other networks used for analyses are shown as triangles. The overview map has been modified from Mints et al. (2020).

After the stage of microcontinent amalgamation, the created Fennoscandian continent underwent widespread continent collisions with the Laurentia, Sarmatia and Amazonia continents and an unknown microcontinent shaping the initial Baltic Shield ~1.79 Ga ago. The present exposed Svecofennian domain can be separated into a volcanic north and south sub-province and a metamorphic central district (Gaal & Gorbatschev, 1987). All three sub-provinces are found in eastern Sweden as well as in central and southern Finland.

These episodes of Paleoproterozoic accretion coincide in time with the evolution of the Baltic-Bothnian megashear (BBM) (Berthelsen & Marker, 1986). The NNE-SSW striking BBM is nearly parallel to but likely overprints the Karelia-Norrbotten suture zone (Lahtinen & Huhma, 2019) and presumably extends all the way to Gotland through the Gulf of Bothnia. Another major Proterozoic shear zone is the 30 km wide NW-SE trending Bothnian-Senja fault (BSF) complex (Zwaan, 1995), which probably links up with the much younger offshore Eocene Senja Fracture Zone (SFZ). The BSF has been located by aeromagnetic and gravity anomalies beneath

the Caledonian nappes between Tromsø and Luleå (Olesen et al., 1997).

Episodes of magmatic intrusions formed the TIB crustal emplacement, dated to 1.85-1.65 Ga (partly coeval with the Gothian orogeny 1.75-1.55 Ga), by eastward subduction in the north and northward subduction in the south (Lahtinen et al., 2009; Högdahl et al., 2004). The TIB belt consists mainly of granitoid rocks and can be subdivided into three massifs of different ages. Today, the Paleoproterozoic TIB trends from southeastern Sweden towards the northeast up to the Lofoten peninsula for about 1400 km, where the belt follows the former Svecofennian continental margin.

The Mesoproterozoic Sveconorwegian orogeny between 1.2-0.9 Ga coalesced with the Paleoproterozoic domain and accreted crustal terranes to southernmost Norway and southwestern Sweden by northeastward subduction (Gaal & Gorbatschev, 1987; Gorbatschev & Bogdanova, 1993; Slagstad et al., 2017). Both, during the Gothian and Sveconorwegian-Grenvillian orogenies, the TIB emplacement has been deformed and metamorphosed (Högdahl et al., 2004). The TIB stands out in magnetic and heat flow maps due to its high magnetic susceptibility and high heat production, although only exposed contiguously in southern Sweden and with patchy exposures in central Norway and the Lofoten. Due to the low-density of the TIB crust, its outline is also seen in gravimetric data (e.g., Gradmann & Ebbing, 2015).

After a long period of little tectonic activity, the former Iapetus Ocean began to open about 615-580 Ma ago in late Precambrian due to the continental break-up of Rodinia. This event marks the beginning of the Caledonian Wilson cycle. A series of events in Early and Middle Paleozoic led to the Caledonian orogeny (Roberts, 2003; Brueckner & Roermund, 2004; Krawczyk et al., 2008). The ultimate Caledonian orogeny (Scandian event) commenced in the Silurian-Devonian between 420 and 400 Ma ago when the Baltica plate underthrust the Laurentia plate westward closing the Iapetus Ocean. See next section for more details.

During the Permian, the Oslo Rift Graben has been evolved accompanied by widespread volcanism in several stages with the main episode between 295-275 Ma. The Graben strikes roughly N-S for about 200 km with a width of 35-65 km (Neumann et al., 2004). Another prominent suture zone to the south of the Oslo Graben is the Sorgenfrei-Tornquist Zone (STZ) with its southern extension as the Tornquist-Teisseyer-Zone (TTZ). The TTZ is part of the Trans-European Suture Zone (TESZ) which crosses also Poland and Ukraine. The Tornquist Zone forms a sharp separation between Scandinavia and continental Europe in terms of seismic velocity and lithospheric thickness (Balling, 2000; Cotte et al., 2002). The Tornquist Zone as well as the TESZ result from the collision between Baltica and Avalonia during the Caledonian orogeny.

The latest undisputed tectonic event occurred about 55 Ma ago when the North Atlantic Ocean has been opened as a consequence of the upwelling Iceland plume system. Finally, a passive continental margin was created along the western Scandinavian coast.

Shortly after the Caledonian orogeny, the mountains began to collapse due to repeated extensional and rifting phases (e.g., Braathen et al., 2002; Nielsen et al., 2009b). Since the extent of the Caledonian collapse is still under debate also the causes for the today's high mountain range are controversially discussed (Nielsen et al., 2009b; Smelror et al., 2007; Anell et al., 2009). See next section for more details. The favored explanation is a tectonic uplift in Neogene about 25 Ma ago which would have been the very last tectonic episode in Scandinavia.

Today, the Scandes mountain range can be divided into three segments due to differences

in elevation and east-west extent (Fig. 2.7). The highest summits can be found in southern Norway (2,500 m) with a maximum east-west extension of 400 km. The northern Scandes show a peak elevation of 2,100 m in the Norrbotten province and a horizontal dimension of 250 km. Intermediate heights with a maximum of 1,000 m and east-west dimension of only 150 km characterize the central Scandes. Due to the massive ice coverage in the last glacial period in the Pleistocene, Scandinavia still experiences a vertical land uplift with a maximum of 10 mm/year within the Gulf of Bothnia and along the central Swedish coast line.

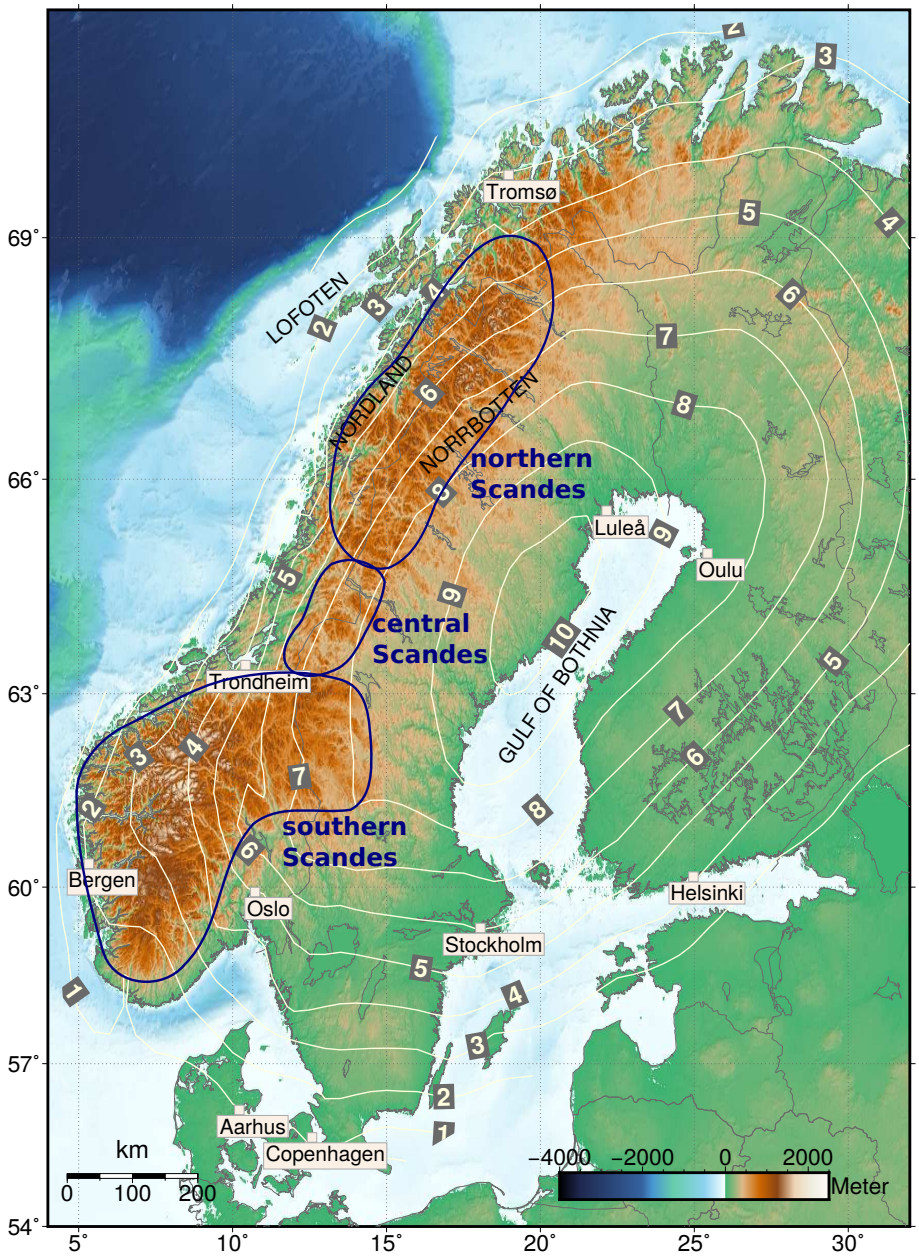

Fig. 2.7: Topographic map of the study area. The Scandes mountain range dominates the western rim of Scandinavia with highest elevation of 2,500 m in southern Norway and 2,100 m in the north (Norrbotten province). White contour lines show the postglacial land uplifts in mm (Vestøl et al., 2019) which are largest around the Gulf of Bothnia and central Sweden.

2.3 The Caledonian orogeny

Caledonian is derived from the Latin word for Scotland, which was initially used in literature and finally adopted for tectonic descriptions in the late 19th century. Already at the turn-of-the-century, geologists where able to identify the spatial and temporal relations between mountain buildings in Scotland, Ireland, Wales and Scandinavia. Nowadays, we regard the Caledonian orogeny in a much wider relation extending to Greenland, Svalbard and the Appalachian mountain range in the northeastern United States.

The tectonic evolution of the Caledonian orogeny in the Early and Middle Paleozoic (500-420 Ma) is illustrated in Fig. 2.8. The northern part of the Caledonian orogen affected Scandinavia and Greenland (Scandian Orogen) due to the collision between the overriding

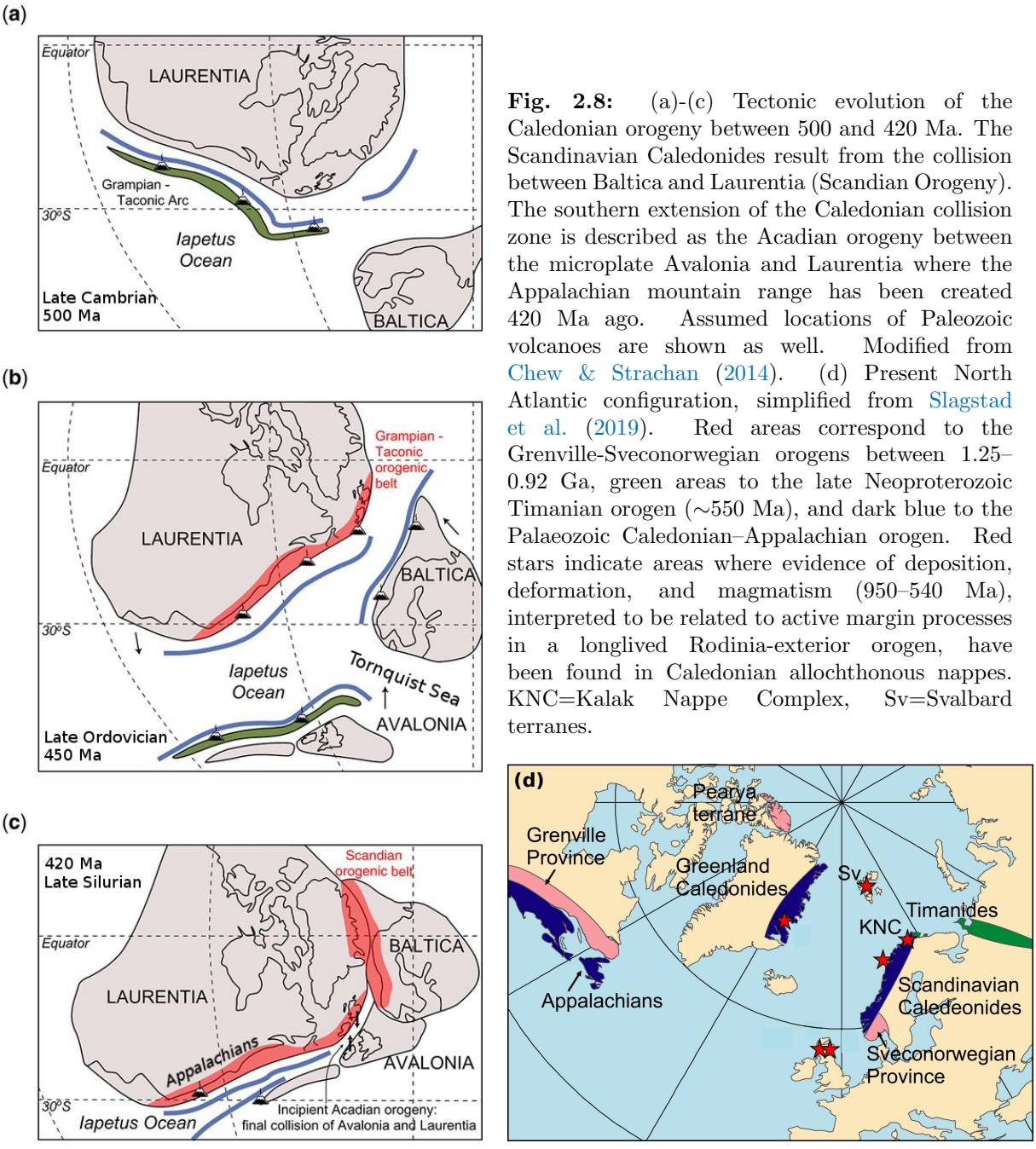

Fig. 2.8: (a)-(c) Tectonic evolution of the Caledonian orogeny between 500 and 420 Ma. The Scandinavian Caledonides result from the collision between Baltica and Laurentia (Scandian Orogeny). The southern extension of the Caledonian collision zone is described as the Acadian orogeny between the microplate Avalonia and Laurentia where the Appalachian mountain range has been created 420 Ma ago. Assumed locations of Paleozoic volcanoes are shown as well. Modified from Chew & Strachan (2014). (d) Present North Atlantic configuration, simplified from Slagstad et al. (2019). Red areas correspond to the Grenville-Sveconorwegian orogens between 1.25–0.92 Ga, green areas to the late Neoproterozoic Timanian orogen (~550 Ma), and dark blue to the Palaeozoic Caledonian–Appalachian orogen. Red stars indicate areas where evidence of deposition, deformation, and magmatism (950–540 Ma), interpreted to be related to active margin processes in a longlived Rodinia-exterior orogen, have been found in Caledonian allochthonous nappes. KNC=Kalak Nappe Complex, Sv=Svalbard terranes.

Laurentian plate and westward subducted Baltica plate. At 420 Ma, northern Scandinavia and Greenland were located close to the Equator. The southern extension of the Caledonian collision zone is described as the Acadian orogeny between Laurentia and the Avalonia microcontinent where Avalonia was subducted underneath Laurentia. Thereby, the Appalachian mountains have been formed (Thomas, 2006). During the Caldonian orogeny the Iapetus Ocean has been closed where several volcanic arc systems have been amalgamated (Fig. 2.9). Cross-section sketches of the Caledonian orogeny are displayed in Fig. 2.9 (left). The top and middle cross-sections show early stages of the Caledonian orogeny and the lower panel displays the final Scandian orogen in Silurian-Devonian times. The direction of the accretion was mainly to the southeast. Four major allochthonous nappes can be identified from the today's surface of the Caledonian mountain belt which have been accreted onto the Precambrian basement of the Baltic Shield (Gorbatschev & Bogdanova, 1993; Corfu et al., 2014). Metamorphic processes of Precambrian rocks during the successive subduction and eduction of Baltica created high-pressure eclogite-facies terranes, gneiss provinces and peridotite intrusions from the mantle into the crust (Brueckner & Roermund, 2004) along the western coast of Norway (Fig. 2.9 right). Parts of the early accreted eclogites and nappes (e.g. SNC) could have been re-subducted during the Scandian orogen (Brueckner, 2006). However, the Lofoten peninsula and the onshore Nordland area were only little affected by the orogeny but resisted the deformation due to a thick granitoid massif (Griffin et al., 1978) additional to a high-density mafic lower crust (Breivik et al., 2017). Therefore, the Lofoten area were likely part of the Baltica plate at the time of the continent collision.

2.4 The Progression of the Scandes mountain range

Shortly after the Caledonian orogeny, a long time period of repeated rifting and extensional phases commenced in Early Devonian probably with a hinterland extension. Evidences for the tectonic extension are given by detachment (e.g. Nordfjord-Sogn) and shear (e.g. Nesna) zones which incise deeply into the basement (e.g., Braathen et al., 2002; Steltenpohl et al., 2011b). Andersen (1998) stated that the Fennoscandian basement further eastward was only little affected by these extensional processes. Thereby, the extensional orientation of the central Scandes is in NE-SW direction while the extension of the northern and southern Scandes occurred mainly perpendicular to the mountain front in E-W direction (Braathen et al., 2002). The origin of the extensional denudation of the Scandes might be a post-orogenic transtensional setting in Late Devonian and Carboniferous times, i.e., a reorganization of the plate-motion configuration from general plate convergence to divergence or transtension (Braathen et al., 2002; Andersen, 1998).

It is widely accepted that the mountain range began to collapse as a result of the rifting and extension processes (Andersen, 1998). However, the extent of the post-orogenic rifting and subsequent collapse is one of the most undetermined questions in Scandinavian tectonics. Therewith also the reason for the today's high-topography is still under debate. The present vertical movement of Scandinavia can be linked to post-glacial isostatic rebound only (Fig. 2.7). Ongoing tectonic uplift is not indicated from GPS measurements by Milne et al. (2001) and also horizontal tectonic motion is less than 1 mm/year.

In Cenozoic times, the North Atlantic region including Scandinavia has been exposed to vertical tectonic uplift (see Anell et al. (2009) for a review) which is proposed by many geological

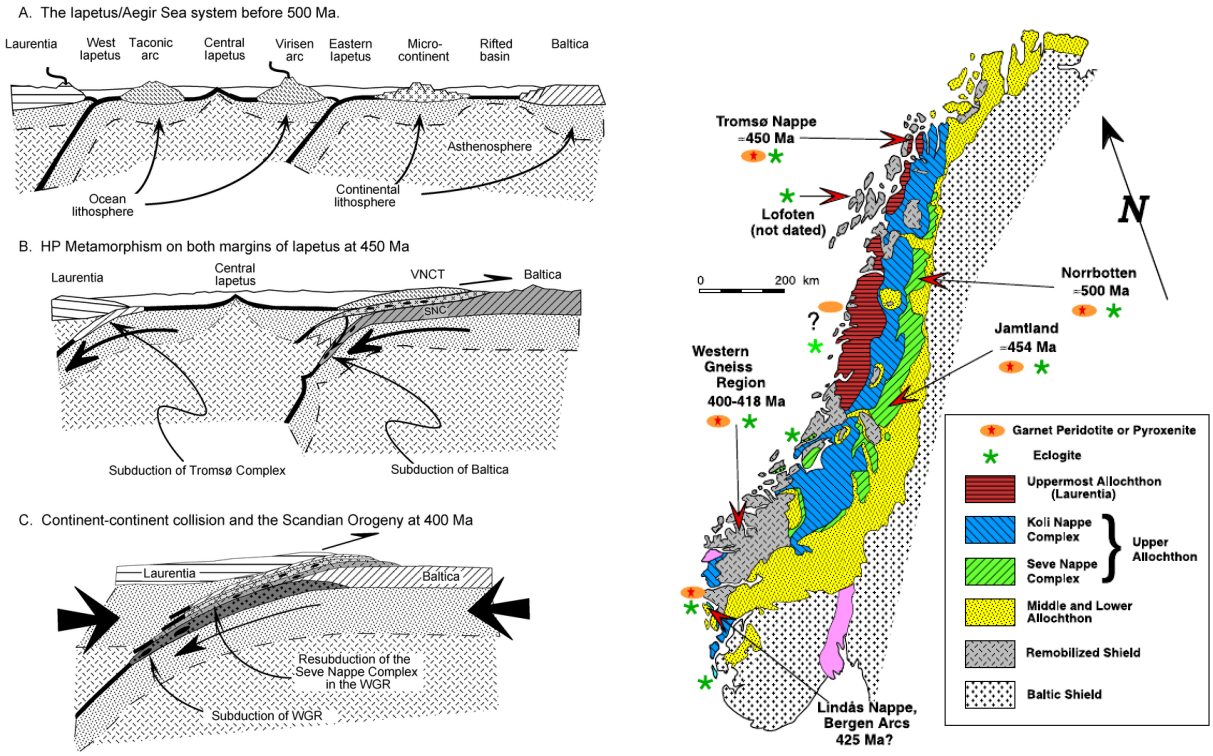

Fig. 2.9: Left: Cross-section sketches of the Caledonian orogeny between 500 and 400 Ma, adopted from Brueckner (2006). (A) and (B) are known as the Finnmarkian and Jämtlandian orogenies, respectively. HP = High-pressure metamorphism; SNC = Seve Nappe Complex. (C) Baltica has been ultimately subducted beneath Laurentia about 400 Ma during the Scandian Orogen. WGR = Western Gneiss Region which consists of reworked Precambrian basement (crystalline rocks). Right: Map of major allochthonous nappes accreted during the Caledonian orogeny, adopted from Brueckner & Roermund (2004).

studies (e.g. Riis, 1996) based on apatite fission tracking. Geomorphological analyses were conducted both on- and offshore as well as age timing of sediments and erosion rates. Generally, vertical and horizontal movements are likely related to the opening of the North Atlantic ocean.

However, different uplift mechanisms and times for the northern and southern Scandes have long been discussed. Riis (1996) and Hendriks & Andriessen (2002) proposed a domal-style uplift in southern Norway that occurred in Neogene with an assumed vertical movement of > 1000 m. The more elongated northern Scandes experienced its latest uplift between Cretaceous to Paleogene times, presumably also with a movement of > 1000 m in the Lofoten area and 600 m further east on the mainland. However, for the Lofoten area major uplift rates are rather related to Neogene and Plio/Pleistocene times (Hendriks & Andriessen, 2002). A coeval subsidence is attributed to the offshore basins (Smelror et al., 2007).

The mechanisms discussed for these uplifts are as manifold as unresolved and no hypothesis is generally applied or accepted. Gabrielsen et al. (2005) concluded that for southern Norway a mantle diapirism model caused by a Rayleigh-Taylor instability is most likely. Thereby, the present high topography of the Scandes is related to large-scale lithospheric processes which are physically able to produce uplifts of $>>$ 100 m. Short-wavelength processes as e.g. faulting within tectonic units induce only $<$ 100 m vertical movements. Based on that general classification and the assumption of nearly isostatic equilibrium of the mountains (cf. Fig. 2.13b), the Neogene uplift might be related to crustal thickening with time or

significant amounts of low-density material which are emplaced in the crust or the mantle. However, a crustal thickening of about 9 km would have been necessary to explain 1000 m uplift which is tectonically not explainable (Gabrielsen et al., 2005). Therefore, mantle (asthenospheric) diapirism is the favored mechanism in southern Norway associated with low-density material that can be accounted for mass compensation of the high-topography mountains (Rohrman & van der Beek, 1996). Hot buoyant material involves a thermal perturbation of the lithosphere and eventually partial melting of the cold continental lithosphere (Artemieva, 2019a). On the other side, there is no evidence for onshore magmatic activity in Norway in Cenozoic times. Rohrman & van der Beek (1996) argued that the lack of volcanism results from a failure of magma rising to the surface during early stages of diapirism. They adopted the diapirism model also for the northern Scandes but without showing a conclusive relation to the plume. A linkage with the Iceland plume is plausible for southern Norway as indicated by more recent North Atlantic tomography studies (Rickers et al., 2013; Schoonman et al., 2017). Whereas the northern Scandes cannot be related to mantle diapirism or convection due to the spatial distance to the proposed plume impingement below southern Norway. Rather, the northern Scandes might result from rift-flank uplift (e.g. flexure of the lithosphere (Stewart & Watts, 1997)) in late Cretaceous to Early Tertiary or isostatic rebound effect after glacial erosion similar to the Barents Sea region uplift (Gabrielsen et al., 2005). Other, possibly intimately tied, mechanisms for regional uplift are:

- Magmatic underplating in the crust if the emplaced material is less dense than the underlying mantle. Otherwise, emplacement of dense, mafic magma would lead to subsidence. But there is no evidence for widespread magmatic underplating (Praeg et al., 2005).
- Crustal delamination caused by eclogitization of the lower crust (Kukkonen et al., 2008).
- Mantle lithosphere delamination (Nielsen et al., 2002) which can also explain offshore subsidence. After Korja et al. (2006), delamination and underplating may consecutively occur leading to isostatic uplift (Fig. 2.4). Full delamination might even trigger crustal melting (Wang & Currie, 2015).
- Differences in mantle density between the oceanic and cratonic lithosphere. Subsidence and uplift may occur when fertile mantle from mantle upwellings interacts with the depleted cratonic lithosphere (Anell et al., 2009).
- Thermal instability causing small-scale convection along the oceanic-continental margin (King & Anderson, 1998).

Praeg et al. (2005) pointed out that a discrepancy exists when adducing mantle diapirism or delamination mechanisms for the uplift since the latest significant uplift occurred only 4 Ma ago in Pliocene. Assuming an interaction with Scandinavia in Neogene, the Iceland plume must have been delayed until > 30 Ma after the onset of the North Atlantic Ocean opening. Praeg et al. (2005) postulated instead an evolution of the upper mantle flow and small-scale convection during the Atlantic ocean opening, associated with plate reorganization, being responsible for coeval subsidence and uplift (referred to as tilting). They assume their hypothesis to be valid for both the northern and southern Scandes. However, they did not discuss the topographic differences along the mountain belt.

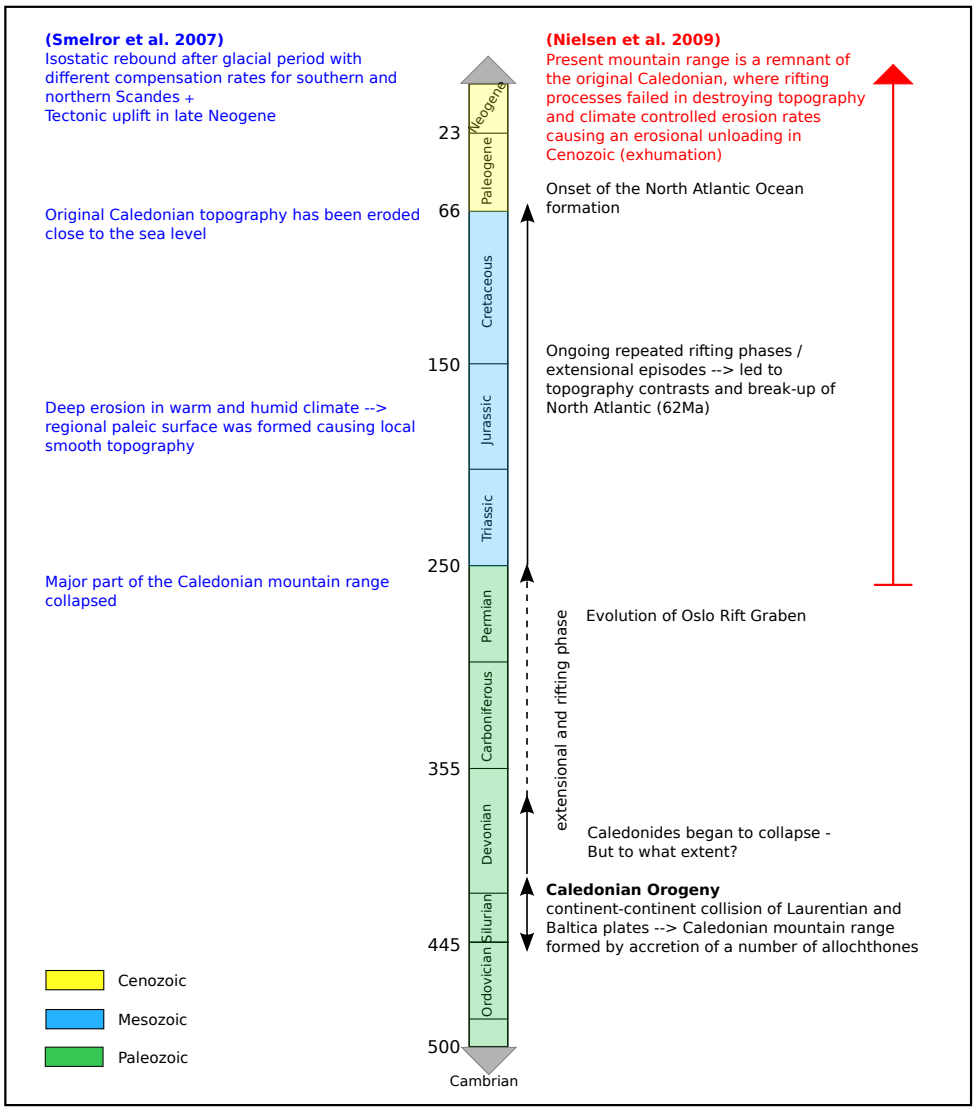

Fig. 2.10: Sketch of two contradictory hypotheses about the fate of the Caledonides after Smelror et al. (2007) and Nielsen et al. (2009b). Black labeled text indicates widely accepted tectonic events.

More recently, two major contradictory hypotheses for the Scandes have been published which are summarized in Fig. 2.10. Smelror et al. (2007) follow mainly the Neogene uplift model with precedent significant climate controlled erosion shaping the paleic surface as the typical fjords. Nielsen et al. (2009b) postulated an alternative model of protracted exhumation of the topography since the Caledonian orogeny based on the same evidences as used for the Neogene tectonic uplift assumption. Thereby, exhumation is caused by gravitational collapse, rifting and erosion whereby tectonic exhumation occurred only during an initial stage. Slow erosion became soon the dominating exhumation factor while tectonic onshore rifting failed in destroying the mountain range. Instead, isostatic buoyancy of the crustal material, which compensates for erosional unloading, is the driving force to preserve the mountains. This theory presumes a much higher topography of the Scandes shortly after the orogeny as it is today.

A vertical tectonic movement during the Neogene have been proposed for numerous mountain ranges all over the world, affecting both active and passive margins and including the Caledonians on both sides of the Atlantic (Hay et al., 2002). However, no unifying and accepted explanation exists for this worldwide uplift. The uplift hypothesis is mainly based on a global observation of

Cenozoic clastic sediments which have been deposited on offshore basins. This deposition might be related to a global climate change which simulates an uplift as an isostatic response to erosion (cf. Nielsen et al., 2009b). On the other hand, a global tectonic effect itself could be responsible for a climate change. This contradictory discussion is known as the climate change paradox where stronger evidence exist for a Cenozoic global climate change than for global tectonic uplift (Anell et al., 2009; Hay et al., 2002). A tectonic origin is difficult to justify. Lithgow-Bertelloni & Gurnis (1997) explained the global Neogene uplift with dynamic topography in consequence of changes in mantle flow patterns associated with a global plate reorganization.

2.5 Results from previous studies

In this section, I summarize the most important findings from previous studies with emphasis on the mantle lithosphere. These studies are mainly based on passive seismic data acquired by the MAGNUS (Weidle et al., 2010), SVEKALAPKO (Bock et al., 2001) and LAPNET (Kozlovskaya & Poutanen, 2006) temporary networks as illustrated in Fig. 5.1.

2.5.1 The Scandes

The most prominent structure of Scandinavia at mantle depth is the low-velocity region below southern Norway (Fig. 2.11 and 2.12), consistently mapped by various studies (Köhler et al., 2012; Medhus et al., 2012; Wawerzinek et al., 2013; Kolstrup et al., 2015; Hejrani et al., 2017) using the MAGNUS network. Significantly reduced seismic shear velocities of 4.4 km/s at 150 km depth were obtained, and Kolstrup et al. (2015) found very low velocities already at 50 km depth below the southwestern Norwegian coast. This shallow LVZ corresponds to a region with high local seismicity but the hypocenters are mainly located in the upper crust (Lund et al., 2017). The potential LAB is surprisingly shallow below the high-topography southern Scandes with a depth <120 km and deepening eastwards with a sharp lateral gradient of about 100 km width across the Oslo Graben. The lateral velocity contrast is up to 5.5% V_S with respect to adjacent southern Sweden (Fig. 2.11f). P- and S-receiver function studies support this thin lithosphere (Frassetto & Thybo, 2013). The low velocities reach at least a depth of 200-250 km. Body wave tomographies map a deeper, contiguous low-velocity anomaly closer to the Oslo Graben and down to at least 400 km depth (Wawerzinek et al., 2013; Kolstrup et al., 2015).

Hejrani et al. (2017) presented a body wave velocity model for the entire western part of Scandinavia but the central and northern Scandes are only poorly resolved (Fig. 2.12). Nevertheless, a sharp transition from very low velocities below the Scandes to higher velocities east of the Caledonian front is seen, similar to southern Norway.

As the lithosphere, also the crustal thickness is generally increasing eastwards below the low-topography Paleoproterozoic domains. Already the FENNOLORA seismic refraction experiment (Guggisberg et al., 1991) revealed a distinctive lower crust with high velocities, i.e., high density, that is thickest below the eastern Baltic Shield and tapers out towards the Scandes. A clear crustal root is absent beneath the highest mountains of the southern Scandes. Receiver function studies by Svenningsen et al. (2007); Stratford & Thybo (2011) and Frassetto & Thybo (2013) imaged only a minor root of ∼39 km depth with an eastward offset by about 60 km from the maximum topography. This is in contrast to the expected mass compensation of Airy-type isostasy for high mountain ranges suggesting that additional types of compensation must be

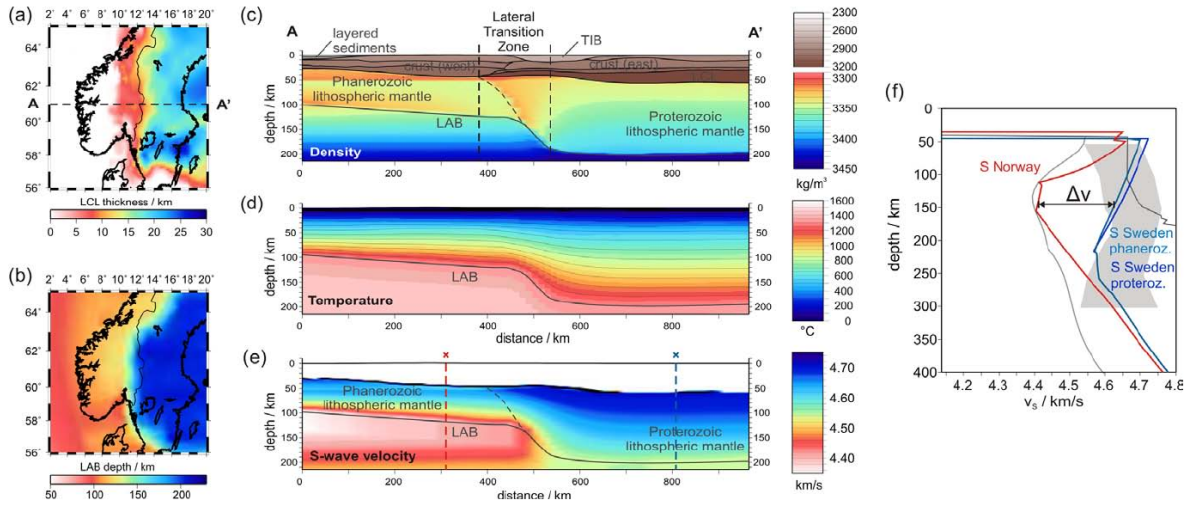

Fig. 2.11: Modeling results from an integrated 3D petro-geophysical approach for southern Norway and Sweden, adopted from Gradmann et al. (2013). (a) and (b) show the thickness of the lower crustal layer and the depth to the LAB, respectively. Both figures are based on measurements from various studies. (c), (d) and (e) Cross-sections along the profile at 61°N shown in (a). The LAB denoted in these cross-sections refers to the 1300°C isotherm which was adjusted during the modeling. The maximum V_S contrast denoted in (f) is around 5.5% at 150 km depth where the grey line refers to the observed data. The red line results from the modeling. The minimum V_S below southern Norway is ∼4.4 km/s.

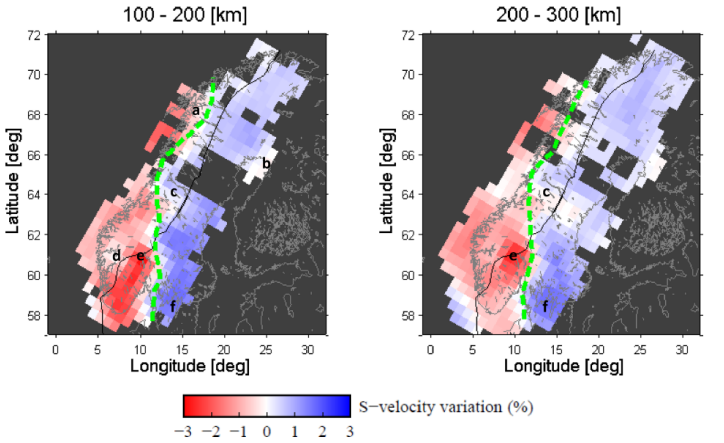

Fig. 2.12: S-wave velocity model at two depth intervals from Hejrani et al. (2017). The green line outlines the upper-mantle velocity boundary which separates the low-velocity mantle below western Scandinavia from the high-velocity Baltic Shield. The black line marks the Caledonian front belt. Letters refer to localized anomalies.

present. Köhler et al. (2012) found a thinning of the crust to ∼30 km towards the coast and the Oslo Graben. Below the northern Scandes, a more pronounced crustal root has been observed by Ben Mansour et al. (2018) with a Moho depth of 46–48 km.

Gravity anomalies must be considered when discussing topography compensation. The complex Free-air gravity anomaly map (Fig. 2.13a) supports the assumption of different types of compensation along the Scandes. In contrast, the Bouguer gravity anomaly map (Fig. 2.13b) indicates a high degree of crustal isostasy since the overall Bouguer gravity low coincides with the topography.

Ebbing (2007) conducted a 3D density modeling and explained the overall isostatic equilibrium of the Baltic Shield with the lateral variation of a high-density lower crust and the

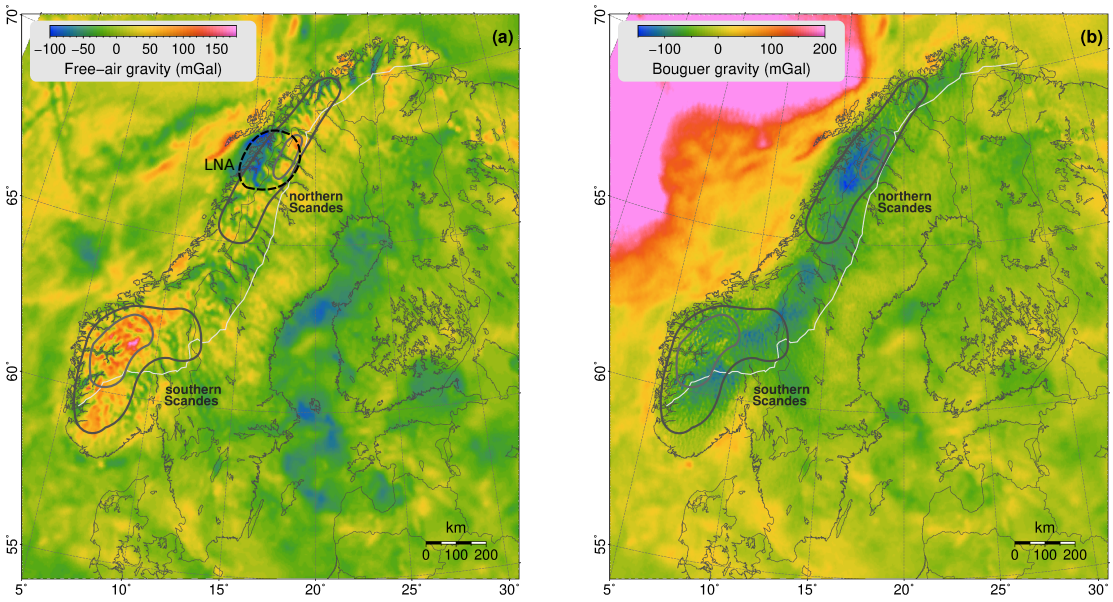

Fig. 2.13: Maps of (a) Free-air (FA) and (b) Bouguer gravity (BA) anomalies of Scandinavia, taken from the EGM2008 model (Pavlis et al., 2008). Grey lines mark the 1,000 m and 1,500 m contour lines. The white line shows the Caledonian deformation front. LNA is the Lofoten-Nordland-Anomaly (see section 5.8). A highly localized negative FA anomaly with dimension 100x150 km appears below the northern Scandes. This anomaly as well as a negative Bouguer anomaly are offset by about 100 km and 50 km, respectively, from the peak elevation. In contrast, the southern Scandes are characterized by positive FA and negative BA gravity anomalies, which coincide with the topography.

lithosphere. Towards the low-topography eastern Baltic Shield the thickness of the dense lower crust is increasing reaching a maximum of 30 km below the Svecofennian southern Finland. Beneath the Scandes, the dense lower crust tapers out to thicknesses of <10 km (Ebbing et al., 2012) in agreement with seismic experiments. Furthermore, Ebbing & Olesen (2005) attributed a strong flexural rigidity of the lithosphere to the southern Scandes. For the southern Scandes, the widespread positive Free-air anomaly (Fig. 2.13a) implies an additional isostatic support by low-density material below the Moho (Ebbing & Olesen, 2005) to fulfill the high-topography load compensation.

The northern Scandes, by contrast, are characterized by pronounced BA and FA lows within the Nordland province which extend over 100x150 km and have a spatial offset of 60 km and 100 km west from the topography maximum, respectively. Gradmann & Ebbing (2015) stated that due to the limited size of the BA and FA anomalies a structural origin seems plausible, rather than a pure dynamic mantle origin. Ebbing & Olesen (2005) concluded that compensating low-density material at shallow crustal depths fit best the Bouguer gravity data derived from their Airy root model. A likely candidate is the TIB structure (Fig. 2.6) with their low-density rocks in the upper crust, but the Bouguer gravity anomaly is not fully consistent with the location of the TIB rocks.

However, the differences of the gravity and geoid gradients along the Scandes indicate a deep source for the northern Scandes gravity anomaly (Gradmann & Ebbing, 2015). A modeled localized and separated fragment from the Archean terrane, placed between 40-100 km depth, within the otherwise Proterozoic mantle below the Nordland province could explain such a negative gravity anomaly. The Archean lithosphere is more depleted in iron, i.e., reduced in density, which creates a positive buoyancy effect. Generally, distinct lateral

density contrasts contribute to such gravity anomalies. Thus, also compositional lithospheric changes e.g., across the ocean-continent margin (which is very close to the Nordland province) or across the Caledonian front (Fig. 2.12) might affect the pronounced gravity low.

Gradmann et al. (2013) carried out 3D petrological-geophysical forward modeling for southern Norway and Sweden (Fig. 2.11) including seismic, gravity and geoid data. To explain the high seismic velocities below depleted Paleoproterozoic southern Sweden, the shallow LAB under Neoproterozoic southern Norway must be deepening down to 200 km. Maupin et al. (2013) and Gradmann et al. (2013) concluded that large differences in temperature (200°C at 200 km depth) and mantle composition across the lithospheric step are needed to explain the laterally varying velocities. Changes in composition are reasonable due to the different tectonic units of different age as the age is a key parameter in controlling the degree of mantle depletion. Additionally, a thick, dense lower crustal layer is incorporated in the model to fit best the gravity data and isostatically compensated elevation (cf. Ebbing & Olesen, 2005).

2.5.2 Svecofennian domains

Below southern Sweden the velocities are much higher up to 4.7 km/s at 150 km depth (Cotte et al., 2002; Shomali et al., 2006; Köhler et al., 2015). The study region in southernmost Sweden links to the former TOR deployment (e.g., Shomali et al., 2006), which revealed a sharply thinning lithosphere with decreasing V_P and V_S values towards the south (Eken et al., 2007)(Fig. 2.14) and across the Sorgenfrei-Tornquist-Zone (Medhus et al., 2012). Along the Svecofennian domain in Sweden, Eken et al. (2007, 2008) conducted P- and S-wave tomographies using the SNSN network (Fig. 2.14). Large portions of the Svecofennian mantle below central Sweden appear with high velocities down to 250 km depth. To the north, the adjacent Norrbotten province (denoted as Archean in Fig. 2.14) can be clearly separated with reduced velocities (up to -3% V_P with respect to the iasp91 reference model) ranging between 100–300 km depth.

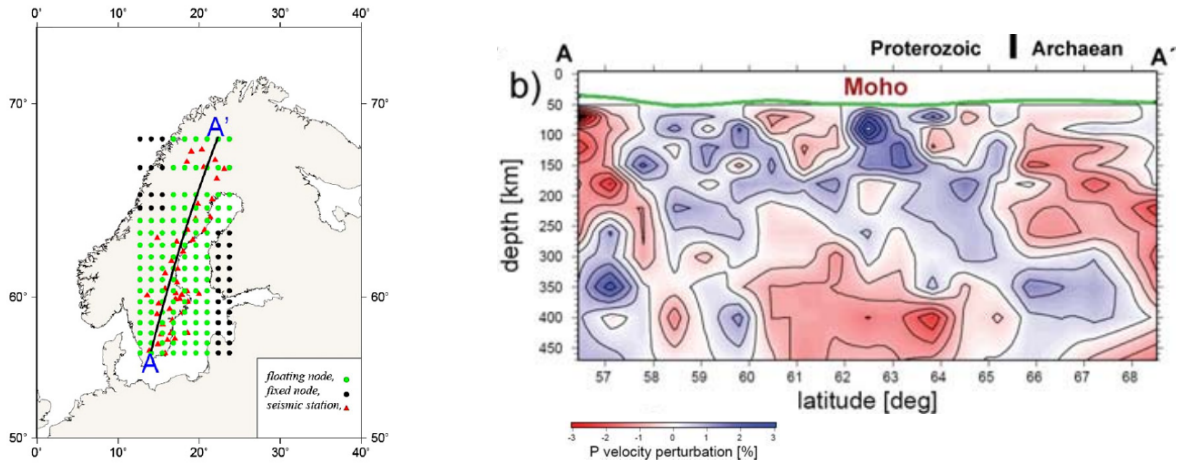

Fig. 2.14: P-wave tomography by Eken et al. (2007). The profile AA' runs from southernmost Sweden through the Proterozoic Svecofennian domain to the Paleoproterozoic Norrbotten craton in northern Sweden, similar to my profile S13-N25 in Fig. 5.15. The green line in (b) defines the Moho.

The Svecofennian terrane in south-central Finland is characterized by the thickest crust of Scandinavia having a Moho depth of ∼65 km (e.g. Sandoval et al., 2003; Hyvönen et al., 2007; Kozlovskaya et al., 2008). The thick crust results from the accretion of several Paleoproterozoic terranes and has been subsequently altered by intra- and underplating, emplacing high-density

material (Central Finnish Granite Massif) (Hyvönen et al., 2007). Sandoval et al. (2004) found from a P-wave tomography using the SVEKALAPKO network a high-velocity lithospheric keel down to at least 300 km depth. The surface wave tomography by Bruneton et al. (2004a), however, revealed a much more complex upper mantle with small-scale lateral variations of <150 km. Below the neighboring Archean domain, the shear velocities are strongly reduced between 80-150 km depth but this area might be affected by the aforementioned crustal effects. Towards the western coast of south-central Finland, the velocities are much higher in the same depth range. Bruneton et al. (2004a) concluded that the complex lithosphere results from variations in the composition of different rock types of the Archean and Proterozoic domains.

2.5.3 Archean and Paleoproterozoic domains

The P-wave tomography by Silvennoinen et al. (2016) (Fig. 2.15) using the LAPNET data imaged the Karelia and Norrbotten cratons in northern Finland and northern Sweden, respectively. They found LVZ with a maximum reduction of -3.5% with respect to the iasp91 reference model at different depth ranges. A shallow LVZ is observed between 100–200 km depth below the Karelia craton slightly deepening to 150–200 km depth under the Norrbotten craton (denoted as IV in Fig. 2.15). The deeper LVZ ranges from 200-300 km depth and seems to connect with the shallow LVZ. The uppermost mantle (80–150 km depth) of the Norrbotten craton is characterized by a fast anomaly (denoted as II in Fig. 2.15) and might correspond to the non-reworked Archean lithosphere.

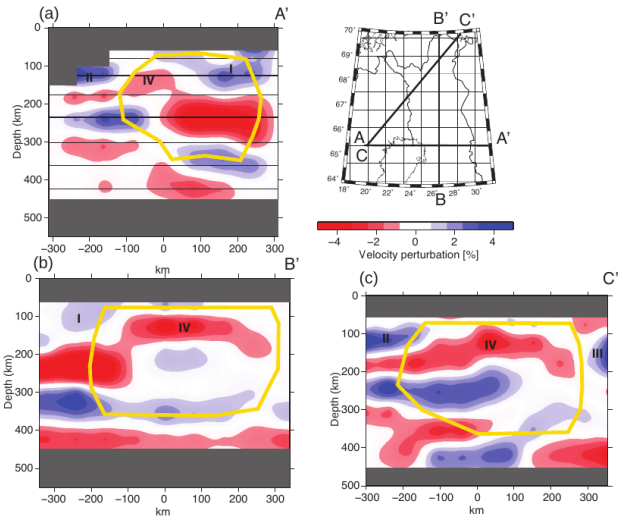

Fig. 2.15: Cross-sections from the teleseismic P-wave tomography by Silvennoinen et al. (2016). They used the LAPNET network deployed on the Archean and Paleoproterozoic northern Finland. Strong low-velocity regions at two different depth ranges were imaged. The yellow lines mark the fairly well-resolved area.

A low-velocity region below northern Finland has also been imaged by Vinnik et al. (2016) with receiver functions. They found the LVZ at depths ranging from 160–240 km with a V_S contrast of -0.2 km/s with respect to an overlying high-velocity layer which is absent in Silvennoinen et al. (2016). Similar velocity contrasts were obtained by Pedersen et al. (2013) where the LVZ is situated between 150-220 km depth. Pedersen et al. (2013) concluded that combined effects of refertilization, temperature and compositional changes are required to satisfy the observed velocity reduction. Vinnik et al. (2016) proposed partial melting as the cause of the LVZ based on the fact that the geotherm is close to the solidus of wet peridotite at the LVZ upper boundary depth (Thybo, 2006).

Chapter 3

Theory & methods

3.1 Surface waves

Two wave types are emerged from any seismic source: Body waves which travel deeply through the Earth and incident from below at the receivers. Surface waves are generated by the interference of body waves and propagate along the Earth's surface. Thereby two types of surface waves can be distinguished: Rayleigh waves and Love waves. The latter are transversely polarized and require a vertical velocity gradient with depth; they do not exist in a halfspace. Love waves originate from constructive interference of multiple reflected SH body waves within a shallow wave guide. I focus on Rayleigh waves which are radially polarized, i.e., they show a combined vertical and radial motion. Rayleigh waves can exist in a uniform halfspace but without showing dispersion. The generation of Rayleigh waves is more complex compared with Love waves. They can be derived from the wave equation where coupled, inhomogeneous P and SV body waves are trapped in an interface below the free surface. The amplitude decay of surface waves with epicentral distance is much less than for body waves, but the displacement amplitude decays, approximately exponentially with depth and proportionally to the horizontal wavelength λ_x. Usually, the particle motion is elliptical and retrograde at the surface and become prograde below a depth of $\sim \lambda_x/5$.

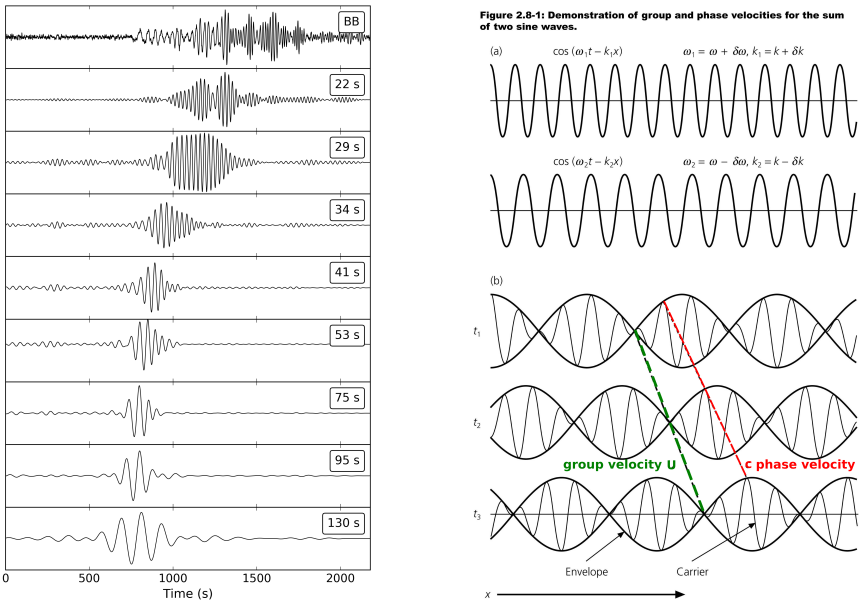

Fig. 3.1: Left: Example of a surface wavetrain from a teleseismic event recorded at the ScanArray station SA27. The unfiltered broadband trace (BB) is shown in the top panel and zoomed around the surface waves. Below, the BB seismogram has been filtered with a sequence of band-pass filters where the center period is labeled on the right. Due to the dispersive nature of surface waves the fundamental mode with longer periods arrives earlier since it samples deeper into the lithosphere with higher medium velocity. Right: Group and phase velocities can be derived from the surface waves as shown here on a synthetic seismogram. Modified after Stein & Wysession (2003).

The most important and useful feature of surface waves is their dispersive nature: For different periods they propagate with different wave speeds (Fig. 3.1 left). The penetration depth of surface waves thereby increases with increasing period. As the surface wave velocity varies with frequency and depth, it is only an apparent velocity along the free surface (in contrast to the intrinsic shear velocity of the medium). We can distinguish between a phase (c) and group (U) velocity as illustrated in Fig. 3.1 right.

$$c(\omega) = \frac{\omega}{k(\omega)} \tag{3.1}$$

The phase velocity c is measured from an individual wave peak or trough as the result of the sum of two waves with slightly different frequency, or in terms of real data, from a narrow-bandpass filtered signal.

$$U = \frac{\mathrm{d}\omega}{\mathrm{d}k} = c\left(1 - k\frac{\mathrm{d}c}{\mathrm{d}\omega}\right) = c - \lambda\frac{\mathrm{d}c}{\mathrm{d}\lambda} \tag{3.2}$$

The group velocity is the velocity with which the energy of a wave packet moves, i.e., U is measured from the corresponding envelope. U is equal to the derivative of ω with respect to the wave number k, i.e., it is the change of the phase velocity. As a rule of thumb, the phase velocity is about 90% of the intrinsic shear velocity.

In terms of the wave equation, the contribution of the Rayleigh mode j to the vertical component of seismogram s(x,t) is

$$s(x,t) = \int_{-\infty}^{+\infty} A(p_j(\omega),\omega) * \exp\left\{i[-\omega t + \underbrace{\omega p_j(\omega)x}_{\mathrm{k}(\omega)\mathrm{x}} + \Phi_j(\omega)]\right\}\mathrm{d}\omega \tag{3.3}$$

with source amplitude A, recorded at epicentral distance x at time t after the earthquake origin, frequency ω, slowness $\mathrm{p}_j(\omega)$ and $\Phi_j(\omega)$ as the source phase term where the phase velocity $c(\omega) = 1/p_j(\omega)$. This formulation is valid only along a great-circle propagation. By taking the Fourier transformation of seismogram s(x,t) (eq. 3.3), the phase Ψ is obtained

$$\Psi = \omega t - k(\omega)x + \Phi_j(\omega) + 2n\pi = \omega[t - x/c(\omega)] + \Phi_j(\omega) + 2n\pi \tag{3.4}$$

The first term refers to the phase variation in time and space. Φ_j is the initial phase due to the source and any phase shift caused by the seismometer. The last term is known as the 2π cycle-skip ambiguity where the phase would be indistinguishable from multiple cycle arrivals. A potential bias caused by cycle-skipping is discussed in Tilmann et al. (2020) and seen in Fig. D.5. In surface wave tomography one nearly always assumes n=0. Otherwise, $2n\pi$ can be found empirically with a reasonable phase velocity at long periods (Thurber & Ritsema, 2015), e.g. from synthetic tests, or by using robust reference dispersion curves (Sadeghisorkhani et al., 2018).

Phase velocities can be generally determined by measuring phases from phase differences between multiple stations (array), phase differences between source and receiver (multiple earthquake analyses), multi-mode synthetics or two-station method. All of these methods cancel out the source term. The two-station method requires the two receiver locations to be aligned with the propagation azimuth, maybe within a tolerance of 5°. This reduces the

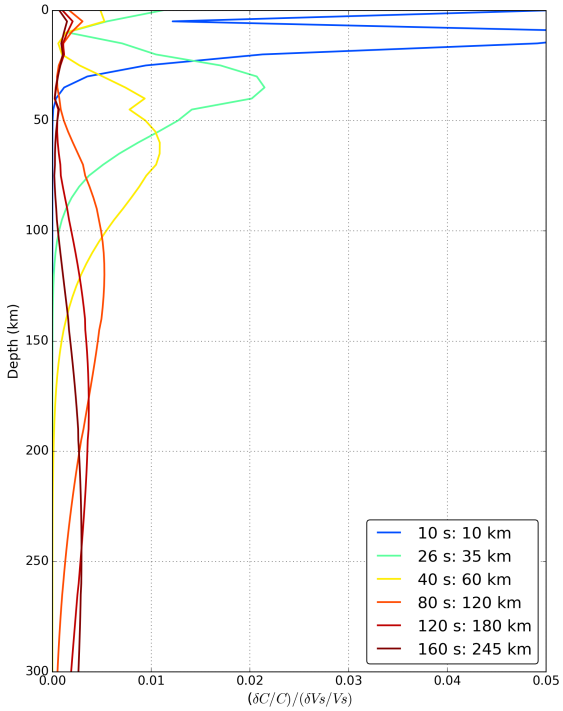

Fig. 3.2: Sensitivity kernels relate the phase velocity to the Earth's structure (Levshin et al., 1989). The fundamental mode of the Rayleigh wave is shown here for various periods calculated from a model of southern Finland (Bruneton et al., 2004a). The depth where the sensitivity kernel is maximum is noted in the legend. It is seen that Rayleigh waves are sensitive to the upper mantle over a broad depth range. Input phase velocities are taken from the dispersion measurements in chapter 5.

amount of paths significantly, resulting in lower lateral resolution, compared with multiple array station analysis where an azimuthal alignment is not required. In case of a single-station method, the source must be explicitly known and synthetic references, or alternatively regional average dispersion curves, are needed. Due to the 2π ambiguity, a direct phase velocity measurement from only one station is mostly not achievable even if the source term would have been known (Laske & Widmer-Schnidrig, 2015).

The fundamental mode of surface waves is generally sensitive to the shear velocity structure down to depths of about one third of the wavelength. Good signal-to-noise ratios of the surface wave train are typically obtained for periods <200 s. Therefore, surface waves are well suited to resolve upper mantle heterogeneities. Fig. 3.2 shows the sensitivity kernels for the fundamental Rayleigh mode of various periods up to 160 s, calculated for an appropriate velocity model for the Baltic Shield. The kernels have been calculated with *senskernel-1.0* after Levshin et al. (1989). Rayleigh waves for a given period are sensitive to the shear velocity structure over a broad depth range.

3.1.1 Surface wave tomography

The key requirement in surface wave tomography is to isolate an individual mode (e.g., fundamental Rayleigh mode) and using the frequency variation to create a phase velocity dispersion curve. Since the physical relation between surface wave dispersion and the velocity structure of the medium is nonlinear, the classic inversion needs to be done in two steps. There are recent advances to carry out the depth inversion directly from the period-dependent phase measurements, (e.g., Zhang et al., 2018), but this is beyond the scope of this thesis. In the classic approach, the first step requires the calculation of 2D phase velocity maps. Hence, for each geographical location a dispersion curve is obtained. The geographical location can be either a discrete point resultant from one-station phase velocity analysis or it corresponds to the average path between two stations, interpolated at discrete grid nodes. The latter method

is easier to conduct because knowledge of the source parameters is not required. Generally, two or multiple station methods (e.g., Prindle & Tanimoto, 2006; Jin & Gaherty, 2015) involve the cross-correlation of the surface wavetrains to examine the relative phase shift and therewith the phase velocity between the station pairs (see chapter D). In the second step of tomography, a 1D (non-)linear inversion of each dispersion curve is necessary to obtain the intrinsic shear velocity. Ultimately, a 3D shear velocity model can be constructed. Group velocities tend to be more sensitive to lower depths than phase velocities, i.e., shallower crustal structures. Covering lower periods are useful to reduce the trade-off between crustal depth and uppermost mantle velocities. Instead of using group velocities, I use phase velocity measurements of the short-period ambient noise to resolve the crustal structure.

A vital approximation which is widely used in (surface wave) tomography is the path-average approximation (PAVA) introduced by the pioneering ray based tomographic inversion by Woodhouse & Dziewonski (1984). The PAVA theorem is valid when the lateral dimension of the heterogeneity is much larger than the dominant wavelength and the heterogeneity is present along the path integral between source and receiver. The phase perturbation is finally recorded as the average along this great-circle path. Surface waves are perturbed by only little deviations from the great-circle path. Hence, PAVA is often equated with a great-circle approximation but is in general also true for curved ray paths. After the notation in Woodhouse & Dziewonski (1984), perturbations of the phase Ψ affected by a lateral heterogeneity are approximated by

$$\delta\Psi = \int_0^t \delta\omega_{local}\ \mathrm{d}t \tag{3.5}$$

with the integral respect to the group travel time t along the great-circle path and $\delta\omega_{local}$ being the local frequency shift due to any smooth lateral inhomogeneity. The latter can be expressed with

$$\delta\omega_{local} = \delta\omega_{local}(\theta, \Phi) = k\delta c(\theta, \Phi) \tag{3.6}$$

where k is the wave number times the perturbation to the phase velocity c at epicentral distance θ. The total phase perturbation $\delta\Psi$ is expressed with two integrals along the major (minor) arc with group travel time t_x and along the complete great circle with group travel time T

$$\delta\Psi = \int_0^{t_x} \delta\omega_{local}\ \mathrm{d}t + n\int_0^{T} \delta\omega_{local}\ \mathrm{d}t \tag{3.7}$$

The phase perturbation in eq. 3.7 can be reproduced by introducing a fictitious frequency shift $\delta\hat{\omega}$ and a fictitious perturbation in epicentral distance $\delta\theta$ with

$$\delta\Psi = \pm(l + 1/2)\delta\theta + \delta\hat{\omega}(t_x + nT) \tag{3.8}$$

This leads to eq. 3.9 which is the valid form of the phase perturbation for all orbits and n complete great circles

$$\delta\hat{\omega} = \frac{1}{T}\int_0^{T} \delta\omega_{local}\ \mathrm{d}t = \text{great-circle average} \tag{3.9}$$

It is shown that the apparent frequency shift $\delta\hat{\omega}$ is the great-circle average of $\delta\omega_{local}$. Both the apparent frequency and distance shifts are different for each mode and each path.

In PAVA, perturbations due to structure next to the path (i.e. finite-frequency effects) are ignored and only the path contributions for the first-order perturbation in the phase is accounted for. Additional terms for source and receiver perturbations are neglected thereby (Dahlen & Tromp, 1998).

3.1.2 Limitations of surface wave tomography

Aside from trivial resolution limits owing to unequal source and receiver distributions, I summarize further tomography limitations. Generally, surface waves have a lower lateral but better depth resolution compared with body waves. By using only the fundamental Rayleigh mode, the depth resolution within the uppermost mantle is about 30-50 km (Artemieva, 2011). The lateral resolution, i.e., the smearing of the velocity structure, depends on the wavelength, defined by V_S times the dominant period.

Constraining the lithospheric thickness, i.e., imaging the seismic LAB, strongly depends on the regularization scheme where a trade-off exists between smoothing of amplitudes and the gradients of velocity anomalies. Regularization can be achieved by damping (minimization of amplitudes) or smoothing (minimization of first or second order model derivatives). A common regularization is the damped mean (least) square approach where a weighting parameter controls the difference between the data misfit and model variance. It is suited best for models with large-scale velocity anomalies while small-scale perturbations should be carefully interpreted. Kennett (2006) stated that strong structural contrasts, as in case of ocean-continent transitions, damping will not match the real structure but likely underestimate the true velocity perturbations.

The choice of the starting (reference) model is another factor. A comparison between different tomography models should be drawn carefully with attention to the reference model used and absolute versus relative velocities. When relative velocity perturbations are considered, an imaged LVZ could be an artefact, especially if the PREM reference model is applied to continental regions. The PREM model includes a sharp velocity drop at 220 km due to the dominance of oceanic mantle structure. This can produce a significant bias when continental areas are investigated (Artemieva, 2011; Pedersen et al., 2009). To overcome such a bias, inversion schemes based on Markov chain Monte Carlo (McMC) techniques can be used.

Since ray theory is a high-frequency approximation, inaccuracies of the widely applied PAVA are well-known as neither for body nor for surface waves the finite-frequency effects are considered (Liu & Gu, 2012). Deviations from PAVA are well documented for both short periods around 20 s (see Fig. 4.5), which are sensitive to crustal scatteres (multipathing effect), and long periods $>$ 100 s causing anomalous amplitude variations among multiple wavetrain circles (focusing effect) (Romanowicz, 2002). Large deviations from the great-circle path, which violates the basic assumption of this theorem, have often been reported (e.g., Cotte et al., 2000; Chen et al., 2018). Off great-circle path propagation might generate an error of up to 6% in the measured phase velocities (Laske & Widmer-Schnidrig, 2015).

With increasing degree of structural heterogeneity, the high-frequency approximation, as well as the plane wave assumption on a regional scale are violated. Different perturbations along the propagation path can occur as multipathing (diffraction and scattering of the wave) and wavefront healing, resulting in distorted velocity measurements.

3.1.3 Phase velocity inversion with TPW

Surface waves are usually distorted by inhomogeneous structure along the propagation path and do not arrive with planar energy at the receivers. To account for this multipathing effect the incoming wavefield can be assumed, to a first order, as the superposition of two simple plane waves, a method established by Forsyth & Li (2005). This study is known as the two plane waves method (TPW) and utilizes a local, event-based coordinate system, which is aligned with the great-circle path between the epicenter and a reference station. This type of coordinate system accounts effectively for the curvature of the incoming wavefront and aims to flatten it but preserves distances between the grid nodes. The site with the maximum amplitude of all array stations is chosen as the reference site, as the two waves can be assumed to have interfered fully constructively at this location. The predicted displacement at frequency ω relative to the reference station due to the interference of the two horizontally traveling waves can be described as

$$U_i^k = {}_iA_1(\omega)\exp(-i\ {}_i^k\Phi_1(\omega)) + {}_iA_2(\omega)\exp(-i\ {}_i^k\Phi_2(\omega)) \tag{3.10}$$

where i the event recorded by station k and $A_{1,2}$ are the amplitudes. The phase terms ${}_i^k\Phi_{1,2}(\omega)$ can be split into a term describing the phases at the reference station and a term describing the phase difference to the reference station to account for the 2D velocity variations and the direction of propagation. Therefore, only six parameters at each frequency define the wavefield, i.e., the amplitudes, the reference phases and directions of the two waves.

With this technique the phase velocities can be inverted for lateral and azimuthal variations. The phase velocity is regarded as azimuthally anisotropic in each grid node j and given by the formulation after Smith & Dahlen (1973):

$${}_iC_j = B_{0,j} + B_{1,j}\cos 2{}_i\theta_j + B_{2,j}\sin 2{}_i\theta_j \tag{3.11}$$

where ${}_i\theta_j$ is the backazimuth from grid node j to event i.

The inversion occurs in two major steps. In the first step, velocities are fixed (either with the starting model or previous iteration values) and wave parameters are inverted via grid search for each event individually. A grid search is used in my code version instead of a the simulated annealing approach described in Forsyth & Li (2005). The second inversion step uses the generalized least-square technique after Tarantola & Valette (1982) to invert simultaneously for changes to the phase velocity and azimuthal anisotropy as well as the six wave parameters at each grid node.

The TPW method approximates scattering best for only smoothly varying amplitudes and phases between neighboring stations. Likewise, the bandpass filtered input waves should not contain multiple beats (see Fig. C.5).

3.1.4 Inversion with transdimensional McMC

Linear inversion schemes (Aster et al., 2013) have been applied to geophysical problems for many decades, in the beginning mainly in the interest of computational costs. Nonlinear problems in seismic tomography have been often linearized by adopting the pioneering work by Tarantola & Valette (1982) which incorporates a trial solution and an iterative approach to improve the model, resulting in one optimum model. However, a simple grid search over model parameters becomes insufficient when sampling a huge parameter space to find the best model. Therefore,

purely nonlinear approaches, which avoid any linearization, became increasingly popular with increasing computational power (Rawlinson et al., 2014).

Global optimization methods such as Monte Carlo are the most common fully nonlinear inversion types where the best fitting model is found directly by repeated randomly drawn parameters from a multidimensional parameter space. Several direct search Monte Carlo techniques have been developed for geophysical problems, among them simulated annealing, genetic algorithms, neighbourhood algorithms and Markov chain Monte Carlo (McMC) (Sambridge & Mosegaard, 2002). I introduce here the concept behind the latter method, as McMC inversion techniques are applied to the 2D ambient noise (Tilmann et al., 2020) and 1D shear velocity inversions (Dreiling et al., 2020) in this thesis.

Markov chains describe sequentially random changes to a sample drawn from the multidimensional parameter space through a random walk, i.e., a sequence of models is generated within a chain. Each model is therefore a perturbation of the last one. After Sambridge & Mosegaard (2002), a McMC procedure is then defined as a multidimensional random sampling where the ensuing sample only depends on the position of the current sampling point. The class of McMC (or in general Monte Carlo) techniques makes often usage of the Bayesian framework (Sambridge & Mosegaard, 2002; Sisson, 2005).

The formalism of Bayesian inference after Bayes (1763) combines *a priori* model information (i.e., information about model unknowns that are independent of the data) with the information from new data (Rawlinson et al., 2014). All information is hereby represented by probabilistic terms (e.g., Smith, 1991). The prior information (represented by an *a priori* probability distribution) is updated by the information from observed data (represented by a likelihood function). Bayes' theorem (Bayes, 1763) in eq. 3.12 gives an estimation of the probability distribution of the model parameters, $\mathbf{m}$, given the observed data, $\mathbf{d}_{obs}$, and an *a priori* probability distribution of the model parameters, $\mathrm{p}(\mathbf{m})$,

$$\underbrace{p(\mathbf{m}|\mathbf{d}_{obs})}_{\text{posterior}} \propto \underbrace{p(\mathbf{d}_{obs}|\mathbf{m})}_{\text{likelihood}} \underbrace{p(\mathbf{m})}_{\text{prior}} \tag{3.12}$$

where $p(\mathbf{m}|\mathbf{d}_{obs})$ is the *a posteriori* probability of the model. The probability of observing the data given a particular model is the likelihood function, $p(\mathbf{d}_{obs}|\mathbf{m})$.

Bayesian *transdimensional* tomography provides a new class of seismic imaging (Sisson, 2005). The term *transdimensional* refers to the varying number of model unknowns in addition to their values to be inverted for through the random walk. Therefore, the posterior is defined across spaces with different dimensions. This inversion scheme produces an ensemble of posterior probability density distributions of the models from which the absolute best or mean model can be retrieved along with the corresponding standard deviation. The model probabilities implicitly quantify the expected value and model uncertainty and therewith the degree of model resolution.

Many transdimensional McMC inversion techniques adopt a generalization of the Metropolis-Hastings algorithm (Metropolis et al., 1953; Hastings, 1970), established as reversible jump-Markov chain Monte Carlo (rj-McMC) scheme by Green (1995); Bodin & Sambridge (2009) and applied by Tilmann et al. (2020) and Dreiling et al. (2020). Below I summarize the inversion procedure adopted in the software package *BayHunter* by Dreiling et al. (2020), following the method of Bodin et al. (2012b), which I used for the 1D V_S-depth inversion.

I invert for the 1D velocity-depth structure, the number of layers and the so-called noise

Table 3.1: Overview of proposal methods. ModVd = Modification of V_S-depth structure.

#	Method	Attributes
a	Change of V_S	ModVd, nucleus modified from V_S prop. dist.
b	New placement of Voronoi nucleus	ModVd, nucleus modified from depth prop. dist.
c	Change of noise parameters	r or σ selected from uniform distribution
d	Birth of new layer	Number of layers change, ModVd, depth drawn from prior dist., new nucleus born
e	Death of random layer	Number of layers change, ModVd, random nucleus deleted

parameters which describe the data errors. As the number of layers are unknown, the dimension of the model space is itself a variable that has to be inverted. The velocity-depth model is described by a variable number of Voronoi nuclei where the vertical and horizontal position of each nucleus is defined by the depth and V_S, respectively. Here, the interface depth of a layer lies equidistant between two nuclei. For surface wave data, the data uncertainty, or data noise σ, is assumed to be Gaussian distributed and uncorrelated between neighboring periods. This implementation is an extension of the classic rj-McMC and known as Hierarchical Bayes algorithm (Gelman et al., 2013). The value of σ is assumed as unknown and has to be estimated in the random walk of each Markov chain. Forward modeling of surface wave dispersion curves is achieved by the standard routine after Herrmann (2013).

For each chain, the initial model parameters (starting model) are drawn randomly from the *prior distributions*, i.e., distributions for the velocity, depth, number of layers and noise parameter σ. The initial model is parameterized by the specified minimum number of layers that determines also the number of Voronoi nuclei to be drawn. A density value is estimated by the relation V_P*0.32+0.77 where V_P is calculated from the *a priori* V_P/V_S ratio, a constant value for all iterations and depths.

After the model initialization, a proposal method is drawn randomly at each proceeding iteration step of each chain to propose a new model. The new proposed model is only dependent on the current model. Five different proposal methods are available and summarized in Table 3.1. The current model is perturbed by the corresponding method's *proposal distribution*.

Proposal distributions are regarded as Gaussian distributions, centered around zero. Note that the methods (d) and (e) imply a change in dimension. These distributions are only initial values as the width of the normal distribution changes with progressing iteration in each chain to reach a given acceptance rate.

After each model proposal, the likelihood and acceptance probability α are calculated in order to evaluate the convergence of each chain. From eq. 3.12 we see that the likelihood is defined as the probability of observing the observed data $\mathbf{d}_{obs}$ given a particular model $\mathbf{m}$. Eq. 3.13 describes the likelihood function for Gaussian measurement error distributions dependent on the data error covariance matrix C_e and the Mahalanobis distance $\Psi(m)$ (eq. 3.14).

$$p(\mathbf{d}_{obs}|\mathbf{m}) = \frac{1}{\sqrt{(2\pi)^n |C_e|}} \times \exp\{\frac{-\Psi(m)}{2}\} \tag{3.13}$$

$$\Psi(m) = (g(\mathbf{m}) - \mathbf{d}_{obs})^T C_e^{-1} (g(\mathbf{m}) - \mathbf{d}_{obs}) \tag{3.14}$$

$\Psi(m)$ is a measure for the fit to observations and a replacement of the least-square measure

and the distance between the observed data, $\mathbf{d}_{obs}$, and the estimated data vectors, $g(\mathbf{m})$. The acceptance probability α is a combined probability and involves the computation of the prior, likelihood and proposal ratios from the proposal model $\mathbf{m}'$ to the current model $\mathbf{m}$

$$\alpha(\mathbf{m}'|\mathbf{m}) = \frac{p(\mathbf{m}')}{p(\mathbf{m})} \times \frac{p(\mathbf{d}_{obs}|\mathbf{m}')}{p(\mathbf{d}_{obs}|\mathbf{m})} \times \frac{q(\mathbf{m}|\mathbf{m}')}{q(\mathbf{m}'|\mathbf{m})} \times |\mathbf{J}| \tag{3.15}$$

where $\mathbf{J}$ is the Jacobian matrix of the transformation from $\mathbf{m}$ to $\mathbf{m}'$ and needed for transdimensional changes. $q(\mathbf{m}'|\mathbf{m})$ is the proposal generation probability density for the transition from $\mathbf{m}$ to $\mathbf{m}'$. If any of the proposal model parameters is not within the defined prior distributions, the proposed model is declined. α is compared against a random number u, drawn from a uniform distribution between 0 and 1. As long as $u < \alpha$, the proposal model gets accepted (always true for $\alpha > 1$), and is appended to the chain models. Otherwise, the proposal model is declined and the current model will be added to the chain.

Generally, the inversion is separated into a burn-in and main phase, each with a specific number of iterations. In practice, the burn-in phase should be assigned with more iterations to ensure that a convergence level is reached before entering the main (posterior) phase. If the number of burn-in iterations was large enough, the samples from the posterior phase should represent a good approximation of the *posterior distribution* for the model parameters. To catch non-converged chains, a threshold is determined by the deviation of the maximum median likelihood of the posterior phase of all chains. After all iterations have been processed, the resultant final chain models, excluding the outliers and burn-in phase iterations, are considered for the transdimensional *posterior distribution*. Every i-th model <= the maximum models is considered for the final ensemble, as the models within one chain are independent. A mean model can then be calculated from this thinned model ensemble together with its standard deviation.

The technique by Tilmann et al. (2020) differs by the parameterization where slowness perturbations in 2D are inverted instead of absolute velocities. A key aspect is the usage of a mixed probability density function instead of pure Gaussian distribution for the data uncertainty. Moreover, a parallel tempering method (Sambridge, 2014) is applied (see section 5.5.3).

3.2 Ambient noise

Ambient seismic noise originates from coupling between the solid Earth's surface with oceans and atmosphere and is recorded together with other seismic sources (e.g., earthquakes). Typically, seismic noise is dominated by surface waves and ranges from periods between 3 s to 50 s with two high-energy peaks around 7 s and 14 s, known as the secondary and primary microseisms, respectively (Fig. 1.2 and C.16).

The basic noise theorem regards this noise as randomly distributed in space and time and uncorrelated. The noise cross-correlation theory states that the time derivative of cross-correlated random wavefields, recorded continuously at two receivers, converges to the Green's function between these receivers (eq. 3.16) (Snieder & Wapenaar, 2010).

$$\lim_{T\to\infty} \frac{\partial}{\partial t} C_{AB}(t) \approx F(t) \otimes [\underbrace{G_{AB}(t)}_{\text{causal lag}} - \underbrace{G_{BA}(-t)}_{\text{acausal lag}}] \tag{3.16}$$

$C_{AB}(t)$ is the cross-correlation of signals which have been recorded at receivers A and B. The Green's function $G_{AB}(t)$ is the impulse response to a source of the Earth's medium (along the ray path), where $G_{BA}(-t)$ is the reciprocal Green's function. F is the autocorrelation function of the ambient noise in the time domain (Shapiro et al., 2011). Each receiver can be treated as a virtual point source which emits a wavefield described by the cross-correlation function.

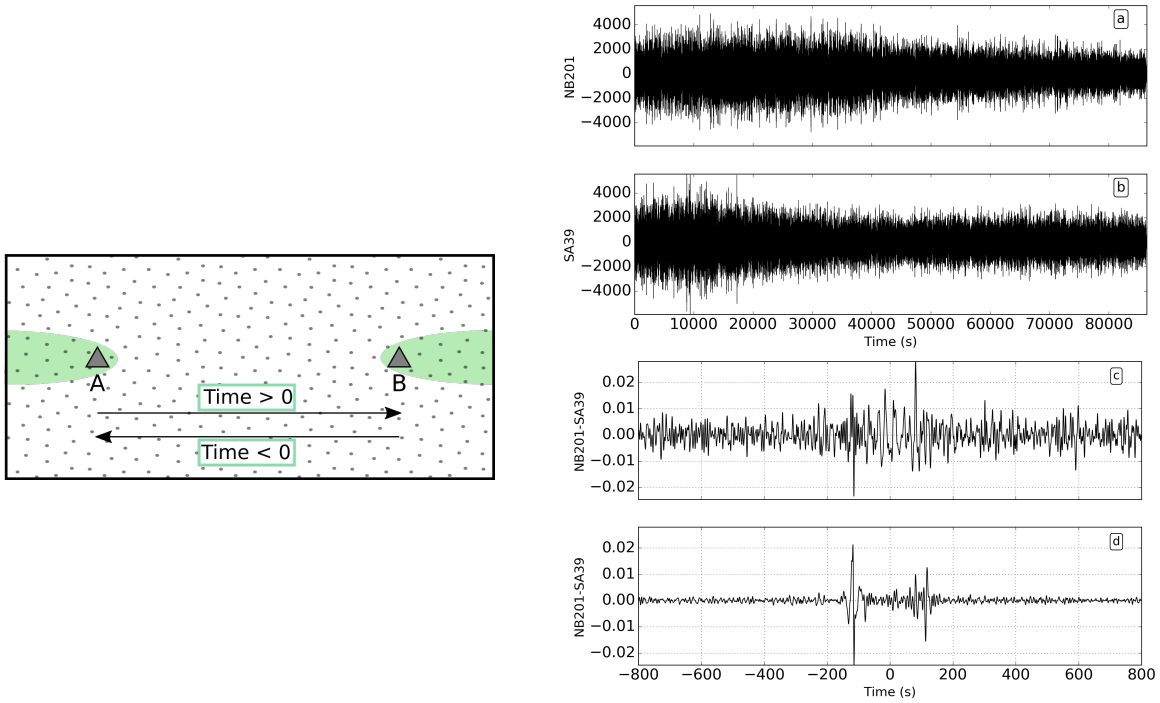

Fig. 3.3: Left: Sketch of homogeneously distributed noise sources (grey dots), recorded at two receivers A and B. Green zones show the area of constructive interference corresponding to the theoretical arrival time. Arrows point in the direction of wave propagation from receiver A to B and B to A resulting in a correlated signal on the positive and negative time lag, respectively. Right: (a) and (b) Continuous noise measurements recorded on one day at stations NB201 and SA39 with a station distance of 366 km. All signals have been bandpass filtered between 5–40 s. (c) Cross-correlations for one day only and (d) the stack over one year. The noise recorded at stations NB201 and SA39 produce dominant signals on both time lags.

The concept of building the cross-correlation function is shown in Fig. 3.3. The sketch on the left side shows homogeneously distributed noise sources, recorded on both receivers. They generate constructive interferences of the noise correlation function within the green zones at the theoretical arrival time corresponding to the wave propagation from receiver A and B (signal appears on the positive time lag = causal) or B and A (signal appears on the negative time lag = acausal). This case is a full reconstruction of the Green's function stated in eq. 3.16. The cross-correlation in the time domain is simply a multiplication in the frequency domain (convolution theorem). The so-called correlogram in Fig. 3.3(c) is the product of the multiplied raw noise measurements (Fig. 3.3a and b) and converted back to the time domain. While the cross-correlation function calculated from any recording length is theoretically sufficient to produce a coherent signal, in practice, the signal-to-noise ratio (SNR) can be significantly increased when cross-correlations are stacked over longer time periods (Fig. 3.3d) (Sabra et al., 2005). The longer the stacked time period, the higher the SNR.

In the past two decades, noise studies have been widely applied to many regions unveiling

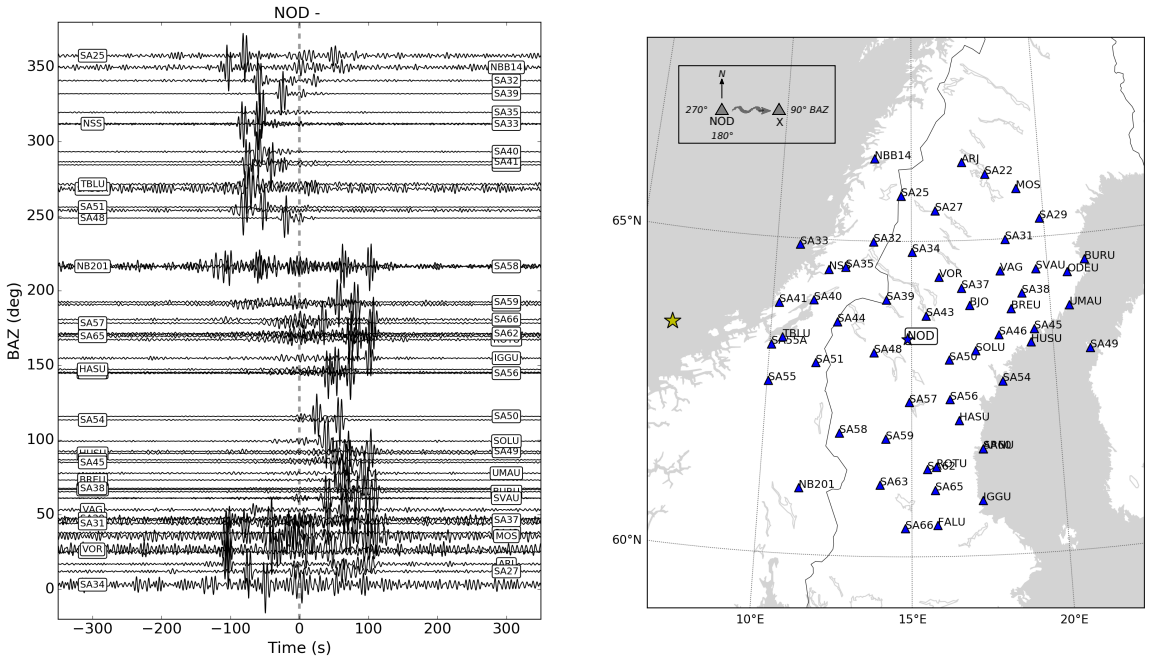

Fig. 3.4: Left: Noise correlation functions respect to station NOD and stations within a distance range of 350 km (station names are labeled on the sides), band-pass filtered between 4–8 s. The correlograms are sorted by the inter-station azimuth where NOD is always the receiver and the other stations are regarded as event. Right: Station map with NOD in the center. The yellow star marks the potential high-energy noise source location for periods between 4–8 s after Sadeghisorkhani et al. (2016).

non-uniform distributed noise sources (e.g., Stehly et al., 2006). Depending on the geographical location, the resulting noise wavefields are neither stationary in space, time nor in the frequency range. In some cases, the noise sources can be located. Sadeghisorkhani et al. (2016) conducted a noise source localization for Scandinavia. They identified a high-energy noise source off the coast west of southern Norway. Fig. 3.4 demonstrates the deviation of the noise correlation function from the ideal homogeneous case. All station pairs respect to station NOD in central Sweden within a distance range of 350 km are regarded here. In the presence of the potential high-energy noise source, only parts of the Green's function are reconstructed, seen as signals on only one time lag. The interference on either the positive or negative time lag depends on the azimuth and distance of the receiver pairs to the noise source. For stations located closer to the western coast, i.e., closer to the potential noise source, a coherent signal is seen on the negative time lag. Stations towards the eastern coast generate a constructive correlation function on the positive time lag. Those station pairs which are oriented parallel to the coast line (around 30° azimuth) yield signals on both time lags since the azimuth to the noise source is similar. See the appendix C.2 for more details on the noise data set.

Chapter 4

Anomalous azimuthal variations with 360° periodicity of Rayleigh phase velocities observed in Scandinavia

4.1 Summary

We use the recently deployed ScanArray network of broadband stations covering most of Norway and Sweden as well as parts of Finland to analyse the propagation of Rayleigh waves in Scandinavia. Applying an array beamforming technique to teleseismic records from ScanArray and permanent stations in the study region, in total 159 stations with a typical station distance of about 70 km, we obtain phase velocities for three sub-regions, which collectively cover most of Scandinavia (excluding southern Norway). The average phase dispersion curves are similar for all three sub-regions. They resemble the dispersion previously observed for the South Baltic craton and are about 1% slower than the North Baltic shield phase velocities for periods between 40 and 80 s. However, a remarkable $\sin(1\theta)$ phase velocity variation with azimuth is observed for periods >35 s with a 5% deviation between the maximum and minimum velocities, more than the overall lateral variation in average velocity. Such a variation, which is incompatible with seismic anisotropy, occurs in northern Scandinavia and southern Norway/Sweden but not in the central study area. The maximum and minimum velocities were measured for backazimuths of 120° and 300°, respectively. These directions are perpendicular to a step in the lithosphere-asthenosphere boundary (LAB) inferred by previous studies in southern Norway/Sweden, suggesting a relation to large lithospheric heterogeneity. In order to test this hypothesis, we carried out 2D full-waveform modeling of Rayleigh wave propagation in synthetic models which incorporate a steep gradient in the LAB in combination with a pronounced reduction in the shear velocity below the LAB. This setup reproduces the observations qualitatively, and results in higher phase velocities for propagation in the direction of shallowing LAB, and lower ones for propagation in the direction of deepening LAB, probably due to the interference of forward scattered and reflected surface wave energy with the fundamental mode. Therefore, the reduction in lithospheric thickness towards southern Norway in the south, and towards the Atlantic ocean in the North provide a plausible explanation for the observed azimuthal variations.

4.2 Introduction

It has long been known that intrinsic azimuthal anisotropy affects the phase velocities of propagating surface waves primarily due to the alignment of olivine crystals in the lithosphere. Smith & Dahlen (1973) have shown theoretically that the azimuthal variation of the Rayleigh phase velocities has a predominantly 180° periodicity (2θ) in the presence of a weakly anisotropic medium. An early observation of such azimuthal variation was made by Forsyth (1975) with a maximum anisotropy of 2% at 70 s period. Montagner & Nataf (1986) demonstrated that very shallow anisotropy may even affect the azimuthal variation of

long-period waves. The 2θ periodicity is a vital assumption for inversions based on dispersion curve measurements as depth-dependent azimuthal anisotropy (e.g., Montagner & Nataf, 1986) and phase velocity tomography. Eikonal tomography studies (e.g., Lin et al., 2009) rely on the azimuthal variation as well as two-station methods (e.g., Gomberg & Masters, 1988; Prindle & Tanimoto, 2006) and array based approaches as the two plane wave method (Forsyth & Li, 2005). Although rarely reported in the past, the expected azimuthal variation of phase velocities can be biased in the presence of local strong lateral heterogeneities (Menke & Levin, 2002; Lin & Ritzwoller, 2011a,b). In these studies, a 360° periodicity has been observed for periods >33 s at different locations in the United States, partly overwhelming the present 180° periodicity Lin & Ritzwoller (2011a). While surface waves are propagating through lateral heterogeneities, the wave train becomes perturbed by finite frequency effects as backward and forward scattering (e.g., Snieder, 1986, 2002) where the latter gets masked by wavefront healing (e.g., Nolet & Dahlen, 2000). Such wavefield perturbations are strongest when the incident wavelength is similar to or larger than the dimension of the anomaly, yielding to the failure of the ray theory (e.g., Wielandt, 1993). Significant phase shifts and amplitude perturbations can occur that imply arrival time deviations of the wavefield (e.g., Snieder & Lomax, 1996; Friederich et al., 2000; Spetzler et al., 2002). As a consequence, the phase velocities are locally perturbed which might lead to relatively strong measurement variations within small scales as shown for 3D models by Bodin & Maupin (2008). Accordingly, Lin & Ritzwoller (2011b) have shown that also surface wave tomography can be affected by local phase velocity variations leading to over- or underestimated structures. Such a bias becomes substantial when events with uneven azimuthal distributions are used (e.g., Ruan et al., 2019; Zhao, 2019).

During the past 25 years southern Norway and Finland, and to a lesser extent central Norway and Sweden, has been explored with 2D temporary networks as SVEKALAPKO (Bock et al., 2001), LAPNET (Kozlovskaya & Poutanen, 2006) and MAGNUS (Weidle et al., 2010) (see Fig. 5.1) and several passive profiles (e.g., Svenningsen et al., 2007), SCANLIPS (England & Ebbing, 2012) and TOR (Cotte et al., 2002). Some temporary networks (Ben Mansour et al., 2018) and active offshore profiles (e.g., Mjelde et al., 1995; Breivik et al., 2017) covered the Lofoten peninsula and surrounding areas. The permanent Swedish National Seismic Network (SNSN) allows studies of entire Sweden (e.g., Eken et al., 2007).
In previous studies (see Maupin et al. (2013) and Ebbing et al. (2012) for reviews), an unusually thin crust has been found beneath the high-topography of southern Norway, i.e., the southern part of the Scandinavian mountain range seems to lack a crustal root. In fact, the lower topography regions of southern Sweden have a thicker crust than southern Norway, in contrast to the principles of Airy isostasy. A thin, high density layer in the lower crust of Sweden (Ebbing et al., 2012) is insufficient to account for this discrepancy. Instead, a pronounced low-velocity zone (LVZ) in the upper mantle beneath southern Norway at depths larger than 100 km has been observed with Rayleigh wave phase dispersion analysis (Maupin, 2011; Schaeffer & Lebedev, 2013) (Fig. 5.2). A sharp transition in the lithospheric thickness approximately across the Oslo Graben has been confirmed with body wave tomography (e.g., Medhus et al., 2012; Wawerzinek et al., 2013; Kolstrup et al., 2015; Hejrani et al., 2017). Although, the estimates of LAB depths below Sweden differ between the different studies, a depth of >200 km is generally agreed upon. The topographic differences therefore seem to be primarily supported in the mantle, although there might be a contribution from Pratt isotropy,

Table 4.1: Overview of the networks used for this study. UiB = University of Bergen, SNSN = Swedish National Seismic Network, GEUS = Geological Survey of Denmark and Greenland.

Network Code	Project/ Network Name	Operation Time	Stations	Reference
1G	ScanArray Core	2012-2017	72	Thybo et al. (2012)
2D	NEONOR2	2013-2016	28	UiB, NORSAR
ZR	SCANLIPS3D	2013-2014	20	England et al. (2015)
UP	SNSN	permanent	72	SNSN (1904)
HE	Finnish National Seismic Network	permanent	15	Institute of Seismology University of Helsinki (1980)
NS	Norwegian National Seismic Network	permanent	8	Lieser et al. (2015)
FN	Northern Finland Seismological Network	permanent	4	Lieser et al. (2015)
NO	Norwegian Seismic Array Network	permanent	3	NORSAR
DK	Danish National Seismic Network	permanent	3	GEUS
IU	Global Seismograph Network	permanent	2	Albuquerque Seismological Laboratory (ASL)/USGS (1988)

i.e., density variations within the crust (Ebbing et al., 2012).

In comparison, northern Norway is only poorly imaged but existing studies, based on sparse data (e.g., Hejrani et al., 2017), indicate a transition to low velocities near the coast.

Rayleigh phase velocities in southern and central Finland are similar to those in southern Norway for periods mostly sensitive to crustal structure (< 34 s) but on average velocities increase much faster for longer periods, however, with small-scale lateral variations (Bruneton et al., 2004a,b). Further array-based studies using both Rayleigh and Love waves have been conducted in Finland by Pedersen et al. (2006) and Pedersen et al. (2015). They find that radial anisotropy is dominant within the lithosphere whereas azimuthal anisotropy is only significant in the asthenosphere at depths exceeding 200 km.

The new ScanArray temporary array data set (2012-2017) connects the existing temporary networks and covers mainly Central and Northern Sweden and Norway (Fig. 5.1), with a few stations along the west coast of Finland. Here, we apply the beamforming technique from Maupin (2011) to this new data set for various sub-regions of Scandinavia in order to investigate regional-scale Rayleigh phase velocity and its azimuthal variations. We demonstrate, that the observed unusual azimuthal variations with 360° periodicity can be related, to a first order, to the strong local lateral variation of the lithosphere structure.

4.3 Tectonic setting

The Scandinavian mountains (Scandes) were formed by the Caledonian orogeny in the Paleozoic age as a result of the continent-continent collision between the Laurentian and Baltica plates. During the Caledonian orogeny mountains have been created also in Scotland, Greenland (Krawczyk et al., 2008) and northeastern United States which are known as the Appalachians (Hatcher, 2010; Thomas, 2006). The Scandes runs approximately parallel to the

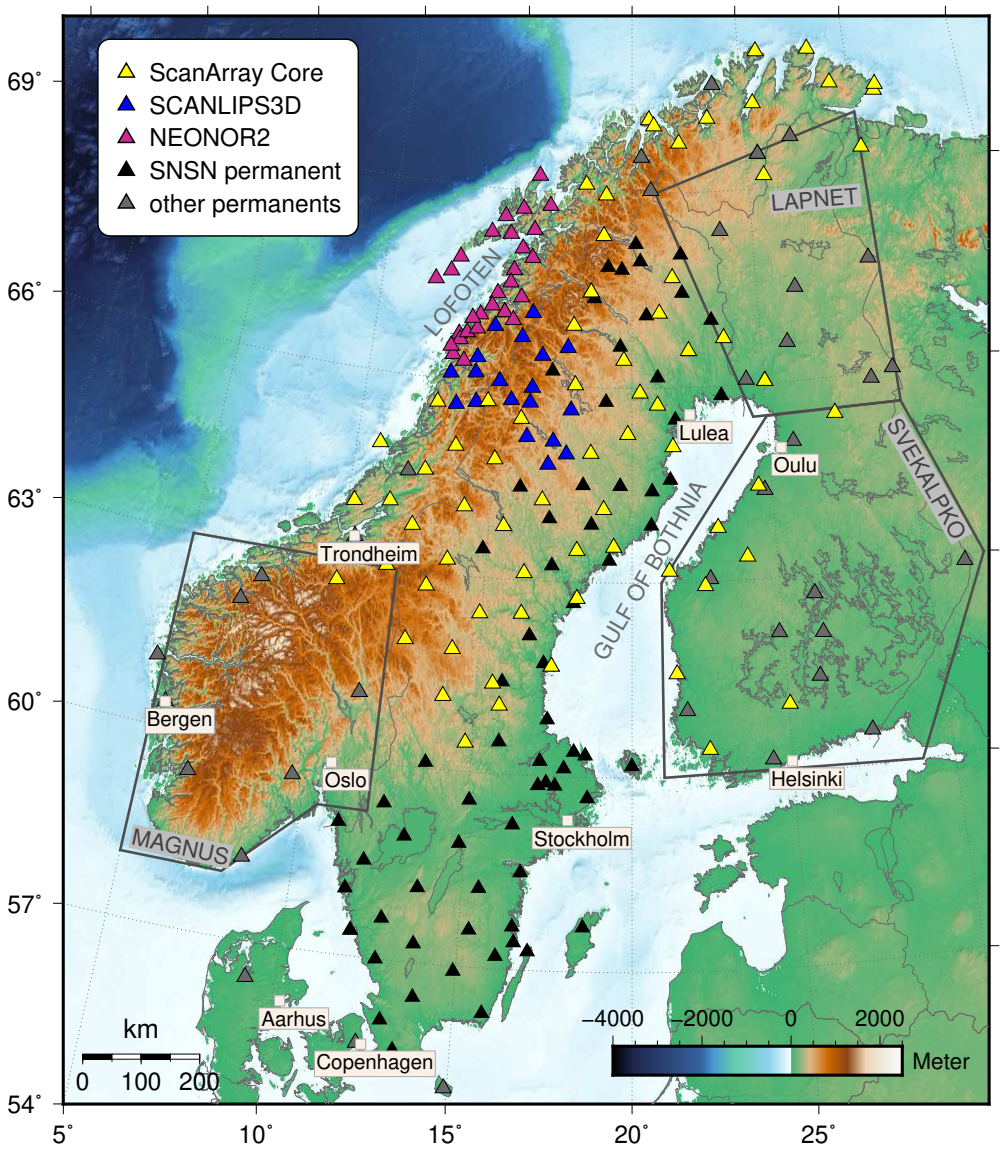

Fig. 4.1: Map of study area with the temporary and permanent stations contributing to the virtual ScanArray network. The gray boxes encircle previous temporary networks which are referred to in the text. The Scandinavian mountain range dominates the western coast with the highest topography in southern Norway.

western coast of Norway. The highest topography is found in southern Norway (southern Scandes) and northern Sweden (northern Scandes) with peak elevations up to 2500 m and 2100 m, respectively (Fig. 5.1). Towards the east, Scandinavia consists of the Precambrian Baltic Shield (e.g., Gorbatschev & Bogdanova, 1993) with very low topographies (Fig. 5.2). Geological reconstructions revealed repeating rifting episodes in the Paleozoic and Mesozoic when the Caledonian mountains have collapsed (e.g., Andersen, 1998; Braathen et al., 2002). However, it is still under debate to what extent the mountain range destruction took place (e.g., Nielsen et al., 2009b; Anell et al., 2009) as the present-day topography is still unusually high for a passive margin. Consequently, the question arises how the topography could be sustained without recent active tectonic forces. The most accepted hypothesis is a tectonic uplift in the Neogene about 30 Ma (Hay et al., 2002), as post-glacial isostatic rebound can only be a second-order effect (Gabrielsen et al., 2005).

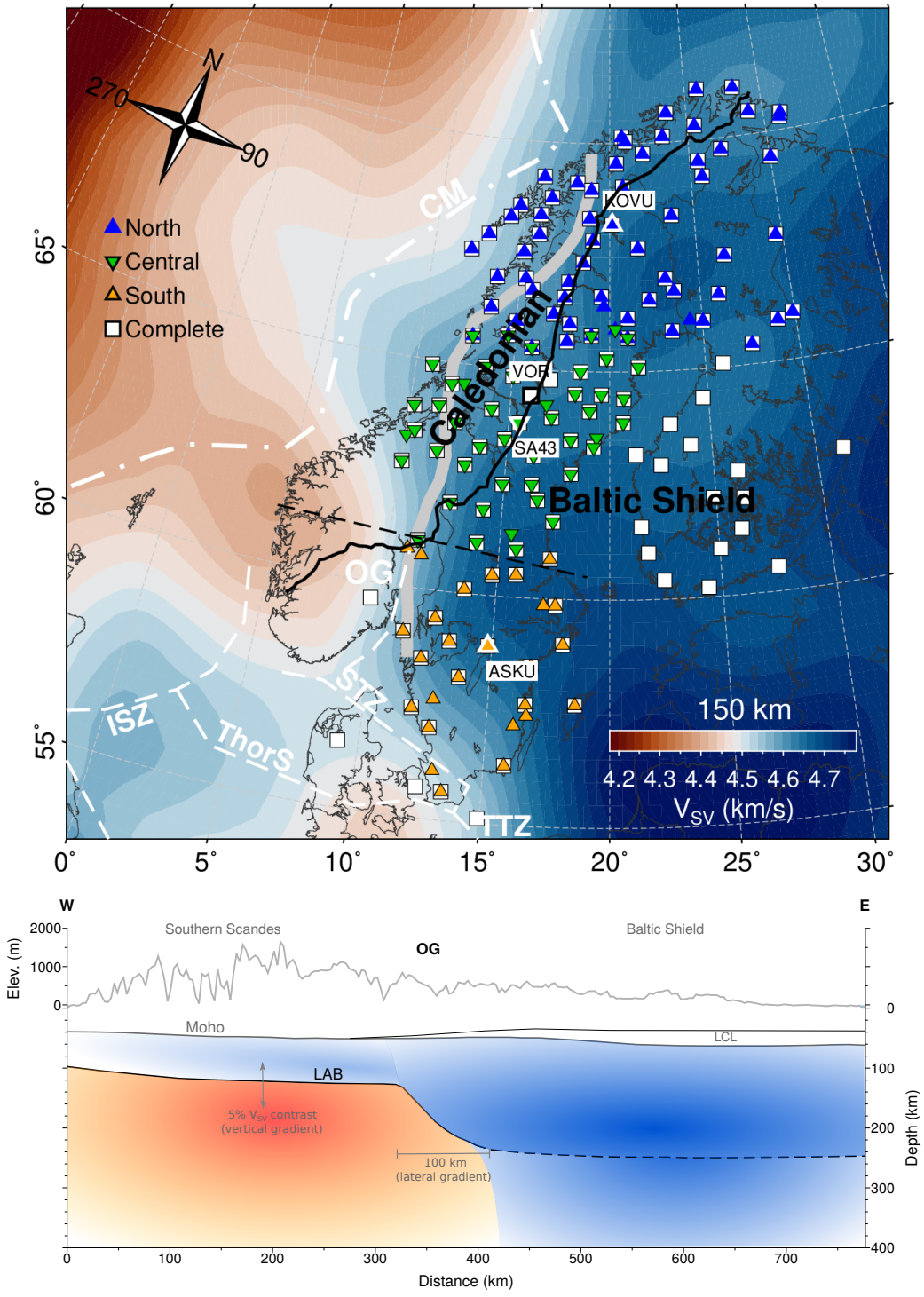

Fig. 4.2: Top: Definition of the subarrays in the context of the global surface waveform tomography shear velocity model by Schaeffer & Lebedev (2013) (version SL2013sv, updated April 2018). Note that the model uncertainty is high for central and northern Norway and Sweden due to the lack of data coverage for their model. The reference station of each array is highlighted with its name. The black line marks the Caledonian front and separates the thrust sheets of the Scandes. OG = Oslo Rift Graben. ISZ is the potential Iapetus-Suture-Zone; ThorS = Thor suture; CM = Continental Margin. The Sorgenfrei-Tornquist Zone (STZ) is the northern extension of the Tornquist-Teisseyre-Zone (TTZ). The gray shaded zone outlines the sharp transition in LAB thickness derived from Kolstrup et al. (2015); Hejrani et al. (2017). Bottom: Schematic west-east cross-section through southern Norway and Sweden, marked by the dashed black line on the map. LCL is a high-density lower crustal layer after Ebbing et al. (2012). The transition in LAB thickness is constrained to be <∼100 km wide by the body wave tomography of Kolstrup et al. (2015).

4.4 Data

The ScanArray network designates a virtual temporary network of more than 220 broadband stations consisting of the following contributing networks: 72 stations from ScanArray Core (1G network), which were deployed in Norway, Sweden and Finland by the ScanArray consortium (Thybo et al., 2012) specifically for imaging the crust and lithospheric structure below central and northern Scandinavia, 28 stations from NEONOR2 deployed in the Lofoten region (2D network), 20 stations from the SCANLIPS3D experiment in central Norway and Sweden (ZR network), 72 stations from the permanent Swedish National Seismic Network (SNSN; UP network) and 35 permanent stations from the Finnish (FN, HE), Danish (DK) and Norwegian (NO, NS) permanent networks (Fig. 5.1, Table 4.1). The average inter-station distance of the ScanArray Core network is about 70 km. 15 out of the 72 seismic stations have corner periods of 240 s; all others are equipped with 120 s instruments. The SNSN permanent stations cover much of Sweden, but some sites are installed with 30 s or 60 s instruments. Here, we do not include stations equipped with 30 s instruments into the analysis. The exact operation times of the temporary networks differ slightly, but all the stations overlap from spring 2014 to fall 2016, with the exception of the SCANLIPS3D data collected during 2013–2014. Therefore, we only included teleseismic earthquakes from 2014–2016 in the analysis. In total, we considered 257 events with surface wave magnitudes $M_S >= 5.6$, source depths less than 150 km and epicentral distances up to 130°. The instrument response was deconvolved to obtain velocity seismograms, which were then bandpass-filtered between 0.5 s and 200 s and downsampled to 5 Hz. Some stations were significantly misoriented, which we corrected (Grund et al., 2017).

4.5 Beamforming processing

4.5.1 Method

We apply the beamforming technique after Maupin (2011) to investigate Rayleigh phase velocities in several sub-regions of our study area (Fig. 5.2). This method has been previously applied to the MAGNUS network (Weidle et al., 2010) in southern Norway, which makes possible a consistent and direct comparison with our data (Maupin, 2011). Surface wave beamforming on a regional scale yields two pieces of information: (1) phase velocity for the region of the array and for each event, and (2) the direction of propagation, or equivalently the measured backazimuth (baz), which when compared to the great-circle baz can indicate a systematic deviation. Cross-correlations are calculated in the frequency domain for all possible station pairs within the defined sub-array and summed to obtain the final cross-power spectra. We use an event-dependent coordinate system as developed by Forsyth & Li (2005) to account for the curvature of the incoming wave front which cannot be neglected for our regional-scale arrays. As a result of this, and because the defined sub-arrays are not perfectly isotropic, the array response functions (ARF) vary slightly with azimuth from one event to another.

However, we forgo the additional deconvolution of ARF as done in Maupin (2011). Preliminary tests have shown no significant improvement in the final dispersion curves. The main purpose of ARF is to decrease the beam width to unveil potential higher modes and interfering wavetrains, but actually no example has been found where a beam shift improved the detection of higher modes. The slowness is calculated in a local event-dependent

coordinate system with a reference point chosen at the centroid of each sub-array (Fig. 5.2). Tests show negligible influence of the position of the reference point on the beamforming results when the position slightly deviates from the centroid.

The phase velocity (c) and deviation from great-circle direction (δ_{BAZ}) are determined from the calculated slowness value pair (s_x,s_y) corresponding to the peak beam power according to

$$c = 1/\sqrt{s_x^2 + s_y^2} \tag{4.1}$$

and

$$\delta_{\mathrm{BAZ}} = \tan^{-1}(s_y/s_x). \tag{4.2}$$

The slowness s_x points into the epicentral direction and s_y into the transverse direction where positive s_y values refer to a clockwise great circle path deviation.

The defined sub-arrays are displayed in Fig. 5.2. Scandinavia was separated into a northern (67 stations), central (49 stations) and southern (27 stations) sub-region mainly covering Norway and Sweden. In defining the sub-arrays we aimed to make them comparable in size and for them to have an aspect ratio close to 1 in order to minimize the anisotropy of the ARF. In addition, the limits of the arrays were adjusted to correspond approximately to the changes in the Scandes topography along their western margin. Of course, the size and shape constraints needed to be relaxed a bit in order to cover the whole study area. We also processed the superset of these three sub-arrays in addition to stations in southern Finland as a single array across Scandinavia, referred to in the following as Complete array (143 stations). Not all stations available within these defined areas were used for the processing since evenly distributed receivers are beneficial for an even sampling of the studied area. In total, we used 159 out of the $>$ 220 available ScanArray stations. The three sub-arrays differ slightly in their aperture, but the regional arrays resolve waves of periods up to 90 s and the Complete array up to 120 s.

All seismograms were windowed between Rayleigh group velocities of 2.7 km/s and 4.6 km/s. Outside this window a 500 s cosine taper is applied. We performed the beamforming in ten frequency bands with 20% overlap and center periods of 22 s, 25 s, 29 s, 33 s, 40 s, 50 s, 57 s, 66 s, 76 s and 86 s. Three additional frequency bands, centered on 100 s, 110 s and 120 s were measured with the Complete array. Events with low signal-to-noise ratio on too many stations of an array were discarded by a fully automatic selection code as described in Maupin (2011). In short, the threshold for discarding traces whose envelopes are too far from the average was set to 1.7 where the average envelope is calculated iteratively after the rejection of one trace. After the final iteration, a minimum number of 10 remaining traces is required for each event.

Finally, 168 events were accepted for the South sub-array, 172 events for the Central sub-array, 187 events for the North sub-array and 188 events for the Complete sub-array (see Fig. 4.3 for the analysed events for the Complete sub-array). The event coverage is acceptable in terms of azimuth and distance for all sub-arrays, with each 30° segment having at least 5 events. In contrast to Maupin (2011) we use the same parameters for the analysis of teleseismic and regional events. We incorporate also some very deep events since we find the fundamental mode very coherent across the array without overlapping with higher modes from visual inspection of the data. Further, the upper limit of 4.6 km/s for the applied group velocity window reduces the interaction of higher modes.

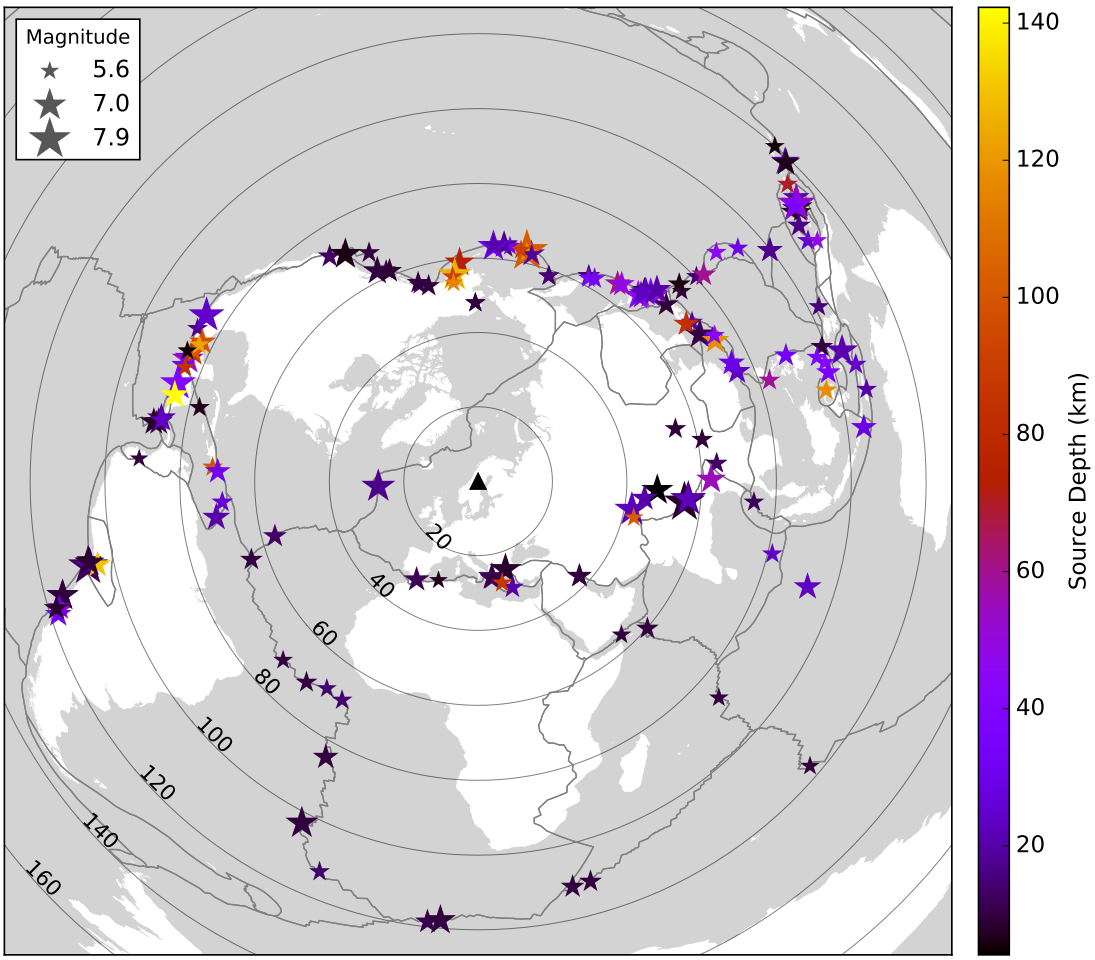

Fig. 4.3: Distribution of the events used for beamforming for the complete array. The black triangle displays the center of the study area. Grey circles denote 20° epicentral intervals. Grey solid lines mark the major plate boundaries.

4.5.2 Results

An example of the beamforming procedure from the North sub-array is shown in Fig. 4.4. The error bars in Fig. 4.5 and 4.6 are defined arbitrarily by the 98% contour of the maximum beam strength in the s_x - s_y plane as shown in Fig. 4.4 and therefore primarily reflect the resolution capability of the array at the respective period. The 98% contour was chosen to make the measure comparable with the results from Maupin (2011). Although the beam width will have some dependency on the coherency of the incoming wavefield, this measure cannot be interpreted as an estimate of the absolute error, but reflects the relative resolution of the array in baz and absolute slowness direction. We note that it is therefore not meaningful to compare the size of the error bars across different periods because naturally longer wavelengths will result in a wider beam. However, it does not follow that the slowness is necessarily measured with less precision. As can be expected, measurements for the complete array result in smaller error bars.

The measured deviations from the great-circle paths are shown for all events in Fig. 4.5 at 22 s, 40 s and 86 s. At short periods < 29 s the deviations from the great circle path are very high, up to $\pm$ 30° across all regions. This observation can be explained by waves that traverse heterogeneous lithosphere, including (multiple) plate boundary zones. Short wavelengths are much more affected, which results in complex wave trains due to scattering and multipathing

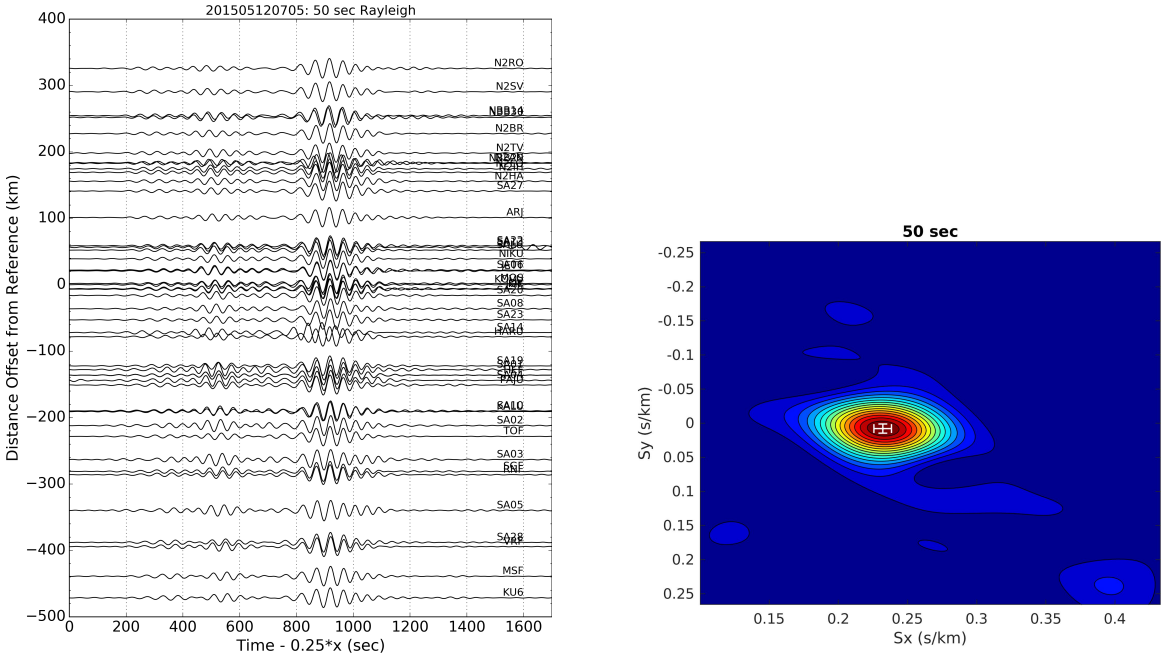

Fig. 4.4: Beamforming example for one event from Nepal on 2015/05/12 07:05 UTC for the North sub-array. Left: Record section bandpass filtered with a narrow bandpass around 50 s. Bad traces have been removed. The mean epicentral distance is 55.5° and the mean theoretical backazimuth is 101°. Right: Corresponding beam in the slowness plane from which the phase velocities and backazimuth are measured. s_y indicates the deviation from great-circle path which is slightly resolved better than s_x, the slowness in the great-circle direction, due to the array and event configuration. White error bars mark the 98% interval around the maximum beam.

as observed in many studies before (e.g., Cotte et al., 2000; Tanimoto & Prindle, 2007; Foster et al., 2014; Chen et al., 2018). No systematic variation with azimuth is observed. If there are any systematic trends here at all, these at most affect events from a particular source region and a very narrow azimuth band. For longer periods with propagation paths in the uppermost mantle the baz deviation reduces to about ± 10°.

Owing to the resolution decrease at very long periods the 86 s baz deviation measurements result in larger error bars. Interestingly, very distant events from Papua New Guinea/Solomon Islands at 50° baz are less scattered at 86 s than at 40 s, whereas the far distant events with 260° baz show more scatter again. All of these characteristics are independent from the source depth.

Pedersen et al. (2015) carried out a Rayleigh waves array analysis for northern Finland (LAPNET network) with focus on great-circle deviations. They found a significant variation with period with a maximum of 9° deviation from the mean over all events used at 20 s. Deviation decreased to about 3° at 100 s. The maximum deviation for individual events at a period of 20 s was 22° in agreement with our measurements shown in Fig. 4.5.

Fig. 4.6 shows the phase velocities as a function of baz and epicentral distance for the four arrays at 22 s and 40 s where the measured (rather than the great-circle) baz is used. The variation of phase velocity with baz does not appear to be correlated with the baz deviation.

At a period of 22 s we do not observe any clear differences between the arrays. Neither can we identify any pronounced azimuth related variation or event clusters with characteristic anomalies. Only the intermediate-distance events between 0-50 ° baz measured with the North sub-array and events from 250 ° (South America) to 300 ° (Central America) are slightly more

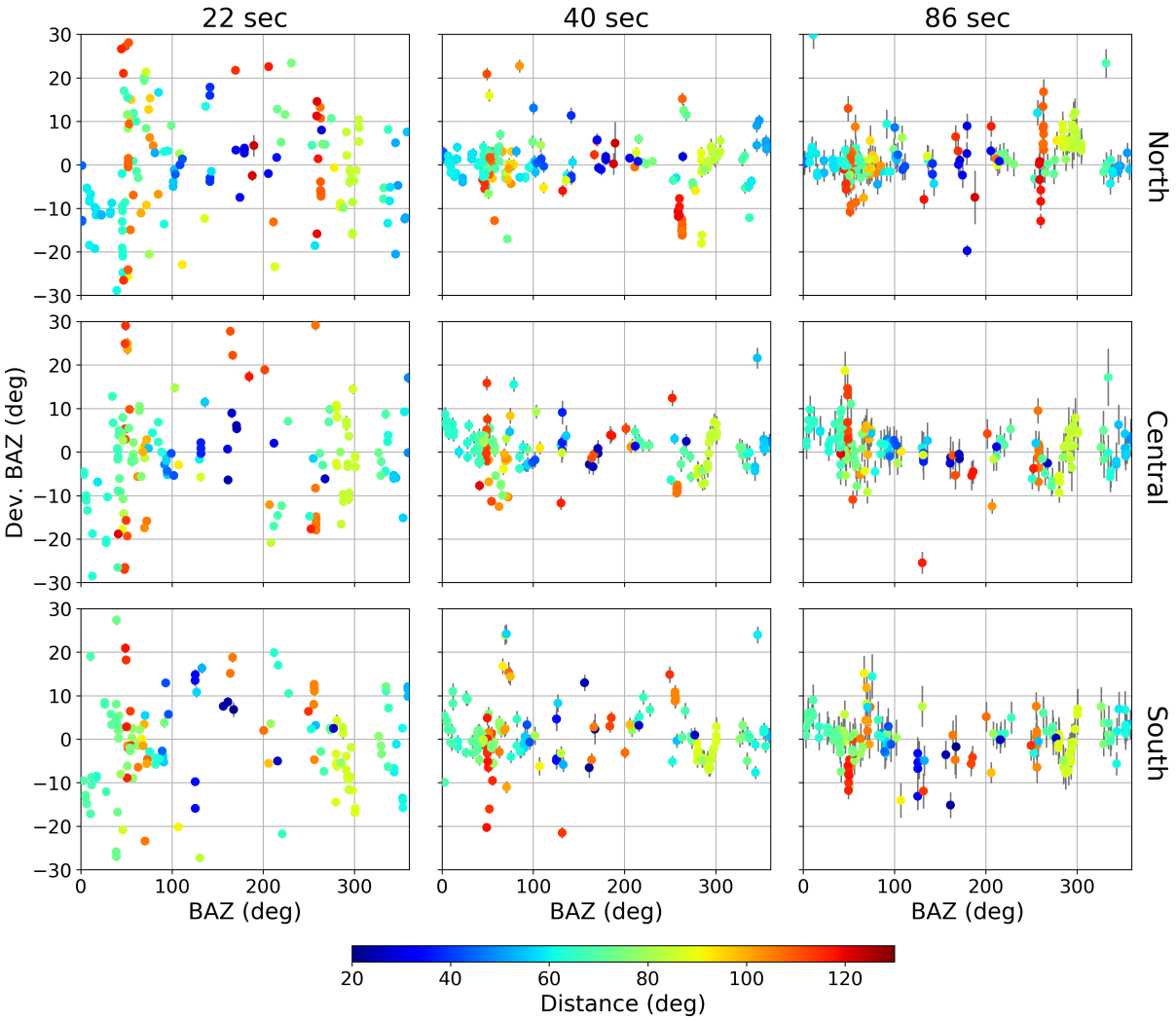

Fig. 4.5: Deviation of the predicted backazimuth as a function of the theoretical value for the sub-arrays at 22 s, 40 s and 86 s. Short periods are more strongly affected by scattering effects. Error bars are derived from the width of the beam, see text for details.

scattered than events from other azimuths. As mentioned above, the surface waves from these directions propagate across multiple subduction zones and both oceanic and continental crust.

At a period of 40 s the three sub-regions yield remarkable differences. Whereas the central area lacks systematic azimuthal deviations, the northern and southern regions reveal a significant 360° periodicity, i.e., sin(1θ) variation of the phase velocity with baz (Fig. 4.6b). The 1θ feature is most pronounced in northern Scandinavia where the maximum and minimum velocities vary by ±2.5% (i.e., ±0.1 km/s) around the average velocity of 4.05 km/s at 40 s, measured from opposite directions at 120 and 300° baz, respectively. From the South sub-array we determine a maximum velocity deviation of around ±2%. We exclude the possibility that our observed 1θ feature is caused by anomalies far away from the array locations somewhere along the propagation path since we observe this pattern independently of epicentral distance. Neither is it affected by event depth or magnitude. The phase velocities calculated from the Complete array also show this azimuthal effect as an average over all sub-regions.

The azimuthal variation of surface wave velocities in weakly azimuthally anisotropic media has the following form (Smith & Dahlen, 1973).

$$c(\omega,\theta) = C_0(\omega) + A_2(\omega)cos(2\theta) + B_2(\omega)sin(2\theta) + A_4(\omega)cos(4\theta) + B_4(\omega)sin(4\theta) \tag{4.3}$$

The equation implies that waves traveling along a direction θ should have the same speed as waves traveling in the opposite direction. Here, c(ω,θ) is the measured phase velocity as a function of the frequency ω and the propagation azimuth θ. C_0 refers to the isotropic phase velocity. The 2θ term corresponds to a 180° periodicity and is the dominant part of the azimuthal anisotropy for Rayleigh waves, whereas, the 4θ term (90° periodicity) is less pronounced for Rayleigh waves (Maupin, 1985; Maupin & Park, 2015) and will be neglected here. The coefficients A_n and B_n are also frequency dependent and depend on the variation of the anisotropic parameters of the medium with depth (Montagner & Nataf, 1986). The azimuthal variation of observed phase velocities in the northern and southern region are clearly not well described by the 180° symmetry expected from azimuthal anisotropy. Therefore, we tentatively attribute the observed 1θ variation to structural heterogeneity.

In order to quantify the observed 360° periodicity we fit the following equation, which, compared to eq. 4.3, includes the 1θ harmonic contribution as an additional term and drops the 4θ dependence:

$$c(\omega,\theta) = C_0(\omega) + A_1(\omega)cos(\theta) + B_1(\omega)sin(\theta) + A_2(\omega)cos(2\theta) + B_2(\omega)sin(2\theta) \tag{4.4}$$

We inverted for the coefficients using a robust L1 norm. We present the fits for the 1θ term (orange lines) only, the 2θ (green lines) only and both terms (blue lines) in Fig. 4.6c. To reduce the potential bias due to the uneven azimuthal distribution, we used median binned phase velocities to perform the model fitting. Each black scatter point in Fig. 4.6c represents a median phase velocity within a 10° wide bin; bins are spaced with 5° overlap. Error bars give the standard deviation of all single measurements within each bin.

Outliers have been defined by a threshold of 1.25 times the standard deviation of the residuals relative to a first fit with all data and then removed before the final model fitting. Only a few outliers were identified by this threshold (red crosses in Fig. 4.6c) but due to the

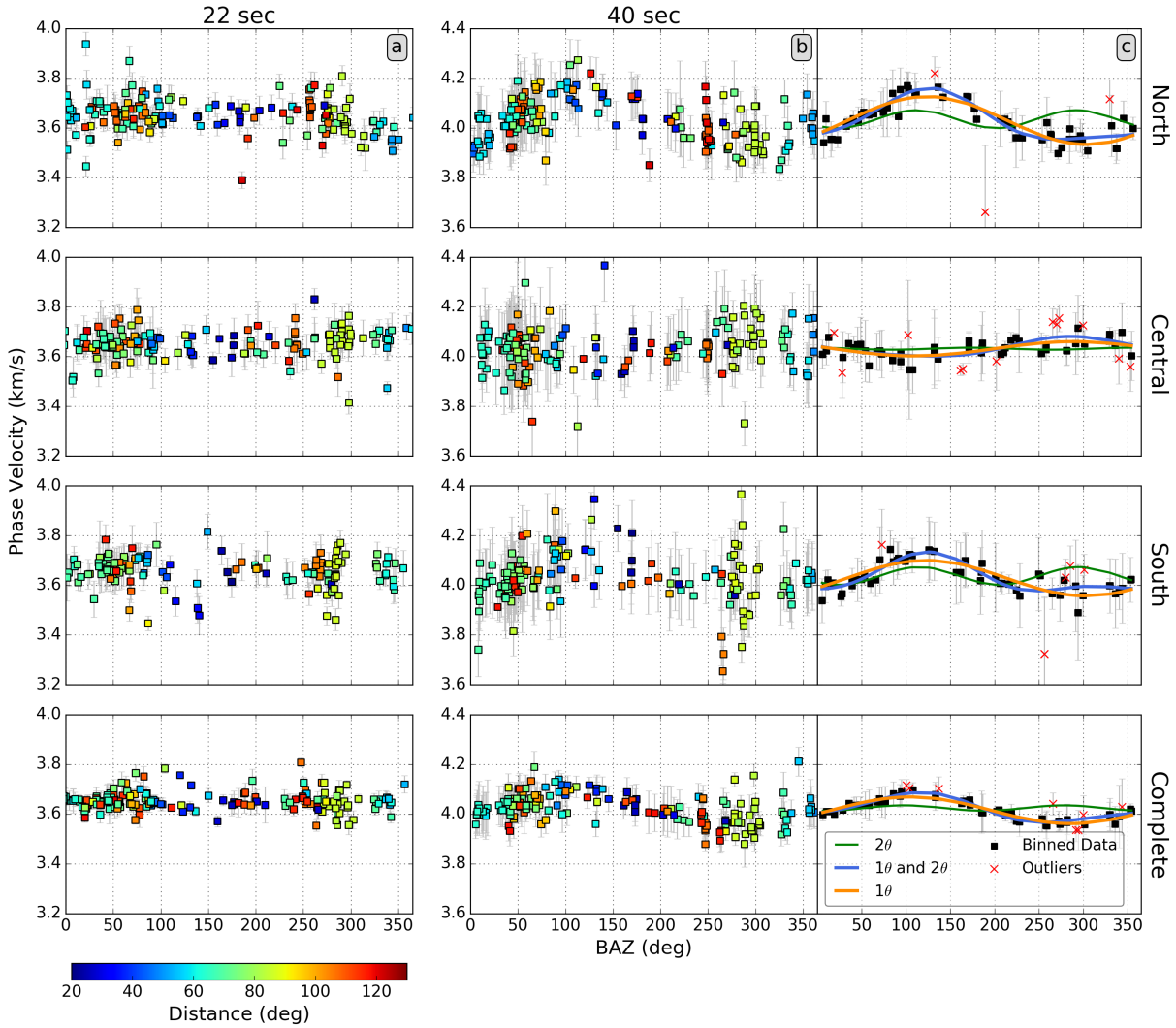

Fig. 4.6: Phase velocities as function of measured backazimuth resulting from the beamforming processing for the North, Central, South and Complete arrays (from top to bottom). (a) and (b) show the measurements with error bars for each event at periods of 22 s and 40 s, respectively, color-coded by the epicentral distance. The same color scale as in Fig. 4.5 is used here. Note the different y-axis scales. (c) displays the median binned measurements at 40 s with 10° bin widths and 5° overlaps together with their standard deviations (gray error bars). The binned values were fitted to 1θ (orange line), 2θ (green line) and 1θ+2θ (blue line) harmonic functions. Outliers are marked as red crosses and have been discarded from the fitting (see text).

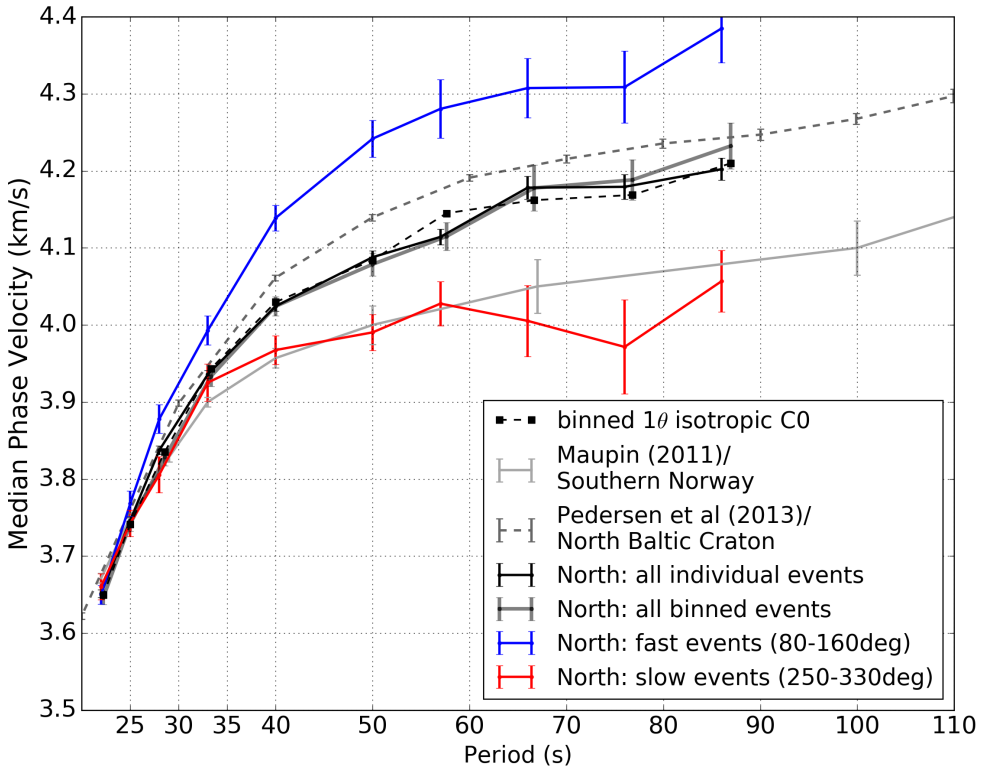

Fig. 4.7: Dispersion curves for the North array. The solid black curve shows the median over all individual events used for beamforming where the solid dark grey line gives the median over all binned measurements. The blue and the red curves are the median over the events from the fast and slow observed directions, respectively. For comparison, also the median dispersion curves for southern Norway from (Maupin, 2011) and for northern Finland (LAPNET network) (Pedersen et al., 2013) are shown. The isotropic phase velocities resultant from fitting the coefficients in eq. 4.4 are shown as dashed line.

robustness of the L1 inversion, the detailed choice of threshold only has a minor influence on the resulting fits. Both the 1θ (orange lines) and 1θ+2θ (blue lines) models fit the observed data within the error estimates and differ little from each other, whereas neither the 2θ (green lines) assumption implied by seismic anisotropy nor an isotropic phase velocity assumption are able to explain the phase velocity variation from the North and South sub-arrays. Since the azimuthal variation of the phase velocity is <1% for the Central array, a single isotropic phase velocity value is sufficient to explain the measurements.

The phase dispersion curves for various subsets of events are shown in Fig. 4.7 for the North array. The events from the E and SE (blue curve) are up to 0.15 km/s faster than the median over all events (black line). Events from the W and NW are up to 0.2 km/s slower than the median curve, i.e., the total azimuthal variation is >5% for periods >40 s, as seen also in the harmonic function fits. Note that the azimuthal variation is much larger than the lateral variation expected in Scandinavia according to previous studies (Maupin, 2011; Pedersen et al., 2013). No clear systematic variation with azimuth is resolved at periods less than 33 s. This is also true for the southern and complete region. In the central area this azimuthal fluctuation is absent at all periods.

As expected, the isotropic phase velocities C_0 calculated by fitting eq. 4.4 (black dashed line) are very close to the median curve over all individual and binned events. The isotropic and the individual median velocities for the other sub-arrays are in good agreement as well. Averaging

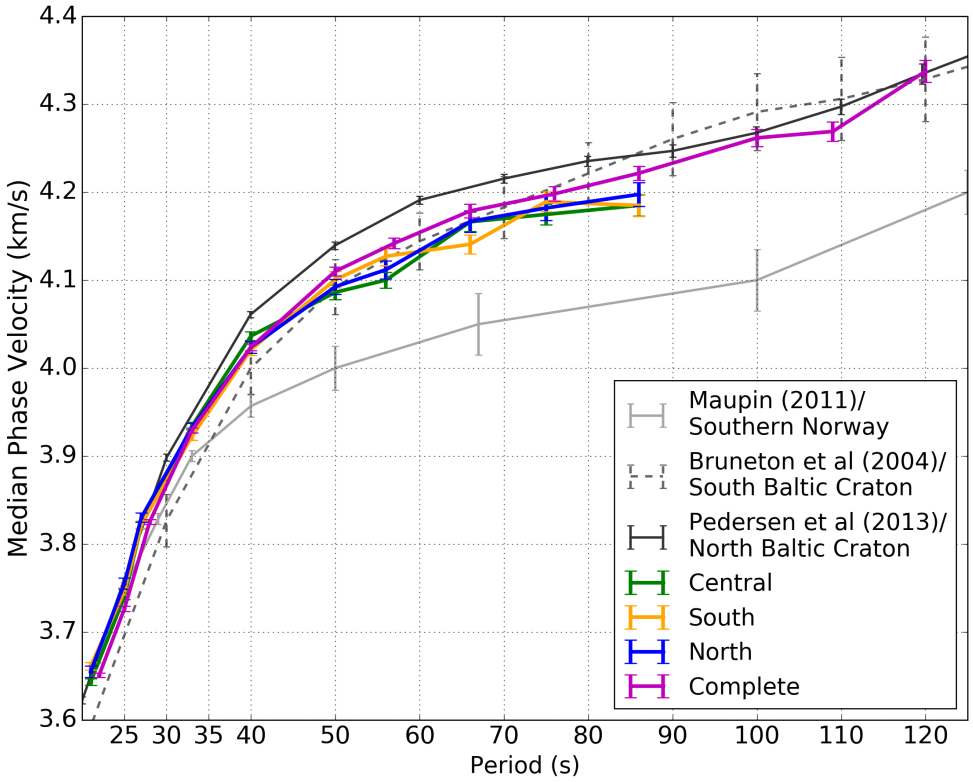

Fig. 4.8: Median regional dispersion curves for the arrays defined in Fig. 5.2. For periods < 32 s the median phase velocities are similar to southern Norway. For higher periods the phase velocities are comparable with the average values from the South Baltic craton.

over all azimuths yields a sufficiently good evaluation of the isotropic phase velocity at each period (see Fig. 4.7). No bias is observable between the isotropic fit of C_0 and the average of the azimuthally binned measurements. The regional median dispersion curves are obtained from all single measurements at each period and compared in Fig. 4.8. Despite the substantial difference of the phase velocity variation with azimuth in the different regions, no significant difference is apparent between the median dispersion curves, except that the Complete array shows slightly faster velocities at long periods. This is reasonable since the Complete array includes some additional stations in southern Finland, which is known to have a high-velocity lithospheric keel (Sandoval et al., 2004). The median velocities are similar to the results from the Paleoproterozoic domain in South Finland (SVEKALAPKO network) (Bruneton et al., 2004a) for > 45 s. The dispersion curve in southern Sweden (South sub-array) indicates higher velocities ($\sim$2.2% at 70 s) than for neighboring southern Norway (solid gray line in Fig. 4.8). Our measured phase velocities from all sub-arrays are $\sim$1% lower than the velocities obtained by Pedersen et al. (2013) from the Archean domain of the Baltic Shield in North Finland (LAPNET network). Although the North sub-array overlaps the LAPNET area significantly, the difference is not surprising, as it extends westward to the Norwegian coast, where lower mantle velocities appear to be present (Hejrani et al., 2017; Mauerberger et al., 2021b).

To cross-validate our observations of the remarkable azimuthal variation of phase velocity, we applied a different beamforming method based on slant-stacking in the frequency-wavenumber domain (following Park et al. (1998), modified by Rindraharisaona et al. (2021)). In this implementation the reference station is the farthest station for each event and the beam signal with respect to the reference station is summed over all stations,

not over all cross-correlated station pairs as in the method of Maupin (2011). We applied this technique to our North and Central sub-arrays using the same teleseismic events as before. Both sub-array measurements are in good agreement with the previous beamforming results and confirm the exceptional azimuthal behavior in northern and southern Scandinavia. Again, the central part lacks any significant phase velocity variation with azimuth.

4.6 2D surface wave modeling

4.6.1 Method

As discussed in the Introduction, previous studies from southern Norway and Sweden (e.g., Medhus et al., 2012; Wawerzinek et al., 2013; Kolstrup et al., 2015; Hejrani et al., 2017) indicate a pronounced step of the LAB at around 13°E and 61°N (cf. Fig. 5.2). Below this LAB the shear wave velocities decrease significantly by about 5.5% (Maupin et al., 2013). Less is known about the upper mantle structure below the North sub-array, but a shallowing LAB towards the west at the transition from the Baltic Shield to the Caledonian unit or from continental to oceanic lithosphere is also expected (Hejrani et al., 2017). As this known lithospheric step is at the western edge of our South sub-array with the fast observed phase velocity perpendicular to the step, this lithospheric scale heterogeneity is a prime candidate for causing the peculiar Rayleigh wave variations. Here, we aim to test with simplified synthetic models whether a structural anomaly on a regional scale could be responsible for the 360° periodicity of the Rayleigh wave velocity anomalies. Thereby, we try to understand the extremes of the variation for waves propagating in opposite directions perpendicular to the strike of the structure. We thus expect to be able to understand the basics of this effect based on 2D simulations. We do not seek to invert our observed seismograms or dispersion curves exactly, as this is beyond the scope of this paper.

We make use of the *Salvus* software package (Afanasiev et al., 2019). The spatial discretisation is implemented with the spectral-element method of continuous Galerkin style. A completely automatic association of the entire elements in arbitrary complex models is capable by the implementation to handle fully unstructured domains, instead of regular grids, which save computational time where the medium is rather homogeneous. This approach holds true for any dimension and any scale. To avoid artificial reflections from the model edges first order approximations of absorbing boundary conditions are implemented in *Salvus* adopting the approach by Clayton & Engquist (1977). Accordingly, energy is absorbed efficiently for nearly all incidence angles.

To simulate teleseismic surface waves which are well separated from the body waves and also not interacting with the model edges the lateral dimension of the mesh has to be sufficiently large. We choose a lateral extent of 10,000 km and a total depth of 400 km for our initial model which is a satisfactory trade-off between the prerequisites mentioned before and computational time. The mesh has been created to be suitable down to a period of 10 s. Together with a resolution criterion of two mesh elements per wavelength a horizontal grid spacing of 8 km is obtained where the mesh is a simple rectangular grid. The vertical grid size is about 15 km on average. Across boundary layers and edges the mesh size is automatically refined depending on the physical properties of the interface. We built the lithospheric topography starting at a depth of 105 km down to 350 km where the step has a horizontal dimension of 100 km according to

previous studies (e.g., Wawerzinek et al., 2013; Kolstrup et al., 2015). Shear-wave velocities are also adopted from these previous studies: The crust has three layers and the shallow lithosphere velocity is lower on the thin than on the thick side.

The minimum shear-wave velocity within the low-velocity zone (LVZ) is 4.4 km/s immediately to the West of the step. Towards the western margin the velocities increase smoothly in order to have a localised LVZ and to avoid an additional step in the model. It is implausible that such a strong heterogeneity exist along the entire path. The maximum vertical Vs contrast across the defined LAB is about 5 % and the lateral Vs contrast is 6.4 % (cf. Fig. 5.2 and 4.9). The Vp structure is set by using a Vp/Vs ratio of 1.78 and the density (in kg/m^3) is approximated by the relation Vs(m/s)-1000. We construct two different models representing a source located either to the west or east of the lithospheric step (Fig. 4.9 (a) and 4.9 (b)). These two model set-ups are labelled 270° BAZ and 90° BAZ, which represents the observed slow and fast phase velocity directions (see Fig. 4.6 and 4.7), respectively. Absorbing boundaries have been set at the left, right and bottom margins of the model.

A moment tensor source is applied with a dominant frequency of 0.03 Hz. This source has been placed 4,500 km away from the model boundaries at a depth of 30 km. 13 receivers are located symmetrically above the lithospheric step with a spacing of 50 km corresponding approximately to our real average station spacing. We model the ground velocity and use the vertical component to measure the dispersion curves.

4.6.2 Results

Since we are dealing with synthetic data where our receivers are placed along a straight line (Fig. 4.9a and b) we have chosen to apply the beamforming technique by Rindraharisaona et al. (2021) to measure phase velocities from the synthetic waveforms. As mentioned above, we have verified that both beamforming techniques yield consistent results by inspection.
The dispersion curves derived from all synthetic waveforms (receivers R1-R13) are shown in Fig. 4.9 (e). Two reference dispersion curves are also shown based on 1D laterally homogeneous models which are equal to the left (thin lithosphere) and right (thick lithosphere) step side as marked in Fig. 4.9 (c). The corresponding Vs-depth profiles are shown in Fig. 4.9 (d).

For propagation in the direction of decreasing lithospheric thickness (90° baz source model) in Fig. 4.9(a) the phase velocities are clearly increased at the longer periods $>$ 45 s (blue line) compared to both 1D reference models. The error bars were estimated from the beam in the wavenumber domain for selected frequencies assuming that the individual beams correspond to a normal Gaussian density. A 68% confidence interval around each individual maximum beam was taken. We obtain the final phase velocity mean and variance by sampling from the wavenumber beam distribution.

For propagation in the opposite direction (270° baz case), we observed significantly lower phase velocities for the longer periods. These results are in qualitative agreement with our observed velocities and demonstrate that a strong vertical and horizontal velocity gradient in the lithosphere can produce the 1θ variation of intra-array phase velocities. Note that despite the absence of added noise, the error bars in the heterogeneous models are larger than in the 1D models, attesting to the more complex nature of the wavefield in these models.

To investigate the effects on phase velocities in more detail, we considered the left (R1-R6, on thinner lithosphere) and right (R7-R13, on thicker lithosphere) subsets of the simulated array

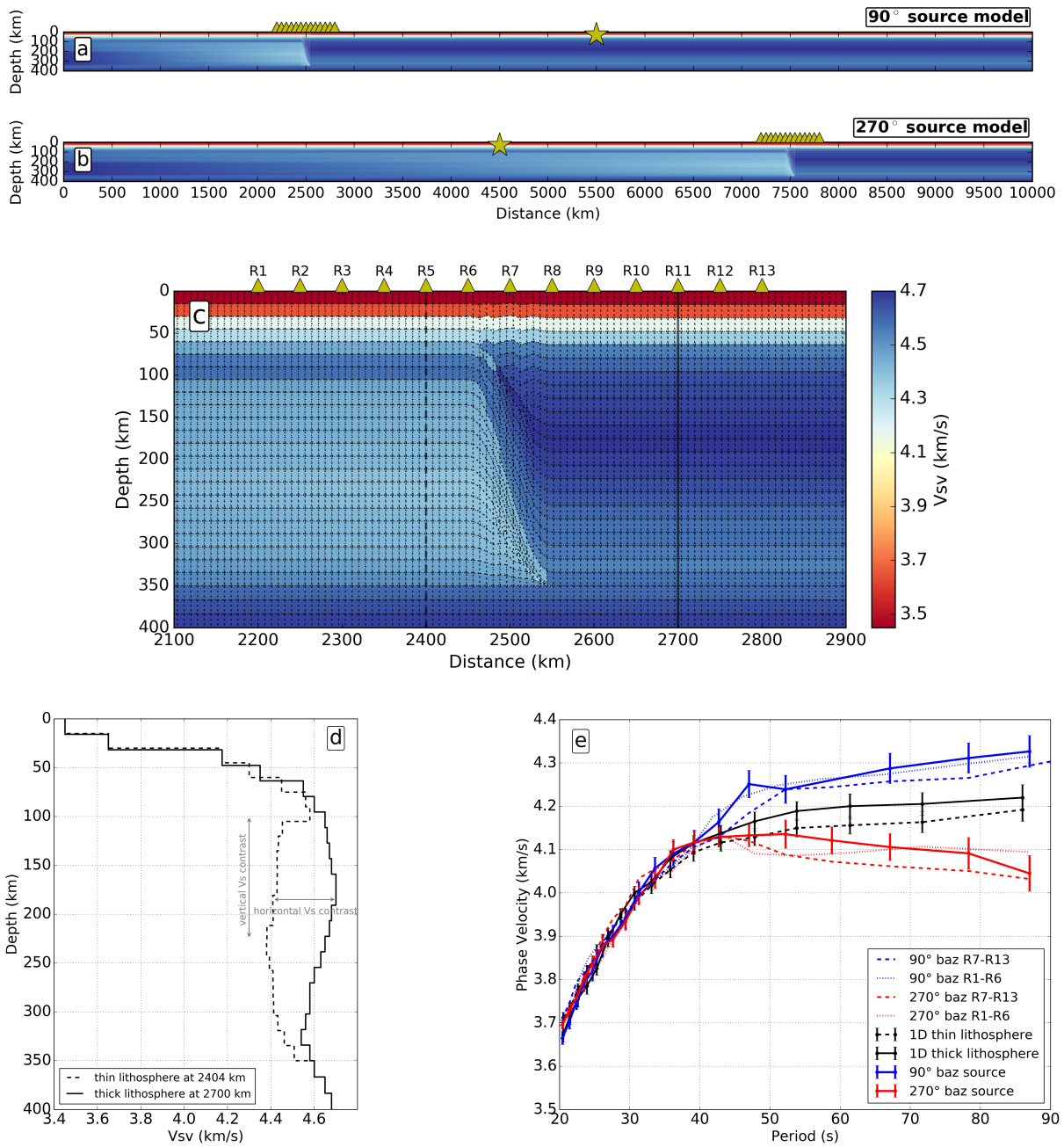

Fig. 4.9: (a) and (b) Synthetic 2D models used for full waveform forward modeling. Yellow stars mark the source, yellow triangles across the lithospheric step are the receivers. Source-receiver distances are equal for both models. (c) Zoom of model (a) which is equal to model (b) around the lithospheric step. (d) Shear wave velocity with depth for the thin lithosphere at 2404 km distance (dashed line, left step side) and thick lithosphere at 2700 km distance (solid line, right step side). Both profiles are marked in (c). (e) Phase velocity dispersion curves retrieved from the models shown in (a) and (b). The thin and thick lithosphere dispersion curves result from 1D reference models with velocity models shown in (d). For the model with the source to the right (90°) much higher velocities are obtained for periods > 45 s. The left source (270°) model results in significantly lowered velocities which is in agreement with our data observations shown in Fig. 4.7. See text for a description of the interpretation of error bars.

separately, where the latter is likely to simulate our real recording configuration both in the North and in the South, with stations located eastwards of the potential LAB step (Fig. 5.2). For each source direction, we compare the results at the subsets of proximal (closest to the source) and distant (further away) stations where we find four noticeable characteristics: (I) We note first that the variation depends more on the propagation direction than on the subset of stations used. (II) By comparing the azimuth-dependent variations for the left and right sub-arrays, we observe that the velocities measured at the proximal sub-arrays (R1-R6 for 270° baz source and R7-R13 for 90° baz source) are generally closer to the 1D case than at the distant sub-arrays. (III) At sub-array R1-R6, the velocities are roughly equal to those measured with the full array for both source directions, and therefore display the same variation with propagation direction as the full array. (IV) The R7-R13 measurements also show considerable variation with propagation direction but the velocities are lower than in the R1-R6 subset cases, although that the stations are located on the thicker and therefore faster lithosphere.

We note that the wavelength at 60 s is about 250 km which is the distance between the first and last stations and the lithosphere step. As it may take some distance for the velocity information at depth to reach back to the surface, it is reasonable that it is not only the structure beneath the array but also the structure somewhat shifted towards the source that determines the measured velocity at a given array. Such a lateral shift is observed in Bodin & Maupin (2008) and also imaged in the phase velocity maps by Lin & Ritzwoller (2011a). This might explain to some degree why the velocities with the 90° baz source are higher than with the 270° baz source for which the wavetrain has propagated through the entire LVZ. However, that does not explain the fact that the direction-dependent velocity variation significantly exceeds the difference expected from the difference between the thick and thin lithosphere 1D models.

As we observe the distant sub-arrays to be more affected than the proximal sub-arrays, we may attribute the larger phase velocity deviations primarily to forward scattering and a related mode-coupling mechanism. On the other hand, the proximal sub-array velocities are also affected, so there appears to be some influence of reflected (backscattered) waves (Lin & Ritzwoller, 2011a), but weaker than the forward scattering effect.

Some snapshots from the surface wave train propagation are shown at different time steps in Fig. 4.10(a-d) for the 90° baz model to investigate the wave field perturbation and scattering around the lithosphere step. The leading shorter wavelength wave train seen at e.g., 2000 km distance in Fig. 4.10(a) is likely a higher mode with amplitudes lowered by about 50 compared to the main wave train. They are also well separated in time on the seismograms from which the phase velocities have been measured. As we observe this feature also in the 1D reference models with their simple dispersion curves, we rule out any influence on the origin of the 1θ azimuthal variation.

The dispersive effect of the Rayleigh waves can nicely be seen with the longer periods sampling deeper structures (Fig. 4.10a). When the fundamental mode traverses the lithospheric step and the LVZ strong perturbations of the wave field occur where the long-period waves are predominantly affected as seen from the dispersion curves in Fig. 4.9. Ultimately, the waves are backward scattered and interfere with the forward propagating wave train (Fig. 4.10b and c). The more advanced the wave propagation, the more clearly the backward scattered waves appear (Fig. 4.10d). Similar scattering effects can be seen for the 270° baz model.

An interference of the incident main wave train and backscattered waves produces phase

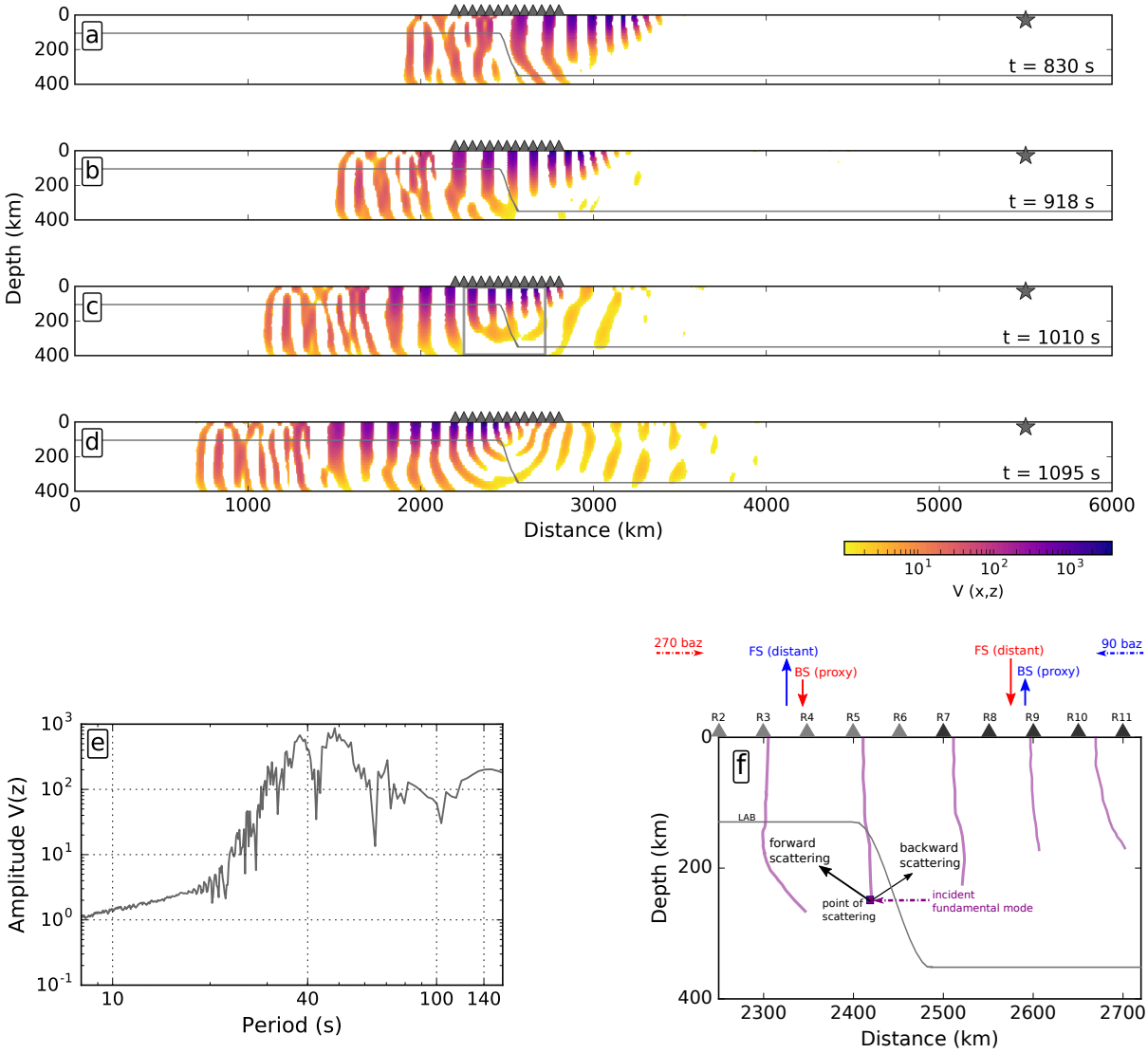

Fig. 4.10: (a)-(d) Time step snapshots of the surface wave train propagation across the lithospheric step at 830, 918, 1010, 1095 s after origin to demonstrate the wave perturbation and scattering effects around the LAB step. The vertical component of the velocity wave field is shown with a logarithmic color scale, negative values are masked to highlight the wave perturbations. The source is located to the right of the step on the thick lithosphere side (90° baz source). See Fig. 4.9 for more details. Grey line outlines the LAB. The inset in (c) refers to the sketch in (f). (e) Amplitude spectrum of V(z) for the wave train shown (d). (f) Summary sketch of the proposed scattering mechanism and main results. The forward propagating fundamental mode from 90° baz (shown as purple lines) is simplified from the inset in (c). The fundamental mode is scattered at the LAB step and within the LVZ both in forward and backward direction illustrated by the black arrows. An interference occurs of the scattered wave with the main wave train. Grey and black triangles indicate the sub-arrays R1-R6 and R7-R13, respectively. The size of the blue and red arrows above the receivers corresponds to the order of phase velocity variation in Fig. 4.9. Forward scattering (FS) leads to higher velocity variations than backward scattering (BS).

variations with a wavelength equal to half of the incident wavelength (Maupin, 2001). Measured at an array with a dimension of at least one wavelength, the backscattered waves are therefore expected to produce noise in the measured phase velocities but not a systematic shift. Considered with our synthetic dispersion curves and the presumed forward scattering, backward scattering seems to have only a secondary impact on the phase velocity variation.

In search of the origin of the 1θ variation we have tested additional models with various shallow lithosphere structure and LAB configurations . In a first test, we altered only the shallow lithosphere above the LAB that we made faster on the thin side and slower on the thick side (i.e., vice versa to the reference model in Fig. 4.9) as seen in other continental margins (e.g., van der Lee, 2002; Fishwick et al., 2008) and possibly below the North sub-array (Fig. SB.2). We obtained a qualitatively similar pattern of phase velocity variations as before (cf. Fig. SB.2 bottom right and Fig. 4.9) which is maybe not surprising considering that vertical and lateral Vs contrasts are very similar to the reference model. In another test, we incorporated a high-density lower crustal layer (LCL) on the thick lithosphere side in the model of Fig. 4.9 according to the study by Ebbing et al. (2012) (Fig. 5.2). Again, the magnitude of phase velocity perturbations is comparable to the reference model. Therefore, the lowermost crust and shallow lithosphere structure seems not to be a decisive factor for the occurrence of the phase velocity perturbations, and maybe surprisingly, does not introduce propagation direction dependent variation at smaller periods, at least in the modeled 2D case. The discrepancies between the observed and synthetic data with respect to the onset of the 1θ variations (>35 s for observations, >50 s for synthetics) must therefore be explained in a different way and might be related to shallow 3D scattering in the lithosphere.

Models where we have modified the properties of the LAB transition are illustrated in Fig. 4.11. A simple model containing three crustal layers as in Fig. 4.9 but only a homogeneous LVZ with an uniform velocity and enclosed by a homogeneous fast medium is illustrated in Fig. 4.11 a. This model leads to nearly equal phase velocities for both source directions , although the vertical and lateral Vs contrast is almost 5% as in the reference model. We conclude that the presence of a lithospheric step alone is not sufficient to create a 1θ variation, rather, a pronounced heterogeneous velocity structure is necessary.

By comparing the phase velocity differences between the 90° and 270° baz source models in Fig. 4.11(b-d), we note a significant effect of both the lithospheric step width (in km) and the vertical or lateral Vs contrast (i.e., the strength of the LVZ anomaly, where the vertical and lateral Vs contrasts are similar, cf. Fig. 4.9d). In case of a 100 km step width and a very strong 11% vertical Vs contrast (Fig. 4.11 b) we measure distinct fast and slow phase velocities for the two source directions. However, the velocity discrepancy for the 270° baz source is slightly higher compared to a 5% vertical Vs contrast as shown in Fig. 4.9, whereas the 90° baz source gives rather similar velocities. Hence, the dispersion curves are not simply proportional to the vertical Vs contrast. For a much broader step width of 400 km, even with a strong vertical Vs contrast (Fig. 4.11 c), or a sharp transition (100 km step width) but a weak vertical Vs contrast (Fig. 4.11 d), the phase velocity variations further reduce and become increasingly less affected by the propagation direction.

Fig. 4.12 summarises the phase velocity measurements made in some additional models with various LAB configurations for a period of 80 s. The relative phase velocities are determined with respect to the 1D thick lithosphere reference model as shown in Fig. 4.9d

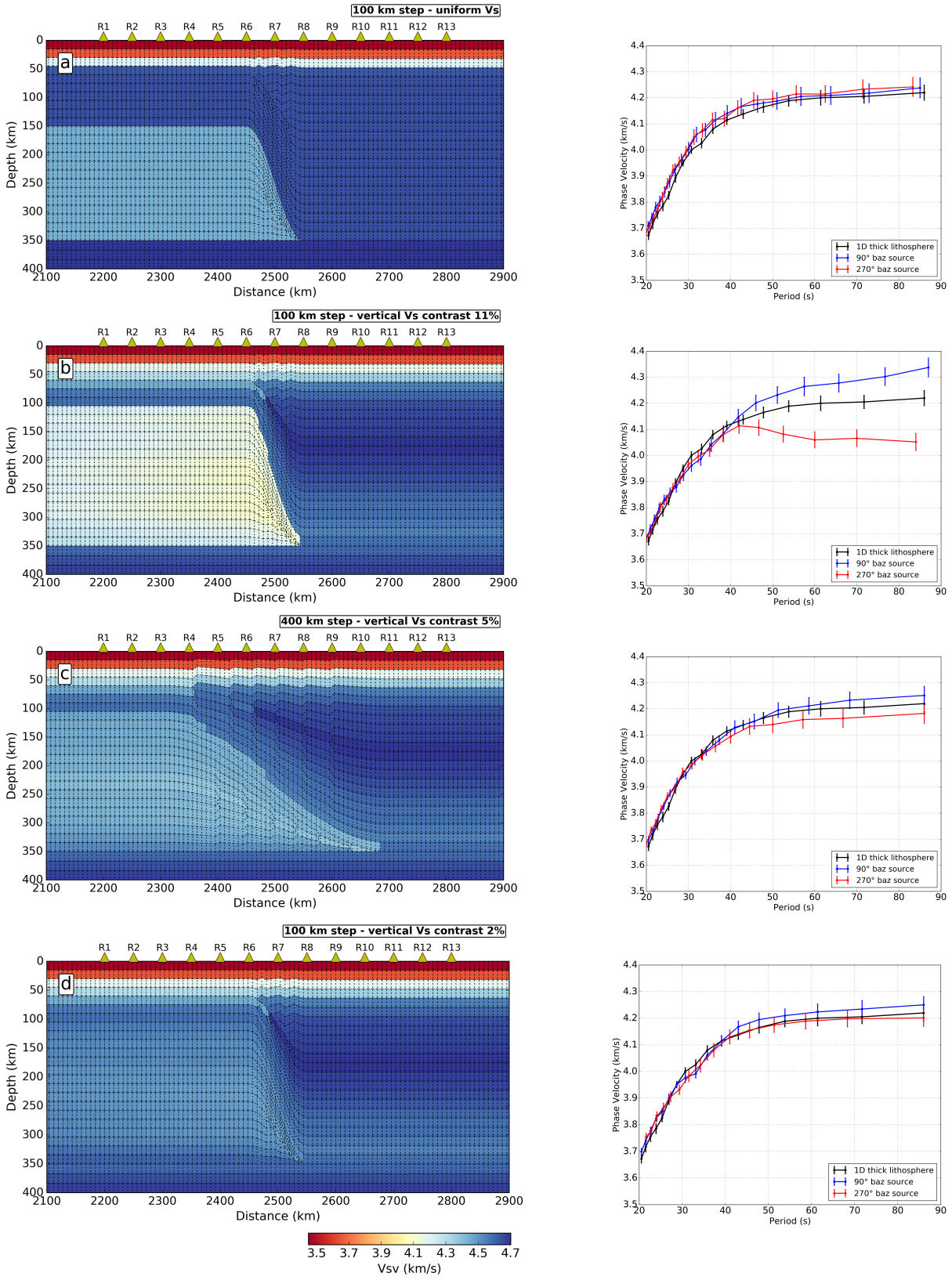

Fig. 4.11: Examples of models with their corresponding dispersion curves. Only the region around the lithospheric step is shown similar to Fig. 4.9c. The label above the receivers denotes the model setting. The black dispersion curve is the same reference curve as in Fig. 4.9 as the velocity structure on the thick lithosphere side does not vary between the models (b-d). See text for details.

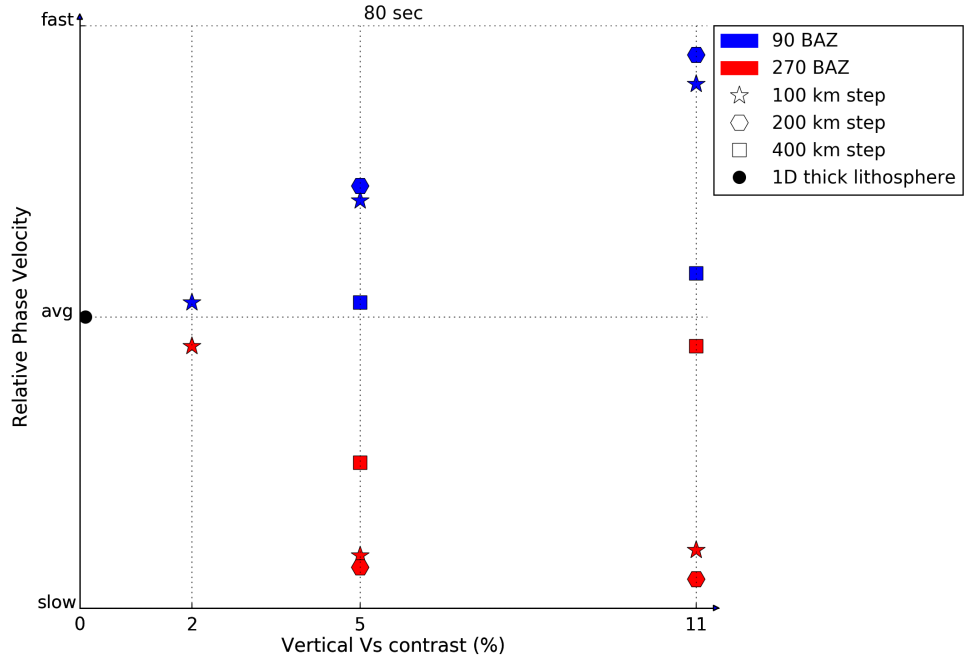

Fig. 4.12: Overview of the phase velocity results from various 2D models for 80 s with 400 km depth, respectively. The vertical Vs contrast refers to the largest velocity difference across the LVZ (cf. Fig. 4.9d). The fast and slow phase velocities are determined with respect to the homogeneous reference model as shown in Fig. 4.9. Blue colors indicate a modeled source to the right of the lithospheric step (90° baz), i.e., propagation towards shallower lithosphere and red colors show the results from a source to the left, i.e., propagation towards deeper lithosphere. See Fig. 4.11 for details.

since the structure to the right of the step is the same for all models. Generally, the phase velocity discrepancy drops down approximately proportionally to the vertical Vs contrast. Similar azimuthal velocity differences are obtained for both 100 and 200 km wide steps. However, for 400 km wide lithospheric step models the phase velocity discrepancy reduces significantly, independently of the strength of the LVZ. In conclusion, the azimuthal bias becomes negligible for smooth vertical and lateral gradients.

We remark that we did not reproduce propagation direction dependent variations for moderate periods at around 40 s as seen in the observed data (Fig. 4.7). Although the modeled medium is similar to the observed Vs and depth structure as we know so far from southern Norway, we unambiguously reproduce the directional velocity effect only for periods > 50 s.

4.7 Discussion

We observed a remarkable Rayleigh phase velocity variation with backazimuth in the northern and south-eastern part of Scandinavia, which cannot be explained by seismic azimuthal anisotropy. We will discuss this surprising result in terms of its theoretical interpretation, tectonic implications and further seismic observations.

4.7.1 Theoretical considerations

Bodin & Maupin (2008) analysed the influence of isotropic anomalies on synthetic phase velocities where the array dimensions are about of the size of the heterogeneity (20–140 km), and both are smaller than the wavelength ($\lambda \sim$ 80–400 km). They also evaluated an azimuthal

bias of the anomalies on the phase velocities. Generally, they find coupling to higher modes and Love waves negligible compared to the self-coupling of the fundamental Rayleigh mode. Arrays which are placed very close to such anomalies can generate a combined 1θ and 2θ phase velocity variation with azimuth. This 1θ component, however, is weaker compared to our observations and diminishes very rapidly with increasing distance of the array from the anomaly. At 100 km distance from the anomaly, which is further away than our left and right sub-arrays (section 4.6.1), they did not observe significant phase velocity variations anymore. This could be due to the 3D nature of their heterogeneity and related wavefront healing which is insignificant in a 2D setting (e.g., Nolet & Dahlen, 2000). The array modeled by Bodin & Maupin (2008) is only 60 km wide and is further away from the heterogeneity than in our case, where the array starts right of the edge of the heterogeneous region. At 20 km distance, i.e., in proximity to the heterogeneity, the synthetic data by Bodin & Maupin (2008) show a significant 1θ variation of apparent phase velocity.

Heterogeneities which are smaller than half of the wavelength may perturb the phase velocities (Lin & Ritzwoller, 2011a). When regarding single phase measurements from only one azimuth waveforms are distorted by reflections and diffractions due to the anomaly. However, these artefacts can be related to the small array dimensions compared to the wavelengths considered and larger aperture arrays such as ScanArray are usually expected to give more robust measurements.

The concept of scattered waves after Aki & Richards (1980) (chapter 13, Fig 13.11) depends on the ratio between the dominant wavelength of the seismic wave, λ, and the scale of the anomaly, a, expressed as the correlation length ratio $ka = \frac{2\pi a}{\lambda}$ on a logarithmic scale. Strong scattering occurs if the dimension of the structural perturbation and the dominant wavelength are of similar size, i.e., ka is around 1. This is the case for the lithospheric step in southern Scandinavia with the observed 1θ effect for periods longer than around 40 s ($\lambda >\sim 200$ km) and consistent with the findings of Bodin & Maupin (2008). From our modeling results, summarised in Fig. 4.12, the threshold for a measurable 1θ variation is a ~400 km wide horizontal velocity gradient and a 5% Vs contrast in the lithosphere. In terms of the scattering classification after Aki & Richards (1980), we can therefore evaluate $ka = 0.3 - 1.0$. Hence, the 1θ effect could be placed in the low scattering regime in the Aki & Richards (1980) scheme. Numerical methods are needed to quantify the scattering effects affecting regional arrays.

Datta et al. (2017) conducted a theoretical study of surface wave mode coupling in the presence of various lateral heterogeneities but with a larger dimension than in our case. A waveform amplitude gain of converted modes due to mode conversion appears mainly for higher modes at periods < 30 s which is below our observed 1θ variation period range. Generally, the effect influences the fundamental mode less than the overtones and affects Love more than Rayleigh waves. Taking additionally into account our observed waveforms with a dominant fundamental mode (Fig. 4.4), we consider any bias by an anomaly caused by higher mode conversion as unlikely but we cannot rule out this completely as coupled higher modes would not appear as separated wavetrains in the seismogram. Neither do our modeling results from Fig. 4.9 conform to local mode expectations (Maupin, 2007) as the sub-array velocity measurements do not represent the average structure below.

Since there is no evidence for higher mode coupling or conversion, we consider the occurrence of self-mode coupling at the lithosphere step, i.e., the coupling of the fundamental mode to itself as the likely dominant process. The lithospheric step with its lateral and vertical abrupt

variations acts hereby as a scatterer, as illustrated in Fig. 4.10f. A mode coupling originates at the point of scattering where a phase shift is directly induced from the coupling (cf. eq. 26 in Snieder (1986); Maupin (2007)). In an equivalent formulation, the coupling implies a phase velocity variation of the mode. Note that the sketch in Fig. 4.10f idealises the problem with a point scatterer. However, due to the long wavelengths $\lambda >\sim 200$ km of the incident wave field, the scattered wave should be rather considered as an integration over the lateral extent of the whole scatterer (Snieder, 1986) as seen in Fig. 4.10. According to our modeling results, forwarded scattering caused by an incident wave from 270° baz would result in a large negative phase shift to produce the observed lowered phase velocities east of the step. By contrast, scattering in backward direction would cause a lower positive phase shift to match with the increased velocities at these arrays. This behavior is vice versa for a propagating wave train from 90° baz. However, that hypothesis cannot be confirmed at the current stage.

The effect of longer-wavelength heterogeneities on surface wave velocities is described by the path-average approximation (PAVA) (Woodhouse & Dziewonski, 1984). The PAVA, which is generally valid when the lateral scale of the heterogeneous structures is significantly larger than the wavelength, is one of the most vital assumptions in ray theory based tomography, or in general plane wave approximations, since Woodhouse & Dziewonski (1984) formulated their waveform inversion scheme. It states that the effective phase velocity perturbation for a path corresponds to an average of the phase velocity perturbations predicted for the velocity-depth structure below each point of the path. This implies that the direction in which the path is traversed has no influence on the inferred perturbations. Our results indicate that PAVA is locally violated (Fig. 4.9). This is maybe not surprising as at a period of 40 s the wavelength is about 160 km whereas the lateral inhomogeneous structure is only 100 km wide. We emphasize that we describe a local PAVA violation only as a result of strong heterogeneities immediately below a regional array. It does not necessarily imply that the phase velocity perturbations along the whole propagation path between source and receiver, as used for example in global group velocity tomography, are not properly described by PAVA even when traversing a strong heterogeneity.

We note that PAVA is often used together with the great circle approximation (GCA) where the wave is assumed to propagate nearly along the great circle path. In this study, however, we clearly distinguish between these two approximations. In contrast to PAVA, any GCA violations appear to only add to the scatter of individual event measurements but not cause a bias as we did not observe systematic variations from the theoretical azimuth (Fig. 4.5). Neither is the great-circle path deviation larger than in other phase velocity studies that showed either no significicant azimuthal variation or the 2θ pattern expected for anisotropic structure. Furthermore, the azimuth of propagation is treated as an unknown in the beamforming, implying that any deviation is effectively taken into account in the determination of the phase velocity. In our measurements, phase velocities for observed opposite propagation directions result in highly different velocities, without any correlations with backazimuthal deviations (Fig. 4.5). Therefore, the 1θ effect appears to arise from intra-array wavefield interference, or interactions in the immediate neighborhood of the array, as also demonstrated by the synthetic tests (section 4.6.1).

Whereas we noticed and studied the 1θ effect based on beamforming array analysis, it would affect all approaches reliant on ray theory to interpret measurements of phase differences between stations of a regional array, such as the two-station method (e.g., Gomberg & Masters, 1988;

Soomro et al., 2016), tomographic inversions reliant on two-station measurements (Prindle & Tanimoto, 2006) or also the two-wave method of Forsyth & Li (2005).

In the traditional PAVA approximation only the propagation path is accounted for the phase perturbation while contributions for source and receiver are neglected (Dahlen & Tromp, 1998). However, the newly observed local violation is induced from strong perturbations right below the receivers which might give rise to the discrepancy.

Conceptually, the simplest way to overcome these pitfalls would be the abandonment of the PAVA in preference to more accurate finite frequency schemes (Spetzler et al., 2002) or full-waveform inversion. Another helpful methodology applies the concept of coupled modes (e.g., Maupin, 1988, 2001; Li & Romanowicz, 1995).

The 1θ variation we observe with beamforming is expected to occur also, and possibly more severely, for studies based on a detailed local tracking of the phase of the wavefront within the network of stations, such as Eikonal tomography (Friederich, 1998; Lin et al., 2009). As shown by Wielandt (1993), the gradient of the phase is equal to the structural phase velocity only for wavefields with a constant amplitude (equivalent to plane wave assumption), and all methods relying on the phase only to measure the velocity will to some degree suffer from deviations from the plane wave model, even within small arrays (Friederich, 1998). Two (or several) plane wave models can be used to account for heterogeneities located outside the network (Forsyth & Li, 2005), but near-by scattering is more difficult to account for. If coupling to overtones and Love waves is negligible, as discussed before, the solution is to introduce a correction based on the lateral first and second order derivatives of the amplitudes (Wielandt, 1993), known as Helmholtz equation. Although this method has been shown to be very effective on synthetic data (Friederich et al., 2000; Bodin & Maupin, 2008), and used on real data (Jin & Gaherty, 2015; Lin & Ritzwoller, 2011b), the requirements in terms of precision of the measurement of the amplitude are not met in many studies, including ours. The necessity to mitigate biases due to non-plane wave geometry by a good but also rather uniform azimuthal distribution of paths should be emphasized, also for Eikonal tomography.

We recommend to balance the azimuthal event distribution used for tomographic studies either by sub-sampling events from well-covered azimuths or by applying a weighting scheme that compensates for unequal backazimuthal coverage. Whereas this does not guarantee to completely remove the bias, our synthetic tests suggest that the azimuthally averaged value is close to the expected value (Fig. 4.7, S B.1). We point out that for phase velocity analysis with dense regional arrays, which aims to resolve and interpret detailed structures, considerable phase velocity artefacts may occur and thus bias the inferred shear velocity structures. Body wave tomographic artefacts due to non-uniform source distributions have been discussed previously (e.g., Zhao, 2019). The impact of such azimuthal bias on tomographic inversion results for surface waves is demonstrated in Mauerberger et al. (2021b). Whereas for global imaging with large-scale station distances the velocity or structural bias might be neglected.

The observation of the 1θ effect might also has an implication on anisotropy studies. In the presence of pronounced heterogeneities below the receivers, the structural azimuthal anisotropy might be masked by 1θ variations. In addition, the 1θ effect of the heterogeneities is just the lowest order in azimuth of a more complex azimuthal variation (e.g., Bodin & Maupin, 2008). The fact that so strong 1θ variations occur suggests that significant 2θ anisotropy due to heterogeneities may also occur and be mistaken for seismic anisotropy. Lin & Ritzwoller (2011a) have discussed biased 2θ anisotropy and proposed this can be mitigated when finite frequency

effects are considered for the inversion.

In conclusion, we deduce from our modeling that self-mode coupling of the fundamental mode as a result of forward scattering, caused by strong vertical and lateral velocity contrasts at the LAB as well as sharp lithosphere step widths, generates larger phase velocity variations than backward scattering. However, it is important to note that the prevailing scattering mechanism and therewith a potential phase shift, depends on the propagation direction and the location of the regional (sub)-array (Fig. 4.10f). A predominantly self-mode coupling hypothesis is also supported by the synthetic tests of Bodin & Maupin (2008). Nevertheless, we cannot determine with certainty the origin of the 1θ effect from a wave propagation point of view.

In this paper, we considered only wave propagation in 2D models with opposite propagation directions, simulating propagation perpendicular to the strikes of geological structures. For a further examination of the 1θ effect, modeling of oblique propagation in 2.5D models (e.g., Maupin, 1992; Takenaka et al., 2003) would be interesting and could be done in a future study.

4.7.2 Observations in other regions and tectonic implications

1θ variations of Rayleigh phase velocities have been reported previously by Menke & Levin (2002) and Lin & Ritzwoller (2011a). Menke & Levin (2002) observed this effect at the eastern rim of the Appalachian mountain range in the northeastern United States - which are the orogenic pendant to the Scandinavian Caledonides (Thomas, 2006), i.e., both represent conjugate structures. The lithospheric structure beneath the Appalachians is therefore mirrored compared to Scandinavia. Here, an unusual thin lithosphere (about 100 km thickness) with very low shear velocities (about 10% Vs contrast) in the asthenosphere (e.g., North Appalachian Anomaly) associated with a sharp thickening towards the western Proterozoic craton has been imaged by many studies (e.g., van der Lee, 2002; Li et al., 2002; Rychert & Fischer, 2007). This strong 10% vertical Vs contrast along with the observed ±5% variation around the average phase velocity at 33–50 s period (Menke & Levin, 2002) corresponds well to our modeling results (Fig. 4.12). Moreover, the fast and the slow observed phase velocity directions by Menke & Levin (2002) are also mirror-inverted where the fast direction is facing the LAB step. This means they made the same observation with regard to the velocity and structural contrast as in Scandinavia. In both cases the lithospheric edge is mainly perpendicular to the continental margin and to the mountain front, i.e., the transition to the craton.

The lithosphere beneath the Appalachians was subjected to various tectonic processes through time as subduction by the Avalonia plate, active volcanism, hot spot tracks and the opening of the Central Atlantic Ocean about 200 Ma ago (Thomas, 2006; Menke et al., 2016). Nevertheless, the Scandinavian and Appalachian lithosphere are very similar, resulting in the 1θ observations. The last known tectonic process which is supposed to have affected both conjugate structures is an uplift in Cenozoic times about 30 Ma (Hay et al., 2002). From these indicators, we can speculate that the imaged lithospheric structures have been created in recent times overprinting Mesozoic and Paleozoic processes.

Lin & Ritzwoller (2011a) detected a 1θ apparent anisotropy in northwestern United States across the Snake River Plain (Idaho) which is also related to local strong velocity contrasts

(Schmandt & Lin, 2014) . They find increasing 1θ variations for periods > 50 s which is consistent with our observations. Although the geological regime is very different due to the Yellowstone hot spot track, the common feature is a sharp transition in uppermost mantle structure with a pronounced velocity contrast. However, unlike the Scandinavia and Appalachians settings, the fast directions of the 1θ variation point toward the location of the faster structure. By simulations with finite frequency kernels, Lin & Ritzwoller (2011a) propose prevailing backward scattering near the receiver site to be responsible for the 1θ variation. A dominating backscattering effect on the phase velocity would be strongest when the receivers are very close to a sharp lateral gradient, i.e., within a distance of $\sim$3/16 of the wavelength or $\sim$50 km at 60 s. This corresponds well to our modeling results and can be nicely seen in the wave propagation snapshots in Fig. 4.10. Otherwise, no impact of backward scattering can be expected for short periods with wavelengths $<$200 km which nearly corresponds to the observed 1θ emergence at 35 s.

South of Scandinavia, at the border to the European continent, a sharp transition in the lithosphere had been reported by Cotte et al. (2002) across the STZ. Here, the change from thin (120 km) to thick (200 km) lithosphere strikes roughly WE in contrast to the NS orientation across the Oslo Graben but phase velocity variations were not investigated in that study. Another example of shallow LAB with a sharp lateral step and strong velocity changes can be found in southeast Australia (e.g., Fishwick et al., 2008; Rawlinson et al., 2017). From these conclusions we predict a high potential of observing a 1θ variation across the Greenland Caledonians (Artemieva, 2019b), southeast Australia and the STZ.

Moreover, due to the 1θ variation seen from the North sub-region in this study, we expect a sharp lithospheric step in the order of 100 km with a pronounced LVZ below the LAB having a Vs contrast of $> 5\%$. We estimate a higher Vs contrast in the north since the 1θ variation is more pronounced than in the south.

The corresponding lithospheric step in the north might result from the transition of the Precambrian craton (Baltic Shield) to the Paleozoic terrane across the Caledonian front as indicated by a recent body wave (Hejrani et al., 2017) and surface wave tomography (Mauerberger et al., 2021b). Another candidate could be the ocean-continent transition because the continental margin is very close to the North sub-array (Fig. 5.2). Also a combined influence of both strong gradients seems reasonable, at least in the north because in the south the continental margin is further away from the coast and the onshore lithosphere gradient.

In contrast, a smoothly varying lithosphere with weak lateral heterogeneities might be responsible for the absence of a 1θ variation in the central area of Scandinavia. By comparison of the reported 1θ effects and in the context to the tectonic features described above, we assume significant lateral heterogeneities on small scales in terms of velocity and LAB thickness lead to 1θ observations.

In southern Norway (Maupin, 2011), there is only little evidence (at 50 s period) for a systematic phase velocity variations with azimuth in the MAGNUS dataset. This might be due to the fact that she used stations which are mainly located above the flat part of the LAB beneath southern Norway and some stations which coincide with the central sub-array in this study where the azimuthal variation is absent.. Therefore, some of the stations of the array used by Maupin (2011) are presumably barely affected by scattering related perturbations which mitigate the 1θ variation.

Pedersen et al. (2006) conducted an array-based anisotropy survey for both Rayleigh and Love waves in central/southern Finland (SVEKALAPKO network) with moderate 2θ variation for all periods considered. No 360° periodicity was observed. Again, the lack of 1θ variation supports our assumption that for generating this phase velocity effect sharp steps in lithosphere thickness along with strong vertical and lateral velocity gradients are necessary. The lithosphere below central/southern Finland seems to be very complex on small scales, however, there is no indication for any sharp step with large velocity perturbations as seen across the Oslo Graben (Bruneton et al., 2004a).

4.8 Conclusion

From the recent ScanArray project and taking advantage of many permanent stations, we were able to analyse the average phase velocity structure with a beamforming technique. By forming sub-arrays covering the North, Central and South regions of Scandinavia, we were able to unveil exceptional phase velocity variations. In the North and the South we observe a 360° periodicity (1θ variation) of the phase velocity with propagating azimuth for periods > 35 s. Fast velocities were obtained from eastern directions and very low velocities from western azimuths with a maximum deviation of 5%. In the central area the 1θ variation is absent for all periods. By averaging over all propagation azimuths we can nevertheless obtain a stable phase velocity estimate for each sub-array, finding little difference between the regions. At mantle depth, the average phase velocities are slightly lower compared to previous results from Finland. The 1θ variation implies also the importance and necessity of an even azimuthal event distribution to avoid biased phase velocity measurements.

Since we suspected a relationship between the lithospheric structure and the observed 1θ variation, we conducted a 2D waveform modeling for the Rayleigh surface waves. By simulating various structures, we found increased phase velocities for waves propagating from thicker to thinner lithosphere whereas for waves propagating from thinner to thicker lithosphere the phase velocities are clearly decreased. From analysis of the variation of apparent phase velocities for sub-arrays located to the left and right of the main lithospheric heterogeneity in synthetic tests, we identify forward scattering as the main contributor to the 1θ phase velocity variation. Investigation of the wave train propagation indicates the presence of backward scattering near the lithospheric step, which, however, is likely to be less important than forward scattering as cause for the azimuthal variations in phase velocity measurements.

A 1θ anisotropy has been observed before (Menke & Levin, 2002) across the north-eastern Appalachian Mountains which have also been created during the Caledonian orogeny. Here, the LAB step as well as the fast and slow phase velocity directions are mirror-inverted compared to Scandinavia. We conclude that sharp horizontal structural gradients in combination with strong vertical and lateral velocity contrasts in the lithosphere lead to 1θ variations. Since we observed the 1θ effect also in northern Scandinavia, we assume a distinct east-west orientated lithospheric structure with pronounced velocity contrasts in that region. Strong horizontally lithospheric gradients could exist due to the Paleozoic-Precambrian transition across the Caledonian front and/or the ocean-continent transition. Finally, we see high potential to observe 1θ variations across the Greenland Caledonians and southeast Australia as those regions also exhibit strong changes in lithosphere thickness associated with large velocity contrasts.

Chapter 5

A shear-wave velocity model for the Scandinavian lithosphere from Rayleigh waves and ambient noise - Implications for the origin of the topography of the Scandes mountain range

5.1 Abstract

The passive margin along western Scandinavia is characterized by a ∼420 Ma old mountain range (the Scandes) with a peak elevation of 2,500 m but significant variations in the height of topography along the strike of the margin, and also with large variations in its width. The Scandes mountains were deeply eroded after the orogeny, raising the question what compensates the high topography today. East of the Scandes, Scandinavia consists of Archean and Proterozoic terranes. We present a new 3D shear-wave velocity model and Moho map of Scandinavia, which is based on the inversion of the merged phase dispersion curves from ambient noise and earthquake-generated Rayleigh waves. We use a classic two step inversion scheme where first maps of phase velocities at different periods are derived, and then a 1D transdimensional Bayesian method is applied to determine the V_{SV}-depth structure.

While the southern Scandes lacks a pronounced crustal root, we observe a crustal root below the northern Scandes that is decreasing towards the central Scandes. A ∼10 km thick high-density lower crustal layer is present below the northern Scandes and generally thickening to the east below the Baltic Shield. The lithosphere-asthenosphere boundary (LAB) below the Scandes is deepening as well from west to east with a sharp step and a strong V_{SV} decrease with depth of 9% in the north and of 5.5% in the south. The LAB of the thinner lithosphere is at 150 km depth in the north and varies from 90–120 km depth in the south. Surprisingly, both LAB steps coincide with the mountain front. The central area shows rather smoothly varying structures (170 km LAB depth, -4% V_{SV} with depth) towards the east and no clear spatial match with the front. We infer therefore distinct uplift mechanisms along the Scandes. The southern Scandes might sustain their topography due to dynamic support from the mantle, while the northern Scandes experience both crustal and mantle lithosphere isostasy. In both cases, we suspect a dynamic support from small-scale edge-driven convection that developed at the sharp lithospheric steps. Beneath the Archean Karelia craton in northern Finland, we find low-velocity areas below 150 km depth while a 250 km deep lithospheric keel is imaged below the Paleoproterozic southern Finland. The Norrbotten craton in northern Sweden can be identified at mantle depths as a unit different from the Karelia craton, Scandes and Paleoproterozic Sweden.

5.2 Introduction

Scandinavia has a long history of geophysical and petrological investigations due to its unique tectonic setting: Its eastern part is composed of one of the oldest Archean cratons (Fennoscandian or Baltic Shield) while the western rim of Scandinavia is shaped by the segmented Scandes mountain range, which originated from the Caledonian orogeny ∼420 Ma ago. Elevations are up to 2,500 m in the southern Scandes and 2,100 m in the northern Scandes. The east-west extension of the mountain belt is about 400 km in the south but only 200 km for the northern Scandes. The central part of the Scandes shows an average topography of 1,000 m and a much narrower mountain chain (Fig. 5.1). Close to the northern Scandes, the continental margin separates sharply the shallow oceanic shelf from the abyssal sea (Olesen et al., 2010), whereas the central and southern Scandes are separated by extensional basins from the continental shelf edges.

Since Scandinavia lacks recent compressional tectonic forces, it provides an opportunity to study the geodynamic evolution of crustal and mantle structures at today's passive continental margins and its linkage to the present topography. The enduring history of extensional activity throughout the Mesozoic and Cenozoic, involving Devonian post-orogenic collapse and continental rifting, is summarized by Andersen (1998) and Braathen et al. (2002). The final phase of rifting in the Paleocene is related to the onset of continental breakup and the opening of the North Atlantic Ocean, thought to be initiated by the Iceland plume.

The fundamental question is what sustains the Scandes, and by extension other 'fossil' mountain belts, since Paleozoic times in the face of exposure to extensional tectonics and erosion. High-topography mountain belts far from active plate boundaries are also known from other passive margins such as the northeastern United States (Appalachians) (e.g., Hatcher, 2010), Greenland Caledonides (e.g., Gee et al., 2008), trans-Antarctic region (van Wijk et al., 2008) as well as southeastern Australia (Fishwick et al., 2008).

A long-standing multi-disciplinary debate exists about the fate of the Scandes mountain range that can be described in terms of two end-member models: For one side, the current-day topography is rooted in geological processes much more recent than the Paleozoic Caledonides and, specifically, is thought to have resulted from Cenozoic tectonic uplift at about 25 Ma (Hay et al., 2002) following post-orogenic collapse, as favored for example by Lidmar-Bergström et al. (2000); Smelror et al. (2007); Anell et al. (2009). Alternatively, the present high topography is seen as a remnant of the original Caledonides as argued by Nielsen et al. (2009b); Lidmar-Bergström & Bonow (2009); Nielsen et al. (2009a) and the differences between the southern, central and northern Scandes is controlled by varying erosion rates rather than tectonic processes.

Many of the studies agree that different episodes of uplift and denudation have shaped the Scandes. The entire mountain chain might have experienced major Neogene epeirogenic uplift of about 1–1.5 km (Japsen & Chalmers, 2000), as derived from apatite fission track thermochronology in the South (Rohrman & van der Beek, 1996) and the North (e.g., Riis, 1996; Hendriks & Andriessen, 2002). Denudation in the southern mountain range produced a dome-like structure (Rohrman & van der Beek, 1996), while the elongated northern Scandes have resulted from much more denudation on their western side, towards the continental margin (Hendriks & Andriessen, 2002). The elevation of the southern Scandes has been related to mantle diapirism (Rohrman & van der Beek, 1996) due to an impingement of the Iceland plume in Neogene times. In addition, lithospheric delamination (Nielsen et al., 2002; Korja

et al., 2006), magmatic underplating (Gabrielsen et al., 2005; Korja et al., 2006; Nielsen et al., 2009b) or metasomatism (Maupin et al., 2013) could all have contributed to the observed domal uplift pattern in southern Norway. In contrast, high topography in the northern Scandes has been attributed to either rift-shoulder uplift in Cretaceous to Paleogene times or to isostatic rebound after glacial erosion as discussed by Hendriks & Andriessen (2002) and Gabrielsen et al. (2005). The Lofoten peninsula in the north and the southern Scandes underwent their final uplift episodes in the Plio/Pleistocene (Smelror et al., 2007). Episodes of (coeval) subsidence are attributed to the offshore basins along the Norwegian coast (e.g., Japsen & Chalmers, 2000; Smelror et al., 2007), where major subsidence occurred in the Plio/Pleistocene due to glacial deposition. However, a significant contribution of post-glacial isostatic rebound to the present Scandes elevation has been ruled out by Milne et al. (2001).

For an understanding of the origin of the topography, information on the crustal and mantle structure is necessary. Below we highlight the results of the most important findings with emphasis on the lithosphere structure. The first indications for a sub-crustal support of the southern Scandes came from an early Rayleigh wave tomography study (Calcagnile, 1982). Although it was based on only a few permanent stations it already showed hints of the thickening of the lithosphere from western to eastern Scandinavia and unusually low velocities in the mantle underneath southern Norway. Subsequently, our knowledge about the lithosphere has benefited enormously from the data acquired with a number of temporary networks (see Fig. 5.1). The MAGNUS network in southern Norway (Weidle et al., 2010) revealed much lower P- and S-wave velocities than expected for the Proterozoic domain (Medhus et al., 2012; Köhler et al., 2012; Wawerzinek et al., 2013; Kolstrup et al., 2015; Hejrani et al., 2017) (summarized in Maupin et al., 2013)) below 100 km depth with a sharp transition to higher velocities beneath Sweden across the Oslo Graben, indicating a very shallow lithosphere-asthenosphere boundary (LAB) below the high topography of southern Norway. The average shear velocity of the Proterozoic lithosphere decreases to a minimum of 4.4 km/s at 150 km depth (Maupin, 2011). No clear crustal root is indicated below the highest elevation of the southern Scandes (e.g. Svenningsen et al., 2007; Ebbing et al., 2012; Maupin et al., 2013) which contradicts the expectations of Airy isostasy.

In the Lofoten region, older seismic reflection profiles had suggested a very shallow Moho at only ∼20 km depth, especially towards the continental margin (Mjelde et al., 1995). However, a recent on- and offshore reflection seismic survey by Breivik et al. (2017) showed a much thicker Moho of about 36 km beneath the Lofoten peninsula. They also demonstrated that the reflector interpreted by Mjelde et al. (1995) to be the Moho is really the top of a high-density lower crustal layer. The recent receiver function analysis by Ben Mansour et al. (2018), using the high-density SCANLIPS3D network (England et al., 2015), refuted an extremely shallow Moho, too, and imaged a 38–40 km thick crust below the Nordland/Norrbotten region, with significant local variations. Below the high-topography northern Scandes they imaged a Moho depth of 46–48 km. Ebbing & Olesen (2005) and Gradmann & Ebbing (2015) pointed to different mass compensations along the Scandes by lateral density variations from west to east within the crust. In particular, Pratt isostasy might act below the central and northern Scandes but not below the southern Scandes.

P- and S-wave tomography of Sweden (Eken et al., 2007, 2008, 2010) with data from the permanent Swedish network (SNSN) revealed a low velocity anomaly below the Archean domain of Northern Sweden extending to ∼150 km depth (with a 3-4% velocity reduction with respect

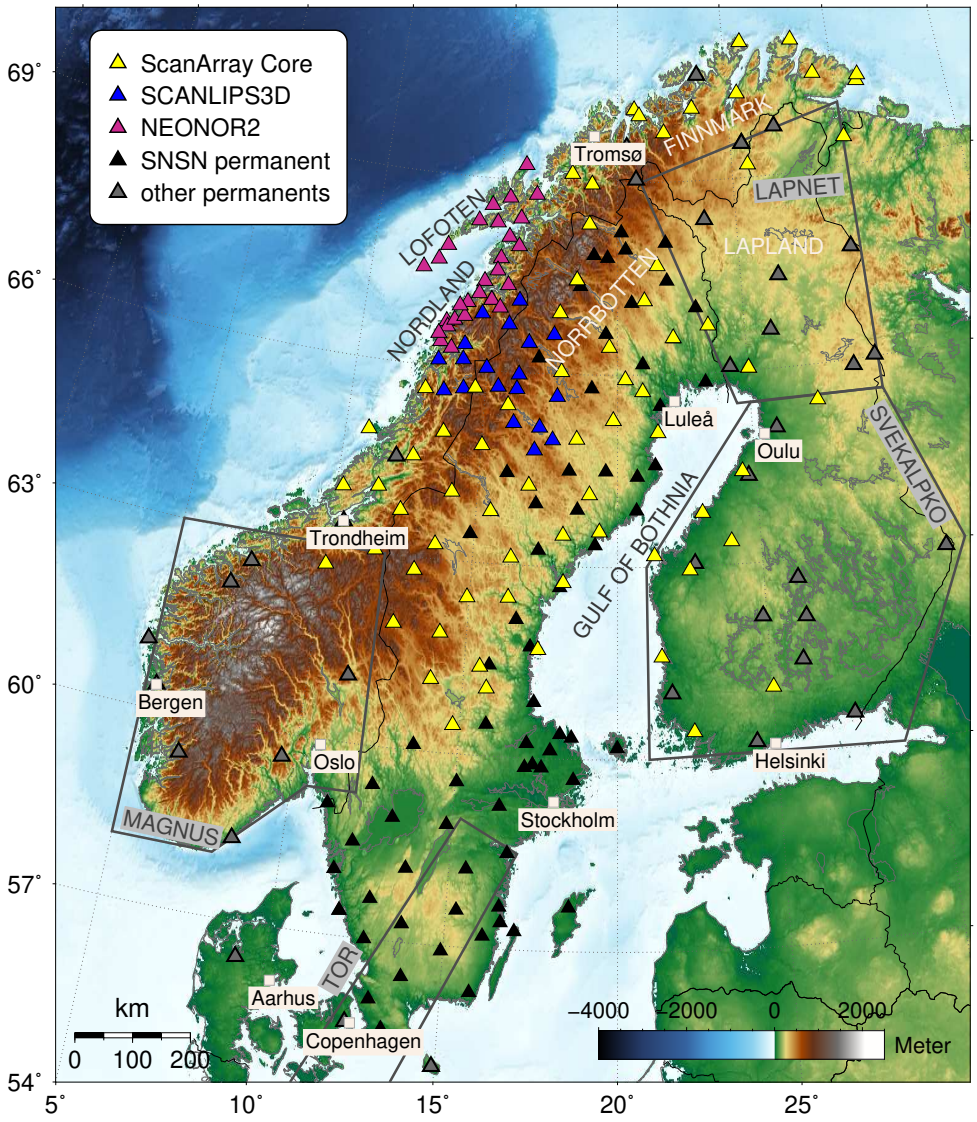

Fig. 5.1: Topography map of Scandinavia with all temporary and permanent seismic stations used for the teleseismic Rayleigh wave dispersion measurements shown as triangles. The ambient noise study used the same station set, but also additional stations from the MAGNUS temporary deployment in southern Norway (only outline marked in map). The Caledonian mountain range (referred to as the Scandes) dominates the western edge of Scandinavia, with its highest elevation of about 2,500 m in southern Norway and around 2,100 m in the north (Norrbotten province). The areas of previous temporary networks (MAGNUS (Weidle et al., 2010), LAPNET (Kozlovskaya & Poutanen, 2006), SVEKALAPKO (Bock et al., 2001) and TOR (Shomali et al., 2006)) are marked with gray boxes.

to the IASP91 reference model), underlain by faster material. Sadeghisorkhani et al. (2021) imaged southern Sweden with ambient noise data showing a relatively faster lower crust along the south-western coast, in agreement with Köhler et al. (2015).

South and central Finland has been covered with the SVEKALAPKO temporary network (Bock et al., 2001) and revealed the thickest crustal structure in Scandinavia with up to 65 km Moho depth (e.g. Sandoval et al., 2003; Hyvönen et al., 2007; Kozlovskaya et al., 2008). The thick Paleoproterozoic crust has been accreted from several terranes and subsequently altered by intra- and underplating, emplacing high-density material (Central Finnish Granite Massif) (Hyvönen et al., 2007). A fast cratonic keel down to at least 250 km depth has been found by Sandoval et al. (2004), while Bruneton et al. (2004a); Hjelt et al. (2006) presented a highly varying mantle structure on small lateral scales across the Archean and Proterozoic domains with $\leq$200 km characteristic anomaly scale. Such small-scale seismic anomalies are difficult to explain with temperature variations but could arise due to compositional variations or as artifacts of anisotropy. Thermobarometric analysis has been conducted on mantle xenolith samples (Kukkonen & Peltonen, 1999; Kukkonen et al., 2003) taken from the kimberlite pipes in central Finland located close to the Archean-Proterozoic suture zone (Fig. 5.2). The xenolith samples can be related to a mantle depth interval between 114–243 km. The mineralogical composition indicates that the xenoliths are unmetasomatised (dry). A lithosphere thickness of at least 240 km is therefore implied, in agreement with the seismic study by Sandoval et al. (2004).

Receiver function as well as body and surface wave tomography studies with data from the POLENET/LAPNET experiments (Kozlovskaya & Poutanen, 2006) characterized the Precambrian lithosphere beneath northern Finland as surprisingly heterogeneous (Pedersen et al., 2013; Vinnik et al., 2016; Silvennoinen et al., 2016; Lebedev et al., 2018). Towards northern Archean Finland with Paleoproterozoic cover, the crust is markedly thinner than in southern Finland, but varies significantly between 43–55 km (Artemieva & Thybo, 2013; Silvennoinen et al., 2014). Pronounced mantle low-velocity zones have been found in various studies (Pedersen et al., 2013; Silvennoinen et al., 2016; Eken et al., 2008) but the depth ranges and lateral scales differ. Pedersen et al. (2013) inferred from average surface dispersion curves a high-velocity lithospheric lid with 4.7 km/s at 140 km depth and significantly decreasing velocities below, with 4.45 km/s at 230 km depth. In contrast, Silvennoinen et al. (2016) imaged a low-velocity structure with -4% V_P perturbation (with respect to the IASP91 reference model) above 170 km depth and a fast medium underneath.

The recent international temporary seismic network ScanArray (Thybo et al., 2021) provides data for previously sparsely covered areas of Scandinavia. Here, we use the ScanArray data, which is supplemented with the permanent broadband stations in Scandinavia, to investigate the lithosphere structure down to 250 km depth. Ambient noise and Rayleigh surface wave data are combined to construct composite dispersion curves, which are then inverted for the velocity-depth structure. A high-resolution 3D shear-wave velocity model of entire Scandinavia is obtained, from which we can produce a Moho depth map. We provide new constraints on different mechanisms that sustain the topography based on significant structural differences along the Scandes.

5.3 Tectonic history

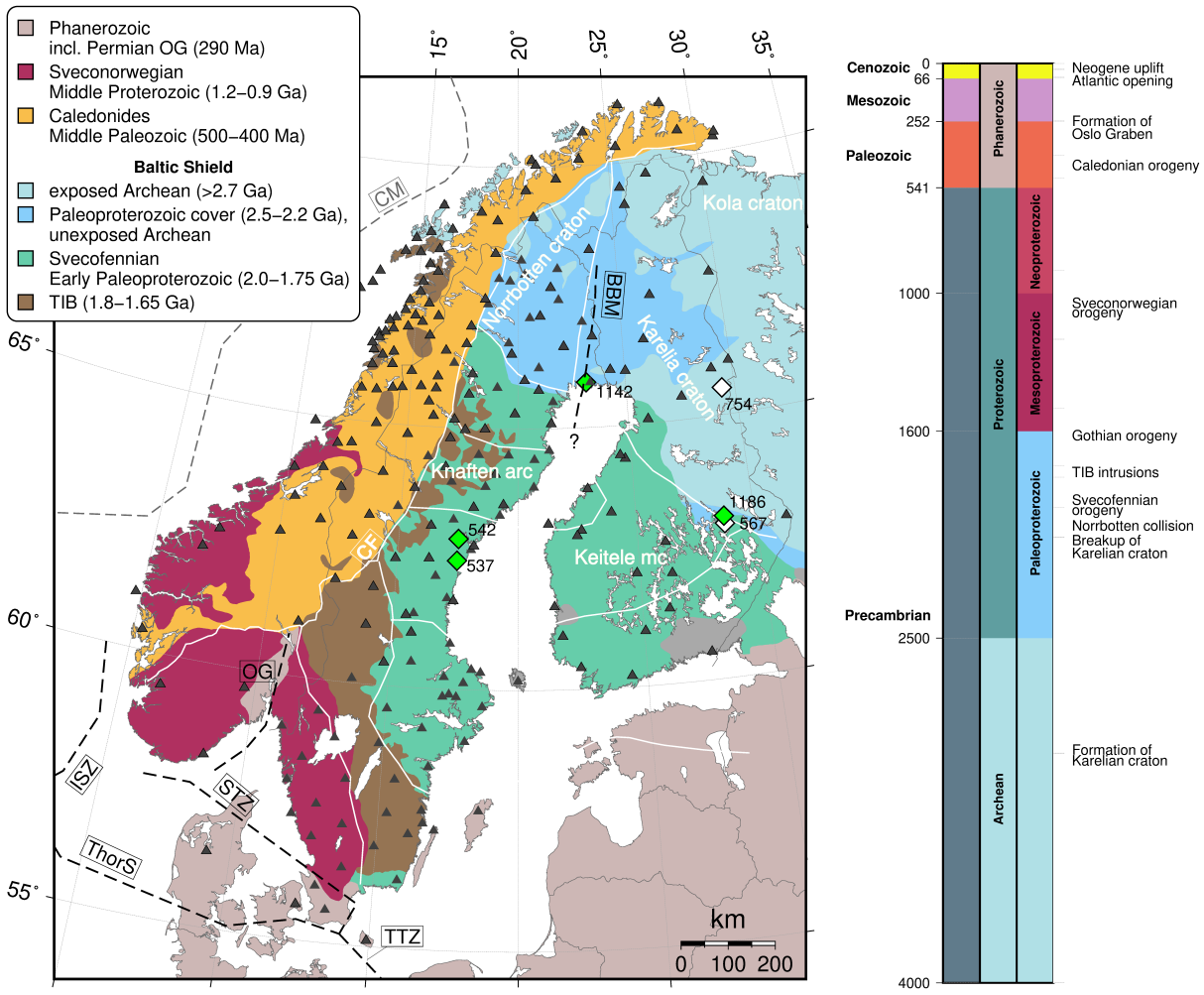

Fig. 5.2: Left: Geological map of the major tectonic units, suture and fault zones as well as station distribution. The age statements in the legend refer to the time of tectonic evolutions. The Baltic Shield is shown in cold colors. The Transscandinavian Igneous Belt (TIB) traverses Sweden and Norway in NNW-SSE direction. The Rapakivi granitoids (gray shaded) are located in southern Finland. OG = Oslo Rift Graben. ISZ = Iapetus-Suture-Zone; ThorS = Thor suture; CM = Continental Margin. The Sorgenfrei-Tornquist Zone (STZ) is the northern extension of the Teisseyre-Tornquist-Zone (TTZ). BBM = Baltic-Bothnian megashear. White lines outline the major Paleoproterozoic terranes, modified after Lahtinen et al. (2005). CF = Caledonian front and the Keitele microcontinent is denoted in southcentral Finland. Diamonds indicate the location of kimberlite pipes (containing either perovskite (white diamonds) or phlogopite (green diamonds)) with number showing age in Ma after Tappe et al. (2018). Right: Simplified geological time scale with the major tectonic events marked.

In this section we describe the tectonic evolution with a focus on the Precambrian amalgamation while the history of the Scandes was reviewed in the Introduction. A geological map with the major fault zones and tectonic units is displayed in Fig. 5.2. Northeastern Scandinavia consists of one of the oldest terranes on Earth with rocks more than 3 Ga old. The Baltic Shield (Fennoscandian Shield) consists of this Archean part as well as Proterozoic terranes in southern Finland and eastern Sweden, known as the Paleoproterozoic Svecofennian domain (2.0-1.75 Ga). Between 3.1-2.9 Ga, the Karelia craton has been formed, the oldest Archean crust of the shield, which is still exposed at some spots (Gaal & Gorbatschev, 1987).

A long phase of rifting (2.5-2.1 Ga) culminated in continental breakup of the Karelia craton ∼2.06 Ga. Subsequently, subduction and back-arc rifting acted on the Lapland-Kola area which consists of the Karelia and Kola Archean continents. Between 2.0-1.75 Ga, the Svecofennian orogeny (Nironen, 1997; Lahtinen et al., 2005; Lahtinen & Huhma, 2019) describes the important accretion period starting with the collision of the Kola and Karelia cratons (∼1.91 Ga (Lahtinen & Huhma, 2019)) where the Karelia craton in Lapland was affected by magmatism and crustal reworking. Partly overlapping in time (∼1.9 Ga), the Karelia craton collided with both the Norrbotten craton and the Keitele microcontinent where the western boundary of the Karelia craton has been reworked again (Berthelsen & Marker, 1986; Lahtinen et al., 2005). Ongoing collision episodes resulted in the accretion of further microcontinents (e.g., Bothnia) and island arcs (Knaften and Bergslagen arcs) to the Karelia and Norrbotten cratons forming the present Svecofennian domains in Sweden and Finland. Subsequent continent-continent collisions of Laurentia, Amazonia and Sarmatia with the amalgamated Fennoscandian continent (1.87–1.79 Ga (Lahtinen et al., 2005)) completed the Baltic Shield that forms the Precambrian basement for the Caledonian nappes.

These Paleoproterozoic accretion episodes coincide in time with the evolution of the Baltic-Bothnian megashear (BBM) (Berthelsen & Marker, 1986). The NNE-SSW striking BBM is nearly parallel to but likely overprints the Karelia-Norrbotten suture zone (Lahtinen & Huhma, 2019) and presumably extends all the way to Gotland through the Gulf of Bothnia.

Episodes of magmatic intrusions related to subduction formed the TIB crustal emplacement, dated to 1.85-1.65 Ga (partly coeval with the Gothian orogeny 1.75–1.55 Ga) (Lahtinen et al., 2009; Högdahl et al., 2004). The TIB belt consists mainly of granitoid rocks and can be subdivided into three massifs of different ages. Although only exposed contiguously in southern Sweden and with patchy exposures in central Norway and the Lofoten, the TIB stands out in magnetic and heat flow maps due to its high magnetic susceptibility and high heat production. Due to the low-density of the TIB crust, its outline is also seen in gravimetric data (e.g., Gradmann & Ebbing, 2015).

The Mesoproterozoic Sveconorwegian orogen coalesced between 1.2–0.9 Ga with the Paleoproterozoic domain and accreted crustal terranes to southernmost Norway and southwestern Sweden following northeastward directed subduction (Gaal & Gorbatschev, 1987; Gorbatschev & Bogdanova, 1993; Slagstad et al., 2017). Both, during the Gothian and Sveconorwegian-Grenvillian orogenies, the TIB emplacement has been deformed and metamorphosed (Högdahl et al., 2004), such that today it trends from southeastern Sweden towards the northeast up to the Lofoten peninsula for about 1400 km, where the belt follows the former Fennoscandian continental margin.

After a long period of little tectonic activity, a series of events in Early and Middle Paleozoic led to the Caledonian orogeny (e.g., Roberts, 2003; Brueckner & Roermund, 2004; Corfu et al., 2014). The latest phase of the Caledonian orogeny (Scandian event) commenced in the Silurian-Devonian between 420 and 400 Ma when the Baltica plate underthrust the Laurentia plate westward closing the former Iapetus Ocean. Three major allochthons can be distinguished within the Caledonian fold belt. The western edge of the Norrbotten craton has been buried under the Caledonian unit (Lahtinen et al., 2009). However, the Lofoten area was not much affected by the orogeny but resisted the deformation due to incorporated high-density mafic blocks (Breivik et al., 2017). The Scandinavian Caledonides were part of an extensive mountain chain whose remnants are also present in Scotland, Greenland, Svalbard and Northeast America.

During the Permian, the Oslo Rift Graben was formed, accompanied by widespread volcanism in several stages with the main episode between 295-275 Ma. The Graben strikes roughly N-S for about 200 km with a width of 35–65 km (Neumann et al., 2004). A prominent suture zone to the south of the Oslo Graben is the Sorgenfrei-Tornquist Zone (STZ) with its southern extension as the Teisseyre-Tornquist-Zone (TTZ). The Tornquist Zone forms a sharp separation between Scandinavia and continental Europe in terms of seismic velocity and lithospheric thickness (Balling, 2000) as a result of the collision between Baltica and Avalonia during the Caledonian orogeny.

Shortly after the Caledonian orogeny, the mountains began to collapse due to repeated extensional and rifting phases (e.g., Andersen, 1998; Braathen et al., 2002; Nielsen et al., 2009b; Anell et al., 2009). Finally, about 55 Ma ago the Iceland plume system associated with the opening of the North Atlantic Ocean created the present passive continental margin.

5.4 Data

For our study, we use the virtual ScanArray network which consists of more than 220 seismic stations (Fig. 5.1 and Fig. 5.2) of the following contributing networks: The ScanArray Core (1G network) consists of 72 broadband instruments which were operated by the ScanArray consortium (Thybo et al., 2012) between 2013–2017 mainly in central Sweden and Norway with a few stations in Finland and northern Norway. 28 stations from the NEONOR2 (2D network; NORSAR and University of Bergen) were deployed in the Lofoten region between 2013–2016. The SCANLIPS3D (ZR network; (England et al., 2015)) comprised 20 stations in central Norway and Sweden (Nordland/Norrbotten provinces), which were deployed 2013–2014. Additionally, we include 72 permanent stations from the Swedish National Seismic Network (SNSN; UP network; (SNSN, 1904)) as well as further 35 permanent stations from the Finnish (HE (Institute of Seismology University of Helsinki, 1980), FN (Sodankylä Geophysical Observatory University of Oulu, 2005)), Danish (DK), Norwegian (NO (NORSAR, 1971), NS (University of Bergen, 1982)) and international IU (Albuquerque Seismological Laboratory (ASL)/USGS, 1988) networks. Since the exact operation times of the different temporary networks differ, we analyse data between 2014 and 2016, when most of the stations were operational.

The average inter-station distance of the ScanArray Core network is about 70 km. 57 out of the 72 stations were equipped with 120 s instruments while the others were equipped with 240 s seismometers. Some sites of the SNSN network are operated with wide-band (30 s and 60 s) instruments which we excluded from the teleseismic surface wave analysis, but included in the ambient noise tomography. The pre-processing of the data involved the removal of a linear trend, application of a band-pass filter between 0.5 s and 200 s, downsampling to 5 Hz and deconvolution of the instrument response to obtain velocity seismograms. We also corrected for the misorientations stated in Grund et al. (2017).

5.5 Ambient noise tomography

5.5.1 Computation of ambient noise cross-correlation functions

In view of the large amount of available data and heavy computational load, we removed some nearly redundant stations which are very close to each other (e.g., from the NEONOR2 and

SCANLIPS3D networks) from the cross-correlation computation. Generally, we kept the stations with the lowest noise level. In total, we obtained 20,847 station pairs from 212 stations.

Following the standard processing scheme after Bensen et al. (2007) to obtain the empirical Green's functions, we subtracted the mean from the time windows and applied a time-domain normalization and spectral whitening to our pre-processed one-day files. In contrast to Bensen et al. (2007), we found much higher signal-to-noise ratios (SNR) for the clipping normalization at three standard deviations compared to the 1-bit normalization. Fig. C.1 illustrates the SNR difference between the 1-bit and clipping time-domain normalization.

For the cross-correlation calculation of all component combinations, the one-day files were split into four 6-hour segments and the resulting traces were then stacked to obtain daily average cross-correlation traces. Finally, we stacked the daily traces, with a maximum of 1001 and a median of 502 contributing days. The histograms in Fig. C.2 show the range of inter-station distances and azimuths of all correlated station pairs. The mean inter-station distance is ∼400 km, and the maximum inter-station distance is 1,858 km. Due to the geographical shape of Scandinavia the majority of the station pairs are NE-SW oriented.

Fig. 5.3 shows all ZZ correlograms with respect to station FABU in southern Sweden for two period ranges. For both period ranges, the fundamental mode Rayleigh is still clearly seen on both the causal and anti-causal lags for most station pairs up to the maximum inter-station distance of ∼1,700 km.

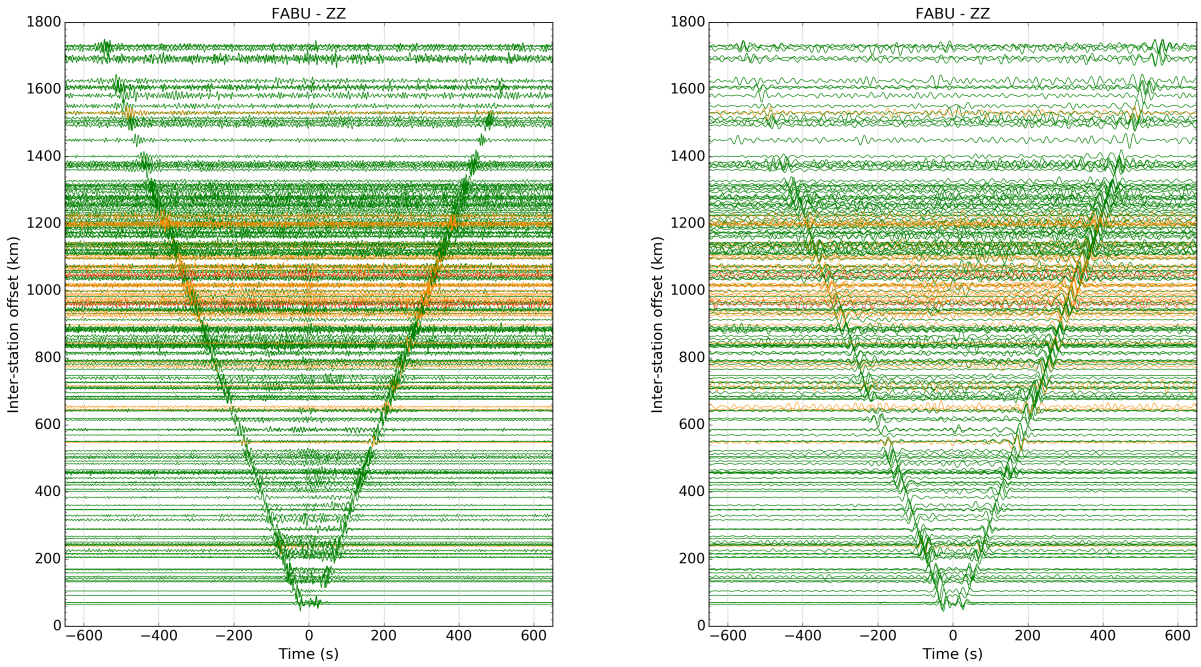

Fig. 5.3: Vertical component stacked record section with respect to station FABU in southern Sweden, filtered between 5-15 s (left) and 15-40 s (right). Stacked traces based on more than 12 months of overlapping data are shown in green. Orange and red traces were stacked over less than 12 and 3 months, respectively.

5.5.2 Dispersion curve measurement

Inter-station phase-velocity measurements were obtained from the ZZ correlation traces using an extension of the software package *GSpecDisp* by Sadeghisorkhani et al. (2018) able to carry

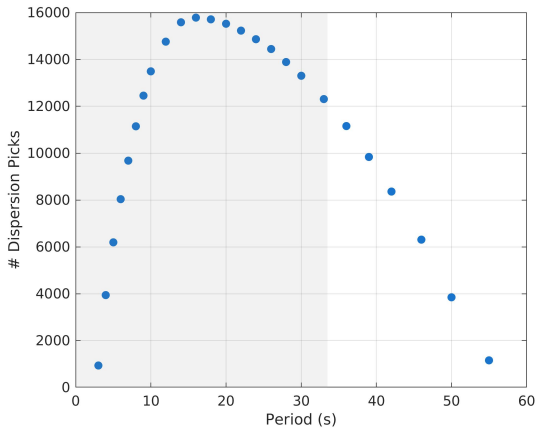

Fig. 5.4: Number of accepted measurements for station pairs of the ScanArray network for each period (blue dots). Gray shaded background highlights the period range actually used for the inversion.

out fully automatic phase velocity picking based on the method of Ekström et al. (2009). Path average phase velocities are retrieved from matching the real part of the spectrum to the exact zeroth-order Bessel function at the respective zero crossings. The automatic picker uses a reference curve to pick the correct branch (to elude the 2π ambiguity) at long periods and progresses to shorter periods for each of the single noise correlations, where the reference curve is also used to check the plausibility of the obtained velocity estimates. We used a subset of ∼15,800 cross-correlations (excluding some permanent stations in southern Norway) to estimate the reference dispersion curve used for all subsequent measurements. We manually re-picked cross-correlations from the Lofoten region after some 2D tomography tests observing very low phase velocities at short periods. We found that necessary because the reference curve may not be suitable for this region and these periods. Based on the quality criteria for the automatic dispersion picks (see the supplementary material for details), we obtain a varying number of phase velocity measurements with period, illustrated in Fig. 5.4. Additionally, we included previous dispersion measurements from southern Norway (MAGNUS deployment) and Sweden as well as from northern Denmark (Köhler et al., 2012, 2015), which significantly improved the coverage of southern Norway and the Oslo Graben at short periods.

5.5.3 2D ambient noise inversion

The noise phase velocity dispersion curves were inverted for 2D phase velocities adopting the transdimensional Markov chain Monte Carlo (McMC) technique by Tilmann et al. (2020). Generally following the reversible jump-McMC method by Bodin & Sambridge (2009) and Bodin et al. (2012a), Tilmann et al. (2020) employed a slightly different parametrization, inverting for slowness perturbations instead of absolute velocities, and recasting the constant slowness Voronoi cells to an underlying inversion grid (30×30 km) in order to conveniently store and compare models. For the calculation of travel times and their derivatives with the fast marching method, we interpolate this grid onto a 7.5×7.5 km forward-modelling grid. Instead of modelling the data uncertainty distribution as a Gaussian distribution as in Bodin et al. (2012a) we assumed a mixture of a Gaussian (with unknown standard deviation σ) and an uniform distribution in order to account for valid measurements and outliers, respectively. The ratio between both components of the distribution (outlier fraction, $\mathbf{f}$) is also assumed to

be an unknown parameter which has to be estimated together with σ, and the physical model parameters (slowness and grid node location for each Voronoi cell) as part of the Markov chain exploration.

Tilmann et al. (2020) have already tested the technique on the 4 s period measurements from ScanArray. Here, we extend the analysis to the whole period range and an extended data set, including the measurements by Köhler et al. (2012, 2015). We are calculating 135 chains (in three groups of 45 each), where each chain is running with 1,200,000 iterations, of which 800,000 iterations are used for burn-in and thus do not contribute to the final model average.

We applied the parallel tempering method as introduced by Sambridge (2014) for geophysical applications, using the implementation in Tilmann et al. (2020). 30 out of the 45 chains within each group were run at a temperature $T = 1$, i.e., with the unmodified Metropolis-Hasting acceptance rule. These chains were the only ones contributing to the final estimate. The other 15 chains were run at increasingly higher temperatures, which increases the acceptance probability of models fitting less well than their predecessors in the chain. This can prevent the chains from being trapped in local minima, but in practice the higher temperature chains also served during the burn-in phase to effectively remove poorly converging chains from the final average. An exchange between chains of different temperatures is possible every 10,000 iterations. Ray paths were recalculated every 300,000 iterations, based on the average models of each of the three groups, to account for potential ray bending due to heterogeneities but in any case the structural heterogeneity in Scandinavia is quite small, such that ray bending is negligible except in the Oslo Graben. After each recalculation of ray paths, a new burn-in phase is introduced in order for the model to readjust to the new ray paths; these additional burn-in phases are already taken into account in the total given above. The final mean model is calculated from the model ensemble of the 90 chains at $T = 1$ in the posterior sampling phases.

The data fit is generally declining with increasing period (Fig. C.4). In further processing we only utilize the 2D inversion of the phase velocities at periods between 3 s and 33 s because the misfit reduction becomes negligible for periods above 35 s.

In addition to the Voronoi cell parametrization and the McMC technique, we also tested a classic damped least squares inversion, and a hybrid approach (see section C.3), where the average model resulting from the McMC was used as a starting model for a damped least squares inversion. When comparing the three ambient noise derived models with the phase velocity derived from teleseismic earthquakes (see section 5.6.1) in the overlapping period range (25-33 s) we found that the pure McMC approach resulted in the best agreement, and we therefore continued to use the McMC model for further analysis.

Some resultant McMC phase velocity maps are shown in Fig. 5.5. The model uncertainty has a median standard deviation of 0.05–0.07 km/s with little period dependence. In the central study area the uncertainty is a little lower, and towards the edges it increases to ∼0.2 km/s.

At periods 3–10 s, we notice a sharp lateral east-west separation (following closely the Norwegian-Swedish border) between slow southern Norway and extremely slow Lofoten/Nordland province on one side, and the faster rest of Scandinavia on the other side. At intermediate periods between 10 s and 20 s, a slow NNW-SSE trending zone from southern Sweden to the Lofoten/Nordland region becomes apparent, which spatially matches quite well with the TIB. The central area of southern Norway is also slow and surrounded by faster structure towards the coast, a feature that has already been imaged by Köhler et al. (2012). Lower than average velocities are also seen in south-central Finland and coincide with the

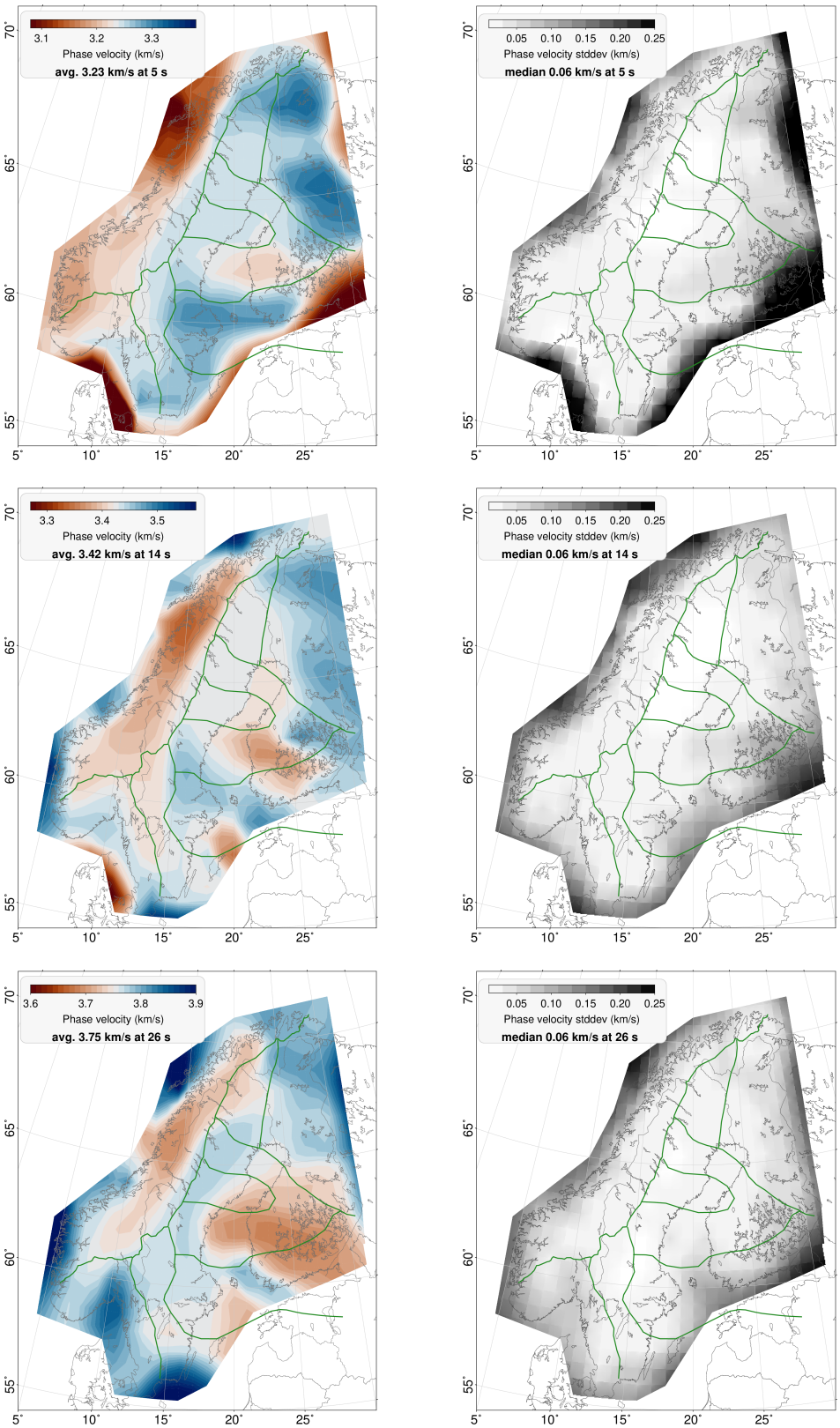

Fig. 5.5: Ambient noise phase velocity and corresponding standard deviation maps at 5 s, 14 s and 26 s resultant from the McMC inversion. Color scale is set to ±0.15 km/s around the labeled average phase velocity. Green lines mark the major Paleoproterozoic terranes simplified after Lahtinen et al. (2009) as well as the TIB and Sveconorwegian margins (see Fig. 5.2).

lateral extension of the Keitele microcontinent (cf. Fig. 5.2). We can further distinguish the Karelia craton with its high velocities from the Svecofennian domain and Norrbotten craton with intermediate velocities. For longer periods (25–30 s), the low velocities in western Scandinavia follow mainly the Scandes mountain range, whereas the Swedish Svecofennian domain exhibits higher phase velocties. The Lofoten peninsula now reveals faster structure pointing to a shallower Moho, whereas the low velocities in southern Finland presumably reflect a deep Moho.

5.6 2D teleseismic surface wave inversion

5.6.1 Method

We now turn to the analysis of the Rayleigh waves generated by teleseismic events to construct the 2D phase velocity maps. When measuring lateral variations of phase velocity from earthquake induced surface wave fields with regional arrays, the simplest assumption is an incident planar or regularly curved wave field propagating along the great circle path direction. In this case distortions in the wavefield can be directly interpreted in terms of phase delay caused by local heterogeneity. However, teleseismic surface waves frequently do not arrive as a single (plane or curved) wave at the receivers. To account for this multipathing effect, which originates outside the study area, the incoming wavefield can be modeled to a first order as the superposition of two plane waves, which is the approach developed by Forsyth & Li (2005). This method is known as the two-plane-waves method (TPW), shortly summarized below.

The incoming wavefield of two interfering surface waves can be described by six period-dependent parameters, which are the amplitudes and relative phases with respect to the reference station and the propagation azimuth for each of the two waves. The TPW approach can be applied for isotropic or azimuthally anisotropic phase velocity tomography. We adopt the latter in order to avoid artifacts in the isotropic model caused by ignoring anisotropic structure. Instead of the initial spatial resolution criteria (based on a Gaussian-shaped weighting function) described in Forsyth & Li (2005), we apply a TPW version using 2D sensitivity kernels, introduced by Yang & Forsyth (2006b), to account for finite-frequency effects due to heterogeneous media. Yang & Forsyth (2006b) applied a Gaussian averaging function for phase velocity interpolation between the grid nodes, which effectively smoothes the sensitivity kernel. In the TPW implementation used in this study, the Gaussian interpolation scheme is replaced by a linear one.

Each period is inverted separately. The inversion occurs in two steps. In the first step the velocity model (taken either from a prior uniform or heterogeneous starting model or a previous iteration) is fixed and the six wave parameters are inverted via grid search for each event. A grid search is used instead of the original simulated annealing approach (Forsyth & Li, 2005; Yang & Forsyth, 2006a). In the second step the classic linearized least-square technique is applied to invert simultaneously for changes to the phase velocity and and azimuthal anisotropy at each grid node (2D inversion), as well the six wave parameters for each event. Then the first step is repeated with the improved model. We set the maximum number of iterations to 10 but the inversion terminates early if the convergence limit is reached.

Since our study area has a maximum extension of 1800 km by 1500 km, we split the inversion into a northern (includes Finland) and southern subset with an overlap in central Scandinavia

between 65°N and 63°N (cf. Fig. C.6) to ensure that the source phase contribution is the same for all stations for each event, respectively (Li & Burke, 2006). For both inversion subsets, we use the same events and a regular grid size of $0.5° \times 0.5°$ (Fig. C.6). The grid exceeds the actual study region because the grid edges are designed to absorb the non-planar wavefield portion to avoid biasing velocity variations within the study area due to anomalies outside. In the overlapping areas, the phase velocities resulting from both inversions are averaged.

All extracted waveforms have been inspected manually after automatic pre-processing. In total, we considered 257 events with surface wave magnitudes $M_S \geq 5.6$, source depths <150 km and epicentral distances up to 140° (Fig. 5.6). The pre-processed data have been filtered in 15 overlapping frequency bands between 25 s and 160 s with a ±20% band width around the center periods. Fundamental modes filtered at periods <25 s resulted in scattered, complex wavetrains, irrespective of the source distance or azimuth, which violates the prerequisite of the two plane wave interference by the TPW method. Initially, the time windows were set by assuming group velocities between 2.8–5.0 km/s. The envelopes of each trace as well as the mean over all individual envelopes were calculated to reject poor quality data. To align all envelopes, we determined the times of the individual envelope peaks and calculated the difference from the mean envelope peak. Subsequently, traces with low signal-to-noise ratios were iteratively discarded when the difference between the individual envelope peak and the mean envelope peak is less than 1.4, a value determined from investigating the data. Traces are also rejected if the peak of the envelope has a time offset >70 s with respect to the expected group arrival time, estimated by a linear regression between the times of the nearest and most distant envelope peaks. The whole event is discarded if less than 20 stations are left after the envelope-based selection. To isolate the fundamental mode, a narrower time window ranging between 500 and 1000 s is placed around the maximum envelope peaks where the window width depends on the period and group velocity. A 50 s cosine taper has been applied to this time window. Finally, the tapered time series is Fourier transformed to calculate the period-dependent phases and amplitudes at each station as input to the inversion. 198 events are retained for the phase velocity inversion (Fig. 5.6) across all periods but the number of available traces varies strongly from 39 events at 25 s up to 110 events for the longer periods. A data example is shown in Fig. C.5.

During the inversion, poorly fitting events are downweighted to further reduce the influence of complex wavefields in the final model. This is implemented by carrying out the TPW inversion twice. In the first stage, the *a priori* data standard deviation is set to 0.2 km/s for all events. Afterwards, an *a posteriori* data standard deviation is estimated for each event. In the second stage, each event is then weighted by the inverse of this standard deviation. The second stage starts with the model of the latest iteration. Between 70 s and 110 s the *a posteriori* data standard deviations are on average 30% higher for the northern subset than for the south.

5.6.2 Inversion

We first considered the choice of starting model. In a first inversion run, we used uniform *a priori* phase velocities for the entire study area, taken from the whole-array beamforming results of Mauerberger et al. (2021a) for periods ≤120 s, and from the average SVEKALAPKO results from Bruneton et al. (2004a) for longer periods up to 160 s. The resultant phase velocity maps revealed a poorly resolved low-velocity region below southern Norway for periods >80 s. Southern Norway

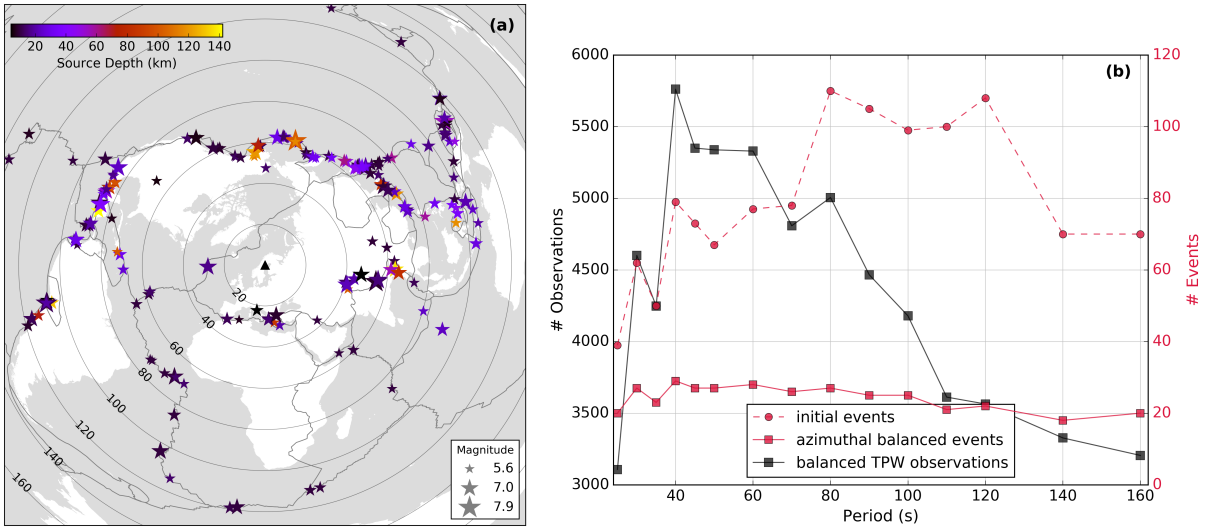

Fig. 5.6: (a) Map of all 198 events used for the phase velocity inversion. Note that the events differ for each period. (b) Number of events used for each period. Initial event selection (red dots, cf. left map) and events used after azimuthal balancing (red squares) are shown. The grey squares give the total number of observations (number of events × number of stations) used for the TPW inversion. Note that the y-axis does not start at zero.

appears to be faster using uniform *a priori* phase velocities than observed previously (Maupin et al., 2013; Kolstrup et al., 2015). Moreover, both the Archean and Paleoproterozoic terranes of Finland seemed to be too slow compared to the results by Pedersen et al. (2013).

Therefore, in a second inversion we have created *a priori* phase velocity models by dividing Scandinavia into six *a priori* regions, each with a uniform starting phase dispersion curve (Fig. C.6 and C.8a). Neighboring *a priori* regions overlap with each other and within the overlapping areas we averaged the phase velocities of both regions. For southern Norway we applied the median dispersion results from the MAGNUS network (Maupin, 2011). Northern Finland was assigned the phase velocities from LAPNET (Pedersen et al., 2013), and in southern Finland the velocities were set based on the SVEKALAPKO dispersion analysis (Bruneton et al., 2004a). For southern Sweden, central Norway/Sweden and northern Norway/Sweden we take the beamforming results from Mauerberger et al. (2021a). The misfit of the TPW phase parameter is reduced by ∼7% compared to the results from the uniform *a priori* phase velocities for the intermediate periods (Fig. C.9). The maximum velocity change throughout the iterations converge in general more rapidly for the southern subset, whereas in the north the enhancement by using 2D *a priori* velocities is lower (Fig. C.9). On average the misfit reduction in the north is less than half of the misfit reduction in the south. The misfits of the TPW wave amplitude parameter do not differ significantly, neither in the north nor in the south. Fig. C.8 shows a direct comparison of starting and final model for the 2D inversion. In the following we present the phase velocity maps generated using the 2D *a priori* phase velocities.

The two modeled plane waves can be regarded as a primary and secondary wave where the primary wave is defined by the larger amplitude. Primary waves generally deviate from the great circle by less than 5° for all periods. The amplitudes of secondary waves roughly represent the importance of multipathing. Generally, the amplitude of the secondary wave is decreasing with increasing period, representing the well-known reduced heterogeneity of the Earth at larger

depths. Deviations of secondary waves are increasing with period, presumably reflecting both lower signal-to-noise ratios and the increasing instability of direction measurements when the amplitude of the second wave is small. We also note higher secondary wave deviations for the northern than for the southern inversion subset, slightly increasing with the period, but they are mostly still smaller than ±20° for both subsets. No systematic relationship of deviations with source distance or azimuths could be discerned for either primary or secondary waves, indicating that the multipathing generally arises due to smaller scale structures along the great circle path.

5.6.3 Bootstrap testing: assessing the influence of backazimuthal distribution

We now consider the influence of the backazimuthal distribution of the events. Mauerberger et al. (2021a) observed a strong azimuthal variation of the phase velocities, measured with beamforming, with a 360° periodicity (1θ variation). Measured phase velocities from eastern directions were much higher than velocities from the west. This 1θ effect was observed for periods >35 s in sub-arrays formed from ScanArray stations in the north and south, but not in its central section. They attributed the 1θ pattern to be an effect of strong lateral and vertical velocity gradients, specifically variation in the LAB depth known from previous results (Maupin et al., 2013; Yakovlev et al., 2012; Lebedev et al., 2018). By averaging over all propagation azimuths, Mauerberger et al. (2021a) obtained physically reasonable phase velocity estimates for all subsets.

Therefore, we suspect also biases in the phase velocity inversion when unbalanced event distributions are used. To assess this potential bias, event bootstrap samples have been generated for a period of 80 s, which is sensitive to the depth of the presumed LAB gradient. In order to define a consistent definition and to assess the effect of azimuthal distributions, we use fixed bin widths for the bootstrapping. We chose bin widths of 10°, allowing for multiple events in each bin. The bootstrap results are illustrated in Fig. 5.7. The real, azimuthally unbalanced distribution of the 110 high-quality events (cf. Fig. 5.6b) and the corresponding phase velocity map returned from the TPW inversion are shown in Fig. 5.7(a).

In a first bootstrap sample, we drew random event distributions 100 times from this unbalanced event set. Generally, each of the 100 bootstrap examples yielded different phase velocity perturbations in the north, some with more extreme values and some with less. One example is shown in Fig. 5.7(b); more can be found in Fig. C.10. The exceptional small-scale phase velocity variations are most pronounced below the Lofoten/Nordland province above 65°N. These anomalies differ significantly for different azimuthal event distributions whereas for the rest of Scandinavia consistent phase velocities are obtained (cf. Bruneton et al., 2004b), except that some bootstrap samples show minor variations in central Finland around 65°N. These significant variations are also reflected by the high standard deviations of the bootstrap results in these regions (Fig. 5.7c).

In a second bootstrap sample, we apply azimuthally balancing, with one event per 10° bin. This single event for each bin is drawn randomly from the unbalanced event set. We constructed phase velocity maps with 100 different isotropic event distributions and calculated its mean and standard deviation as done for the 100 unbalanced distributions. In contrast, when we impose a more uniform event distribution by azimuthal balancing, the strong velocity perturbations diminish in the North, though not fully disappear (Fig. 5.7d). Compared to the azimuthally unbalanced solution the balanced bootstrap standard deviation is decreased by up to 30%.

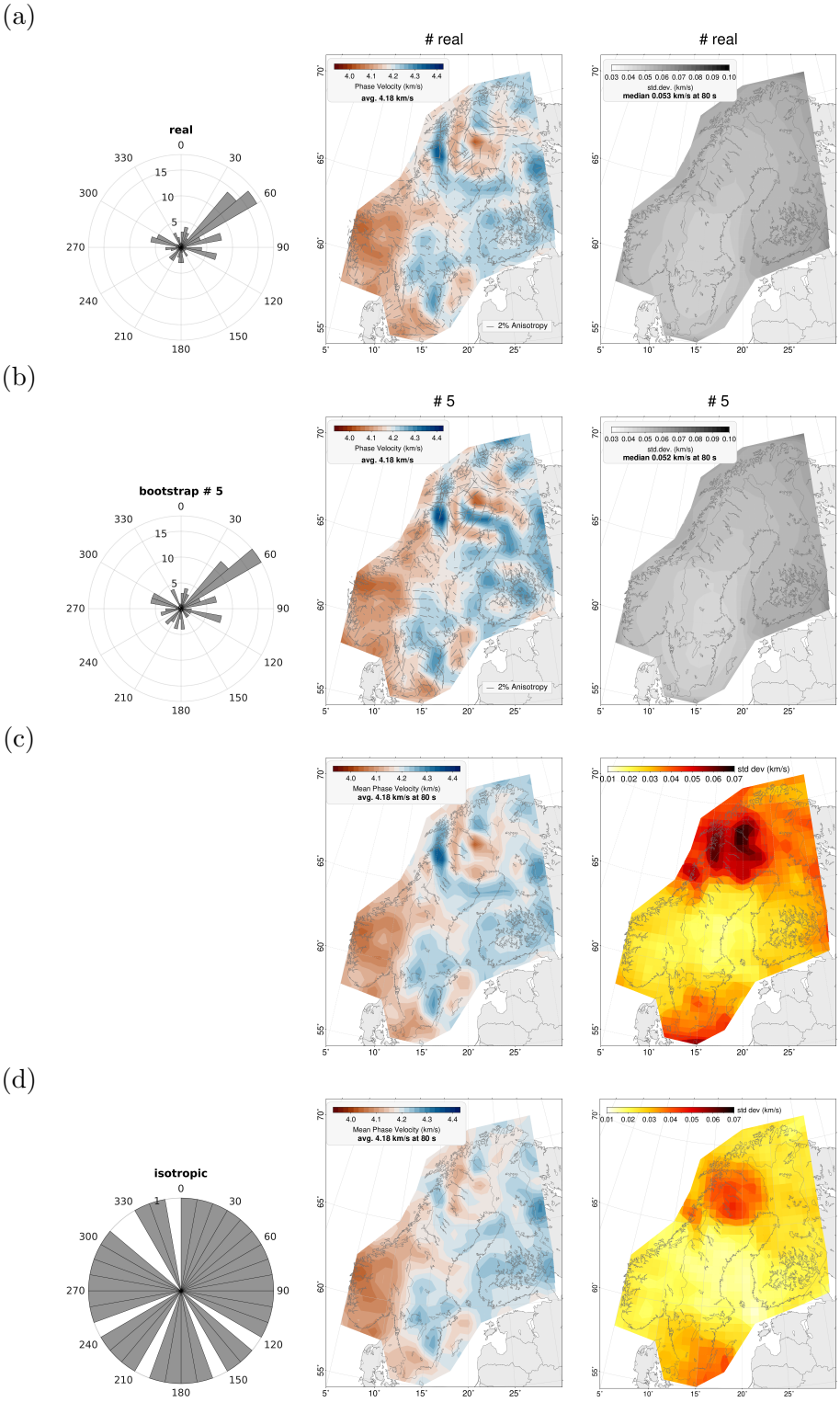

Fig. 5.7: Bootstrap test at a period of 80 s. The polar histograms display the backazimuthal distribution of events used for the phase velocity inversion with the TPW method. In the map views areas outside the station coverage have been masked. Gray lines indicate the fast azimuthal anisotropy direction at each grid node where the line length is proportional to the anisotropy amplitude. (a) Phase velocity inversion with all 110 events with the corresponding standard deviation returned from the TPW inversion. (b) Random bootstrap sample with similar event distribution and the corresponding standard deviation returned by the inversion. (c) Mean over all 100 bootstrap samples and the standard deviation of the bootstrap samples. Non-uniform event distributions create pronounced small-scale artifacts in northern Scandinavia above 65°N, leading to a large standard deviation there. Note that a different color scale is used for standard deviation here to highlight the fact that it is different from the standard deviation shown in a, b. (d) Mean over 100 azimuthally balanced bootstrap samples and their standard deviation. For the isotropically balanced event distribution the small-scale artifacts in the North diminishes, and smaller standard deviations are obtained everywhere.

For the final selection of isotropically balanced event sets we seek to exclude those events with complex wavetrains. Therefore, in each bin we selected the event with the smallest estimated *a posteriori* data standard deviation obtained in an initial test inversion including all data (see section 5.6.1). We also tested the azimuthal balancing based on a 5° bin width. However, this choice resulted in more pronounced small-scale artifacts, so we utilized the 10° bin width in our preferred inversion.

Azimuthal anisotropy results are overlain on the phase velocity maps in Fig. 5.7a and b as grey lines. By visual inspection, both the fast anisotropy direction and amplitude depend on the event distribution resulting in unstable orientation and large amplitudes, mainly in the north, respectively. In case of the balanced event distribution, the azimuthal anisotropy is more stable but still laterally varying within small scales. Although we see some anisotropy patterns consistent with previous studies in southern Norway and southern Finland, we forgo an interpretation of the azimuthal anisotropy results at all periods as these results are not as robust as the velocity maps. Nevertheless, we use the TPW anisotropy inversion to avoid any additional bias on the phase velocities due to the trade-off between the isotropic and anisotropic terms, although in any case the good azimuthal coverage in the balanced set should reduce this bias (e.g., Maggi et al., 2006).

In conclusion, the bootstrap testing demonstrates that model errors are less than 0.025 km/s in most of the study domain but we have to be cautious about small-scale velocity perturbations in the area between northern Sweden and Lofoten, with errors up to 0.043 km/s.

5.6.4 Phase velocity maps

Due to the necessity of azimuthally balanced events, the final number of earthquakes used for each period in the final phase velocity inversion is reduced. At 40 s, we obtained a maximum number of 29 events. The smallest number of good events were found at 140 s with 18 earthquakes (cf. Fig. 5.6b). Although the difference between the periods seems large, the ray coverage as shown in Fig. C.11 is sufficient at all periods due to the dense station spacing and the good azimuthal event coverage. Fig. 5.8 presents the final azimuthally anisotropic 2D phase velocity maps at selected periods. At 25 s we resolve a distinct low-velocity arc with ~3.70 km/s between Trondheim and the Norwegian-Swedish border similar to Köhler et al. (2012) (see black dashed line in Fig. 5.8). Towards the Norwegian and Swedish southern coasts phase velocities become higher (>3.80 km/s), which was also seen by the local inversions of Köhler et al. (2012) for southern Norway and Sadeghisorkhani et al. (2021) for southern Sweden. These heterogeneities might be related to varying Moho depths. Generally, our surface wave analysis reveals more lateral phase velocity perturbations compared to the noise results, which is probably attributable to the natural parsimony of transdimensional Bayesian inversions.

For periods > 40 s the prominent large-scale low-velocity region below southern Norway is imaged as before (Medhus et al., 2012; Wawerzinek et al., 2013; Kolstrup et al., 2015; Hejrani et al., 2017) with its sharp transition across the Oslo Graben. Lower velocities below south-central Finland between 30–50 s are also in agreement with studies by Bruneton et al. (2004a) and Alinaghi et al. (2003), and are probably related to the exceptionally thick crust there. The 120 s map reveals variations in lithospheric thickness and structure. Notable features, in addition to the well known low-velocity region below the southern Scandes, are a velocity contrast roughly

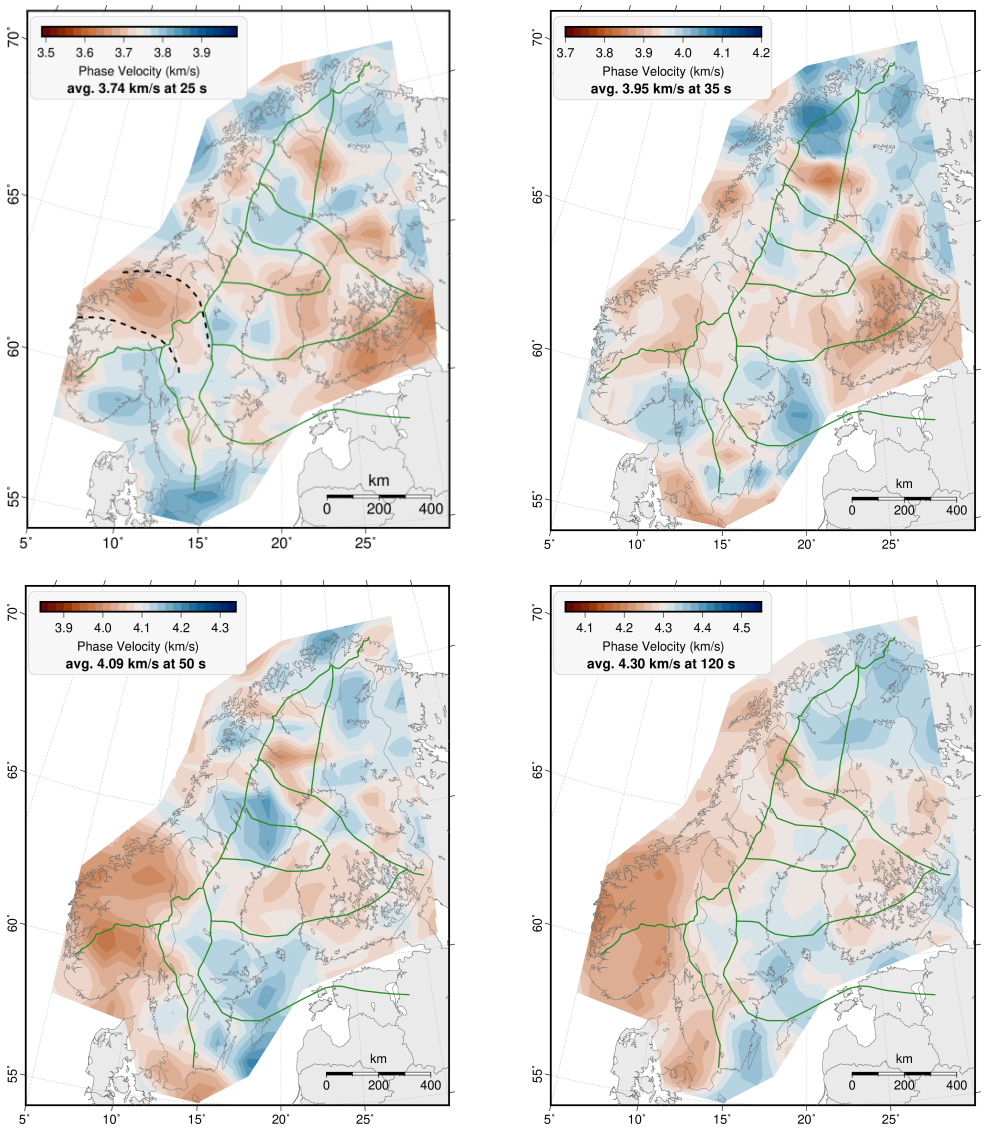

Fig. 5.8: Final phase velocity maps at different periods based on TPW inversion, using the isotropically balanced event distributions. Color scales are chosen to be ±0.25 km/s (ca. ± 6%) around the average value denoted in the legend. Phase velocities have been cut outside the station coverage. Black dashed lines at 25 s highlight a distinct low-velocity arc, see text for details. Green lines mark the major Paleoproterozoic terranes simplified after Lahtinen et al. (2009) as well as the TIB and Sveconorwegian margins (see Fig. 5.2).

along the Caledonian front (with slower velocities to the west).

We were able to reduce potential artifacts by rebalancing the backazimuthal distribution. Regarding the velocity error evaluation, generally lower phase velocity standard deviations (Fig. C.12) are obtained for the southern subset with e.g., a median standard deviation of 0.05 km/s at 50 s; for the northern subset we get a median standard deviation of 0.06 km/s. Errors increase towards the edges of the study area due to the lower station coverage. At a period of 160 s the median standard deviation exceeds 0.09 km/s for the entire study area. Therefore, we did not determine phase velocity maps for longer periods. We deduce a spatial resolution of ∼150 km at 50 s period and ∼250 km at 100 s period. For southern Norway the resolution is less due to the reduced station coverage.

5.7 Shear velocity inversion

5.7.1 Dispersion curves

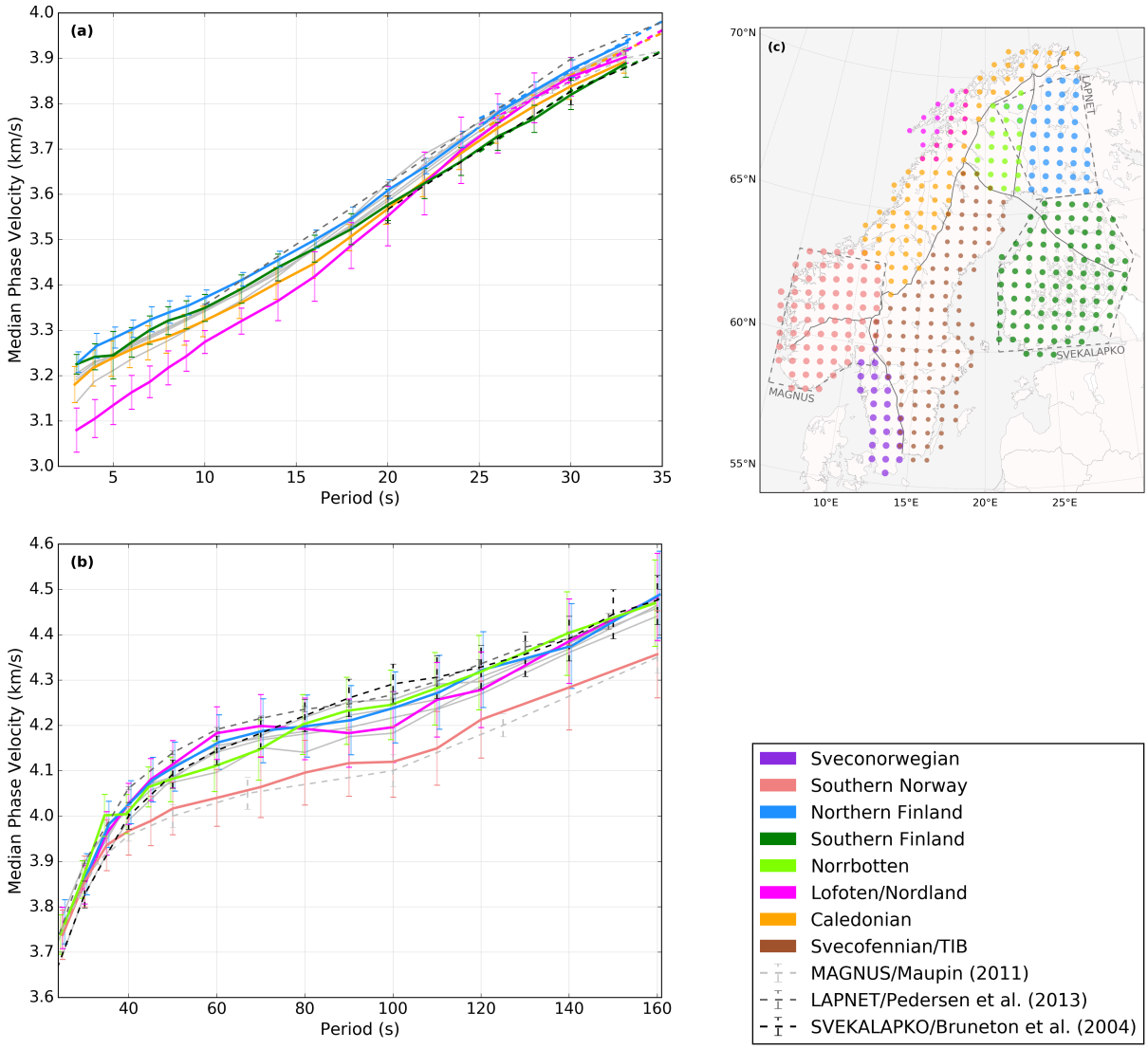

Fig. 5.9: Comparison of median dispersion curves from the ambient noise (a) and surface wave (b) phase velocity inversions for the sub-regions shown in (c). The points in (c) are the TPW grid nodes defined in section 5.6.1. For each point a dispersion curve has been extracted and then the median curve is determined for each sub-region. The dispersion curves of selected regions (different ones in (a) and (b)) are shown as colored lines in order to highlight particular features (see text); grey dispersion curves are from the other sub-regions. The colored dashed lines in (a) show the median surface wave dispersion curves in the overlapping period range 25–33 s. Error bars reflect the variance between the grid node results within the sub-regions. Note that the error bars have been slightly shifted on the x-axis to avoid overlap. In (c), black lines mark the major tectonic units (cf. Fig. 5.2). Dashed grey boxes outline the coverage areas of previous networks.

We extracted the dispersion curves at each grid node of the TPW inversion, obtaining a joint dispersion curve at each node location with data points from both the ambient noise and TPW tomography in the overlapping period range (25-33 s). We grouped the nodes into eight regions, partly corresponding to the tectonic domains (Fig. 5.9c), and extracted the median dispersion curve in each subregion. The ambient noise observations (3-35 s) are mostly sensitive

to crustal structure (Fig. 5.9a). Lower phase velocities are observed in the Caledonian unit (orange dispersion curve in Fig. 5.9a) than in the Baltic craton in Finland (blue and dark green dispersion curves) below 20 s. This contrast is even more pronounced for the Lofoten peninsula and the neighboring Nordland province (magenta dispersion curve), where we measure the overall lowest velocities at this period range. For longer periods (>23 s), the velocity below the Caledonides increases reaching the values of the much older terranes. Southern Finland becomes slower than the Caledonian and Lofoten/Nordland regions reflecting the very deep Moho below the Finnish Svecofennian terrane. We see a good agreement between the noise and surface wave dispersion curves (colored dashed lines) in the overlapping period range between 25–33 s.

Fig. 5.9b shows the median surface wave dispersion curves between 25 s and 160 s period. In the period range 25–45 s the various tectonic units reveal similar phase velocities, except for southern Norway where the significantly reduced velocities start at 35 s (in agreement with Maupin (2011)). The velocities in southern Norway are on average 0.13 km/s lower than for the remaining Scandinavia. We notice remarkable differences of the velocities in northern Scandinavia for intermediate periods between 50–75 s. The Norrbotten craton (green dispersion curve) has much lower velocities (up to 0.08 km/s) than the Lofoten/Nordland region (magenta line) and northern Finland (blue line) in that period range. Around 80 s a significant change occurs where the Lofoten/Nordland region points to a strong low-velocity zone. On average, we obtain lower velocities for northern Finland (blue dispersion curve) compared to the results by Pedersen et al. (2013) but we also observe relatively reduced velocities between 80–110 s. The other sub-regions shown in Fig. 5.9c have less distinctive velocities (solid grey dispersion curves in Fig. 5.9a and b).

5.7.2 Depth inversion

At each grid node of the 2D TPW inversion, we perform a 1D shear velocity-depth inversion based on the dispersion curve extracted as described above. Note that we did not average the overlapping data points for the inversion (Fig. 5.10d). The second step in our inversion procedure is likewise achieved by a transdimensional rj-McMC scheme as described in Dreiling & Tilmann (2019); Dreiling et al. (2020), following the method of Bodin et al. (2012b). In the following, we summarize the major aspects and required parameters for the transdimensional inversion.

Fig. 5.10 illustrates the data fit and inversion scheme at two locations in Nordland and central Norway. The model is parametrized by 1D Voronoi cells, equivalent to constant V_{SV} layers, where the interfaces are half way between the nuclei. The data uncertainty, or data noise σ, is assumed to be Gaussian distributed and uncorrelated between neighboring periods. The value of σ is assumed unknown and has to be estimated as part of the Markov chain Monte Carlo (Fig. 5.10c). To set the limits of the σ prior probability distribution for each individual grid node, we use the minimum and maximum standard deviations of the corresponding dispersion curve, obtained from the phase velocity inversions. Forward modeling of surface wave dispersion curves (Fig. 5.10d) is achieved by the standard routine after Herrmann (2013). Five proposal distribution methods are implemented: Perturbation of V_S, new placement of Voronoi nucleus, change of the noise parameter σ, layer birth and layer death.

The model prior probability distribution for the velocity V_{SV} is a uniform distribution between 3.0 and 5.5 km/s (as thick sedimentary layers are not present in Scandinavia). 1–15

model layers are permitted with an equal prior probability, and the model domain covers the depth range 0–400 km, where the velocity of the lowest layer is also assumed to apply for an underlying half-space. Furthermore, we assume a constant V_P/V_S ratio of 1.78 (Hyvönen et al., 2007; Kukkonen et al., 2003).We tested also lower V_P/V_S ratios, as described by Vinnik et al. (2016), but found the influence on the resultant shear velocity models to be negligible. We rule out an effect of water layers as the average seafloor depth in the Gulf of Bothnia is only 60 m and in the Vestfjorden Basin about 300 m.

We performed in total 605 1D inversions, one for each grid node. Each inversion ran 75 Markov chains for 1,000,000 iterations where the first 700,000 iterations have been discarded as burn-in (Fig. 5.10a). To obtain the posterior distributions, from which we interpret the mean models (Fig. 5.10e) below, the models from accepted chains are thinned to a maximum of 600,000 models. Prior to averaging, outlier chains, defined as having an average posterior likelihood less than 95% of the best median posterior likelihood, were removed. The threshold was determined by limited experimentation. When a higher threshold of, e.g., 98% is set, too many chains are discarded. On the other hand side, for lower thresholds, models with poor fits, which very often seemed to be associated with a very gradual Moho, are included in the averaging, so that the Moho is obscured in the mean model. The posterior misfit and noise standard deviation (σ) distributions in Fig. 5.10b and c have a predominately Gaussian shape, but the longer tails to the right indicate the presence of some remaining outlier chains. In order to help convergence of the Markov chain, an interface was placed near the Moho depth in the *EUNAseis* crustal model (Artemieva & Thybo, 2013) in the initial model. In practice the initial Moho depth was drawn from a uniform distribution within ±5 km of the EUNAseis Moho, and then the Voronoi nuclei were placed at equal, also random distance above and below this nominal interface. As no constraints were placed on the V_S model, and the nuclei could move freely, this procedure is unlikely to have biased the final result.

We reject models from each chain (cf. Fig. 5.10a) with implausibly high or low shear velocities in the mantle based on petrological constraints (Garber et al., 2018). Particularly in northern Scandinavia, numerous models occurred in individual chains with V_{SV} values exceeding 5.0 km/s at about 150 km depth or less than 4.1 km/s at depths below 60 km, which are not reasonable from a petrological point of view, even if a certain amount of eclogite in the cratonic lithosphere is considered (e.g., James et al., 2004; Garber et al., 2018). Those extreme models arise in an attempt to fit the strong fluctuations in the assembled dispersion curves (Fig. 5.10d) and contribute to exceeding low and high velocity zones in the corresponding posterior V_S-depth profiles. However, the overall misfit is generally not any lower for these implausible models (Fig. C.13). The rejection of such extreme V_{SV} models from the individual chains results in more stable posterior mean models. Similar findings have been reported recently by Green et al. (2020) for unrealistic layers above the Moho.

In the following we discuss the shear velocity model results to a maximum depth of 250 km as for greater depths the fundamental mode surface waves up to 160 s have negligible sensitivity at larger depths. The quality of the data fit is represented by the median likelihood of the resultant posterior distribution and summarized in Fig. C.14. The best data fits are obtained for central Sweden and Norway whereas the northern part is imaged with lower likelihood reflecting the stronger phase velocity anomalies and higher uncertainties in that region. The likelihood is also decreasing towards the edges of the study area.

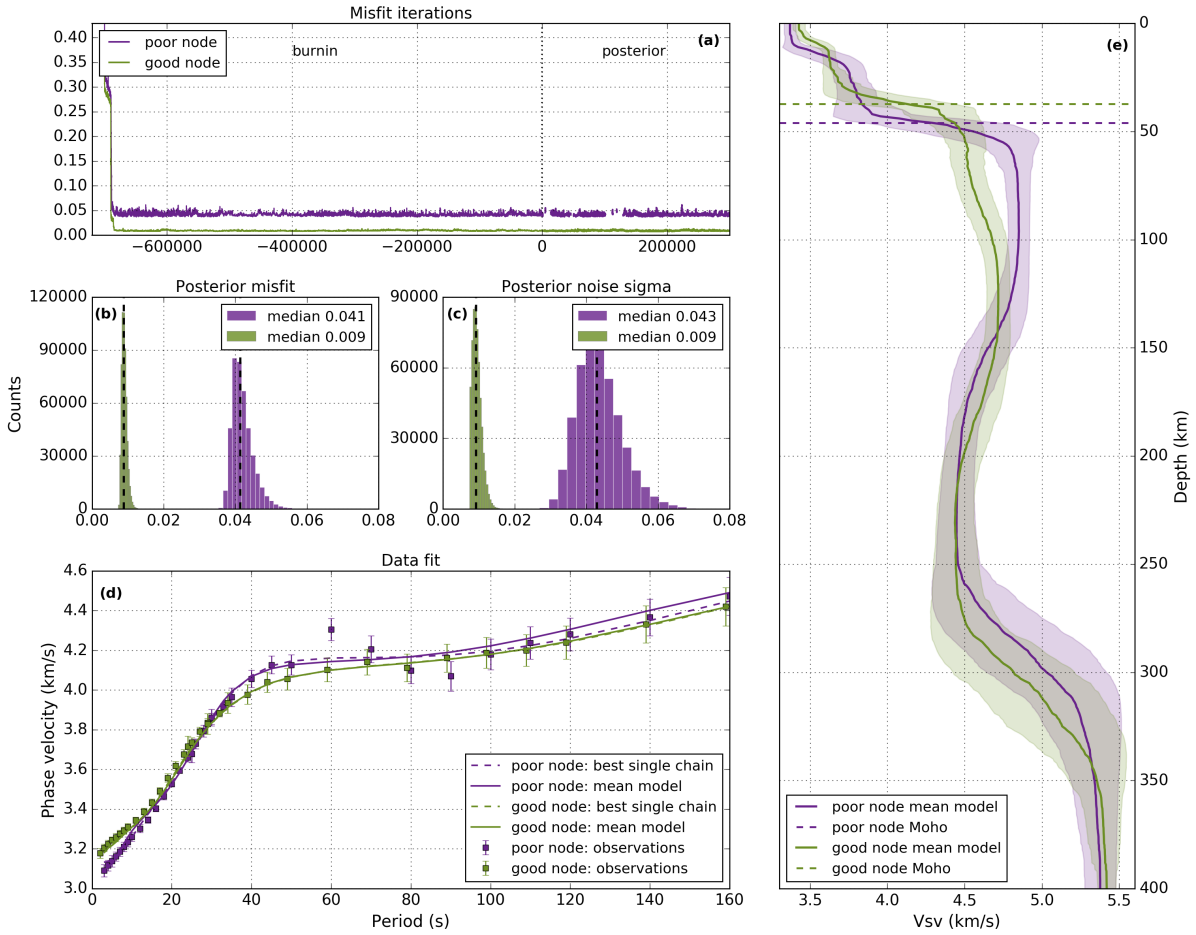

Fig. 5.10: Example of 1D depth inversion scheme for two different geographical points (grid nodes). A poor (purple, near Lofoten) and good (green, central Scandes) node in terms of the misfit and likelihood have been chosen which are marked as white crosses in Fig. C.14. (a) Misfit evolution of one arbitrary Markov chain for each node. The likelihood (not shown) has an equivalent evolution. (b) Posterior distribution of misfit from all accepted chains. Outlier chains have been discarded before. See text for details. (c) Posterior distribution of noise sigma. (d) Data fit to the composite dispersion curves resultant from ambient noise and surface wave analyses including the corresponding standard deviations shown as error bars. Note that the observation points of the good node have been shifted by 1 s for visualization. Dashed lines show the best forward model from one arbitrary chain for each node and the mean curve (solid line) over all accepted chains. (e) Resultant V_{SV}-depth profile for the posterior mean over all accepted chains. Shaded areas show the corresponding standard deviation. The calculated Moho depths are also indicated as dashed lines (cf. Fig. 5.13).

5.8 Shear velocity results

5.8.1 Crust

Our final 3D shear velocity model is presented in Figs. 5.11–5.15, assembled from the individual 1D depth inversions. In the shallow crust (top 15 km) (Fig. 5.11, top panels), the Lofoten peninsula and Nordland province are characterized by very low velocities up to 6% less than the average velocities at these depths, with a strong gradient below (Fig. 5.12). In active seismic profiles, Breivik et al. (2017) recently observed a strong reflector at 15 km depth between the Lofoten and the onshore coastal areas, which they associated with the bottom of a TIB granitoid. A prominent low-velocity band at 15 km depth, striking SSE-NNW, connects the

upper-crustal low velocities in the Nordland/Lofoten region to southern Sweden. The presence of TIB granitoids with their low density and high heat flow (Olesen et al., 2010; Veikkolainen et al., 2017) suggests a straightforward interpretation of this upper crustal low velocity region. Gravity and isostatic modeling constrained the maximum TIB thickness to 12–20 km (e.g., Ebbing, 2007), which is consistent with our seismic observations. It should be noted that the trend of the crustal TIB granitoids is different from their surface expression (Fig. 5.2), likely because of the overthrusted Caledonian nappes.

We observe similarly low upper crustal velocities of 3.4–3.5 km/s in southern Norway, down to $\sim$ 10 km depth, in agreement with Köhler et al. (2012). East of the Caledonian front the uppermost crustal layers reveal predominantly faster structures. In the 50 km depth map (Fig. 5.11), southern Finland stands out with lower velocities characterizing a thicker crust in agreement with the exceptional deep Moho observed in Svecofennian south-central Finland by previous studies (e.g., Kozlovskaya et al., 2008). For the rest of Scandinavia uppermost mantle velocities >4.4 km/s are seen at this depth.

In Fig. 5.13 we present a Moho depth map composed from all individual 1D depth inversions where the Moho depth was determined from the average of the depths of the maximum positive velocity jumps for velocities >4.2 km/s in the individual posterior models. As surface waves have low sensitivity to the absolute positions of discontinuities, uncertainties are relatively high, with a median standard error of 5.8 km for the Moho depth, where the largest uncertainties of $\sim$10 km occur in central Finland and north-central Sweden. The deepening of the Moho under the Paleoproterozoic Svecofennian domain can also be seen in the cross-sections in Fig. 5.12. Below the southern Scandes receiver functions have imaged only a minor crustal root in the central area of southern Norway with an offset to the east of $\sim$60 km from the highest topography (e.g., Svenningsen et al., 2007; Stratford et al., 2009; Frassetto & Thybo, 2013). We obtain similarly a Moho at 40 km depth below the central southern Scandes (Fig. 5.13), thinning to $\sim$30 km towards the coast and the Oslo Graben. A significant lateral offset of the maximum Moho depth from the peak elevation is not imaged by our model. In contrast, our model reveals a clear crustal root beneath the high-topography of the northern Scandes at around 46 km depth (N68-N62 profile, cf. Fig. 5.13). Recently, Ben Mansour et al. (2018) observed very similar Moho depths from receiver functions with a clear deepening below the highest topography of the northern Scandes. The Moho beneath the Lofoten peninsula appears at 36 km depth in the seismic profiles described by Breivik et al. (2017), which is consistent with our results. Towards the east (along the N68-N62 profile), the crust of the adjacent Paleoproterozoic Norrbotten craton thins by $\sim$5–10 km before thickening again under the Archean Karelia craton. Under the central mountain range, where the surface elevation is lower than in the south and the north ($\sim$62-64°N), the crustal root gradually diminishes from north to south. The deepest Moho is found beneath south-central Finland, reaching a maximum depth of 53 km which is slightly less than obtained by Kozlovskaya et al. (2008) but our station coverage is sparse in that region.

Finally, our velocity model allows the identification of a high-velocity lower crustal layer (LCL), with velocities $\sim$3.9–4.1 km/s, that is generally thickening from west to east (cf. Fig. 5.12, 5.13b). The presence of a high-density layer was previously suggested on the base of isostatic balancing (Ebbing, 2007). Our observations allow us to map the variation of its thickness across Scandinavia in detail. We find it to be $\sim$15–20 km thick below the Svecofennian and Archean terranes and over 25 km thick beneath south-central Finland. The LCL shows significant variations between the southern, central and northern Scandes. While

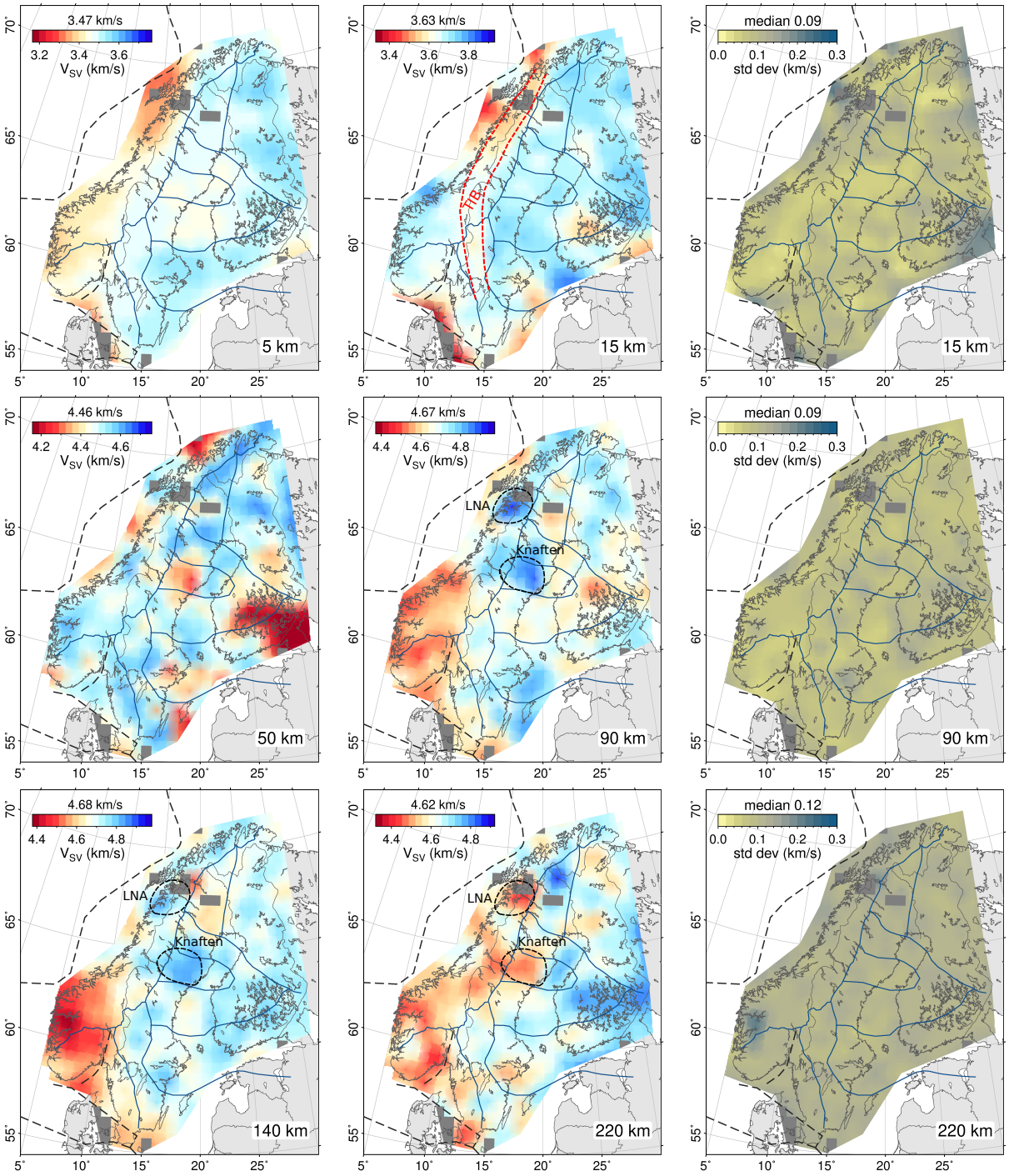

Fig. 5.11: Horizontal slices of absolute shear velocities through the final 3D model at various depths. Poor results are shaded in grey (cf. Fig. C.14). Blue lines mark the major Paleoproterozoic terranes simplified after Lahtinen et al. (2005) as well as the TIB and Sveconorwegian margins (see Fig. 5.2 and Fig. 5.5). At 15 km depth the TIB, defined by the lower velocities and in congruence with magnetic data (Olesen et al., 2010), is outlined. The color scales are indicating absolute velocities but are adjusted for each depth slice, such that the range is ±0.3 km/s (ca. ±8.5%) around the average value denoted in the legend. The regions encircled by black, dashed lines mark the Lofoten-Nordland anomaly (LNA) and the Knaften anomaly (see text). Right panels show the standard deviation for the depth slices in the middle panel.

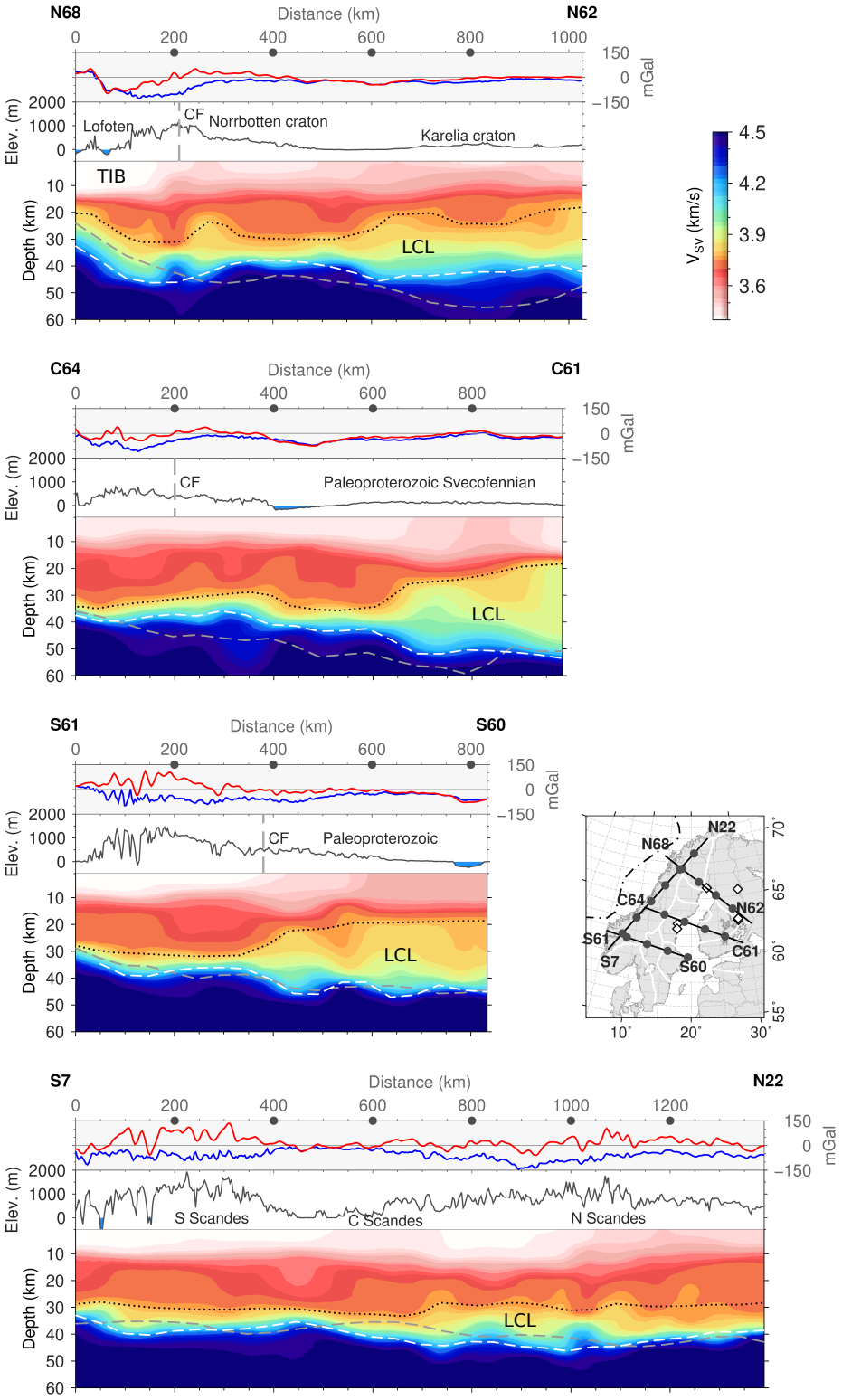

Fig. 5.12: Cross sections of absolute shear velocities along west-east profiles through northern, central and southern Scandinavia as well as along the Scandes down to 60 km depth. The profile locations are shown as black lines in the map inset where profile labels refer to the start and end latitudes. Solid circles mark 200 km distance increments. White lines and diamonds denote the tectonic units and kimberlite pipes, respectively, as in Fig. 5.2. The topography profiles (grey lines) are shown on top of the V_{SV} models as well as the Free air gravity anomaly (red lines) and the Bouguer anomaly (blue lines), taken from EGM2008 (Pavlis et al., 2008). White dashed lines are the estimated Moho depths from this study; black dashed lines indicate the EUNAseis Moho depths (Artemieva & Thybo, 2013) for comparison. TIB is the Transscandinavian Igneous Belt; LCL and the dotted lines mark a high-density lower crustal layer.

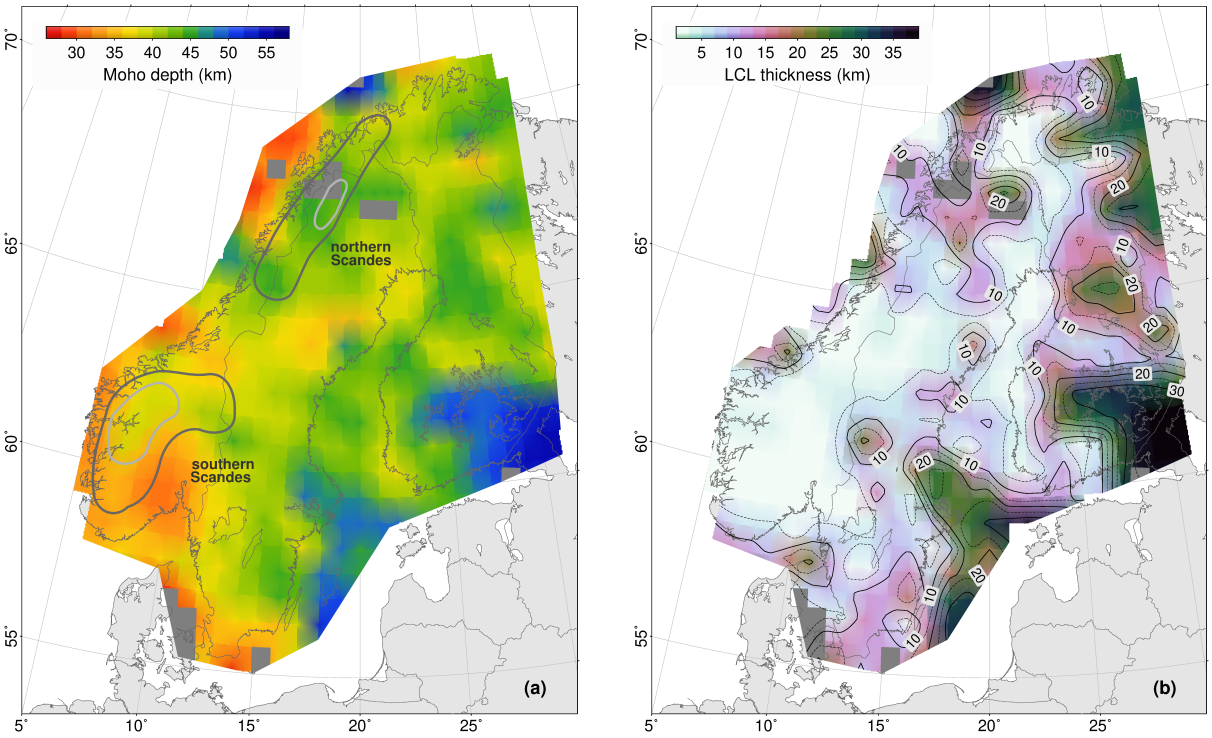

Fig. 5.13: (a) Moho depth map obtained from the 1D V_{SV}-depth inversions. The Moho depth was calculated from the average of the depths of the maximum positive velocity jumps for velocities >4.2 km/s in the individual posterior models. Dark and light grey lines outline the 1,000 m and 1,500 m elevations, respectively. Poor results are shaded in grey (cf. Fig. C.14). (b) Map of the lower crustal layer (LCL) thickness where the top of the LCL layer was calculated analogously to the Moho depth but for maximum positive velocity jumps for velocities >3.85 km/s.

beneath the southern Scandes there is no evidence for a substantial LCL (<5 km thickness), we can equivalently interpret the high velocities beneath the northern Scandes between ~20–40 km depth as a high-density layer, a finding recently supported by Makushkina et al. (2021). Below the central Scandes, a LCL seems to be present but is clearly thinner than beneath the northern Scandes with a maximum thickness of 10 km. Accordingly, the differences in crustal thickness across the Scandes can be largely attributed to the thickness variations in the LCL (Fig. 5.12, profile S7-N22). In fact, on the scale of whole Scandinavia, there is a visually strong correlation between LCL thickness and Moho depth, i.e., a large part of the thickness variation of the crust is related to the LCL thickness variations, with only minor contributions of thickness variations of the upper crust.

5.8.2 Mantle structures

In the following, we define the transition from a high-velocity mantle structure (lid) to underlying low V_{SV} as the depth where the maximum negative velocity gradient is attained. We consider this depth to be the base of the seismic lithosphere, unless otherwise noted. The corresponding V_{SV} contrast is calculated from the difference between the maximum velocity within the lithospheric lid and the minimum velocity in the medium below. Since this definition requires the presence of a strong negative gradient it is not possible to construct a map for the entire study region as at some locations the transition is too smooth.

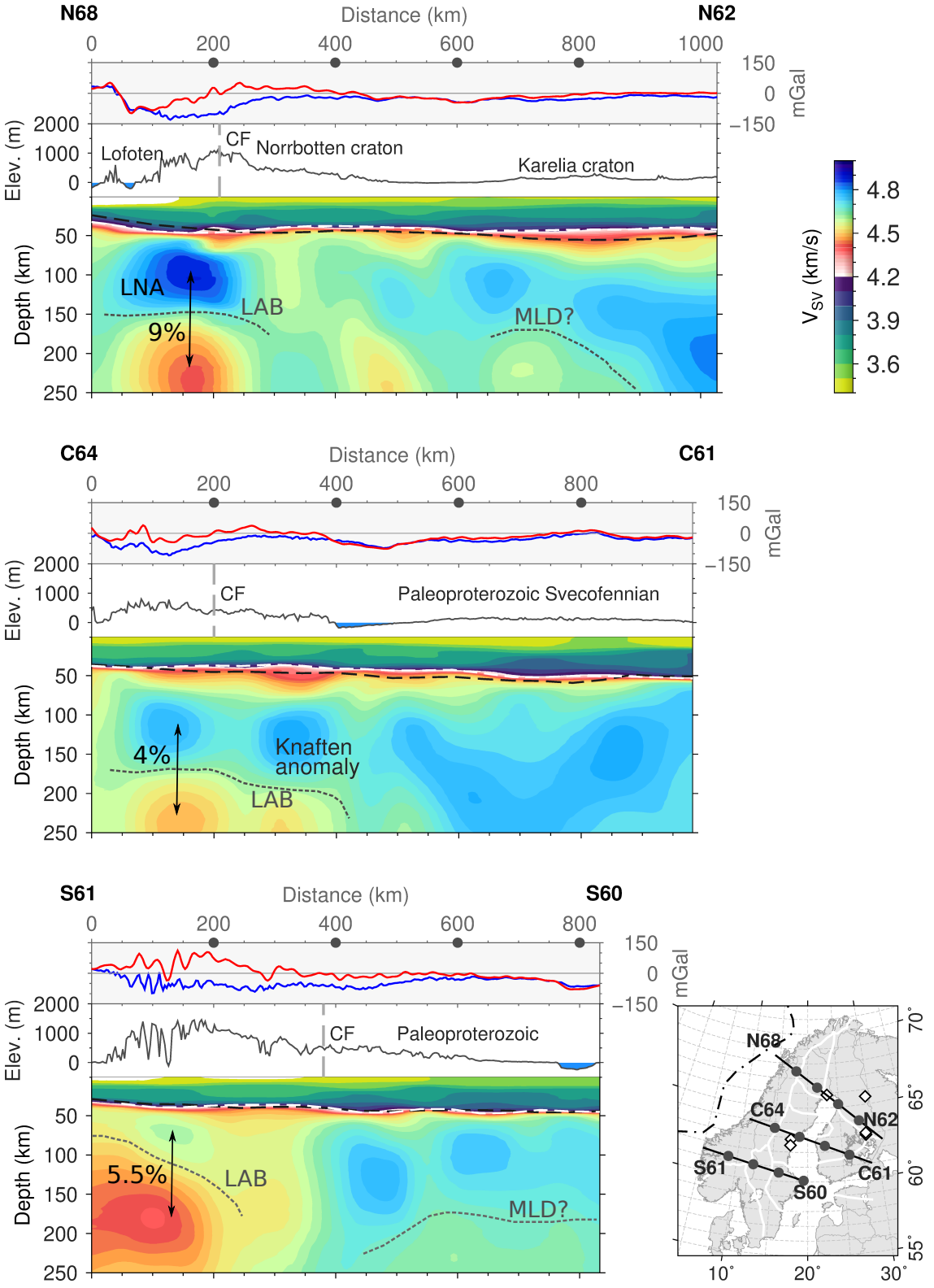

Fig. 5.14: Same as Fig. 5.12 but down to 250 km depth. The label LNA (Lofoten-Nordland anomaly) refers to both the high-velocity lid and the underlying strong low velocity zone. The numbers denote the maximum vertical V_{SV} contrast at the potential LAB. MLD is the mid-lithospheric discontinuity.

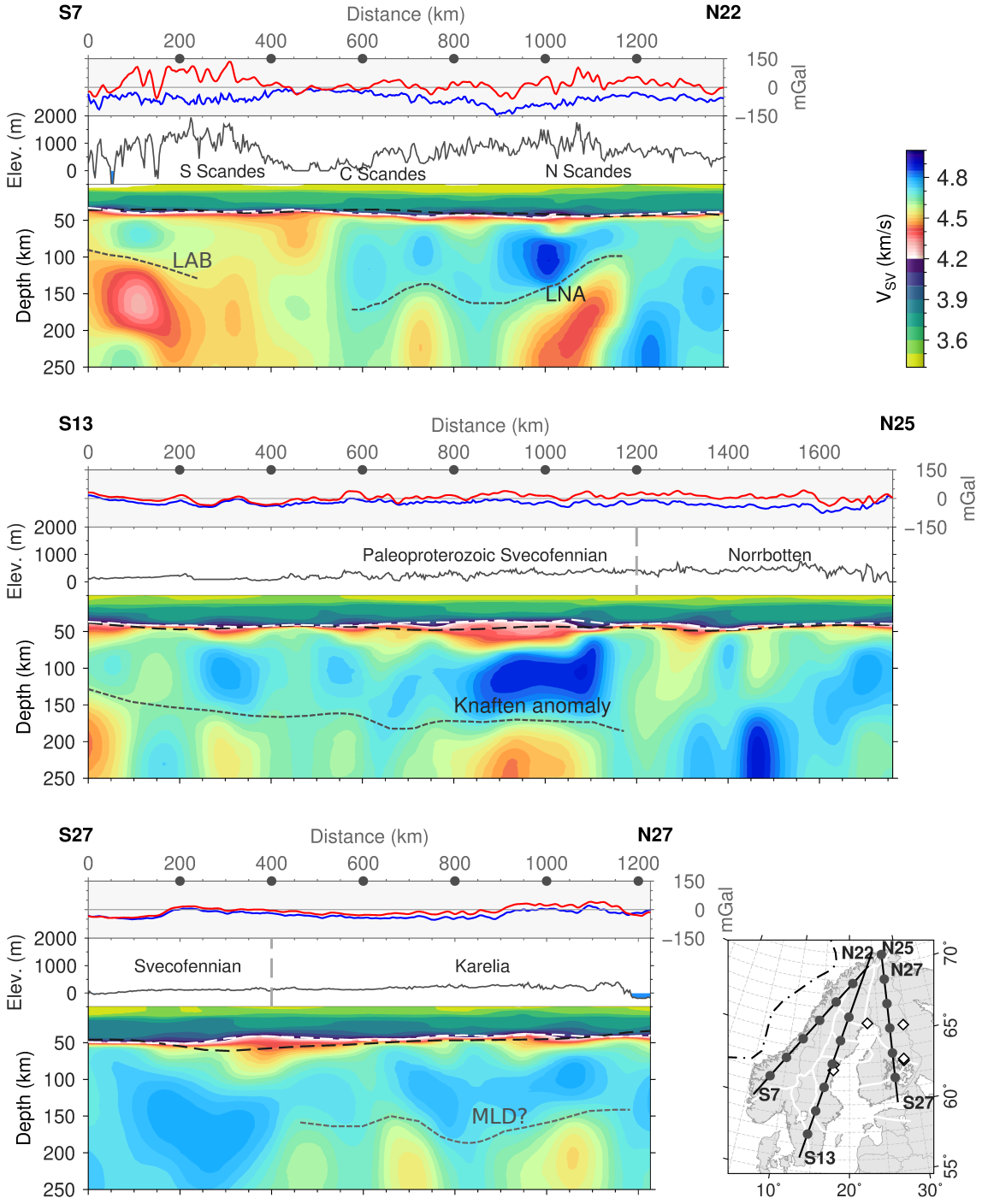

Fig. 5.15: Same as Fig. 5.14 but for north-south profiles through the Caledonides (N22-S7), and Svecofennian and Archean terranes in Sweden and Finland. Profile labels refer to the start and end longitudes.

5.8.2.1 Scandes

One striking feature in our tomography appears below the Lofoten peninsula and Nordland province, between 67°N and 69°N. We observe a high-velocity lid with unusually high velocities up to 4.85 km/s in the depth range 70–150 km, situated directly below the high-topography northern Scandes and with a lateral extent of about 300x200 km (Fig. 5.11, V_{SV} 90 km depth). The standard deviation for the high-velocity lithosphere is ∼0.075 km/s, a typical value we found throughout the study region for the depth range 100–150 km (Fig. 5.11, std dev map at 90 km depth). We note that the standard deviation of the anomaly might be underestimated due to the rejection of extreme models (see above, and Fig. C.13). Even if we consider the uncertainty, the high-velocity lid is faster than standard peridotite mantle with a V_S of 4.7 km/s (see discussion below). Below 150 km depth the shear velocity drops rapidly to a minimum of 4.4 km/s which corresponds to a V_{SV} contrast of ∼9%. In the transition to the underlying low-velocity zone, which we regard as LAB, we obtain higher standard deviations of ∼0.12 km/s. Nevertheless, the fast lid velocities and strong contrast across the LAB are robust features, although we had to omit some poor 1D inversion nodes in this region (Fig. C.14). We denote this entire anomalous structure (high velocity lid and low velocity zone) as Lofoten-Nordland anomaly (LNA).

Below the southern Scandes we obtain a similar V_S of ∼4.4 km/s at depths >150 km. However, the lithosphere is characterized by more moderate velocities around 4.65 km/s. The LAB is seen at a shallower depth between 90–120 km and is sharply dipping to the east. This dip and the vertical velocity contrast of ∼5% are in agreement with many previous studies, including those based on the analysis of the dense MAGNUS network (e.g., Wawerzinek et al., 2013; Kolstrup et al., 2015; Hejrani et al., 2017), although we have a much poorer density of stations in southern Norway. The central Scandes mantle structure appears with a thicker lithosphere of 170 km and smoother lateral and vertical velocity contrasts. The north-south profile S7-N22 in Fig. 5.15 through the Scandes is in broad agreement with the body-wave tomography by Hejrani et al. (2017) but our resolution and data coverage is much better.

Both the southern and northern Scandes are associated with a sharp eastward deepening of the LAB, also seen as an eastward velocity increase (Fig. 5.14 S61-S60, at 400 km profile distance, and N68-N62 at 250 km profile distance). In the south, we locate the sharp west-east velocity increase below the Oslo Graben. In the north, the transition occurs roughly where the high topography of the Scandes drops down toward the gently sloping Norrbotten craton. While the transition in lithospheric thickness approximately coincides with the Caledonian front below the northern and southern Scandes (Fig. 5.14), this is not the case for the central Scandes, where a transition towards a thicker lithosphere occurs about 200 km east of the Caledonian Front, near the Swedish Baltic Sea coast. In any case, due to the thicker lithosphere and reduced V_S contrast below the Central Scandes, this contrast is less pronounced.

5.8.2.2 Norrbotten craton

By comparing various cross section profiles in the north (Fig. 5.14 profile N68-N62 and 5.11 at 90 km, 140 km ant 220 km depth), we perceive the Middle Paleoproterozoic Norrbotten craton as a separate structure, which is bounded in the west by the Caledonian front (or the LNA) and in the east by the Archean Karelia craton. A sharp transition is also observed towards the south to the Late Paleoproterozoic Svecofennian domain around 66–67°N at lithosphere depths (Fig. 5.15, S13-N25, at 1200 km profile distance). The shallow part of the mantle lithosphere of

the Norrbotten craton has velocities of ∼4.65 km/s (down to 160 km depth), which is lower than for the adjoining regions. At larger depths the velocity is increasing to a maximum of 4.75 km/s. In the northernmost part of the Norrbotton region towards Finnmark, >69°N (Fig. 5.15, N25-S13, north of 1600 km), a rather thick cratonic lithosphere is imaged with velocities >4.7 km/s, at least down to 160 km depth. This fast lithosphere keel continues below the Caledonian overthrusts, also on the other two profiles in Fig. 5.15 (N22-S7 >68.5°N, north of 1200 km and N27-S7 >70°N, north of 1150 km).

5.8.2.3 Svecofennian domain

Along the S13-N25 profile in Fig. 5.15, with the transition (around 66°N, 1200 km) to the Paleoproterozoic Svecofennian domain, the lithospheric velocity increases abruptly southward, exceeding 4.8 km/s V_{SV} at its peak. This very fast mantle lid extends for ∼300 km in N-S direction and persists to 170 km depth with low-velocity material of ∼4.5 km/s below. Moving south, the high-velocity lid velocities are reduced slightly to ≤4.75 km/s and the contrast between the lid and underlying low velocity layer is reduced. As this structure correlates with the location of the Knaften arc (Fig. 5.2), we denote this striking feature as Knaften anomaly. The thin layer of reduced velocities between the inferred Moho and the high-velocity lid of the Knaften anomaly might be related to a trade-off between crustal and mantle structures indicating a localized fast lower crust (see section 5.9.3). South of 58°N (south of 200 km profile distance in S13-N25), the mantle material becomes slower over the full depth range. The southernmost point in Sweden of our study region links to the former TOR deployment (e.g., Shomali et al., 2006), which revealed a sharply thinning lithosphere with decreasing V_P and V_S values towards the south and across the Sorgenfrei-Tornquist-Zone (Medhus et al., 2012).

Eken et al. (2007, 2008) conducted P- and S-wave tomography studies across a N-S profile through Sweden (57°N-68°N), coinciding with our N25-S13 profile (Fig. 5.15). Surprisingly, we find a better agreement with their P-wave tomography than with their S-wave model. Similar to our study they imaged a sharp transition between the Paleoproterozoic and Archean domains of the Norrbotten craton as well as a high-velocity lid with underlying low-velocity medium (cf. Fig. 9 in Eken et al., 2007). However, the lid in Eken et al. (2007) is deeper (∼200 km depth), which can presumably be attributed to the poorer depth resolution of body waves. Likewise, Eken et al. (2007) observed low velocities down to at least 200 km depth in southernmost Sweden.

In Fig. 5.14 (profile C64-C61) and Fig. 5.15 (profile S27-N27) we image a fast lithospheric root of 4.75–4.8 km/s in south-central Finland down to 250 km depth, where its northern edge is clearly bounded by the Svecofennian-Archean suture. The body wave and surface wave tomography models in that area by Sandoval et al. (2004) and Bruneton et al. (2004a), respectively, revealed some discrepancies in the vertical and lateral distribution of positive and negative velocity anomalies. While Sandoval et al. (2004) can trace the keel down to at least 250 km depth, and surrounded by lower velocities, Bruneton et al. (2004a) found the Archean-Proterozoic mantle much more heterogeneous with small-scale lateral V_S perturbations within 200 km length scale. A pronounced cratonic root in the central area of southern Finland, as imaged by our study and Sandoval et al. (2004), is not indicated in their tomography. Instead, a moderate low-velocity zone (LVZ) has been found beneath the central area and a strong LVZ, with decreasing V_S from 4.75 km/s to 4.63 km/s, beneath the Archean crust at depths between 80 km to 125 km (cf. Fig. 11a in Bruneton et al., 2004a), while the

adjacent region to the west shows a V_S increase at the same depth range. It remains questionable if such small mantle anomalies can be reliably resolved with long-wavelength surface waves. However, having far less stations in south-central Finland, we image also lower velocities around 4.5 km/s at 70–110 km depth (cf. Fig. 11a in Bruneton et al., 2004a) roughly between 62.5°N and 64.5°N (Fig. 5.15, S27-N27 between 300–450 km profile distance at the suture). By inspecting our 1D V_S-depth profiles of the corresponding grid nodes, we rule out a trade-off with the Moho depth as the velocity jump around our preferred Moho depth is well constrained. On the other hand, we find our shear velocity model in better agreement with the less heterogeneous cratonic root imaged below 70 km depth by Sandoval et al. (2004). A recent receiver function study by Vinnik et al. (2016) supported this observation and inferred V_S up to 4.8 km/s in southernmost Finland.

5.8.2.4 Karelia craton

Our shear-wave velocity model allows the clear delimitation of the Archean Karelia craton also at mantle depths from the adjacent Paleoproterozoic Svecofennian domain and Norrbotten craton. The Karelia craton in northern Finland is thereby characterized by a fast lithospheric mantle of 4.7 km/s up to 150 km depth, underlain by lower velocities between 4.55–4.62 km/s, corresponding to a V_S contrast of 2.2% (Fig. 5.15, S27-N27, and Fig. 5.16a, black line). This region has previously been analyzed in several studies based on the temporary LAPNET deployment. The P-wave tomography by Silvennoinen et al. (2016) revealed a major LVZ in central-northern Finland between 100–150 km depth, partly down to 200 km depth, surrounded by the faster lithospheric material of the adjacent Norrbotten and Kola cratons. The mantle structure in Silvennoinen et al. (2016) therefore suggests a much shallower LVZ than in our model, which is hardly explainable with different resolution sensitivities of body and surface waves. Results from other studies are ambiguous. From surface waveform tomography, Lebedev et al. (2018) also obtained low velocities below northern Finland already at >110 km depth. In agreement with our results (solid black line), however, Pedersen et al. (2013) observed a high-velocity lid up to 4.72 km/s, above 150 km depth, although velocities in the LVZ drop more sharply by 5.5% (Fig. 5.16a, black dashed line), reaching the very low velocities observed beneath southern Norway (∼4.45 km/s). Also similar to our results, Vinnik et al. (2016) found low velocities at depths between 160–240 km from receiver functions, with a high-velocity lid above.

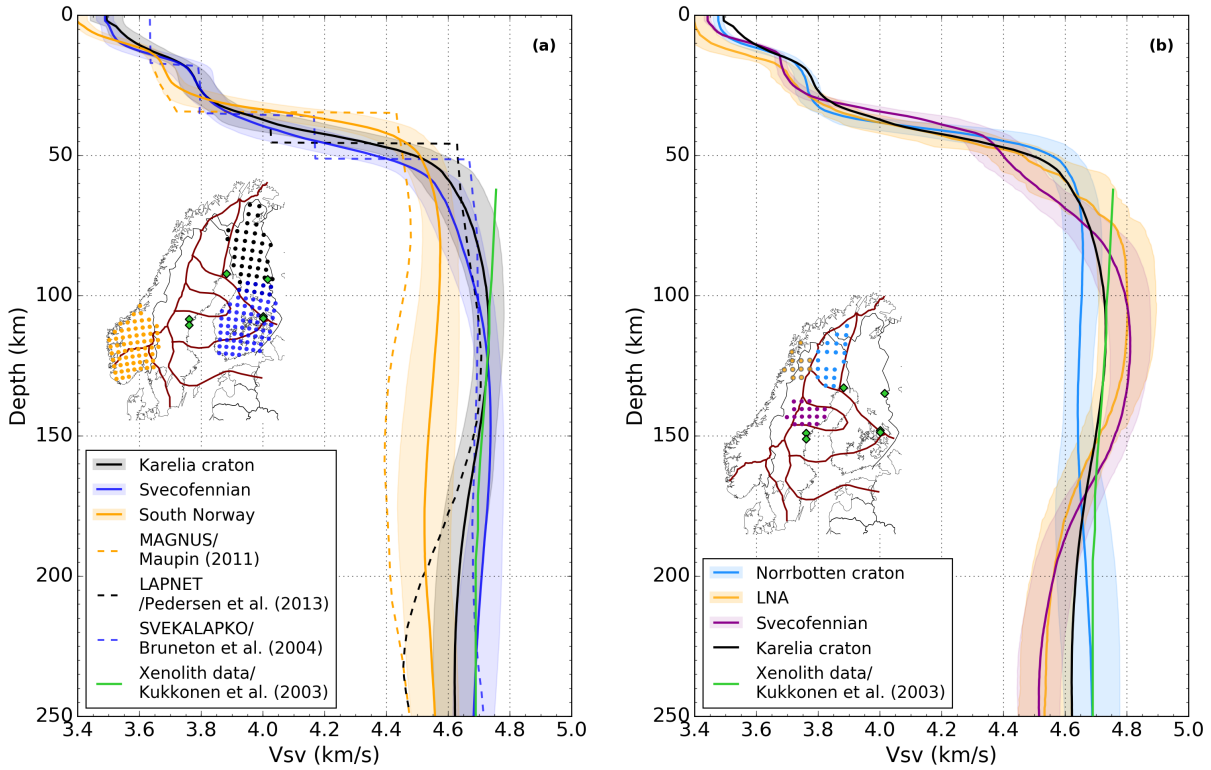

Fig. 5.16: Average V_{SV}-depth profiles for various regions calculated from the individual profiles marked as dots in the inset. Shaded areas mark the standard deviation. Purple lines and green diamonds denote the tectonic units and kimberlite pipes, respectively, as in Fig. 5.2. The green lines in (a) and (b) show the xenolith-derived velocities (samples taken from the kimberlite province in south-central Finland) calculated by Kukkonen et al. (2003) for a 250 km thick lithosphere. (a) Profiles for north and south Finland and south Norway in comparison with previous surface wave studies. The average V_S models from this study are shown as solid lines. The Moho interfaces were set to a fixed depth in the previous studies, where we did not set a Moho constraint in the inversion and therefore our mean velocity curves show instead a gradient model all the way to the surface. (b) Profiles for the Lofoten-Nordland-Anomaly (LNA), the Norrbotten craton and Svecofennian domain in central Sweden which belongs to the Knaften arc. Note that the curve of the Karelia cration and the xenolith-derived model are replotted for easier cross-comparison between the figures.

5.9 Discussion

The present lithospheric structure of Scandinavia has resulted from the complex tectonic activity and assemblage throughout 3 Ga. The onset of the Iceland and Jan Mayen plume activity and the associated opening of the North Atlantic Ocean was the last major geodynamic event (Meyer et al., 2007). We proceed in the discussion from the geologically oldest provinces to the younger ones. Here, we pay particular attention to the structure below the Caledonian Scandes.

Some fundamental questions arise from our velocity model: Why does the northern Scandes have a crustal root while a root is effectively missing below the southern and the central Scandes? Where do the sharp LAB gradients come from? Why do we see the LAB step associated with the Caledonian front (in the north and the south, but not in the central area), although it is assumed that the Caledonian overthrust only affected the crust (e.g., Corfu et al., 2014)? Why do we image a high-velocity lid below the northern but not below the southern Scandes?

5.9.1 Why are the Norrbotten and Karelia cratons distinct at mantle depth?

We observe a clear difference in the velocity structures of the Precambrian Norrbotten and Karelia cratons (Fig. 5.15, 5.16b). While the Karelia craton has a ∼175 km thick high-velocity lithosphere underlain by a zone of reduced velocities, it is vice versa for the adjacent Norrbotten craton, but with a smoother and smaller positive velocity gradient. The Karelia structure seems to be rather typical for cratonic areas as similar observations were made, for example, for the Superior craton (Darbyshire et al., 2007) and the Kaapvaal craton (Li & Burke, 2006; Pedersen et al., 2009). In consideration of the large lithospheric velocity contrasts between the two cratons (on average ∼2.5% V_{SV} contrast at 120 km depth) a pure temperature variation is implausible, as long-term cooling after the last tectonic event should have resulted in thermal equilibrium and the erasure of major thermal differences (e.g., Goes et al., 2000; Hieronymus & Goes, 2010). Rather, a compositional heterogeneous mantle lithosphere is inferred with different degrees of depletion. Pedersen et al. (2013) proposed a chemically layered lithosphere for the Karelia craton, with a dry, iron-depleted peridotitic mantle above 160 km depth to explain the high velocities and a more fertile composition (more iron and/or hydrous minerals) below to account for the reduced velocities. The origin of such a metasomatized cratonic base remains enigmatic but the kimberlite pipes surrounding the Karelia craton (Fig. 5.2) can provide some clues. High-density perovskite has been found in magmatic pipes at the eastern Finnish border (Tappe et al., 2018), dated to 754 Ma, which might contribute to the higher velocities in the upper part of the craton mantle lithosphere. Otherwise, the adjacent Kola peninsula consists of ultramafic, alkaline and carbonatite magmatic rocks including phlogopite which are attributed to a short-period magmatic event between 360–380 Ma possibly linked to extensive Devonian rifting (e.g., Downes et al., 2005). Alkaline-carbonatitic intrusions containing phlogopite (Tappe et al., 2018), dated to 1142 Ma, have been also found close to the suture zone of the Norrbotten craton. Phlogopite is a mineral that is stable throughout the lithosphere and indicates mantle metasomatism. Seismic velocities can be significantly lowered (>0.1 km/s) in the presence of hydrous and/or carbonate minerals such as 5 wt% phlogopite (Eeken et al., 2018). Xenolith samples, dated to ∼600 Ma (Kukkonen & Peltonen, 1999), have also been found in central Finland at the Karelia-Svecofennian suture zone. The geotherm derived from these samples and its intersection with the solidus of wet peridotite suggests partial mantle melting below 160 km

depth (Kukkonen & Peltonen, 1999). As the Finnish xenolith samples contain only traces of phlogopite but are already close to wet peridotite conditions, only small amounts of additional phlogopite may allow melting and therewith reduced velocities. The determined ages (Tappe et al., 2018) only partly correlate with known tectonic episodes but might have contributed to the current stage of chemical stratification. A southwestward subduction of oceanic lithosphere that likely reworked the Karelia craton occurred >1.925 Ga (Lahtinen & Huhma, 2019). The Timanides orogen 570–600 Ma ago formed on the northeastern margin of the Baltic Shield (Gee et al., 2006) due to southwest oriented subduction. Roberts & Siedlecka (2002) assumed a subsequent slab break-off where calc-alkaline granites were introduced in the upper mantle, potentially bearing phlogopite. That compositional transition in the upper mantle has been attributed to a mid-lithosphere discontinuity (MLD) rather than to the LAB (Selway et al., 2015).

The opposite stratification of the Norrbotten craton is more difficult to explain (Thybo, 2006), but upward increasing metasomatic alteration of the shallow part of the mantle lithosphere might provide an explanation. Eeken et al. (2018) stated that metasomatic phases within the shallow mantle lithosphere could result from the formation of hydrous/carbonate minerals at sub-lithospheric depth when temperatures cross the hydrous/carbonated solidus. Such a hydrated and carbonate-bearing peridotitic mantle might result from the subduction of the Knaften island arc under the Norrbotten craton 1.93 Ga (Lahtinen et al., 2005). We note that a similar Vs-depth profile has been derived for the Slave craton (Pedersen et al., 2009). Metasomatic alteration in the shallow lithosphere might not be common but is certainly not unique to the Norrbotten craton.

Although the crust of the Norrbotten and Karelia cratons underwent nearly coeval underplating (Lahtinen et al., 2005; Lahtinen & Huhma, 2019) different metasomatism processes must have acted on the mantle lithosphere to explain the opposite lithospheric velocity gradients. One may speculate that thermal differences between the Paleoproterozic Norrbotten craton and the Archean Karelia craton are responsible for causing upward and downward increasing degrees of depletion, respectively.

5.9.2 The deep lithospheric keel below Svecofennian south-central Finland

At the suture zone to the Archean terrane, a kimberlite province (∼600 Ma; (Kukkonen & Peltonen, 1999; Tappe et al., 2018); see Fig. 5.2) is present from which xenolith samples were obtained to constrain mantle composition and temperature from geothermobarometry. From those samples, Kukkonen & Peltonen (1999) extrapolated a calibrated geotherm that indicates a thick, depleted lithosphere down to at least 240 km below south-central Finland. Kukkonen et al. (2003) then calculated the corresponding seismic velocities (green line in Fig. 5.16a), which are in good agreement with our seismically inferred structure but also with the results of Sandoval et al. (2004). This lithospheric keel below the Svecofennian domain is likely in stable equilibrium and has not been reworked since its accretion in Early Proterozoic (Fig. 5.2), except for the Paleozoic kimberlite magmatism.

Similarly high seismic velocities have also been found beneath the Yilgarn craton in western Australia (e.g., Pedersen et al., 2009; Fichtner et al., 2010). Griffin et al. (1999) explained the very high seismic velocities in the shallow mantle of this craton with ultra-depleted peridotite mantle. For a primitive garnet or spinel peridotite mantle composition as commonly assumed

for cratonic areas, V_S cannot exceed 4.7 km/s for depths greater than 80 km (James et al., 2004; Garber et al., 2018), however. The V_S of >4.75 km/s, which was also observed by Bruneton et al. (2004a); Vinnik et al. (2016), therefore points to the additional presence of high-density eclogite in the upper mantle (James et al., 2004; Garber et al., 2018). In particular Garber et al. (2018) showed that a combination of eclogite and diamond (<=20 vol.% eclogite and ca. 2 vol.% diamond for a typical cratonic geotherm of 35–40 mW/m^2) can explain such high-velocities in the mantle lithosphere. Assuming a neutrally buoyant, stable cratonic root associated with the absence of a gravity anomaly, a maximum of 20 vol.% eclogite can exist in the cratonic lithosphere.

5.9.3 The Knaften anomaly in Svecofennian Sweden

The central area of the Svecofennian domain in Sweden corresponds to the accreted oceanic Knaften arc (Fig. 5.2) and is characterized by a distinct positive velocity anomaly with significantly reduced velocities above and below (Fig. 5.16b). We note that the shallow low-velocity anomaly (4.2–4.4 km/s) below the Moho might indicate a locally thickened crust (cf. Eken et al. (2008)) whose lowest part is affected by partial eclogitization, as discussed by Makushkina et al. (2021). A high degree of depletion in the upper mantle above 170 km depth must be present to explain the very high velocities within the lithospheric lid (see section 5.9.2). Eken et al. (2008) interpreted this lid as trapped slab within the Proterozoic lithosphere as the structure seems to deepen towards the Archean North in their model. We cannot confirm this hypothesis, although we see a fast velocity fragment at >150 km depth for the Norrbotten craton (Fig. 5.15, S13-N25 profile). The southern edge of the Knaften anomaly (~63°N, visible in Fig. 5.15, S13-N25 profile) is close to alkalin-carbonatitic intrusions containing phlogopite minerals (Tappe et al., 2018). As discussed in section 5.9.1, the presence of phlogopite can indicate a metasomatized layer (Eeken et al., 2018) as in the Karelia craton but the velocities are much lower within the Knaften anomaly.

5.9.4 How is the topography of the Scandes sustained

We first discuss the degree of crustal and mantle compensation of the topographic load before we infer the geodynamic context. We image significant differences in the crustal and mantle structure below the Scandes. These results confirm early assumptions of different local uplift mechanisms for the southern and northern Scandes to explain an elevation amplitude on the order of 1–2 km with an east-west extent of ~400 km and ~200 km, respectively. A summary of the major differences across the Scandes can be found in Table 5.1.

5.9.4.1 Crustal compensation

In accordance with many earlier studies (reviewed in the Introduction), we observe no crustal root below the southern Scandes. Instead, crustal thickness tends to increase eastward in the lower topography parts of Sweden, opposite to the expected relation for Airy isostasy. The thickening of the crust is directly related to the presence of the (high-density) LCL (Fig.5.13) which leads to an overall isostatic compensation of the Baltic Shield (Ebbing et al., 2012) but this does not explain the maintenance of the high topography. We must therefore invoke dynamic topography for the southern Scandes, i.e., density differences in the mantle.

Table 5.1: Overview of structural and tectonic features across the Scandes mountain range. ∼ means weak occurrence.

	Feature	northern Scandes	central Scandes	southern Scandes
Topo	Maximum	2,100 m	1,000 m	2,500 m
	Average	500 m	380 m	800 m
Tectonics	Sveconorwegian reworking	-	-	+
	Oslo Graben reworking	-	-	+
	Caledonian reworking	∼	+	+
	Neogene uplift	+	-	+
Gravity	Free-air gravity anomaly (FA)	-100 mGal	-	+150 mGal
	E-W offset of FA from max. topography	100 km	-	0 km
	Bouguer gravity anomaly (BA)	-160 mGal	-	-
	Offset of BA from max. topography	60 km	-	-
Seismic model	TIB layer thickness (shallow crust)	15 km	∼10 km	-
	LCL thickness (deep crust)	<15 km	<10 km	<5 km
	Crustal root	+	-	-
	LAB depth	150 km	170 km	90-120 km
	Max. Vs in lithosphere	4.85 km/s	4.7 km/s	4.65 km/s
	Min. Vs in asthenosphere	4.4 km/s	4.5 km/s	4.4 km/s
	V_{SV} contrast at LAB	9%	4%	5.5%
	Lithospheric step	sharp	gradual	sharp
	E-W difference in lithospheric thickness	>100 km	>50 km	>130 km
	Surface wave scattering*	+	-	+
Topo support	Airy isostasy	+	-	-
	Pratt isostasy	+	+	-
	Lateral asthenospheric flow	?	-	+
	EDC	+	-	+
	Dynamic support	+	?	+

* An unusual azimuthal variation of the Rayleigh phase velocities with 360° periodicity occurred below the northern and southern Scandes likely caused by the sharp LAB steps and strong V_S contrasts. This feature is absent below the central Scandes where the lithospheric structure is smoother (Mauerberger et al., 2021a).

For the northern Scandes, the crustal root (Fig. 5.13 and 5.12), imaged in this study and in Ben Mansour et al. (2018), will contribute to supporting the topography, i.e., Airy isostasy is active for the northern Scandes. It should be noted that the increased crustal thickness with respect to the central Scandes is mostly related to increased thickness of the (high-density) LCL. Crustal low-velocity material below the Lofoten/Nordland region down to 15 km depth (Fig. 5.12) can be related to the low-density TIB rocks that fit best the Bouguer anomaly (Ebbing & Olesen, 2005), i.e., there is a Pratt isostasy effect. As we infer a combined Airy-Pratt crustal compensation but we observe also density variations in the mantle, the northern Scandes are probably not exclusively compensated in the crust.

The crust beneath the lower topography central Scandes has no root but a thin LCL (<10 km) and consists partly of low-density TIB rocks at shallow depths (Fig. 5.11). We note that the sub-crustal low velocities (Fig. 5.12, profile C64-C61) below the mountains might also point to an eclogitized layer as discussed in section 5.9.3 which would be in agreement with Makushkina et al. (2021). Our model supports the conclusion by Ebbing et al. (2012) that a high-density layer is necessary to achieve isostatic equilibrium below the central Scandes. A Pratt isostasy is therefore likely the main cause of topography compensation. However, a compensating contribution from the low-density sub-lithospheric mantle below 170 km depth might have an impact as well.

On the origin of the LCL many explanations exist. Magmatic underplating has been often adduced (e.g., Mjelde et al., 2002; Korja et al., 2006). There is no evidence for onshore magmatism in Cenozoic times but underplating might have been triggered by crustal shortening during the Caledonian collision (Ebbing et al., 2006). Kukkonen et al. (2008) argued that partial eclogitization of the lower crust could explain the high velocities in the LCL. Eclogites are exposed on the Lofoten islands and within the inland Caledonian allochthons. They have been formed within the basement of the Baltic craton as a result of the underthrusting below Laurentia during the main Caldedonian orogen event ∼430 Ma before being exhumed back to the surface (Steltenpohl et al., 2003; Brueckner & Roermund, 2004). It seems therefore possible that the LCL beneath the northern Scandes might originate from an eclogitization process forming a partially eclogitized lower crust. Since the crustal root below the northern Scandes is less pronounced compared to other high mountain ranges, we can speculate about a partial crustal delamination. A delamination of the high-density eclogitic layer can occur if the density of the LCL exceeds the density of the surrounding mantle. We would expect the crustal root to be completely removed by a full delamination. Possibly, the northern Scandes crustal root could have been deeper in the past. A recent delamination is not indicated as Ebbing et al. (2012) calculated a density of 3200 kg/m^3 for the LCL which is ∼5% less dense than the sub-Moho peridotitic mantle and therefore in agreement with our moderate LCL velocities of ∼4.0 km/s. An eroded crustal root would ultimately result in lower surface topography, therefore an additional compensation by the mantle is required to explain the present elevations.

5.9.4.2 Mantle compensation

Significant reductions of the density structure at sub-lithospheric depths are implied by our velocity model (Fig. 5.14) and pointing to a buoyant mantle below the Scandes. Especially, below the southern Scandes, where we image lowered velocities at shallow mantle depth >90 km, a warm lithosphere is required to achieve local isostatic equilibrium (Kolstrup et al., 2012).

The most striking difference between the northern and southern Scandes at mantle depth is the high-velocity lid of the LNA. Abundant eclogite would be able to explain the high velocities but a contribution of a delaminated eclogitized crust is unlikely. It would be a coincidence that we image the delaminated crust at the time before the layer sinks into the deeper mantle. But such a trapped delaminated layer is implausible as the major uplift occurred in the Paleogene and Early Neogene, i.e. there would have been enough time to sink down. Alternatively, we can regard the LNA lid as inheritance from the Paleoproterozic structure (see 5.9.2). Lahtinen et al. (2005) found the western edge of the Norrbotten craton to be buried under the Caledonian unit and we can speculate that the lid might be a depleted remnant of this Paleoproterzoic craton.

In case of the northern Scandes, Gabrielsen et al. (2005) suggested that the topography instead results from rift-shoulder uplift (Buck, 1986; Cloetingh et al., 1992) or isostatic rebound effects as no seismic model provided evidence for any mantle convection perturbation. A mantle-driven mass compensation for the northern Scandes has been also refuted by Ebbing & Olesen (2005) as they found compensating low-density material within the crust. Gradmann & Ebbing (2015), however, argued that an additional deep source for isostatic compensation of the northern Scandes is necessary as none of their geophysical-petrological models fit the gravity and topography data simultaneously. The model for the northern Scandes needs a re-evaluation since we clearly imaged a high-velocity lid above a low-velocity layer below the high topography (LNA, Fig. 5.14) in addition to a crustal root and lateral velocity variations in the crust (Airy-Pratt isostasy; see above). The presence of very low-velocity material in the asthenosphere part of the LNA below the northern Scandes hints at the influence of mantle-driven buoyancy, which we will discuss in subsection 5.9.4.4.

5.9.4.3 Gravity anomalies

The change of isostatic compensation along the mountains is also indicated by the Free-air and Bouguer gravity anomalies (Fig. 5.12 and 2.13). Negative Bouguer gravity values are associated with the entire mountain belt but have a prominent local negative anomaly (-160 mGal) within the northern Scandes. Positive Free-air gravity anomalies coinciding with the highest topography characterize the southern Scandes and thus point to lowered densities in the mantle. The central Scandes show generally no or little Free-air gravity anomaly indicating nearly isostatic equilibrium. For the northern Scandes, we note an offset between the thickest crust and the highest elevation where the western edge of the crustal root is associated with a small-scale (100×200 km) negative Free-air gravity anomaly (-100 mGal), having a steep gradient around the Lofoten area (Fig. 5.14). Such an offset indicates that the load of the mountains is also partially supported by the flexural strength of the lithosphere (e.g., Ebbing & Olesen, 2005; Gradmann & Ebbing, 2015). Both the crustal root and the LNA coincide with the local negative Bouguer anomaly. A highly depleted LNA might have lower density in the lithospheric mantle and thus contribute to compensate the topography as well as explaining the Bouguer anomaly (Gradmann & Ebbing, 2015). It remains therefore unclear if the crustal root could exclusively explain the negative Bouguer anomaly. Pronounced lateral density contrasts as present within the crust (TIB and LCL) but also across the LNA are able to produce local gravity anomalies. A revised gravity modeling based on our lithospheric model is necessary to clarify the impact of the imaged crustal and mantle heterogeneities.

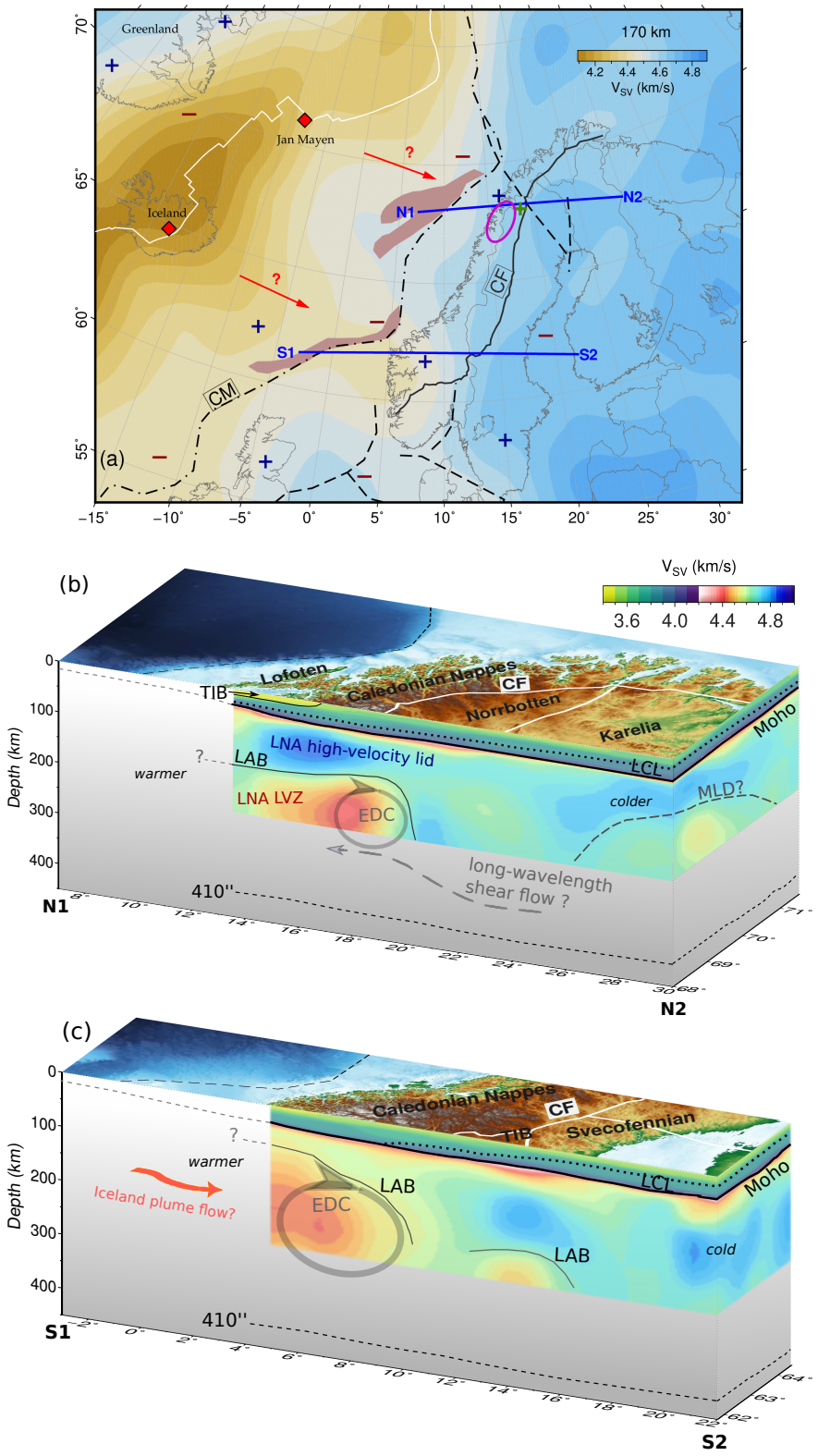

Fig. 5.17: (a) Map of the wider North Atlantic region highlights some important features relevant for the discussion. In the background, the shear-wave velocity model at 170 km depth from the global surface waveform tomography by Schaeffer & Lebedev (2013) (version SL2013sv, updated April 2018) is shown. Red diamonds show the presumed Iceland and Jan Mayen hot spot locations. Arrows mark the potential asthenospheric flow from the hot spots towards the Scandes. The negative Free-air gravity anomaly with -100 mGal (Pavlis et al., 2008) is encircled in purple. Dark blue plus signs denote regions of major Neogene uplift after Japsen & Chalmers (2000), green plus sign marks major Paleogene uplift, and red minus signs mark Cenozoic subsidence regions. Brown shaded areas show the offshore volcanic provinces after Gaina et al. (2014). CM is the continental margin, CF the Caledonian front. Dashed black lines are the same fault zones as in Fig. 5.2. The profiles in (b) and (c) are marked as blue lines. *Continues on next page.*

Fig. 5.17: *Cont. from previous page.* (b) Profile N1-N2: Sketch of an EW section through the continental margin and the northern Scandes. TIB rocks and a minor crustal root as well as a high-velocity lower crustal layer (LCL) are able to support the topography. A small-scale edge-driven convection (EDC) flow pattern might occur at the transition between oceanic and continental lithosphere. Upwelling of hot asthenosphere material under the thin lithosphere could form the LNA low-velocity region below the Scandes leading to additional buoyancy and uplift. (c) Profile S1-S2: Sketch through the southern Scandes. Neither low-density TIB rocks nor a distinctive crustal root are present to support the mountains, which instead are supported by a shallow and hot asthenosphere. A larger EDC cell is expected to form at the LAB step and can contribute to increasing temperatures and lower seismic velocities and densities below the southern Scandes. The 410 km discontinuity is flat (Makushkina et al., 2019) and thus there is no deep-seated source of upwelling below the Scandes.

5.9.4.4 Geodynamic implications

Origin of lithospheric steps

Sharp steps in the lithospheric thickness, separating thinner lithosphere in the west below the Scandes from thicker lithosphere below the cratons in the East, are imaged approximately below the Caledonian front (CF) in the southern and northern Scandes, with a more gradual transition in the central Scandes as associated with the Knaften anomaly (Fig. 5.14). The spatial coincidence of the steps with the CF is quite surprising as the Caledonian thrusting is thought to have affected only the Precambrian crust (e.g., Corfu et al., 2014). The present sharp lateral transition cannot be explained by temperature variations alone, at least not as a stable configuration.

The rifted continental margin, resultant from the North Atlantic opening, implies a stretching and thus thinning of the lithosphere as well as upwelling of the asthenosphere, which might be associated with decompression melting, particularly nearing breakup (see marked volcanic provinces in Fig. 5.17). Since the continental margin has a varying distance to the Norwegian coast, breakup-related melting could have affected the lithosphere below the Scandes by different degrees of sub-crustal stretching, melt upwelling (compositional perturbation) and thermal buoyancy (Lister et al., 1991). The continental margin has the largest distances from the Scandes in the central part where the LAB is deepest in our model with rather smooth lateral and vertical velocity gradients (Fig. 5.14, profile C64-C61). Moreover, the CF does not match well with the lithosphere thickening. Less stretching and therewith less upwelling might contribute to the relatively lower surface topography of the central Scandes. Alternatively, Brueckner & Roermund (2004) stated that subduction of the Baltic plate during the Caledonian orogeny might have metasomatized the adjacent continental lithosphere which then became warmer than the Baltic Shield. The CF as the boundary for the thinned lithosphere is potentially related to post-orogenic stretching in Early Devonian, as the Precambrian basement east of the CF was only little affected by extensional processes (Andersen, 1998; Braathen et al., 2002). These extensional processes might have pre-weakened the lithospheric structure below the Scandes before the Cenozoic rifting took place (Wang et al., 2015). A stretched structure is less stable compared to the adjacent depleted lithosphere.

In view of the different mantle velocities, a generally warmer lithosphere below the southern Scandes compared to the north could be present. We know that the northern Scandes underwent a different tectonothermal history compared to the southern Scandes. The TIB magmatic intrusions, the Caledonian orogeny and the North-Atlantic break-up are the main

events in the North, whereas the southern region was additionally affected by the Sveconorwegian orogen and Permian rifting. It seems that the Caledonian orogeny has failed in reworking the Archean crust of the Lofoten peninsula as only little imprint of the collision is preserved in the rocks (e.g., Steltenpohl et al., 2011a; Breivik et al., 2017). This different setting might explain the presence of the ∼80 km thick high-velocity lid below the northern Scandes while higher temperatures in the south triggered the erosion of the lithosphere. Maupin et al. (2013) concluded that large viscosity and temperature contrasts with regard to the adjacent, and potentially reworked, terranes are necessary to explain the lithosphere step in the south. Slagstad et al. (2017) proposed that the southern Norway low-velocity anomaly could partly result from radioactive thermal effects of the refertilized mantle lithosphere due to the oceanic subduction during the Sveconorwegian orogen. This might cause a long-lived heat contribution. Another candidate for re-heating could be the rifting and magmatic episodes during the Permian that affected the entire North Sea region south-east of southern Norway and created the Oslo Graben (Neumann et al., 2004). An additionally thermal perturbation might occur near the time of the North Atlantic breakup related to the Iceland plume (e.g., Rohrman & van der Beek, 1996).

Finally, we relate the strong lateral and vertical V_S contrasts at the LAB below the southern and northern Scandes to an anomalous azimuthal 360° periodicity of the Rayleigh phase velocities (Mauerberger et al., 2021a).

The linkage to the Iceland plume system

The recent analysis of the mantle transition zone by Makushkina et al. (2019) using the ScanArray data set revealed only slight deepening of the 410 km discontinuity below the Scandes. As deeply hot rising material through the transition zone would generate significant deflections of the 410 km and 660 km discontinuities, this implies that only shallow mantle perturbations are responsible for our imaged sublithospheric low velocities.

The most widely accepted hypothesis for the southern Scandes uplift is asthenospheric diapirism triggered by the impingement of a finger of the Iceland plume head causing isostatic uplift possibly due to Rayleigh-Taylor instability and resultant delamination (Rohrman & van der Beek, 1996; Nielsen et al., 2002; Gabrielsen et al., 2005; Pascal & Olesen, 2009; Maupin et al., 2013). These processes would thin the lithosphere and might explain the extended low-velocity region below southern Norway which we have imaged in accordance with many previous studies. Lithospheric erosion of 35 km thickness can lead to >500 m surface uplift (Nielsen et al., 2002) which would explain the shallower LAB and higher topography in the south compared to the northern Scandes. The plume impingement hypothesis is supported by the presence of elongated low velocities regions in the North Atlantic mantle below 100 km depth, linking Iceland and southern Norway (Weidle & Maupin, 2008; Rickers et al., 2013; Schoonman et al., 2017) (Fig. 5.17a), which might represent a channel of hot plume material. The impact of the Iceland plume has been questioned by (e.g., Pascal & Olesen, 2009; Maupin et al., 2013) as the initially proposed Rayleigh-Taylor instability (Rohrman & van der Beek, 1996) cannot develop if the temperatures of the continental lithosphere or the plume flow or the viscosity of the asthenosphere are too low. Otherwise, re-heating potentially affected the southern Norway lithosphere earlier (see section 5.9.4.4) and the plume flow temperature is likely able to at least warm the lithosphere and therefore reduce its density (Pascal & Olesen, 2009). Burov & Guillou-Frottier (2005) pointed out that the observed uplift is insufficient

(only 400 m) and their lateral extent too large (1500 m) to represent a sufficient amount of plume material to feed the anomaly below the southern Scandes. However, a recent thermo-mechanical modeling study by Koptev et al. (2017) revives the hypothesis of having a long-distance (∼1000 km) horizontal asthenospheric flow originating from the Iceland plume system. Their model predicts an onshore uplift of several hundred meters in the southern Scandes. The mountains may therefore partially sustain their topography by dynamic support from hot mantle, but plume feeding might not be enough to explain today's topography.

Analogous to the prominent southern Norway low-velocity region, we can speculate about an influence of the North Atlantic hot spot system on the low velocity asthenosphere of the LNA. North Atlantic tomography studies (Pilidou et al., 2005; Yakovlev et al., 2012; Rickers et al., 2013) show a low velocity channel at 100–150 km depth which links the Jan Mayen hot spot to the continental margin of northern Norway (Fig. 5.17a). An initial plume impingement and the associated onset of lithosphere thinning would imply buoyancy and dynamic topography. However, the thermal and compositional impact of such a plume branch was apparently less intense compared to the south as the LNA lid seems to have been preserved in this area.

Edge-driven convection

The presence of the steps discussed in the previous section can lead to small-scale edge-driven convection (EDC) as described by King & Anderson (1998). A sketch of the proposed setting below the Scandes is drawn in Fig. 5.17b and c. EDC cells can develop in regimes of preexisting vertical thermal boundaries as present at continent-ocean or craton boundaries. When the convective flow around such lithosphere steps becomes unstable, a small-scale convective cell will form at these edges. Two end-member EDC models can be distinguished (King & Anderson, 1998; Kaislaniemi & van Hunen, 2014). A 'pure-EDC' cell develops due to downwelling of cold material at the relatively cold lithosphere edge, while the upwelling of hot asthenospheric mantle leads to a convective flow next to the lithosphere step. A 'shear-EDC' flow pattern exists where a large-scale horizontal flow from the thicker to the thinner lithosphere dominates in the asthenosphere and overrides the downwelling cold flow. The long-wavelength horizontal asthenospheric flow originates from higher than average temperature below the thick lithosphere, e.g., due to an insulating effect of the cratonic lithosphere. Induced by this long-wavelength shear motion, a smaller-scale EDC cell is generated next to the lithosphere step. In any case, the upwelling emplaces less dense material potentially causing decompression mantle melting (Kaislaniemi & van Hunen, 2014) at sub-lithospheric depths and creating a thermal anomaly which we image as low-velocity region (King & Ritsema, 2000). In turn, this upward flow of hot material under the thin lithosphere induces buoyancy and regional surface uplift, i.e., dynamic topography (Buck, 1986; Vagnes & Amundsen, 1993; Wijk et al., 2010). There is a transition from pure-EDC to shear-EDC when the lateral temperature contrast between the thick and thin lithosphere is >>0.1–1% (King & Anderson, 1998). Although the EDC model has been adduced to explain intraplate volcanism and igneous provinces (e.g., King & Anderson, 1995; Wijk et al., 2010), Córdoba & Ballmer (2020) have recently shown in a 2D modeling that EDC cells can exist over long time scales without producing melts.

The key point of the EDC scenario for the Scandes is that it provides an explanation for the differences in the E-W topography extent along the Scandes which could not be clarified in the past. A shear-EDC is associated with a smaller convection cell, in the order of 150-200 km, than a pure-EDC with around 300-500 km lateral and height dimension (Kaislaniemi & van Hunen,

2014). A shear-EDC is more likely to occur below the northern Scandes which have an E-W topography extent of ∼200 km. Due to the lateral dimension of ∼400 km, the southern Scandes has rather the geometry associated with pure-EDC flow. However, a pure-EDC cell below the southern Scandes seems to be incompatible with an assumed plume flow that would certainly affect the EDC due to the large lateral temperature contrast. The Scandes might therefore be attributed to different degrees of shear-EDC or to the transition to pure-EDC. A combined interaction of pure-EDC and shear-EDC has been modeled by Kaislaniemi & van Hunen (2014) in order to explain the varying lithospheric thickness under the Moroccan Atlas mountains and its piecewise lithosphere delamination.

The EDC concept describes a mechanism but the resulting actual seismic velocities depend on several factors. Unfortunately, no mantle xenoliths have been found in the Scandes (Steltenpohl et al., 2003; Brueckner et al., 1998), such that we have to fully rely on seismic constraints. Menke et al. (2016) estimated that an EDC induced pure thermal anomaly with ∼700°C contrast to the adjacent cold lithosphere, and in the absence (∼0.1%) of partial melt (Dong & Menke, 2017), can account for a V_S drop of 10%. However, such strong temperature contrasts across lithospheric steps are not thermally stable. Maupin et al. (2013) and Gradmann et al. (2013) concluded that both a high temperature contrast of 200°C at 200 km depth and regional changes in composition are needed to interpret the strong gradient with very low seismic velocities beneath southern Norway which are similar to the LNA low velocities. Kolstrup et al. (2012) obtained for southern Norway temperatures >1300°C. The contribution of compositional variations reduces V_S by only ∼1% (Goes et al., 2000; Cammarano et al., 2003), unless hydrous minerals or water content are considered. Thus, thermal perturbation appears to be the dominant factor to produce the observed V_S drops. The EDC modeling by Till et al. (2010) predicts melting next to the lithosphere step between 90–200 km depth for 0.01–3.3 vol% melt, >150 ppm water and mantle temperature at 1350°C. Such conditions would likewise lead to a V_S drop of 5–10%. Subduction and magmatic intrusion events (see section 5.9.4.4) have likely changed the composition and temperature below southern Norway. Whereas the central and northern Scandes might be rather affected by orogen related metasomatism (Brueckner & Roermund, 2004), passive margin rifting, and/or asthenospheric upwelling which probably alters the sub-lithosphere predominantly thermally. The north-south variation in surface elevation cannot be explained with the different EDC styles, but maybe with different thermal perturbations and therewith different degree of dynamic support along with the differences in the crustal structure.

In conclusion, we propose several processes to sustain the northern Scandes topography (also see Table 5.1): (1) The emplacement of low-density TIB granitoids, acting on the shallow crust, along with (2) the lateral variation of a high-density LCL that affects the basal crust point to Pratt isostasy. (3) The crustal root represents an Airy isostasy. (4) An EDC cell at the sharp LAB step induce buoyancy due to rising hot asthenospheric material. The northern Scandes topography may be supported by both crustal isostasy and dynamic support. In view of the southern Scandes uplift, neither low-density TIB rocks nor significant high-density LCL or a pronounced crustal root are observed. Dynamic support seems therefore the most plausible uplift mechanism. The driving process is likely the impingement of the lateral asthenospheric plume flow on the continental lithosphere. The LAB step below the Oslo Graben likely induces EDC as secondary effect which implies further upwelling of hot material

below southern Norway and therewith uplift of the topography. This scenario seems reasonable as the uplift rate caused by the lateral asthenospheric flow is possibly insufficient. The central Scandes are mainly compensated by Pratt isostasy but mantle buoyancy might have an effect as well.

5.10 Conclusion

We present a new shear-wave velocity model for entire Scandinavia down to 250 km depth derived from ambient noise and teleseismic surface waves, which are inverted with a two-step procedure, first calculating period-dependent phase-velocity maps, and then deriving a V_S model. Setting up an event bootstrapping for the surface wave phase velocity maps, we observed various extreme small-scale velocity artefacts in northern Scandinavia for varying event distributions. Using azimuthally balanced event distributions the regional artifacts almost disappear. We conclude that isotropically balancing of event distributions is vital to avoid artificial velocity anomalies in areas of strong lateral gradients (see Mauerberger et al. (2021a)).

A new crustal model is obtained from these results, from which we derive new maps of the Moho depth and the thickness of a high velocity and presumably high density lower crustal layer (LCL). While the southern Scandes lacks a pronounced crustal root, we observe a crustal root below the northern Scandes, decreasing towards the central Scandes. We can clearly trace the low-velocity rocks of the Transscandinavian Igneous Belt at 15 km depth from southern Sweden towards the Lofoten/Nordland region in the north. Furthermore, the LCL is imaged to be up to 25 km thick below the Baltic Shield, and thins to ∼10 and 15 km towards the central and northern Scandes, respectively. Below the southern Scandes the LCL is nearly absent. A striking velocity anomaly is imaged below the northern Scandes with a high-velocity lid (∼4.8 km/s) above 150 km depth and very low velocities below (minimum 4.4 km/s). The LAB below the Scandes is deepening from west to east with a sharp step and velocity drop in the North (150 km depth) in the South (90–120 km depth), both coinciding with the Caledonian front. The central area shows a much smoother thickening of the lithoshere from west to east, where the mantle structure cannot be clearly associated with the Caledonian front. In Precambrian Scandinavia, we find low-velocity areas below 150 km depth beneath the Archean Karelia craton in northern Finland and image the Paleoproterozoic Norrbotten craton at mantle depths which separates the Karelia craton, Caledonides and Paleoproterozic Svecofennian.

We confirm the conclusions of earlier studies that the southern Scandes sustain their topography predominately due to dynamic support from the mantle. The northern Scandes are supported by both crustal and mantle density variations. They are likely compensated by a combined Airy-Pratt isostasy indicated by the shallow TIB rocks, the laterally varying LCL, and a crustal root. In both cases, we suspect the influence of a small-scale edge-driven convection (EDC) at the sharp LAB gradients which help to sustain the presence of hotter asthenospheric material below the northern and southern Scandes. EDC mechanisms are also able to explain the E-W topography differences between the southern and northern Scandes. Pratt isostasy compensates the central Scandes to first order but there might be a minor contribution from mantle buoyancy.

Chapter 6

Conclusion & outlook

In my thesis, I investigated the crustal and mantle lithosphere of entire Scandinavia down to a depth of 250 km. Scandinavia is of particular interest because it consists of Precambrian terranes in the northeastern area and a high mountain range (the Scandes) from the Paleozoic along its western rim which forms a passive continental margin. The present Scandes show a maximum elevation of 2,500 m in southern Norway and 2,100 m in northern Sweden while the central Scandes have a peak topography of 1,000 m. However, rifting episodes and erosion triggered denudation should have been eliminated the topography a long time ago. Since the area lacks of recent compressional tectonic forces, I can investigate the geodynamic evolution of lithospheric structures.

With the analysis of Rayleigh surface waves from teleseismic earthquakes and ambient noise data recorded by 228 stations, mainly from the temporary ScanArray Core network and the permanent Swedish network, I was able to image the lithosphere in unprecedented resolution. My work was thereby driven by two main objectives: First, can surface wave data provide new clues to the maintenance of the high topography? The focus is thereby on the structural variation along the Scandes and the prevailing geodynamic mechanisms. Second, are the various accreted tectonic domains distinguishable on crustal and mantle scales? The intrinsic azimuthal anisotropy which might be 'frozen' in the different domains could be a candidate for providing new evidence as well. These aspects are mainly treated in chapter 5. Details on the biased azimuthal anisotropy can be found in chapter 4.

To constrain the average Rayleigh phase velocity in different regions of Scandinavia, I conducted a beamforming analysis of the teleseismic surface waves (Mauerberger et al., 2021a). By forming sub-arrays covering the north, central and south regions of Scandinavia, I observed exceptional phase velocity variations with propagating azimuth. In the north and the south, a 360° periodicity (denoted as 1θ variation) of the phase velocity with the backazimuth occurs for periods > 35 s. In the central area the 1θ variation is absent for all periods. A 5% deviation between the maximum and minimum velocities were measured for backazimuths of 120° and 300°, respectively. Such a variation is incompatible with the intrinsic azimuthal anisotropy. I assumed a relation to large lithospheric heterogeneity as the slow and fast directions are perpendicular to a step in the lithosphere-asthenosphere boundary (LAB) inferred by previous studies in southern Norway/Sweden. To test this hypothesis, I performed a 2D full-waveform modeling of Rayleigh wave propagation. By the setup of various synthetic models, which incorporate a steep gradient in the LAB and a pronounced reduction in the shear velocity below the LAB, I was able to reproduce the observations. Increased phase velocities were obtained for waves propagating from thicker to thinner lithosphere whereas for waves propagating from thinner to thicker lithosphere the phase velocities are clearly reduced. I conclude that sharp horizontal structural gradients in combination with strong vertical and lateral velocity contrasts in the lithosphere lead to 1θ variations. The smoother the vertical and lateral LAB gradients, the smaller the phase velocity variation. The interference of

forward scattered surface wave energy with the fundamental mode is likely the main contributor to the 1θ phase velocity variation. From analysis of the wave train propagation, I assume a secondary influence of backward scattering near the lithospheric step. Nevertheless, by averaging over all propagation azimuths a stable phase velocity estimate for each sub-array is obtained. The averaged dispersion curves vary only little between the regions. It is important to note that the 1θ variation implies the necessity of an even azimuthal event distribution to avoid biased phase velocity measurements.

To asses this potential bias, I conducted a bootstrap test with different teleseismic event distributions for the inversion of 2D Rayleigh wave phase velocities. I used the two plane waves method (TPW, Forsyth & Li (2005)) to construct the 2D phase velocity maps and to calculate the azimuthal anisotropy. For varying event distributions various extreme small-scale velocity artifacts are observed in the north between the Lofoten and Nordland/Norrbotten provinces. No significant artifacts occur in the south hinting to smoother gradients at the LAB but still strong enough to produce the 1θ variation. Another explanation could be the distance to the sharp ocean-continent margin, which is closer in the north than in the south. Using azimuthally balanced event distributions the regional artifacts almost disappear. I demonstrated therewith that isotropically balancing of event distributions is vital to avoid artificial velocity anomalies in areas of strong lateral gradients (Mauerberger et al., 2021a). This is a vital finding since the influence of the azimuthal distribution of passive sources is neglected in many tomography studies. Scandinavia might be an exceptional case due to unusually strong lithospheric gradients. However, it seems possible that the usage of unbalanced event distributions result in artifacts in lateral phase velocity variations in other regions of the world to a lesser degree, and consequently to an over-interpretation of the structure. The bootstrap test unveiled also the unreliability of the obtained azimuthal anisotropy results. Both the fast anisotropy direction and amplitude depend on the event distribution resulting in unstable orientation and large amplitudes, again mainly in the north. In case of balanced event distributions, the azimuthal anisotropy is more stable but still laterally varying within small scales.

I calculated the final Rayleigh phase velocity maps with balanced event distributions for periods between 25–160 s. The upper crust is resolved by the incorporation of ambient noise data. The noise dispersion curves ranging from 3–33 s period were generated from 20,847 cross-correlated station pairs and used for the 2D phase velocity inversion with a transdimensional Markov chain Monte Carlo (McMC) technique (Tilmann et al., 2020). At each TPW grid node location, I performed the final 1D V_S-depth inversion based on the merged dispersion curves, again by a transdimensional McMC approach (Dreiling & Tilmann, 2019).

From the obtained velocity model, I can derive new maps of the Moho depth and the thickness of a high-velocity and presumably high-density lower crustal layer (LCL). The crust and mantle are surprisingly more heterogeneous than it would be expected from a region with Precambrian cratons and a passive margin. I summarize the most striking observations below:

- The Moho is generally deepening from west to east below the low-topography Baltic Shield mainly as a result of the thickening of the LCL.
- Below the Baltic Shield the LCL is up to 25 km thick, and thins to ∼10 and 15 km towards the central and northern Scandes, respectively.
- A pronounced crustal root is present below the northern Scandes, decreasing towards the

central Scandes.

- Below the southern Scandes, both a crustal root and the LCL are nearly absent.
- I can trace the low-velocity rocks of the Transscandinavian Igneous Belt (TIB) at 15 km depth from southern Sweden towards the Lofoten/Nordland region.
- The lithosphere below the Scandes is thickening from west to east with a sharp lateral step and velocity drop with depth. The LAB of the thinner lithosphere is at 150 km depth with 9% V_{SV} contrast in the north and ranges from 90–120 km depth with 5.5% V_{SV} contrast in the south.
- Both LAB steps coincide with the surface expression of the Caledonian front (CF).
- The central area shows rather smoothly varying structures (170 km LAB depth, 4% V_{SV} contrast) towards the east and no clear spatial match with the front.
- Beneath the Archean Karelia craton in northern Finland, a low-velocity area is found below 150 km depth clearly separated from the 250 km deep lithospheric keel below the Svecofennian southern Finland.
- The Paleoproterozoic Norrbotten craton can be separated from the Karelia craton, Caledonides and Paleoproterozic Svecofennian at mantle depths.
- The Knaften arc, a segment of the Svecofennian domain in central Sweden, stands out with a high-velocity anomaly down to 170 km depth.

My velocity model allows a new perspective on the preservation of the surface topography of the northern and central Scandes, but I can also re-evaluate the southern Scandes uplift. The northern Scandes are supported by both crustal and mantle velocity/density variations. They are likely compensated by a combined Airy-Pratt isostasy as indicated by the shallow low-density TIB rocks, the laterally varying LCL and the crustal root. Based on the inspection of gravity anomalies and the fact that the maximum Moho depth is offset from the peak topography, flexural isostatic response is also likely a contributing factor. As assumed previously, the southern Scandes sustain their topography predominately due to dynamic support from the mantle. However, I suspect the influence of a small-scale edge-driven convection (EDC) at the sharp LAB gradients below the northern and southern Scandes which maintain the presence of hotter asthenospheric material and therewith isostatic buoyancy. An uplift contribution by EDC seems reasonable as none of the previously suggested mechanisms, i.e., asthenospheric diapirism and lithospheric erosion, are able to produce the necessary uplift rates for today's elevation. A previously missing puzzle was an explanation for the different lateral extents of the mountain range from north to south. The EDC hypothesis provides an answer by adducing varying cell dimensions due to different degrees of the convection. The central Scandes are likely compensated by Pratt isostasy to a first order but there might be a minor contribution from mantle buoyancy.

Moreover, a perturbation of the mantle flow caused by the small-scale EDC might also contribute to the incoherent azimuthal anisotropy that I observed, especially in the north. It seems plausible that the frozen-in intrinsic azimuthal anisotropy has been destroyed by recent local perturbations.

With regard to the different tectonic episodes, the lithosphere below the northern Scandes is potentially colder relative to the southern Scandes. This may have left the thick

high-velocity lid below the northern Scandes. Otherwise, the lid could be a remnant of the adjacent Norrbotten craton. Different degrees of metasomatism can be attributed to the heterogeneous mantle lithosphere below the Norrbotten and Karelia craton.

There is a striking coincidence that the high-topography mountains in the north and the south are associated with closer distances to the continental margin and stronger velocity gradients in the subcontinental lithosphere, bounded by the CF, and ultimately resulting in the 1θ variation. An essential objective is the question how the sharp LAB gradients at the edge of the CF evolved and why we see such a correlation. The CF as the boundary for the thinned lithosphere is possibly related to metasomatic weakening of the subcontinental lithosphere as a consequence to the Caledonian orogeny (Brueckner, 2006; Wang et al., 2015). Post-orogenic stretching might be another or additional trigger, as the Precambrian basement east of the CF was only little affected by extensional processes (Andersen, 1998; Braathen et al., 2002). The post-orogenic extensional orientation of the northern and southern Scandes occurred mainly perpendicular to the CF in E-W direction while the extension of the central Scandes occurred in NE-SW direction (Braathen et al., 2002). These extensional processes might have pre-weakened the lithospheric structure below the Scandes before rifting due to the North Atlantic opening formed the passive margin. A speed-up of the thermal-mechanical erosion of the subcontinental lithosphere might be caused by the Iceland plume impingement (Wang et al., 2015).

Finally, the observed abrupt reduction in lithospheric thickness towards the passive margin provides a reasonable origin for the 1θ variation. I clearly relate the strong lateral and vertical V_S contrasts at the LAB below the southern and northern Scandes to the anomalous azimuthal 360° periodicity of the Rayleigh phase velocities.

It might be worth to look at the big picture. Similar sharp changes in the thickness of continental lithosphere have been observed in other regions, often associated with high topography: southeast Australia (Fishwick et al., 2008; Rawlinson et al., 2017), east Greenland (Artemieva, 2019b), the Colorado plateau (Wijk et al., 2010), the Snake River Plain (Lin & Ritzwoller, 2011a; Schmandt & Lin, 2014) and the Appalachians (Menke & Levin, 2002; Schmandt & Lin, 2014). In the latter two cases, a 1θ variation has been already discovered and I assume a high probability of a 1θ observation also in the other regions. It should be emphasized that the 1θ phase velocity variation is not directly linked to the surface topography, it is a secondary effect along with significant mantle inhomogeneities. The lithosphere below the Appalachian mountain range in the northeastern United States is characterized by a strong regional low-velocity anomaly (denoted as North Appalachian anomaly, NAA), with ∼10% V_S reduction at the LAB at <100 km to ∼300 km depth (Schmandt & Lin, 2014). The Appalachian mountain range is, just like the Scandes, a passive margin mountain range bordering the Atlantic, and being related to the Caledonian orogeny. At the location of the NAA, a maximum topography of about 1300 m is reached. Similarly to onshore Scandinavia, the region around the NAA lacks Cenozoic active volcanism. Fishwick et al. (2008) identified multiple lithospheric steps below southeastern Australia related to different geological units with increasing age from east to the west, where largest thickness is reached within the western Archean Yilgarn craton. Such a simple time-dependent lithosphere variation cannot be observed in Scandinavia. Analogous to Scandinavia, above the thinner lithosphere a high mountain range is present along a passive margin without recent active

tectonic forces acting on it. However, active volcanism took place in Australia in Cenozoic times within the thin lithosphere domain.

The common feature among Scandinavia, Appalachians and Australia is the association with a presumed tectonic uplift in Cenozoic times (Hay et al., 2002). A world-wide contemporaneous uplift is however difficult to justify. Global climate change associated with vast depositions of offshore sediments are a possible candidate which would rather imitate a direct surface uplift. Otherwise, if the Cenozoic uplift is associated with the alteration of the subcontinental lithosphere (Lithgow-Bertelloni & Gurnis, 1997), it might give rise to the similar lithospheric structures along the passive margins, overprinting the different Mesozoic and Paleozoic processes.

There are some tasks that need to be done in the future to refine our picture of Scandinavia. The lowest hanging fruit is the joint inversion of P- and S-wave receiver functions from Makushkina et al. (2021) with my noise and Rayleigh surface wave data. In particular, a possible trade-off between Moho depth, high-velocity lower crust and sub-crustal low velocities can be much better constrained by the joint inversion.

Based on my high-resolution velocity model, modeling of temperature and gravity should be revised. Future work comprising seismic attenuation and body wave tomography might be useful to further constrain the temperature anomalies in the subcontinental lithosphere and the potential melt content. The thermal-compositional modeling approach by Eeken et al. (2018) provides an opportunity to take advantage of my study since their method directly applies dispersion curves. I see some potential to get a better understanding of the metasomatic processes of the Norrbotten and Karelia cratons. However, velocity-temperature conversions are subject to some limitations as short-wavelength contrasts in mantle temperature due to the smearing effect of horizontal heat transfer.

Gravity modeling needs a re-assessment as my velocity model has given a new constrains on the different topography compensation along the Scandes. A simple 1D calculation of Airy isostasy is already provided in the appendix section C.5.

Inspired by the impressive resolution of the full-waveform inversion (FWI) conducted by Rickers et al. (2013), I propose an updated FWI tomography for the North Atlantic region using the ScanArray data set as well as recently deployed stations in Greenland and supplemented by stations on the Faeroe Islands. It is amazing how well Rickers et al. (2013) resolved the low-velocity anomaly below southern Norway with its sharp transition to the east with only one station in southern Norway and a few stations in Finland. I expect a high-resolution upper mantle model for the entire North Atlantic region including the recent dense network in Scandinavia. Additionally, I suggest to deploy some more stations on Jan Mayen Island (and maybe some OBS between Iceland and Jan Mayen if this has not already been done) to better resolve the hot spot system. Such a study could further shed light on the possible impingement of a plume finger on Scandinavia.

Bibliography

Afanasiev, M., Boehm, C., Driel, M. V., Krischer, L., Rietmann, M., May, D. A., Knepley, M. G., & Fichtner, A., 2019. Modular and flexible spectral-element waveform modeling in two and three dimensions, *Geophysical Journal International*, **216**, 1675–1692, doi:10.1093/gji/ggy469.

Aki, K. & Richards, P., 1980. *Quantitative Seismology: Theory and Methods. Volume II*, W. H. Freeman and Company.

Albuquerque Seismological Laboratory (ASL)/USGS, 1988. Global Seismograph Network - IRIS/USGS. International Federation of Digital Seismograph Networks. Dataset/Seismic Network. doi:10.7914/SN/IU.

Alinaghi, A., Bock, G., Kind, R., Hanka, W., Wylegalla, K., Groups, T., & Working, S., 2003. Receiver function analysis of the crust and upper mantle from the North German Basin to the Archaean Baltic Shield, *Geophys. J. Int.*, **155**, 641–652.

Andersen, T., 1998. Extensional tectonics in the Caledonides of southern Norway , an overview, *Tectonophysics*, **285**, 333–351.

Anell, I., Thybo, H., & Artemieva, I. M., 2009. Cenozoic uplift and subsidence in the North Atlantic region: Geological evidence revisited, *Tectonophysics*, **474**, 78–105, doi:10.1016/j.tecto.2009.04.006.

Artemieva, I., 2011. *The Lithosphere. An Interdisciplinary Approach*, Cambridge University Press.

Artemieva, I., 2019a. Lithosphere structure in Europe from thermal isostasy, *Earth-Science Reviews*, **188**, 454–468, doi:S0012825218304744.

Artemieva, I. M., 2019b. Lithosphere thermal thickness and geothermal heat flux in Greenland from a new thermal isostasy method, *Earth-Science Reviews*, **188**, 469–481, doi:10.1016/j.earscirev.2018.10.015.

Artemieva, I. M. & Thybo, H., 2013. EUNAseis: A seismic model for Moho and crustal structure in Europe, Greenland, and the North Atlantic region, *Tectonophysics*, **609**, 97–153, doi:10.1016/j.tecto.2013.08.004.

Aster, R. C., Borchers, B., & Thurber, C., 2013. *Parameter Estimation and Inverse Problems*, Academic Press, 2nd edn.

Balling, N., 2000. Deep seismic reflection evidence for ancient subduction and collision zones within the continental lithosphere of northwestern Europe, *Tectonophysics*, **329**, 269–300.

Bayes, T., 1763. An Essay Towards Solving a Problem in the Doctrine of Chances, *Philos. Trans. R. Soc. London*, **53**, 370–418.

Ben Mansour, W., England, R. W., Fishwick, S., & Moorkamp, M., 2018. Crustal properties of the northern Scandinavian mountains and Fennoscandian shield from analysis of teleseismic receiver functions, *Geophysical Journal International*, **214**, 386–401, doi:10.1093/gji/ggy140.

Bensen, G. D., Ritzwoller, M. H., Barmin, M. P., Levshin, A. L., Lin, F., Moschetti, M. P., Shapiro, N. M., & Yang, Y., 2007. Processing seismic ambient noise data to obtain reliable broad-band surface wave dispersion measurements, *Geophysical Journal International*, **169**, 1239–1260, doi:10.1111/j.1365-246X.2007.03374.x.

Berthelsen, A. & Marker, M., 1986. 1.9-1.8 Ga Old Strike-Slip Megashears in the Baltic Shield and their Plate Tectonic Implications, *Tectonophysics*, **128**, 163–181.

Bock, G., Achauer, U., Aiinaghi, A., Ansorge, J., Bruneton, M., Friederich, W., Grad, M., Guterch, A., Hjelt, S. E., Hyvönen, T., Ikonen, J. P., Kissling, E., Komminaho, K., Korja, A., Heikkinen, P., Kozlovskaya, E., Nevsky, M. V., Pavlenkova, N., Pedersen, H., Piomerová, J., Raita, T., Riznichenko, O., Roberts, R. G., Sandoval, S., Sanina, I. A., Sharov, N., Tiikkainen, J., Volosov, S. G., Wielandt, E., Wylegalla, K., Yliniemi, J., & Yurov, Y., 2001. Seismic probing of Fennoscandian Lithosphere, *Eos*, **82**, 621–636, doi:10.1029/01EO00356.

Bodin, T. & Maupin, V., 2008. Resolution potential of surface wave phase velocity measurements at small arrays, *Geophysical Journal International*, **172**, 698–706, doi:10.1111/j.1365-246X.2007.03668.x.

Bodin, T. & Sambridge, M., 2009. Seismic tomography with the reversible jump algorithm, *Geophys. J. Int.*, **178**, 1411–1436, doi:10.1111/j.1365-246X.2009.04226.x.

Bodin, T., Sambridge, M., Rawlinson, N., & Arroucau, P., 2012a. Transdimensional tomography with unknown data noise, *Geophys. J. Int.*, pp. 1–21, doi:10.1111/j.1365-246X.2012.05414.x.

Bodin, T., Sambridge, M., Tkalćić, H., Arroucau, P., Gallagher, K., & Rawlinson, N., 2012b. Transdimensional inversion of receiver functions and surface wave dispersion, *Journal of Geophysical Research: Solid Earth*, **117**, 1–24, doi:10.1029/2011JB008560.

Braathen, A., Osmundsen, T. P., Nordgulen, Ø., Roberts, D., & Meyer, G. B., 2002. Orogen-parallel extension of the Caledonides in northern Central Norway: an overview, *Norwegian Journal of Geology*, **82**, 225–241.

Breivik, A. J., Faleide, J. I., Mjelde, R., Flueh, E. R., & Murai, Y., 2017. A new tectono-magmatic model for the Lofoten/Vesterålen Margin at the outer limit of the Iceland Plume influence, *Tectonophysics*, **718**, 25–44, doi:10.1016/j.tecto.2017.07.002.

Brueckner, H. K., 2006. Dunk, Dunkless and Re-dunk Tectonics: A Model for Metamorphism, Lack of Metamorphism, and Repeated Metamorphism of HP/UHP Terranes, *International Geology Review*, **48**(May), 978–995, doi:10.2747/0020-6814.48.11.978.

Brueckner, H. K. & Roermund, H. L. M. V., 2004. Dunk tectonics : A multiple subduction/eduction model for the evolution of the Scandinavian Caledonides, *Tectonics*, **23**, 1–20, doi:10.1029/2003TC001502.

Brueckner, H. K., Gilotti, J. A., & Nutman, A. P., 1998. Caledonian eclogite-facies metamorphism of Early Proterozoic protoliths from the North-East Greenland Eclogite Province, *Contrib Mineral Petrol*, **130**, 103–120.

Bruneton, M., Pedersen, H. A., Farra, V., Arndt, N. T., Vacher, P., Achauer, U., Alinaghi, A., Ansorge, J., Bock, G., Friederich, W., Grad, M., Guterch, A., Heikkinen, P., Hjealt, S. E., Hyvönen, L. T., Ikonen, J. P., Kissling, E., Komminaho, K., Korja, A., Kozlovskaya, E., Nevsky, M. V., Paulssen, H., Pavlenkova, N. I., Plomerova, J., Raita, T., Riznichenko, O. Y., Roberts, R. G., Sandoval, S., Sanina, I. A., Sharov, N. V., Shomali, Z. H., Tiikkainen, J., Wielandt, E., Wilegalla, K., Yliniemi, J., & Yurov, Y. G., 2004a. Complex lithospheric structure under the central baltic shield from surface wave tomography, *Journal of Geophysical Research: Solid Earth*, **109**, 1–15, doi:10.1029/2003JB002947.

Bruneton, M., Pedersen, H. A., Vacher, P., Kukkonen, I. T., Arndt, N. T., Funke, S., Friederich, W., & Farra, V., 2004b. Layered lithospheric mantle in the central Baltic Shield from surface waves and xenolith analysis, *Earth and Planetary Science Letters*, **226**, 41–52, doi:10.1016/j.epsl.2004.07.034.

Buck, W. R., 1986. Small-scale convection induced by passive rifting: the cause for uplift of rift shoulders, *Earth and Planetary Science Letters*, **77**, 362–372.

Burov, E. & Guillou-Frottier, L., 2005. The plume head – continental lithosphere interaction using a tectonically realistic formulation for the lithosphere, *Geophys. J. Int.*, **161**, 469–490, doi:10.1111/j.1365-246X.2005.02588.x.

Calcagnile, G., 1982. The Lithosphere-Asthenosphere System in Fennoscandia, *Tectonophysics*, **90**, 19–35.

Cammarano, F., Goes, S., Vacher, P., & Giardini, D., 2003. Inferring upper-mantle temperatures from seismic velocities, *Physics of the Earth and Planetary Interiors*, **138**, 197–222, doi:10.1016/S0031-9201(03)00156-0.

Chen, H., Ni, S., Chu, R., Chong, J., Liu, Z., & Zhu, L., 2018. Influence of the off-great-circle propagation of Rayleigh waves on event-based surface wave tomography in Northeast China, *Geophysical Journal International*, **214**, 1105–1124, doi:10.1093/GJI/GGY185.

Chew, D. M. & Strachan, R. O. B. A., 2014. The Laurentian Caledonides of Scotland and Ireland, in *New Perspectives on the Caledonides ofScandinavia and Related Areas*, pp. 45–91, Geological Society, London, Special Publications.

Clayton, R. & Engquist, B., 1977. Absorbing boundary conditions for acoustic and elastic wave equations, *BSSA*, **67**, 1529–1540.

Cloetingh, S., Reemst, P., Kooi, H., & Fanavoll, S., 1992. Intraplate stresses and the post-Cretaceous uplift and subsidence in the northern Atlantic Basins, *Norsk Geologisk Tidsskrift*, **72**, 229–235.

Córdoba, A. M.-C. & Ballmer, M., 2020. The role of Edge-Driven Convection in the generation of volcanism I : a 2D systematic study, *EGU Solid Earth (submitted)*, pp. 1–25, doi:10.5194/se-2020-120.

Corfu, F., Andersen, T. B., & Gasser, D., 2014. The Scandinavian Caledonides: main features, conceptual advances and critical questions, *Geological Society, London, Special Publications*, **390**(1), 9–43, doi:10.1144/SP390.25.

Cotte, N., Pedersen, H. A., Campillo, M., Farra, V., & Cansi, Y., 2000. Off-great-circle propagation of intermediate-period surface waves observed on a dense array in the French Alps, *Geophysical Journal International*, **142**, 825–840, doi:10.1046/j.1365-246X.2000.00187.x.

Cotte, N., Pedersen, H. A., & Group, T. W., 2002. Sharp contrast in lithospheric structure across the Sorgenfrei – Tornquist Zone as inferred by Rayleigh wave analysis of TOR1 project data, *Tectonophysics*, **360**, 75–88.

Dahlen, F. A. & Tromp, J., 1998. *Theoretical Global Seismology*, Princeton University Press.

Darbyshire, F. A., Eaton, D. W., Frederiksen, A. W., & Ertolahti, L., 2007. New insights into the lithosphere beneath the Superior Province from Rayleigh wave dispersion and receiver function analysis, *Geophys. J. Int.*, **169**, 1043–1068, doi:10.1111/j.1365-246X.2006.03259.x.

Datta, A., Priestley, K. F., Roecker, S., & Chapman, C. H., 2017. Surface wave mode coupling and the validity of the path average approximation in surface waveform inversions : an empirical assessment, *Geophys. J. Int.*, **211**, 1077–1098, doi:10.1093/gji/ggx345.

Doin, M.-P., Fleitout, L., & Christensen, U., 1997. Mantle convection and stability of depleted and undepleted continental lithosphere, *Journal of Geophysical Research*, **102**, 2771–2787.

Dong, M. & Menke, W., 2017. Seismic High Attenuation Region Observed Beneath Southern New England From Teleseismic Body Wave Spectra: Evidence for High Asthenospheric Temperature Without Melt, *Geophyscial Research Letters*, **44**, 10958–10969, doi:10.1002/2017GL074953.

Downes, H., Balaganskaya, E., Beard, A., Liferovich, R., & Demaiffe, D., 2005. Petrogenetic processes in the ultramafic , alkaline and carbonatitic magmatism in the Kola Alkaline Province: A review, *Lithos*, **85**, 48–75, doi:10.1016/j.lithos.2005.03.020.

Dreiling, J. & Tilmann, F., 2019. BayHunter - McMC transdimensional Bayesian inversion of receiver functions and surface wave dispersion. doi:http://doi.org/10.5880/GFZ.2.4.2019.001.

Dreiling, J., Tilmann, F., Yuan, X., Haberland, C., & Seneviratne, S. W. M., 2020. Crustal Structure of Sri Lanka Derived From Joint Inversion of Surface Wave Dispersion and Receiver Functions Using a Bayesian Approach, *Journal of Geophysical Research: Solid Earth*, **125**, 1–15, doi:10.1029/2019jb018688.

Ebbing, J., 2007. Isostatic density modelling explains the missing root of the Scandes, *Norwegian Journal of Geology*, **87**, 13–20.

Ebbing, J. & Olesen, O., 2005. The Northern and Southern Scandes — structural differences revealed by an analysis of gravity anomalies , the geoid and regional isostasy, *Tectonophysics*, **411**, 73–87, doi:10.1016/j.tecto.2005.09.002.

Ebbing, J., Lundin, E., Olesen, O., & Hansen, E., 2006. The mid-Norwegian margin: A discussion of crustal lineaments, mafic intrusions, and remnants of the Caledonian root by 3D density modelling and structural interpretation, *Journal of the Geological Society*, **163**, 47–60.

Ebbing, J., England, R. W., Korja, T., Lauritsen, T., Olesen, O., Stratford, W., & Weidle, C., 2012. Structure of the Scandes lithosphere from surface to depth, *Tectonophysics*, **536-537**, 1–24, doi:10.1016/j.tecto.2012.02.016.

Eeken, T., Goes, S., Pedersen, H. A., Arndt, N. T., & Bouilhol, P., 2018. Seismic evidence for depth-dependent metasomatism in cratons, *Earth and Planetary Science Letters*, **491**, 148–159, doi:10.1016/j.epsl.2018.03.018.

Eken, T., Shomali, Z. H., Roberts, R., & Bödvarsson, R., 2007. Upper-mantle structure of the Baltic Shield below the Swedish National Seismological Network (SNSN) resolved by teleseismic tomography, *Geophysical Journal International*, **169**, 617–630, doi:10.1111/j.1365-246X.2007.03351.x.

Eken, T., Shomali, Z. H., Roberts, R., Hieronymus, C. F., & Bodvarsson, R., 2008. S and P velocity heterogeneities within the upper mantle below the Baltic Shield, *Tectonophysics*, **462**, 109–124, doi:10.1016/j.tecto.2008.02.015.

Eken, T., Plomerová, J., Roberts, R., Vecsey, L., Babu, V., Shomali, H., & Bodvarsson, R., 2010. Seismic anisotropy of the mantle lithosphere beneath the Swedish National Seismological Network (SNSN), *Tectonophysics*, **480**, 241–258, doi:10.1016/j.tecto.2009.10.012.

Ekström, G., Abers, G. A., & Webb, S. C., 2009. Determination of surface-wave phase velocities across USArray from noise and Aki ' s spectral formulation, *Geophyscial Research Letters*, **36**, 1–5, doi:10.1029/2009GL039131.

England, R. W. & Ebbing, J., 2012. Crustal structure of central Norway and Sweden from integrated modelling of teleseismic receiver functions and the gravity anomaly, *Geophysical Journal International*, **191**, 1–11, doi:10.1111/j.1365-246X.2012.05607.x.

England, R. W., Ebbing, J., & Mansour, W. B., 2015. SCANLIPS3D - SCANdinavian LIthosphere P and S wave experiment 3 D, Tech. rep.

Fichtner, A., Kennett, B. L. N., Igel, H., & Bunge, H.-P., 2010. Full waveform tomography for radially anisotropic structure: New insights into present and past states

of the Australasian upper mantle, *Earth and Planetary Science Letters*, **290**, 270–280, doi:10.1016/j.epsl.2009.12.003.

Fishwick, S., Heintz, M., Kennett, B. L. N., Reading, A. M., & Yoshizawa, K., 2008. Steps in lithospheric thickness within eastern Australia , evidence from surface wave tomography, *Tectonics*, **27**, 1–17, doi:10.1029/2007TC002116.

Forsyth, D. W., 1975. The Early Structural Evolution and Anisotropy of the Oceanic Upper Mantle, *Geophys. J. R. astr. Soc.*, **43**, 103–162.

Forsyth, D. W. & Li, A., 2005. Array analysis of Two-Dimensional Variations in Surface Wave Phase Velocity and Azimuthal Anisotropy in the Presence of Multipathing Interference, *Seismic Earth: Array Analysis of Broadband Seismograms. Geophysical Monograph Series 157*, pp. 81–97, doi:10.1029/157GM06.

Foster, A., Ekström, G., & Hjörleifsdóttir, V., 2014. Arrival-angle anomalies across the USArray Transportable Array, *Earth and Planetary Science Letters*, **402**, 58–68, doi:10.1016/j.epsl.2013.12.046.

Frassetto, A. & Thybo, H., 2013. Receiver function analysis of the crust and upper mantle in Fennoscandia – isostatic implications, *Earth and Planetary Science Letters*, **381**, 234–246, doi:10.1016/j.epsl.2013.07.001.

Friederich, W., 1998. Wave-theoretical inversion of teleseismic surface waves in a regional network: phase-velocity maps and a three-dimensional upper-mantle shear-wave-velocity model for southern Germany, *Geophys. J. Int.*, **132**(1), 203–225, doi:10.1046/j.1365-246x.1998.00425.x.

Friederich, W., Hunzinger, S., & Wielandt, E., 2000. A note on the interpretation of seismic surface waves over 3-d structures, *Geophysical Journal International*, **142**, 3–6.

Gaal, G. & Gorbatschev, R., 1987. An Outline of the Precambrian Evolution of the Baltic Shield, *Precambrian Research*, **35**, 15–52.

Gabrielsen, R. H., Braathen, A., Olesen, O., Faleide, J. I., Kyrkjebo, R., & Redfield, T. F., 2005. Vertical movements in south-western Fennoscandia: a discussion of regions and processes from the Present to the Devonian, in *Onshore-Offshore Relationships on the North Atlantic Margin*, vol. 12, pp. 1–28, eds Wandas, B., Eide, E., Gradstein, F., & Nystuen, J., Elsevier.

Gaina, C., Medvedev, S., Torsvik, T. H., Koulakov, I., & Werner, S. C., 2014. 4D Arctic : A Glimpse into the Structure and Evolution of the Arctic in the Light of New Geophysical Maps , Plate Tectonics and Tomographic Models, *Surv Geophys*, **35**, 1095–1122, doi:10.1007/s10712-013-9254-y.

Garber, J. M., Maurya, S., Hernandez, J.-a., Duncan, M. S., & Zeng, L., 2018. Multidisciplinary Constraints on the Abundance of Diamond and Eclogite in the Cratonic Lithosphere, *Geochemistry, Geophysics, Geosystems*, **19**, 2062–2086, doi:10.1029/2018GC007534.

Gee, D. G., Bogolepova, O. K., & Lorenz, H., 2006. The Timanide, Caledonide and Uralide orogens in the Eurasian high Arctic, and relationships to the palaeo-continents Laurentia, Baltica and Siberia, in *European Lithosphere Dynamics*, vol. 32, pp. 507–520, Geological Society, London, Memoirs.

Gee, D. G., Fossen, H., Henriksen, N., & Higgins, A. K., 2008. From the early Paleozoic platforms of Baltica and Laurentia to the Caledonide orogen of Scandinavia and Greenland, *Episodes*, **31**(March), 44–51, doi:10.1006/phrs.1993.1113.

Gelman, A., Carlin, J., Stern, H., Dunson, D., Vehtari, A., & Rubin, D., 2013. *Bayesian Data Analysis*, Chapman and Hall/CRC, 3rd edn.

Goes, S., Govers, R., & Vacher, P., 2000. Shallow mantle temperatures under Europe from P and S wave tomography, *Journal of Geophysical Research*, **105**, 11153–11169.

Gomberg, J. S. & Masters, T. G., 1988. Waveform modelling using locked-mode synthetic and differential seismograms: application to determination of the structure of Mexico, *Geophysical Journal*, **94**, 193–218.

Gorbatschev, R. & Bogdanova, S., 1993. Frontiers in the Baltic Shield, *Precambrian Research*, **64**, 3–21.

Gradmann, S. & Ebbing, J., 2015. Large-scale gravity anomaly in northern Norway: Tectonic implications of shallow or deep source depth and a possible conjugate in northeast Greenland, *Geophysical Journal International*, **203**(3), 2070–2088, doi:10.1093/gji/ggv426.

Gradmann, S., Ebbing, J., & Fullea, J., 2013. Integrated geophysical modelling of a lateral transition zone in the lithospheric mantle under Norway and Sweden, *Geophysical Journal International*, **194**(3), 1359–1374, doi:10.1093/gji/ggt213.

Green, P., 1995. Reversible jump Markov chain Monte Carlo computation and Bayesian model determination, *Biometrika*, **82**, 711–732.

Green, R. G., Schönfelder, C. S., Shapiro, N., & Koulakov, I., 2020. Magmatic and Sedimentary Structure beneath the Klyuchevskoy Volcanic Group , Kamchatka , From Ambient Noise Tomography, *Journal of Geophysical Research: Solid Earth*, **125**, 1–22, doi:10.1029/2019JB018900.

Griffin, W., Taylor, P., Hakkinen, J., Heier, K., Iden, I., Krogh, E., Malm, O., Olsen, K., Ormaasen, D., & Tveten, E., 1978. Archean and Proterozoic crustal evolution in Lofoten-Vesteralen, N Norway, *Jl geol. Soc. Lond.*, **135**, 629–647.

Griffin, W. L., Doyle, B. J., Ryan, C. G., Pearson, N. J., Reilly, S. Y. O., Davies, R., Kivi, K., van Achterbergh, E., & Natapov, L. M., 1999. Layered Mantle Lithosphere in the Lac de Gras Area, Slave Craton: Composition, Structure and Origin, *Journal of Petrology*, **40**, 705–727.

Griffin, W. L., Natapov, L. M., Reilly, S. Y. O., & Achterbergh, E. V., 2005. The Kharamai kimberlite field , Siberia : Modification of the lithospheric mantle by the Siberian Trap event, *Lithos*, **81**, 167–187, doi:10.1016/j.lithos.2004.10.001.

Grund, M., Mauerberger, A., Ritter, J., & Tilmann, F., 2017. Broadband Recordings for LITHOS-CAPP: LITHOspheric Structure of Caledonian, Archaean and Proterozoic Provinces, Sep. 2014 - Oct. 2016, Sweden and Finland, Tech. rep.

Guggisberg, B., Kaminski, W., & Prodehl, C., 1991. Crustal structure of the Fennoscandian Shield: A traveltime interpretation of the long-range FENNOLORA seismic refraction profile, *Tectonophysics*, **195**, 105–137.

Hastings, W., 1970. Monte Carlo Sampling Methods Using Markov Chains and Their Applications, *Biometrika*, **57**, 97–109, doi:10.2307/2334940.

Hatcher, R. D., 2010. The Appalachian orogen: A brief summary, in *From Rodinia to Pangeo: The Lithotectonic Record of the Appalachian Region*, pp. 1–19, eds Tollo, R., Bartholomew, M., Hibbard, J., & Karabinos, P.

Hay, W. W., Soeding, E., DeConto, R. M., & Wold, C. N., 2002. The Late Cenozoic uplift – climate change paradox, *Int J Earth Sci*, **91**, 746–774, doi:10.1007/s00531-002-0263-1.

Hejrani, B., Balling, N., Jacobsen, B. H., & England, R., 2017. Upper-mantle velocities below the Scandinavian Mountains from P- and S-wave traveltime tomography, *Geophysical Journal International*, **208**(1), 177–192, doi:10.1093/gji/ggw370.

Hendriks, B. W. H. & Andriessen, P. A. M., 2002. Pattern and timing of the post-Caledonian denudation of northern Scandinavia constrained by apatite fission-track thermochronology, in *Exhumation of the North Atlantic Margin: Timing, Mechanisms and Implications for Petroleum Exploration*, vol. 196, pp. 117–137, eds Dore, A. G., Cartwrigth, J. A., Stoker, M. S., Turner, J. P., & White, N., Geological Society, London, Special Publications.

Herrmann, R. B., 2013. Computer programs in seismology: An evolving tool for instruction and research, *Seism. Res. Lettr.*, **84**, 1081–1088, doi:10.1785/0220110096.

Hieronymus, C. F. & Goes, S., 2010. Complex cratonic seismic structure from thermal models of the lithosphere: effects of variations in deep radiogenic heating, *Geophys. J. Int.*, **180**, 999–1012, doi:10.1111/j.1365-246X.2009.04478.x.

Hjelt, S.-E., Korja, T., Kozlovskaya, E., Lahti, I., Yliniemi, J., Bear, & Groups, S. S. T. W., 2006. Electrical conductivity and seismic velocity structures of the lithosphere beneath the Fennoscandian Shield, in *European Lithosphere Dynamics*, vol. 32, pp. 541–559, Geological Society, London, Memoirs.

Högdahl, K., Andersson, U. B., Eklund, O., Gorbatschev, R., Nyström, J.-O., Wikström, A., Sjöström, H., Bergman, S., Ahl, M., Mansfeld, J., Wahlgren, C.-H., Stephens, M. B., Claeson, D. T., Lundqvist, T., Öhlander, B., Smeds, S.-A., & Sundblad, K., 2004. The Transscandinavian Igneous Belt (TIB) in Sweden: a review of its character and evolution, Tech. rep.

Hyvönen, T., Tiira, T., Korja, A., Heikkinen, P., & Rautioaho, E., 2007. A tomographic crustal velocity model of the central Fennoscandian Shield SB OB, *Geophys. J. Int.*, **168**, 1210–1226, doi:10.1111/j.1365-246X.2006.03242.x.

Institute of Seismology University of Helsinki, 1980. The Finnish National Seismic Network. Deutsches GeoForschungsZentrum GFZ. Other/Seismic Network. doi:10.14470/UR044600.

IRIS DMS, 2014. Data Services Products: ASWMS Automated Surface Wave Phase Velocity Measuring System. doi:10.17611/DP/ASWMS.1.

James, D. E., Boyd, F., Schutt, D., Bell, D., & Carlson, R. W., 2004. Xenolith constraints on seismic velocities in the upper mantle beneath southern Africa, *Geochemistry, Geophysics, Geosystems*, **5**, 1–32, doi:10.1029/2003GC000551.

Janik, T., Kozlovskaya, E., Heikkinen, P., Yliniemi, J., & Silvennoinen, H., 2009. Evidence for preservation of crustal root beneath the Proterozoic Lapland-Kola orogen (northern Fennoscandian shield) derived from P and S wave velocity models of POLAR and HUKKA wide-angle reflection and refraction profiles and FIRE4 reflection transec, *Journal of Geophysical Research*, **114**, 1–34, doi:10.1029/2008JB005689.

Japsen, P. & Chalmers, J. A., 2000. Neogene uplift and tectonics around the North Atlantic: overview, *Global and Planetary Change*, **24**, 165–173.

Jin, G. & Gaherty, J. B., 2015. Surface wave phase-velocity tomography based on multichannel cross-correlation, *Geophysical Journal International*, **201**, 1383–1398, doi:10.1093/gji/ggv079.

Kaislaniemi, L. & van Hunen, J., 2014. Dynamics of lithospheric thinning and mantle melting by edge-driven convection: Application to Moroccan Atlas mountains, *Geochemistry, Geophysics, Geosystems*, **15**, 3175–3189, doi:10.1002/2014GC005414.

Kennett, B. L. N., 2006. On seismological reference models and the perceived nature of heterogeneity, *Physics of the Earth and Planetary Interiors*, **159**, 129–139, doi:10.1016/j.pepi.2006.07.006.

King, S. D. & Anderson, D. L., 1995. An alternative mechanism of flood basalt formation, *Earth and Planetary Science Letters*, **136**, 269–279.

King, S. D. & Anderson, D. L., 1998. Edge-driven convection, *Earth and Planetary Science Letters*, **160**, 289–296.

King, S. D. & Ritsema, J., 2000. African Hot Spot Volcanism : Small-Scale Convection in the Upper Mantle Beneath Cratons, *Science*, **290**, 1137–1141.

Köhler, A., Weidle, C., & Maupin, V., 2012. Crustal and uppermost mantle structure of southern Norway: results from surface wave analysis of ambient seismic noise and earthquake data, *Geophysical Journal International*, **191**, 1441–1456, doi:10.1111/j.1365-246X.2012.05698.x.

Köhler, A., Maupin, V., & Balling, N., 2015. Surface wave tomography across the Sorgenfrei-Tornquist Zone, SW Scandinavia, using ambient noise and earthquake data, *Geophysical Journal International*, **203**(1), 284–311, doi:10.1093/gji/ggv297.

Kolstrup, M. L., Pascal, C., & Maupin, V., 2012. What compensates the topography of southern Norway ? Insights from thermo-isostatic modeling, *Journal of Geodynamics*, **61**, 105–119, doi:10.1016/j.jog.2012.03.008.

Kolstrup, M. L., Hung, S.-h., & Maupin, V., 2015. Multiscale, finite-frequency P and S tomography of the upper mantle in the southwestern Fennoscandian Shield, *Geophys. J. Int.*, **202**, 190–218, doi:10.1093/gji/ggv130.

Koptev, A., Cloetingh, S., Burov, E., François, T., & Gerya, T., 2017. Long-distance impact of Iceland plume on Norway's rifted margin, *Nature Scientific Reports*, **7**, 1–11, doi:10.1038/s41598-017-07523-y.

Korja, A., Lahtinen, R., & Nironen, M., 2006. The Svecofennian orogen : a collage of microcontinents and island arcs, in *European Lithosphere Dynamics*, vol. 32, pp. 561–578, eds Gee, D. G. & Stephenson, R. A., Geological Society, London, Memoir.

Kozlovskaya, E. & Poutanen, M., 2006. POLENET/LAPNET. A multi-disciplinary geophysical experiment in northern Fennoscandia during IPY 2007-2008, *Geophys. Res. Abstr.*, **8**.

Kozlovskaya, E., Kosarev, G., Aleshin, I., Riznichenko, O., & Sanina, I., 2008. Structure and composition of the crust and upper mantle of the Archean-Proterozoic boundary in the Fennoscandian shield obtained by joint inversion of receiver function and surface wave phase velocity of recording of the SVEKALAPKO array, *Geophysical Journal International*, **175**(1), 135–152, doi:10.1111/j.1365-246X.2008.03876.x.

Krawczyk, C. M., McCann, T., Cocks, L. R. M., England, R. W., McBride, J. H., & Wybraniec, S., 2008. Caledonian tectonics, in *The Geology of Central Europe. Volume 1: Precambrian and Palaeozoic*, ed. McCann, T., The Geological Society.

Kukkonen, I. T. & Peltonen, P., 1999. Xenolith-controlled geotherm for the central Fennoscandian Shield: Implications for lithosphere-asthenosphere relations, *Tectonophysics*, **304**(4), 301–315, doi:10.1016/S0040-1951(99)00031-1.

Kukkonen, I. T., Kinnunen, K. A., & Peltonen, P., 2003. Mantle xenoliths and thick lithosphere in the Fennoscandian Shield, *Physics and Chemistry of the Earth*, **28**, 349–360, doi:10.1016/S1474-7065(03)00057-3.

Kukkonen, I. T., Kuusisto, M., Lehtonen, M., & Peltonen, P., 2008. Delamination of eclogitized lower crust : Control on the crust–mantle boundary in the central Fennoscandian shield, *Tectonophysics*, **457**, 111–127, doi:10.1016/j.tecto.2008.04.029.

Lahtinen, R. & Huhma, H., 2019. A revised geodynamic model for the Lapland-Kola Orogen, *Precambrian Research*, **330**, 1–19, doi:10.1016/j.precamres.2019.04.022.

Lahtinen, R., Korja, A., & Nironen, M., 2005. Paleoproterozoic tectonic evolution of the Fennoscandian Shield, in *The Precambrian Bedrock of Finland - Key to the Evolution of the Fennoscandian Shield*, pp. 481–532, eds Lehtinen, M., Nurmi, P., & Rämö, O., Elsevier.

Lahtinen, R., Korja, A., Nironen, M., & Heikkinen, P., 2009. Palaeoproterozoic accretionary processes in Fennoscandia, *Geological Society London Special Publications*, **318**, 237–256, doi:10.1144/SP318.8.

Laske, G. & Widmer-Schnidrig, R., 2015. Theory and Observations: Normal Mode and Surface Wave Observations, *Treatise on Geophysics*, pp. 117–167, doi:10.1016/B978-0-444-53802-4.00003-8.

Lebedev, S., Schaeffer, A. J., Fullea, J., & Pease, V., 2018. Seismic tomography of the Arctic region: inferences for the thermal structure and evolution of the lithosphere, in *Circum-Arctic Lithosphere Evolution*, pp. 419–440, eds Pease, V. & Coakley, B., Geological Society, London, Special Publications.

Levshin, A., Yanovskaya, T. B., Lander, A., & Bukchin, B., 1989. *Seismic Surface Waves in Laterally Inhomogeneous Earth*, Kluwer Academic Publishers.

Levshin, A., Ratnikova, L., & Berger, J., 1992. Peculiarities of surface-wave propagation across central Eurasia, *Bulletin of the Seismological Society of America*, **82**(6), 2464–2493, doi:10.1016/0031-9201(83)90119-X.

Li, A. & Burke, K., 2006. Upper mantle structure of southern Africa from Rayleigh wave tomography, *Journal of Geophysical Research: Solid Earth*, **111**(10), 1–16, doi:10.1029/2006JB004321.

Li, A., Fischer, K. M., & Wysession, M. E., 2002. Crust and upper mantle discontinuity structure beneath eastern North America, *Journal of Geophysical Research*, **107**.

Li, X.-d. & Romanowicz, B., 1995. Comparison of global waveform inversions with and without considering cross-branch modal coupling, *Geophys. J. Int.*, **121**, 695–709.

Lidmar-Bergström, K. & Bonow, J. M., 2009. Hypotheses and observations on the origin of the landscape of southern Norway — A comment regarding the isostasy-climate-erosion hypothesis by Nielsen et al. 2008, *Journal of Geodynamics*, **48**, 95–100, doi:10.1016/j.jog.2009.06.003.

Lidmar-Bergström, K., Ollier, C. D., & Sulebak, J. R., 2000. Landforms and uplift history of southern Norway, *Global and Planetary Change*, **24**, 211–231.

Lieser, K., Harris, J., & Storchak, D., 2015. Summary of the Bulletin of the International Seismological Centre, Tech. rep.

Lin, F. C. & Ritzwoller, M. H., 2011a. Apparent anisotropy in inhomogeneous isotropic media, *Geophysical Journal International*, **186**, 1205–1219, doi:10.1111/j.1365-246X.2011.05100.x.

Lin, F. C. & Ritzwoller, M. H., 2011b. Helmholtz surface wave tomography for isotropic and azimuthally anisotropic structure, *Geophysical Journal International*, **186**, 1104–1120, doi:10.1111/j.1365-246X.2011.05070.x.

Lin, F. C., Ritzwoller, M. H., & Snieder, R., 2009. Eikonal tomography: Surface wave tomography by phase front tracking across a regional broad-band seismic array, *Geophysical Journal International*, **177**, 1091–1110, doi:10.1111/j.1365-246X.2009.04105.x.

Lister, G. S., Etheridge, M. A., & Symonds, P. A., 1991. Detachment models for the formation of passive continental margins, *Tectonics*, **10**, 1038–1064.

Lithgow-Bertelloni, C. & Gurnis, M., 1997. Cenozoic subsidence and uplift of continents from time-varying dynamic topography, *Geology*, **25**, 735–738.

Liu, Q. & Gu, Y. J., 2012. Seismic imaging: From classical to adjoint tomography, *Tectonophysics*, **566-567**, 31–66, doi:10.1016/j.tecto.2012.07.006.

Lund, B., Roberts, R., & Smith, C. A., 2017. 2017:35 Review of paleo-, historical and current seismicity in Sweden and surrounding areas with implications for the seismic analysis underlying SKI report 92:3, Tech. rep.

Maggi, A., Debayle, E., Priestley, K., & Barruol, G., 2006. Azimuthal anisotropy of the Pacific region, *Earth and Planetary Science Letters*, **250**, 53–71, doi:10.1016/j.epsl.2006.07.010.

Makushkina, A., Tauzin, B., Tkalćić, H., & Thybo, H., 2019. The Mantle Transition Zone in Fennoscandia: Enigmatic high topography without deep mantle thermal anomaly, *Geophyscial Research Letters*, doi:10.1029/2018GL081742.

Makushkina, A., Tauzin, B., Miller, M., Tkalcic, H., & Thybo, H., 2021. Opening of the north-eastern Atlantic and onshore mountain rise controlled by Fennoscandian deep structure, *Science (in review)*.

Mauerberger, A., Maupin, V., Gudmundsson, O., & Tilmann, F., 2021a. Anomalous azimuthal variations with 360 periodicity of Rayleigh phase velocities observed in Scandinavia, *Geophys. J. Int.*, **224**, 1684–1704, doi:10.1093/gji/ggaa553.

Mauerberger, A., Sadeghisorkhani, H., Maupin, V., Gudmundsson, O., & Tilmann, F., 2021b. A shear-wave velocity model for the Scandinavian lithosphere from Rayleigh waves and ambient noise - Implications for the origin of the topography of the Scandes mountain range, *Tectonophysics, in review*.

Maupin, V., 1985. Partial derivatives of surface wave phase velocities for flat anisotropic models, *Geophys. J. R. astr. Soc.*, **83**, 379–398.

Maupin, V., 1988. Surface waves across 2D structures: a method based on coupled local modes, *Geophysical Journal*, **93**, 173–185, doi:10.1111/j.1365-246X.1988.tb01396.x.

Maupin, V., 1992. Modelling of laterally trapped surface waves with application to Rayleigh waves in the Hawaiian swell, *Geophys. J. Int.*, **110**, 553–570.

Maupin, V., 2001. A multiple-scattering scheme for modelling surface wave propagation in isotropic and anisotropic three-dimensional structures, *Geophys. J. Int.*, **146**, 332–348.

Maupin, V., 2007. Introduction to Mode Coupling Methods for Surface Waves, in *Advances in Geophysics : Advances in Wave Propagation in Heterogeneous Earth*, vol. 48, pp. 127–155, eds Wu Ru-Shan, Maupin, V., & Dmowska, R.

Maupin, V., 2011. Upper-mantle structure in southern Norway from beamforming of Rayleigh wave data presenting multipathing, *Geophysical Journal International*, **185**, 985–1002, doi:10.1111/j.1365-246X.2011.04989.x.

Maupin, V. & Park, J., 2015. Theory and Observations - Seismic Anisotropy, in *Treatise on Geophysics. Volume 1: Deep Earth Seismology*, pp. 277–305, ed. Schubert, G., Elsevier, 2nd edn.

Maupin, V., Agostini, A., Artemieva, I., & al., E., 2013. The deep structure of the Scandes and its relation to tectonic history and present-day topography, *Tectonophysics*, **602**, 15–37, doi:10.1016/j.tecto.2013.03.010.

Medhus, A. B., Balling, N., Jacobsen, B. H., Weidle, C., England, R. W., Kind, R., Thybo, H., & Voss, P., 2012. Upper-mantle structure beneath the Southern Scandes Mountains and the Northern Tornquist Zone revealed by P-wave traveltime tomography, *Geophysical Journal International*, **189**(3), 1315–1334, doi:10.1111/j.1365-246X.2012.05449.x.

Menke, W. & Levin, V., 2002. Anomalous seaward dip of the lithosphere-asthenosphere boundary beneath northeastern USA detected using differential-array measurements of Rayleigh waves, *Geophysical Journal International*, **149**, 413–421, doi:10.1046/j.1365-246X.2002.01652.x.

Menke, W., Skryzalin, P., Levin, V., Harper, T., Darbyshire, F., & Dong, T., 2016. The Northern Appalachian Anomaly: A modern asthenospheric upwelling, *Geophysical Research Letters*, **43**, 173–179, doi:10.1002/2016GL070918.Received.

Metropolis, N., Rosenbluth, A., Rosenbluth, M., & Teller, A., 1953. Equation of State Calculations by Fast Computing Machines, *J. Chem. Phys*, **21**, 1087–1091, doi:10.1063/1.1699114.

Meyer, R., Van Wijk, J., & Gernigon, L., 2007. The North Atlantic Igneous Province: A review of models for its formation, *The Geological Society of America. Special Paper*, **430**, 525–552, doi:10.1130/2007.2430(26).

Milne, G. A., Davis, J. L., Mitrovica, J. X., Scherneck, H., Johansson, J. M., Vermeer, M., & Koivula, H., 2001. Space-Geodetic Constraints on Glacial Isostatic Adjustment in Fennoscandia, *Science*, **291**(March), 2381–2386.

Mints, M. V., Glaznev, V. N., Muravina, O. M., & Yu, E., 2020. 3D model of Svecofennian Accretionary Orogen and Karelia Craton based on geology, reflection seismics, magnetotellurics and density modelling: Geodynamic speculations, *Geoscience Frontiers*, **11**, 999–1023, doi:10.1016/j.gsf.2019.10.003.

Mjelde, R., Sellevoll, M. A., Shimamura, H., Iwasaki, T., & Kanazawa, T., 1995. Swave anisotropy off Lofoten, Norway, indicative of fluids in the lower continental crust?, *Geophysical Journal International*, **120**, 87–96, doi:10.1111/j.1365-246X.1995.tb05912.x.

Mjelde, R., Kasahara, J., Shimamura, H., Kamimura, A., & Kanazawa, T., 2002. Lower crustal seismic velocity-anomalies; magmatic underplating or serpentinized peridotite? Evidence from the Voring Margin, NE Atlantic, *Marine Geophysical Researches*, **23**, 169–183.

Montagner, J.-P. & Nataf, H.-C., 1986. A simple method for inverting the azimuthal anisotropy of surface waves, *Journal of Geophysical Research*, **91**, 511–520.

Neumann, E.-R., Wilson, M., Heeremans, M., Spencer, E. A., Obst, K., Timmerman, M., & Kirstein, L., 2004. Carboniferous-Permian rifting and magmatism in southern Scandinavia, the North Sea and northern Germany: a review, in *Permo-Carboniferous Magmatism and Rifting in Europe*, vol. 223, pp. 11–40.

Nielsen, S., Paulsen, G., Hansen, D., Gemmer, L., Clausen, O., Jacobsen, B., Balling, N., Huuse, M., & Gallagher, K., 2002. Paleocene initiation of Cenozoic uplift in Norway, in *Exhumation of the North Atlantic Margin: Timing, Mechanisms and Implications for Petroleum Exploration*, vol. 196, pp. 45–65, Geological Society, London, Special Publications.

Nielsen, S. B., Gallagher, K., Egholm, D. L., Clausen, O. R., & Summerfield, M., 2009a. REPLY TO COMMENT, *Journal of Geodynamics*, **48**, 101–106, doi:10.1016/j.jog.2009.06.004.

Nielsen, S. B., Gallagher, K., Leighton, C., Balling, N., Svenningsen, L., Jacobsen, B. H., Thomsen, E., Nielsen, O. B., Heilmann-Clausen, C., Egholm, D. L., Summerfield, M. a., Clausen, O. R., Piotrowski, J. a., Thorsen, M. R., Huuse, M., Abrahamsen, N., King, C., & Lykke-Andersen, H., 2009b. The evolution of western Scandinavian topography: A review of Neogene uplift versus the ICE (isostasy–climate–erosion) hypothesis, *Journal of Geodynamics*, **47**, 72–95, doi:10.1016/j.jog.2008.09.001.

Nironen, M., 1997. The Svecofennian Orogen : a tectonic model, *Precambrian Research*, **86**, 21–44.

Nolet, G. & Dahlen, F. A., 2000. Wave front healing and the evolution of seismic delay times, *Journal of Geophysical Research*, **105**, 19043–19054.

NORSAR, 1971. NORSAR Station Network (Data set). doi:10.21348/d.no.0001.

Olesen, O., Torsvik, T. H., Tveten, E., Zwaan, K. B., Løseth, H., & Henningsen, T., 1997. Basement structure of the continental margin in the Lofoten-Lopphavet area, northern Norway: constraints from potential field data , on-land structural mapping and palaeomagnetic data, *Norsk Geologisk Tidsskrift*, **77**, 15–30.

Olesen, O., Brönner, M., Ebbing, J., Gellein, J., Gernigon, L., Koziel, J., Lauritsen, T., Myklebust, R., Pascal, C., Sand, M., Solheim, D., & Usov, S., 2010. New aeromagnetic and gravity compilations from Norway and adjacent areas: methods and applications, in *Petroleum Geology: From Mature Basins to New Frontiers – Proceedings of the 7th Petroleum Geology Conference*, pp. 559–586, eds Vining, B. & Pickering, S.

Park, C. B., Miller, R. D., & Xia, J., 1998. Imaging dispersion curves of surface waves on multi-channel record, *SEG Expanded Abstracts*.

Pascal, C. & Olesen, O., 2009. Are the Norwegian mountains compensated by a mantle thermal anomaly at depth?, *Tectonophysics*, **475**, 160–168, doi:10.1016/j.tecto.2009.01.015.

Pavlis, N. K., Holmes, S. A., Kenyon, S. C., & Factor, J. K., 2008. An Earth Gravitational Model to Degree 2160: EGM2008., in *EGU General Assembly 2008, Vienna, Austria*.

Pedersen, H. A., Bruneton, M., & Maupin, V., 2006. Lithospheric and sublithospheric anisotropy beneath the Baltic shield from surface-wave array analysis, *Earth and Planetary Science Letters*, **244**, 590–605, doi:10.1016/j.epsl.2006.02.009.

Pedersen, H. A., Fishwick, S., & Snyder, D. B., 2009. Lithos A comparison of cratonic roots through consistent analysis of seismic surface waves, *LITHOS*, **109**, 81–95, doi:10.1016/j.lithos.2008.09.016.

Pedersen, H. A., Debayle, E., Maupin, V., Kozlovskaya, E., Jämsen, T., Silvennoinen, H., Hurskainen, R., Pedersen, H., Pequegnat, C., Achauer, U., Plomerova, J., Kissling, E., Sanina, I., Bodvarsson, R., Aleshin, I., Bourova, E., Brückl, E., Guiguet, T. E. R., Hausmann, H., Heikkinen, P., Houseman, G., Jedlicka, P., Johnsen, H., Kremenetskaya, E., Komminaho, K., Munzarova, H., Roberts, R., Ruzek, B., Shomali, H., Schweitzer, J., Shaumyan, A., Vecsey, L., & Volosov, S., 2013. Strong lateral variations of lithospheric mantle beneath cratons - Example from the Baltic Shield, *Earth and Planetary Science Letters*, **383**, 164–172, doi:10.1016/j.epsl.2013.09.024.

Pedersen, H. A., Boué, P., Poli, P., & Colombi, A., 2015. Arrival angle anomalies of Rayleigh waves observed at a broadband array: A systematic study based on earthquake data, full waveform simulations and noise correlations, *Geophysical Journal International*, **203**, 1626–1641, doi:10.1093/gji/ggv382.

Peterson, J., 1993. Observations and Modeling of Seismic Background Noise, Tech. rep., USGS.

Pilidou, S., Priestley, K., Debayle, E., & Gudmundsson, O., 2005. Rayleigh wave tomography in the North Atlantic: high resolution images of the Iceland, Azores and Eifel mantle plumes, *Lithos*, **79**, 453–474, doi:10.1016/j.lithos.2004.09.012.

Praeg, D., Stoker, M. S., Shannon, P. M., Ceramicola, S., Hjelstuen, B., Laberg, J., & Mathiesen, A., 2005. Episodic Cenozoic tectonism and the development of the NW

European ‘ passive ’ continental margin, *Marine and Petroleum Geology*, **22**, 1007–1030, doi:10.1016/j.marpetgeo.2005.03.014.

Prieto, G. A., Lawrence, J. F., & Beroza, G. C., 2009. Anelastic Earth structure from the coherency of the ambient seismic field, *Journal of Geophysical Research*, **114**, 1–15, doi:10.1029/2008JB006067.

Prindle, K. & Tanimoto, T., 2006. Teleseismic surface wave study for S-wave velocity structure under an array: Southern California, *Geophys. J. Int.*, **166**, 601–621, doi:10.1111/j.1365-246X.2006.02947.x.

Rawlinson, N., Fichtner, A., Sambridge, M., & Young, M. K., 2014. Seismic Tomography and the Assessment of Uncertainty, *Advances in Geophysics*, **55**, 1–76, doi:10.1016/bs.agph.2014.08.001.

Rawlinson, N., Davies, D. R., & Pilia, S., 2017. The mechanisms underpinning Cenozoic intraplate volcanism in eastern Australia: Insights from seismic tomography and geodynamicmodeling, *Geophyscial Research Letters*, **44**, 1–10, doi:10.1002/2017GL074911.

Rickers, F., Fichtner, A., & Trampert, J., 2013. The Iceland – Jan Mayen plume system and its impact on mantle dynamics in the North Atlantic region : Evidence from full-waveform inversion, *Earth and Planetary Science Letters*, **367**, 39–51, doi:10.1016/j.epsl.2013.02.022.

Riis, F., 1996. Quantification of Cenozoic vertical movements of Scandinavia by correlation of morphological surfaces with offshore data, *Global and Planetary Change*, **12**, 331–357.

Rindraharisaona, E., Tilmann, F., Yuan, X., Dreiling, J., Giese, J., Priestley, K., & Rümpker, G., 2021. Velocity structure and radial anisotropy of the lithosphere in southern Madagascar from surface wave dispersion, *Geophys. J. Int.*, **224**, 1930–1944, doi:10.1093/gji/ggaa550.

Roberts, D., 2003. The Scandinavian Caledonides: Event chronology, palaeogeographic settings and likely modern analogues, *Tectonophysics*, **365**(1-4), 283–299, doi:10.1016/S0040-1951(03)00026-X.

Roberts, D. & Siedlecka, A., 2002. Timanian orogenic deformation along the northeastern margin of Baltica, Northwest Russia and Northeast Norway, and Avalonian–Cadomian connections, *Tectonophysics*, **352**, 169–184.

Rohrman, M. & van der Beek, P., 1996. Cenozoic postrift domal uplift of North Atlantic margins: An asthenospheric diapirism model, *Geology*, **24**(October), 901–904.

Romanowicz, B., 2002. 11 Inversion of surface waves: A review, *International Geophysics*, **81**(PART A), 149–173, doi:10.1016/S0074-6142(02)80214-5.

Ruan, Y., Lei, W., Modrak, R., Orsvuran, R., Bozda, E., & Laboratoire, G., 2019. Balancing unevenly distributed data in seismic tomography: a global adjoint tomography example, *Geophys. J. Int.*, **219**, 1225–1236, doi:10.1093/gji/ggz356.

Rychert, C. A. & Fischer, K. M., 2007. P-to-S and S-to-P imaging of a sharp lithosphere-asthenosphere boundary beneath eastern North America, *Journal of Geophysical Research*, **112**, 1–21, doi:10.1029/2006JB004619.

Sabra, K. G., Gerstoft, P., Roux, P., Kuperman, W. A., & Fehler, M. C., 2005. Extracting time-domain Green’s function estimates from ambient seismic noise, *Geophysical Research Letters*, **32**(3), 1–5, doi:10.1029/2004GL021862.

Sadeghisorkhani, H., Gudmundsson, O., Roberts, R., & Tryggvason, A., 2016. Mapping the source distribution of microseisms using noise covariogram envelopes, *Geophysical Journal International*, **205**(3), 1473–1491, doi:10.1093/gji/ggw092.

Sadeghisorkhani, H., Gudmundsson, O., & Tryggvason, A., 2018. GSpecDisp: A matlab GUI package for phase-velocity dispersion measurements from ambient-noise correlations, *Computers \& Geosciences*, **110**, 41–53, doi:10.1016/j.cageo.2017.09.006.

Sadeghisorkhani, H., Gudmundsson, O., Li, K. L., Tryggvason, A., Lund, B., & Högdahl, K., 2021. Shear-wave structure of southern Sweden from precise phase-velocity measurements of ambient-noise data, *Geophys. J. Int.*, **225**, 494–511, doi:10.1093/gji/ggaa598.

Sambridge, M., 2014. A Parallel Tempering algorithm for probabilistic sampling and multimodal optimization, *Geophys. J. Int.*, **196**, 357–374, doi:10.1093/gji/ggt342.

Sambridge, M. & Mosegaard, K., 2002. MONTE CARLO METHODS IN GEOPHYSICAL INVERSE PROBLEMS, *Reviews of Geophysics*, **40**, 1–29, doi:10.1029/2000RG00089.

Sandoval, S., Kissling, E., Ansorge, J., & Group, S. S. T. W., 2003. High-resolution body wave tomography beneath the SVEKALAPKO array : I . A priori three-dimensional crustal model and associated traveltime effects on teleseismic wave fronts Sen en Sandoval , Edi Kissling , J org Ansorge and the SVEKALAPKO Seismic, *Geophys. J. Int.*, **153**, 75–87.

Sandoval, S., Kissling, E., & Ansorge, J., 2004. High-resolution body wave tomography beneath the SVEKALAPKO array - II. Anomalous upper mantle structure beneath the central Baltic Shield, *Geophysical Journal International*, **157**(1), 200–214, doi:10.1111/j.1365-246X.2004.02131.x.

Schaeffer, A. & Lebedev, S., 2013. Global shear speed structure of the upper mantle and transition zone, *Geophys. J. Int.*, **194**, 417–449, doi:10.1093/gji/ggt095.

Schmandt, B. & Lin, F.-C., 2014. P and S wave tomography of the mantle beneath the United States, *Geophyscial Research Letters*, **41**, 6342–6349, doi:10.1002/2014GL061231.Received.

Schoonman, C. M., White, N. J., & Pritchard, D., 2017. Radial viscous fingering of hot asthenosphere within the Icelandic plume beneath the North Atlantic Ocean, *Earth and Planetary Science Letters*, **468**, 51–61, doi:10.1016/j.epsl.2017.03.036.

Selway, K., Ford, H., & Kelemen, P., 2015. The seismic mid-lithosphere discontinuity, *Earth and Planetary Science Letters*, **414**, 45–57, doi:10.1016/j.epsl.2014.12.029.

Shapiro, N., Campillo, M., & Roux, P., 2011. *Encyclopedia of Solid Earth Geophysics: Seismic imaging using ambient noise*.

Shomali, Z. H., Roberts, R. G., Pedersen, L. B., & Group, T. W., 2006. Lithospheric structure of the Tornquist Zone resolved by nonlinear P and S teleseismic tomography along the TOR array, *Tectonophysics*, **416**, 133–149, doi:10.1016/j.tecto.2005.11.019.

Silvennoinen, H., Kozlovskaya, E., Kissling, E., Kosarev, G., Pedersen, H., Plomerova, J., Achauer, U., Sanina, I., Teppo, J., Pequegnat, C., Hurskainen, R., Guiguet, R., Hausmann, H., Jedlicka, P., Aleshin, I., Bourova, E., Bodvarsson, R., Evald, B., Eken, T., Heikkinen, P., Houseman, G., Johnsen, H., Kremenetskaya, E., Komminaho, K., Munzarova, H., Roberts, R., Ruzek, B., Shomali, H., Schweitzer, J., Shaumyan, A., Vecsey, L., & Volosov, S., 2014. A new Moho boundary map for the northern Fennoscandian Shield based on combined controlled-source seismic and receiver function data, *GeoResJ*, **1-2**, 19–32, doi:10.1016/j.grj.2014.03.001.

Silvennoinen, H., Kozlovskaya, E., & Kissling, E., 2016. POLENET/LAPNET teleseismic P wave travel time tomography model of the upper mantle beneath northern Fennoscandia, *Solid Earth*, **7**, 425–439, doi:10.5194/se-7-425-2016.

Sisson, S., 2005. Transdimensional Markov chains: A decade of progress and future perspectives, *J. Am. Stat. Assoc.*, **100**, 1077–1090.

Slagstad, T., Roberts, N. M. W., & Kulakov, E., 2017. Linking orogenesis across a supercontinent ; the Grenvillian and Sveconorwegian margins on Rodinia, *Gondwana Research*, **44**, 109–115, doi:10.1016/j.gr.2016.12.007.

Slagstad, T., Ganerød, M., Kulakov, E., Kirkland, C. L., & Roberts, N. M. W., 2019. Breaking the Grenville – Sveconorwegian link in Rodinia reconstructions, *Terra Nova*, pp. 430–437, doi:10.1111/ter.12406.

Smelror, M., Dehls, J., Ebbing, J., & al., E., 2007. Towards a 4D topographic view of the Norwegian sea margin, *Global and Planetary Change*, **58**, 382–410, doi:10.1016/j.gloplacha.2006.12.005.

Smith, A., 1991. Bayesian computational methods, *Philos. Trans. R. Soc.A.*, **337**, 369–386.

Smith, M. L. & Dahlen, F. A., 1973. The azimuthal dependence of Love and Rayleigh wave propagation in a slightly anisotropic medium, *Journal of Geophysical Research*, **78**, 3321–3333, doi:10.1029/JB078i017p03321.

Snieder, R., 1986. 3-D linearized scattering of surface waves and a formalism for surface wave holography, *Geophys. J. R. astr. Soc.*, **84**, 581–605.

Snieder, R., 2002. SCATTERING OF SURFACE WAVES, in *Scattering and Inverse Scattering in Pure and Applied Science*, chap. Chapter 1., pp. 562–577, eds Pike, R. & Sabatier, P., Academic Press, San Diego.

Snieder, R. & Lomax, A., 1996. Wavefield smoothing and the effect of rough velocity perturbations on arrival times and amplitudes, *Geophys. J. Int.*, **125**, 796–812.

Snieder, R. & Wapenaar, K., 2010. Imaging with ambient noise, *Physics Today*, **63**(9), 44–49, doi:10.1063/1.3490500.

SNSN, 1904. Swedish National Seismic Network. Uppsala University, Uppsala, Sweden. doi:10.18159/SNSN.

Sodankylä Geophysical Observatory University of Oulu, 2005. Northern Finland Seismic Network.

Soomro, R. A., Weidle, C., Cristiano, L., Lebedev, S., Meier, T., & Group, P. W., 2016. Phase velocities ofRayleigh and Love waves in central and northern Europe from automated, broad-band, interstation measurements, *Geophys. J. Int.*, **504**, 517–534, doi:10.1093/gji/ggv462.

Spetzler, J., Trampert, J., & Snieder, R., 2002. The effect of scattering in surface wave tomography, *Geophys. J. Int.*, **149**, 755–767.

Stehly, L., Campillo, M., & Shapiro, N. M., 2006. A study of the seismic noise from its long-range correlation properties, *Journal of Geophysical Research*, **111**, 1–12, doi:10.1029/2005JB004237.

Stein, S. & Wysession, M., 2003. *An Introduction to Seismology, Earthquakes, and Earth Structure*, Blackwell Publishing.

Steltenpohl, M., Hames, W., Andresen, A., & Markl, G., 2003. New Caledonian eclogite province in Norway and potential Laurentian (Taconic) and Baltic links, *Geology*, **31**(11), 985–988, doi:10.1130/G19744.1.

Steltenpohl, M. G., Kassos, G., Andresen, A., Rehnström, E. F., & Hames, W. E., 2011a. Eclogitization and exhumation of Caledonian continental basement in Lofoten , North Norway, *Geosphere*, **7**(January), 1–17, doi:10.1130/GES00573.1.

Steltenpohl, M. G., Moecher, D., Andresen, A., Ball, J., Mager, S., & Hames, W. E., 2011b. The Eidsfjord shear zone, Lofoten-Vesteralen, north Norway: An Early Devonian,

paleoseismogenic low-angle normal fault, *Journal of Structural Geology*, **33**, 1023–1043, doi:10.1016/j.jsg.2011.01.017.

Stewart, J. & Watts, A., 1997. Gravity anomalies and spatial variations of flexural rigidity at mountain ranges, *Journal of Geophysical Research*, **102**, 5327–5352, doi:10.1029/96JB03664.

Stratford, W. & Thybo, H., 2011. Seismic structure and composition of the crust beneath the southern Scandes, Norway, *Tectonophysics*, **502**, 364–382, doi:10.1016/j.tecto.2011.02.008.

Stratford, W., Thybo, H., Faleide, J. I., Olesen, O., & Tryggvason, A., 2009. New Moho Map for onshore southern Norway, *Geophys. J. Int.*, **178**, 1755–1765, doi:10.1111/j.1365-246X.2009.04240.x.

Svenningsen, L., Balling, N., Jacobsen, B. H., Kind, R., Wylegalla, K., & Schweitzer, J., 2007. Crustal root beneath the highlands of southern Norway resolved by teleseismic receiver functions, *Geophys. J. Int.*, **170**, 1129–1138, doi:10.1111/j.1365-246X.2007.03402.x.

Takenaka, H., Tanaka, H., Okamoto, T., & Kennett, B. L. N., 2003. Quasi-cylindrical 2.5D wave modeling for large-scale seismic surveys, *Geophysical Research Letters*, **30**, 1–4, doi:10.1029/2003GL018068.

Tanimoto, T. & Prindle, K., 2007. Surface wave analysis with beamforming, *Earth Planets Space*, **59**, 453–458.

Tappe, S., Smart, K., Torsvik, T., Massuyeau, M., & de Wit, M., 2018. Geodynamics of kimberlites on a cooling Earth: Clues to plate tectonic evolution and deep volatile cycles, *Earth and Planetary Science Letters*, **484**, 1–14.

Tarantola, A. & Valette, B., 1982. Generalized Nonlinear Inverse Problems Solved Using the Least Squares Criterion, *Reviews of Geophysics and Space Physics*, **20**, 219–232.

Thomas, W. A., 2006. Tectonic inheritance at a continental margin, *GSA Today*, **16**, 4–11, doi:10.1130/1052-5173(2006)016.

Thurber, C. & Ritsema, J., 2015. Theory and Observations - Seismic Tomography and Inverse Methods, in *Treatise on Geophysics*, chap. 1.10, pp. 307–337.

Thybo, H., 2006. The heterogeneous upper mantle low velocity zone, *Tectonophysics*, **416**, 53–79, doi:10.1016/j.tecto.2005.11.021.

Thybo, H., Balling, N., Maupin, V., Ritter, J. R. R., & Tilmann, F., 2012. ScanArray Core (1G 2012-2017). The ScanArray consortium. doi:10.14470/6T569239.

Thybo, H., Bulut, N., Grund, M., Mauerberger, A., Makushkina, A., Artemieva, I., Balling, N., Gudmundsson, O., Maupin, V., Ottemoller, L., Ritter, J., & Tilmann, F., 2021. ScanArray – A broad band seismological experiment in the Baltic Shield, *Seism. Res. Lettr.*, pp. 1–13, doi:10.1785/0220210015.

Till, C. B., Tanton, L. T. E., & Fischer, K. M., 2010. A mechanism for low extent melts at the lithosphere asthenosphere boundary, *Geochemistry, Geophysics, Geosystems*, **11**(10), 1–22, doi:10.1029/2010GC003234.

Tilmann, F., Sadeghisorkhani, H., & Mauerberger, A., 2020. Another look at the treatment of data uncertainty in Markov chain Monte Carlo inversion and other probabilistic methods, *Geophys. J. Int.*, **222**, 388–405, doi:10.1093/gji/ggaa168.

University of Bergen, 1982. University of Bergen Seismic Network (Data set). doi:10.7914/SN/NS.

Vagnes, E. & Amundsen, H. E. F., 1993. Late Cenozoic Uplift and Volcanism on Spitsbergen : Caused by Mantle Convection?, *Geology*, **21**, 251–254, doi:10.1130/0091-7613(1993)021¡0251.

van der Lee, S., 2002. High-resolution estimates of lithospheric thickness from Missouri to Massachusetts , USA, *Earth and Planetary Science Letters*, **203**, 15–23.

van Wijk, J. W., Lawrence, J. F., & Driscoll, N. W., 2008. Formation of the Transantarctic Mountains related to extension of the West Antarctic Rift system, *Tectonophysics*, **458**, 117–126, doi:10.1016/j.tecto.2008.03.009.

Veikkolainen, T., Kukkonen, I. T., & Tiira, T., 2017. Heat flow, seismic cut-off depth and thermal modeling of the Fennoscandian Shield, *Geophysical Journal International*, **211**(3), 1414–1427, doi:10.1093/gji/ggx373.

Vestøl, O., Ågren, J., Steffen, H., Kierulf, H., & Tarasov, L., 2019. NKG2016LU: a new land uplift model for Fennoscandia and the Baltic Region, *Journal of Geodesy*, **93**(9), 1759–1779, doi:10.1007/s00190-019-01280-8.

Vinnik, L., Kozlovskaya, E., Oreshin, S., Kosarev, G., Piiponen, K., & Silvennoinen, H., 2016. The lithosphere, LAB, LVZ and Lehmann discontinuity under central Fennoscandia from receiver functions, *Tectonophysics*, **667**, 189–198, doi:10.1016/j.tecto.2015.11.024.

Wang, H. & Currie, C. A., 2015. Magmatic expressions of continental lithosphere removal, *Journal of Geophysical Research: Solid Earth*, **120**, 7239–7260, doi:10.1002/2015JB012112.

Wang, H., van Hunen, J., & Pearson, D., 2015. The thinning of subcontinental lithosphere: The roles of plume impact and metasomatic weakening, *Geochemistry, Geophysics, Geosystems*, **16**, 1156–1171, doi:10.1002/2015GC005784.Received.

Wawerzinek, B., Ritter, J., & Roy, C., 2013. New constraints on the 3D shear wave velocity structure of the upper mantle underneath Southern Scandinavia revealed from non-linear tomography, *Tectonophysics*, **602**, 38–54, doi:10.1016/j.tecto.2012.12.033.

Weidle, C. & Maupin, V., 2008. An upper-mantle S -wave velocity model for Northern Europe from Love and Rayleigh group velocities, *Geophys. J. Int.*, **175**, 1154–1168, doi:10.1111/j.1365-246X.2008.03957.x.

Weidle, C., Maupin, V., Ritter, J., Kvaerna, T., Schweitzer, J., Balling, N., Thybo, H., Faleide, J. I., & Wenzel, F., 2010. MAGNUS–A Seismological Broadband Experiment to Resolve Crustal and Upper Mantle Structure beneath the Southern Scandes Mountains in Norway, *Seismological Research Letters*, **81**, 76–84, doi:10.1785/gssrl.81.1.76.

Wielandt, E., 1993. Propagation and structural interpretation of non-plane waves, *Geophys. J. Int.*, **113**, 45–53.

Wijk, J. W. V., Baldridge, W. S., Hunen, J. V., Goes, S., Aster, R., Coblentz, D. D., Grand, S. P., & Ni, J., 2010. Small-scale convection at the edge of the Colorado Plateau: Implications for topography, magmatism, and evolution of Proterozoic lithosphere, *Geology*, **38**(7), 611–614, doi:10.1130/G31031.1.

Woodhouse, J. H. & Dziewonski, A. M., 1984. Mapping the Upper Mantle: Three-Dimensional Modeling of Earth Structure by Inversion of Seismic Waveforms, *Journal of Geophysical Research*, **89**, 5953–5986.

Yakovlev, A. V., Bushenkova, N. A., Koulakov, I. Y., & Dobretsov, N. L., 2012. Structure of the upper mantle in the Circum-Arctic region from regional seismic tomography, *Russian Geology and Geophysics*, **53**, 963–971.

Yang, Y. & Forsyth, D. W., 2006a. Rayleigh wave phase velocities, small-scale convection, and azimuthal anisotropy beneath southern California, *Journal of Geophysical Research: Solid Earth*, **111**(7), 1–20, doi:10.1029/2005JB004180.

Yang, Y. & Forsyth, D. W., 2006b. Regional tomographic inversion of the amplitude and phase of Rayleigh waves with 2-D sensitivity kernels, *Geophysical Journal International*, **166**(3), 1148–1160, doi:10.1109/TIM.2006.876410.

Zhang, X., Curtis, A., Galetti, E., & Ridder, S. D., 2018. 3-D Monte Carlo surface wave tomography, *Geophys. J. Int.*, **215**, 1644–1658, doi:10.1093/gji/ggy362.

Zhao, D., 2019. Importance of later phases in seismic tomography, *Physics of the Earth and Planetary Interiors*, **296**, 106314, doi:10.1016/j.pepi.2019.106314.

Zhou, Y., Dahlen, F. A., & Nolet, G., 2004. Three-dimensional sensitivity kernels for surface wave observables, *Geophys. J. Int.*, **158**, 142–168, doi:10.1111/j.1365-246X.2004.02324.x.

Zhou, Y., Dahlen, F. A., Nolet, G., & Laske, G., 2005. Finite-frequency effects in global surface-wave tomography, *Geophys. J. Int.*, **163**, 1087–1111, doi:10.1111/j.1365-246X.2005.02780.x.

Zwaan, K. B., 1995. Geology of the West Troms Basement Complex, northern Norway, with emphasis on the Senja Shear Belt: a preliminary account, *NGU - Bull*, **427**, 33–36.

Appendix A

Data

A.1 Data availability

Beside the ScanArray Core and SNSN networks which I have stored in the GEOFON archive, I needed to collect many additional data (Fig. 1.1) from different sources.

Some stations were only available on the ftp server of the University of Bergen and had to be downloaded separately: HE.KIF, NS.HAMF, NO.ARA0, NO.ARE0 and NO.JETT. Stations NS.TBLU, NS.NSS, NO.NB201, IU.KONO and IU.KEV have been requested from the ODC. Further stations of the Finnish permanent network HE were provided upon personal request by the University of Helsinki: KEV, VRF, TOF, KU6, OUF, KEF, KAF, FIA1 and VJF. Data from the SCANLIPS3D network were provided by the University of Leicester upon personal request. The NEONOR2D network is available for the ScanArray partners and could be downloaded from GEOFON. Finally, the permanent stations MSF, OUL, RNF, SGF from the Finnish FN network are available on GEOFON as well as some other HE stations as HEF, JOF, MEF, RAF, SUF and VAF.

Note that in the meantime most of the additional data were bundled and uniformly stored. The entire HE network is now available on GEOFON. The NS and NO stations can be now requested from ODC. Most of the ScanArray Core are already open, and the remaining restricted stations will be opened shortly.

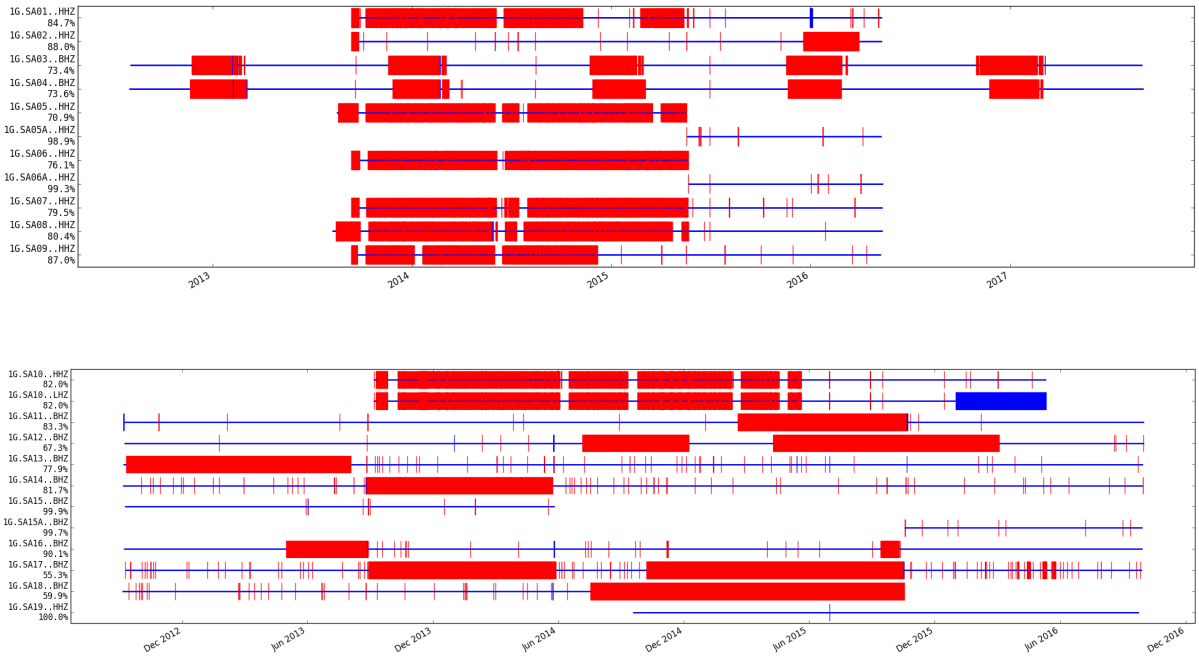

Fig. A.1: Overview of the operational times of the ScanArray Core stations SA0x–SA1x. Note the different time scales. Gaps are plotted as vertical red lines, blue vertical lines indicate overlaps.

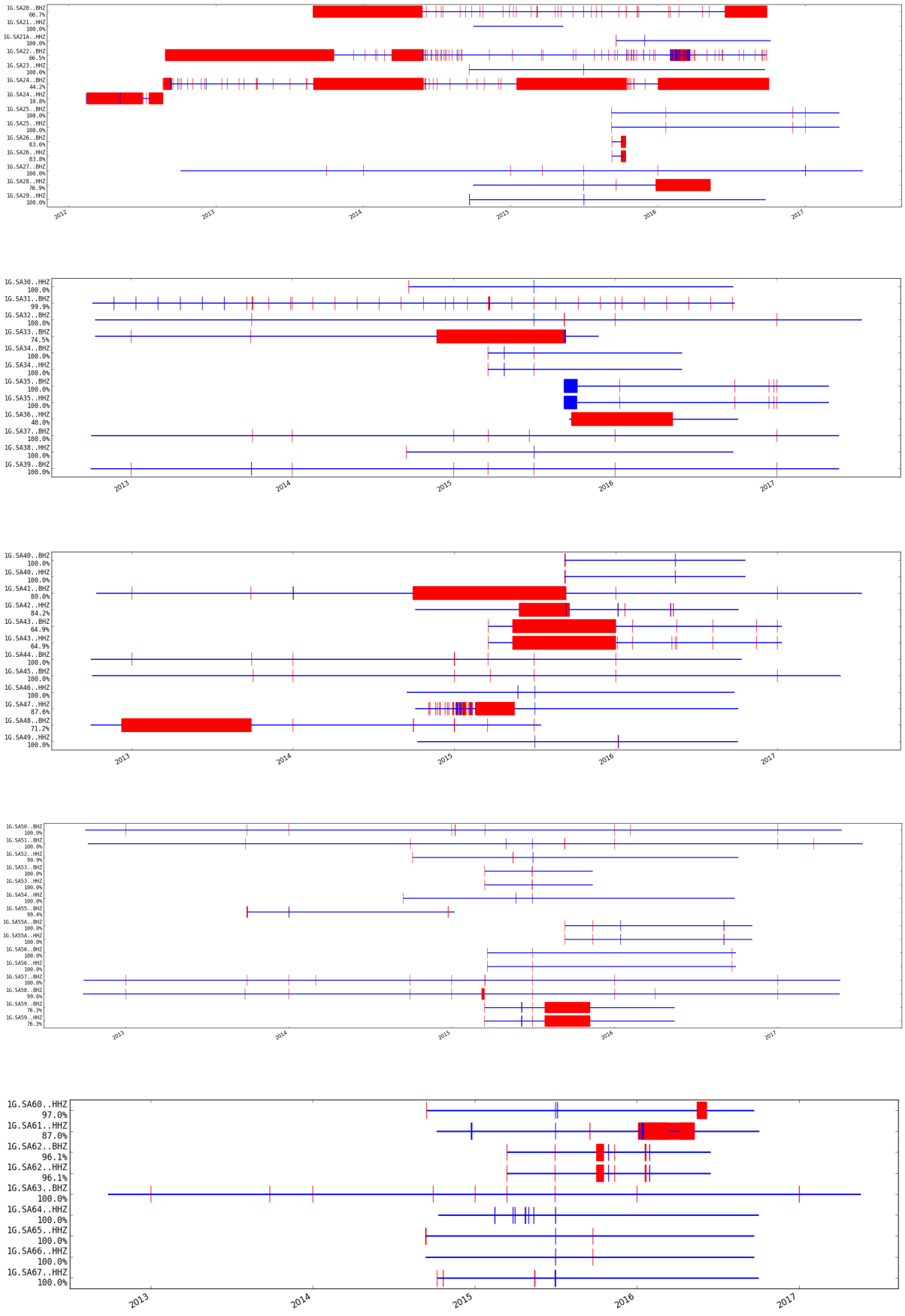

Fig. A.1 (cont.)**:** Overview of the operational times of the ScanArray Core stations SA2x–SA6x. Note the different time scales. Gaps are plotted as vertical red lines, blue vertical lines indicate overlaps.

A.2 ScanArray Core station information

Station	Operation	Latitude (deg)	Longitude (deg)	Elevation (m)	Location		Sensor	Feature
SA01	UiO	71.1111	25.8170	37	Skarsvaag,	Norway	STS2.5	
SA02	UiO	71.0638	28.2417	32	Gamvik,	Norway	STS2.5	time offset
SA03	KU	70.5034	29.0668	272	Monteret,	Norway	STS2	
SA04	KU	70.3192	25.4769	71	Etableret,	Norway	STS2	
SA05	UiO	70.2840	31.0083	38	Kiberg,	Norway	STS2.5	replaced by SA05A
SA05A	UiO	70.3712	31.0994	31	Vardo,	Norway		
SA06	UiO	70.1343	20.7599	41	Lauksletta,	Norway	STS2.5	replaced by SA06A
SA06A	UiO	70.0378	20.9731	77	Skjervoy,	Norway		
SA07	UiO	70.1272	23.3737	32	Kviby,	Norway	STS2.5	
SA08	UiO	69.7642	22.0623	39	Loekvik,	Norway	STS2.5	
SA09	UiO	69.4536	30.0391	64	Svanvik,	Norway	STS2.5	time offset
SA10	UiO	69.2007	25.6916	186	Mareveadji,	Norway	STS2.5	
SA11	AU	69.1321	18.0496	6	Skoelva,	Norway	CMG-3 EX	
SA12	AU	68.9731	18.9144	39	Kirkesdal,	Norway	CMG-3 EX	
SA13	AU	68.3491	18.8369	382	Abisko,	Sweden	CMG-3 TD	
SA14	AU	67.6962	21.6242	248	Vittangi,	Sweden	CMG-3 TD	anomalous time offset, not used
SA15	AU	67.4746	18.3647	383	Fiskflyg,	Sweden	CMG-3 EX	
SA15A	AU	67.4746	18.3647	383	Fiskflyg,	Sweden	CMG-3 TD	
SA16	AU	67.1517	21.0775	334	Sjungberget,	Sweden	CMG-3 TD	anomalous time offset, not used
SA17	AU	66.9529	17.7264	335	Kvikkjokk,	Sweden	CMG-3 TD	
SA18	AU	66.7393	23.5642	173	Rovakka,	Sweden	CMG-3 TD	
SA19	GFZ+KIT	66.5654	22.1788	178	Ertspaen,	Sweden	Trillium 120	
SA20	AU	66.4298	19.6862	380	Jokkmokk,	Sweden	CMG-3 TD	
SA21	GFZ+KIT	66.0406	25.0304	79	Tervola,	Finland	G3ESPC	flooded, replaced by SA21A
SA21A	GFZ+KIT	66.0405	25.0295	79	Tervola,	Finland	G3ESPC	misorientation
SA22	AU	66.0382	17.8591	498	Silverhatten,	Sweden	CMG-3TD	
SA23	GFZ+KIT	65.9263	20.3008	115	Bredsel,	Sweden	G3ESPC	
SA24	AU	65.7356	20.9542	58	Nynaes,	Sweden	CMG-3 TD	
SA25	KU	65.6723	14.2249	0	Hattfjelldal,	Norway	Trillium 240	
SA26	KU	65.6992	12.4383	0	Vevelstad,	Norway	Trillium 240	
SA27	KU	65.4823	15.8965	0	Slussfors,	Sweden	STS2	
SA28	GFZ+KIT	65.4469	27.5106	172	Pudasjaervi,	Finland	Trillium 240	
SA29	GFZ+KIT	65.2879	19.8452	346	Lilltraesk,	Sweden	Trillium 240	
SA30	GFZ+KIT	65.0923	21.4977	6	Jaevrebodarna,	Sweden	G3ESPC	
SA31	KU	64.9911	18.5011	0	Bjoerksele,	Sweden	STS2	

SA32	KU	64.9876	13.5813	0	Limingen,	Norway	STS2	
SA33	KU	64.9033	10.8499	0	Roervik,	Norway	STS2	
SA34	KU	64.8318	15.0313	0	Borgafjaell,	Sweden	Trillium 240	
SA35	KU	64.5340	12.4007	0	Grong,	Norway	Trillium 240	
SA36	GFZ+KIT	64.4402	24.5172	51	Pyhajoki,	Finland	Trillium 120	Only 5 months recordings, misorientation
SA37	KU	64.2467	16.8178	0	Asele,	Sweden	STS2	
SA38	GFZ+KIT	64.1291	19.0003	236	Oertraesk,	Sweden	G3ESPC	
SA39	KU	64.0718	14.0906	0	Valsjoebyn,	Sweden	STS2	
SA40	KU	64.0435	11.3353	0	Steinkjer,	Norway	Trillium 240	
SA41	KU	63.9665	10.2317	0	Afjord,	Norway	STS2	
SA42	GFZ+KIT	63.8265	23.0079	1	Palmantie,	Finland	G3ESPC	
SA43	KU	63.8166	15.5148	0	Tullingsas,	Sweden	Trillium 240	
SA44	KU	63.7052	12.3484	0	Jaerpen,	Sweden	STS2	
SA45	KU	63.5492	19.3658	0	Lagdea,	Sweden	STS2	
SA46	GFZ+KIT	63.4896	18.0945	140	Bredbyn,	Sweden	Trillium 120	
SA47	GFZ+KIT	63.3596	23.9733	106	Pulkkinen,	Finland	G3ESPC	
SA48	KU	63.2305	13.6780	0	Moersil,	Sweden	STS2	
SA49	GFZ+KIT	63.1749	21.2788	6	Soedra Vallgrund,	Finland	G3ESPC	
SA50	KU	63.1140	16.3224	0	Hammarstrand,	Sweden	STS2	
SA51	KU	63.0441	11.6437	0	Tydal,	Norway	STS2	
SA52	GFZ+KIT	62.9381	22.4878	20	Pelmaa,	Finland	Trillium 240	misorientation
SA53	KU	62.8005	13.0527	0	Storsjoekapell,	Sweden	Trillium 240	
SA54	GFZ+KIT	62.7504	18.1489	13	Hemsoen,	Sweden	Trillium 240	
SA55	KU	62.7191	10.0396	0	Innset,	Norway	STS2	replaced by SA55A
SA55A	KU	63.2978	10.0584	78	Eggkleiva,	Norway	Trillium 240	
SA56	KU	62.4859	16.3087	0	Torpshammer,	Sweden	Trillium 240	
SA57	KU	62.4494	14.9213	0	Oeverturingen,	Sweden	STS2	
SA58	KU	61.9449	12.5534	0	Idre,	Sweden	STS2	
SA59	KU	61.8654	14.1203	0	Lillhaerdal,	Sweden	Trillium 240	
SA60	GFZ+KIT	61.6930	17.3794	15	Arnevikon,	Sweden	G3ESPC	
SA61	GFZ+KIT	61.5934	21.4622	2	Maentykallo,	Finland	Trillium 120	
SA62	KU	61.3839	15.5116	0	Voxnabruk,	Sweden	Trillium 240	
SA63	KU	61.1340	13.9566	0	Aelvdalen,	Sweden	STS2	
SA64	GFZ+KIT	61.0537	25.0399	123	Lammi,	Finland	Trillium 240	
SA65	GFZ+KIT	61.0535	15.7699	99	Svabensverk,	Sweden	G3ESPC	
SA66	GFZ+KIT	60.4468	14.7806	239	Bjoerbo,	Sweden	Trillium 120	
SA67	GFZ+KIT	60.4159	22.4439	45	Tuorla,	Finland	G3ESPC	

Fig. A.2: List of all ScanArray Core stations including the type of sensor and the operational institution. UiO = University of Oslo, KU = Copenhagen University, AU = Aarhus University.

Appendix B

Supplementary for chapter 4

B.1 Supplementary material to paper I

The wave propagation movie provided by Mauerberger et al. (2021a) can be accessed via doi:10.1093/gji/ggaa553.

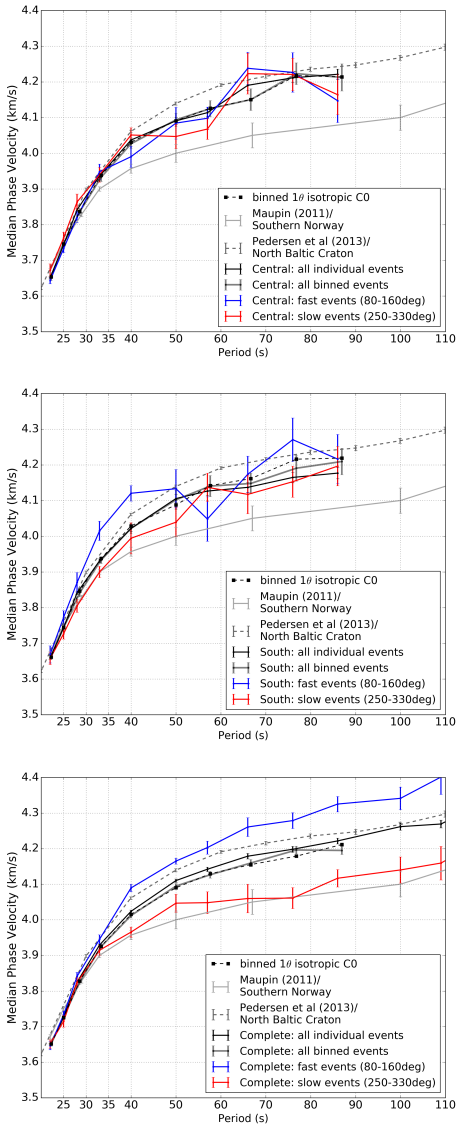

Fig. B.1: Dispersion curves for the other sub-arrays as shown in Fig. 7. From top to bottom: central, south and complete sub-array. The solid black curves show the median over all individual events used for beamforming where the solid dark grey lines give the median over all binned measurements. The blue and the red curves are the median over the events from the fast (between 80 ° and 160°) and slow (between 250 ° and 330°) observed directions, respectively. For comparison, also the median dispersion curves for southern Norway from (Maupin, 2011) and for northern Finland (LAPNET network) (Pedersen et al., 2013) are shown. The isotropic phase velocities resultant from fitting the coefficients in eq. 4.4 are shown as dashed line.

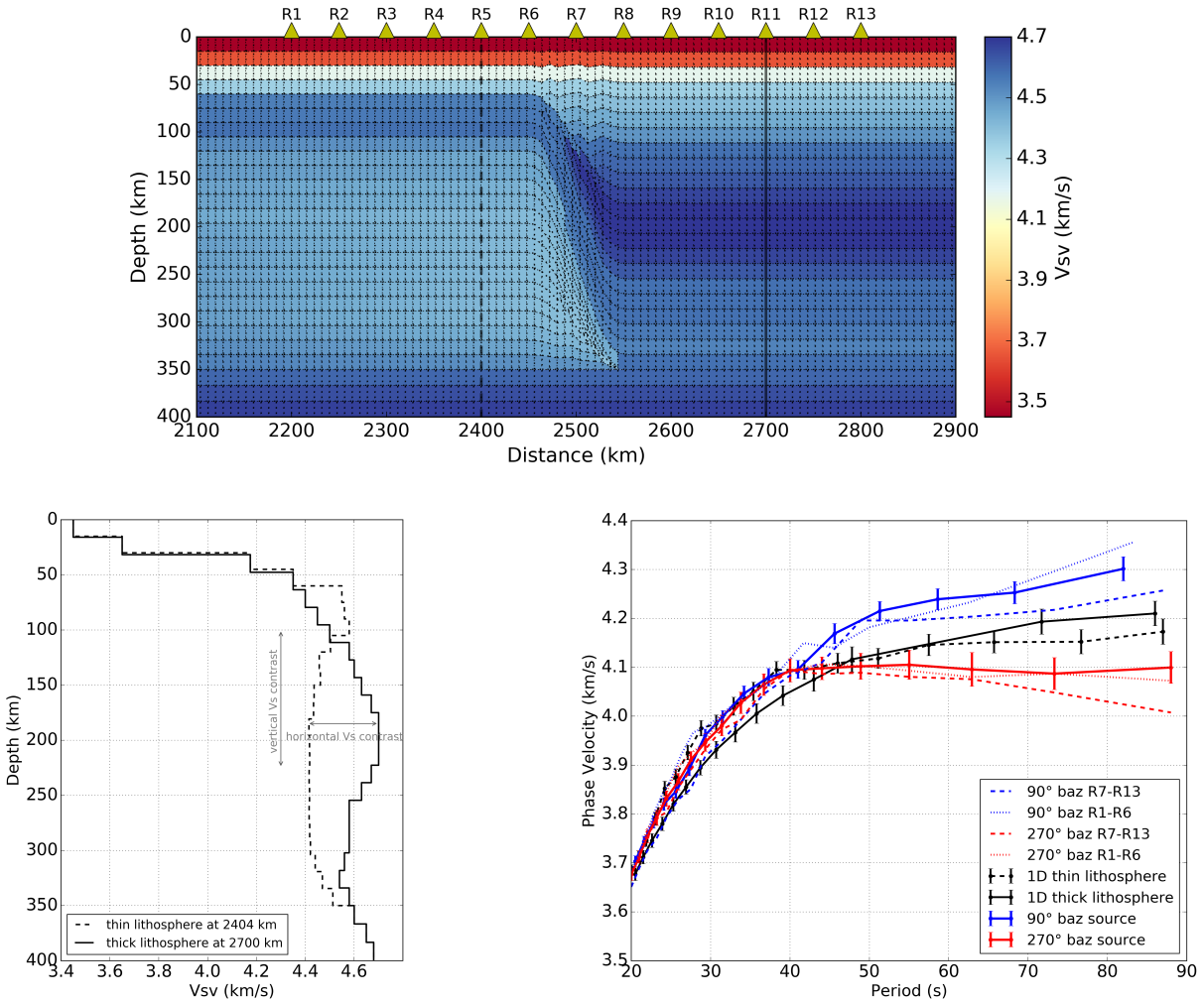

Fig. B.2: Top: Synthetic 2D model 90° baz source, zoomed around the lithosphere step and similar to Fig. 4.9c but with different shallow lithosphere structure. Yellow triangles across the lithospheric step are the receivers. The 270° baz source model is similar. Lower left: Shear wave velocity with depth for the thin lithosphere at 2404 km distance (dashed line, left step side) and thick lithosphere at 2700 km distance (solid line, right step side). Both profiles are marked in the top model. Lower right: Phase velocity dispersion curves retrieved from the models shown above. The thin and thick lithosphere dispersion curves result from 1D reference models with velocity models shown in the left figure. For the model with the source to the right (90°) much higher velocities are obtained for periods > 45 s. The left source (270°) model results in significantly lowered velocities which is in agreement with our data observations shown in Fig. 4.7.

B.2 Cross-validation of beamforming

To cross validate the exceptional findings of a 360° periodicity of the phase velocities (chapter 4, below as referred as Maupin method), a different beamforming method was tested. I only compare the results from the Central and North sub-arrays where the 1θ variation was absent and strongest, respectively. Thereby, I adopted the frequency-domain slant-stacking method by Park et al. (1998) with modifications by Rindraharisaona et al. (2021) (referred to as Park method) to determine the phase velocity. An example is illustrated in Fig. B.3. All stations

within one sub-array have been phase shifted (i.e. aligned) by applying a transfer function $T_n(\omega)$

$$T_n(\omega) = \exp\Big(i\, k_0(\omega)(d_{ref} - d_n)\Big) \tag{B.1}$$

with respect to the farthest station of distance d_{ref} for each event (Fig. B.3a). d_n is the epicentral distance of each station n, i is the unit imaginary number and $k_0(\omega)$ is the wavenumber of the signal with

$$k_0(\omega) = \frac{\omega}{c_0(\omega)} \tag{B.2}$$

An initial phase velocity dispersion curve $c_0(\omega)$ is necessary and was taken from Bruneton et al. (2004a) (see Fig. B.4). In the frequency domain, the transfer function $T_n(\omega)$ is multiplied by the original seismogram $S_n(\omega)$ to be transferred recorded by station n.

$$S'_n(\omega, k_0) = T_n(\omega) \times S_n(\omega) \tag{B.3}$$

$S'_n(\omega, k_0)$ is then the transferred seismogram at a given frequency ω. The phase velocity results from determining the differential wavenumber δk between the seismograms where

$$\delta k = \frac{\omega}{c} - \frac{\omega}{c_0} \tag{B.4}$$

The new wavenumber k can be expressed as the original wavenumber k_0 shifted by a differential wavenumber δk which is related to the phase shift between the seismograms.

$$k = k_0 + \delta_k \tag{B.5}$$

After applying the transfer function (i.e. the phase shift predicted by the reference dispersion curve) to each station n, the slant-stacking technique stacks the amplitude along the wavenumber. This beam of all N stations is defined as

$$B(\omega, \delta k) = \sum_{n=1}^{N} S'_n(\omega, k_0)\, \exp(i\delta k(d_{ref} - d_n)) \tag{B.6}$$

with $\delta k(d_{ref} - d_n)$ being the true differential phase. Assuming great circle path propagation $S_n(\omega, k_0)$ can be written as

$$S_n(\omega, k) = S'_n(\omega, k_0)\, \exp(-i\delta k_{true}(d_{ref} - d_n)) \tag{B.7}$$

where eq. B.6 becomes

$$B(\omega, \delta k) = \sum_{n=1}^{N} S'_n(\omega, k_0)\, \exp(-i\delta k_{true}(d_{ref} - d_n))\, \exp(i\delta k(d_{ref} - d_n)) \tag{B.8}$$

From a grid search over δk at each frequency ω the values of δk_{true} are found as the maximum amplitude (Fig. B.3b). At this beam value, δk equals δk_{true} and the corresponding terms in eq. B.8 cancel each other. Equation B.8 is similar to Maupin (2011) eq. 1. To determine the phase velocity from the slowness plane, two stations are cross-correlated in the frequency domain (Fig. B.3c and d).

Fig. B.4 compares the dispersion curves resultant from the Maupin method (chapter 4) and

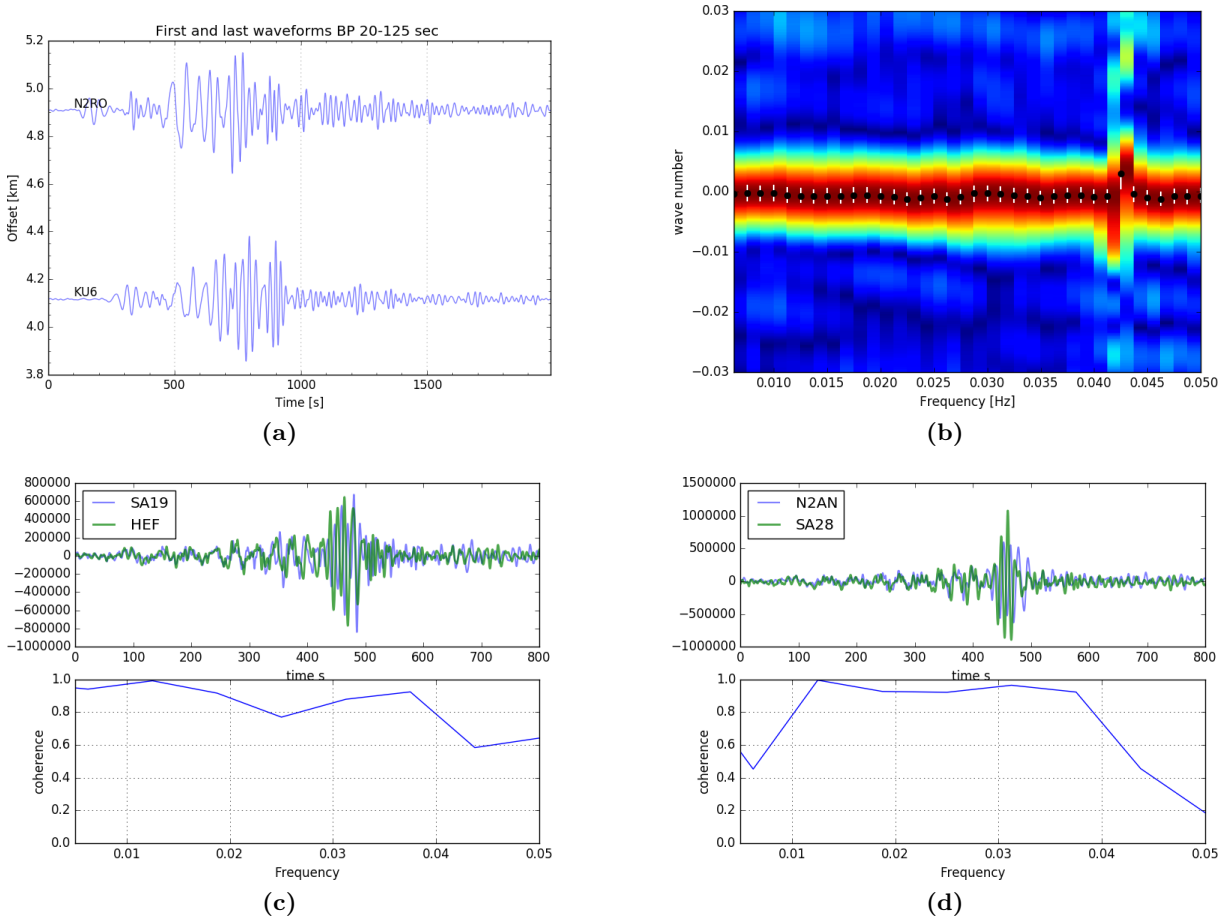

Fig. B.3: Illustration of the beamforming method after the Park method for the 2015/12/07 07:50 event measured from the North sub-array. (a) shows the transferred nearest station (KU6) with respect to the original record at the farthest station (N2RO) for the starting model. (b) is the amplitude of the beam in the frequency-δk plane from which δk_{true} is measured. Black dots mark the automatically picked values where the beam has its maximum. White bars show the 98% interval around the maximum beam. (c) and (d) demonstrates the coherence of two station pairs.

the Park method for the 2015/12/07 07:50 event with 100° baz. Both beamforming methods give consistent results. The phase velocities measured from the North sub-array are clearly higher for periods >35 s compared to the Central sub-array where the values vary around the reference curve.

Fig. B.5 shows the phase velocities as a function of baz and epicentral distance for the Central and North sub-arrays at 40 s. For a better comparison, the results from the Maupin method (Fig. 4.6 of chapter 4) are overlain. The significant 1θ phase velocity variation with baz for the North sub-array is in good agreement with the results shown in Fig. 4.6b and c. No 1θ variation with azimuth is seen for the Central sub-array. Conclusively, this comparison reinforces the exceptional azimuthal variation in northern and southern Scandinavia whereas this feature is absent in the central region.

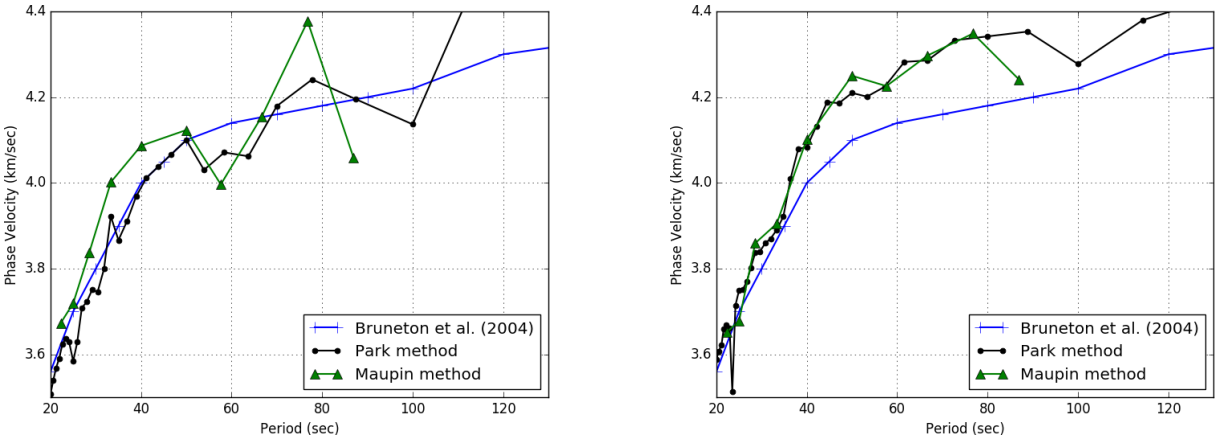

(a) Central sub-array **(b)** North sub-array

Fig. B.4: Comparison of the dispersion curves obtained from the Maupin (green lines) and Park (black lines) methods for an event from 2015/12/07 07:50 with an average distance of 42° and 100° baz measured from the Central (a) and North (b) sub-arrays, respectively. The blue line shows the reference curve from (Bruneton et al., 2004a).

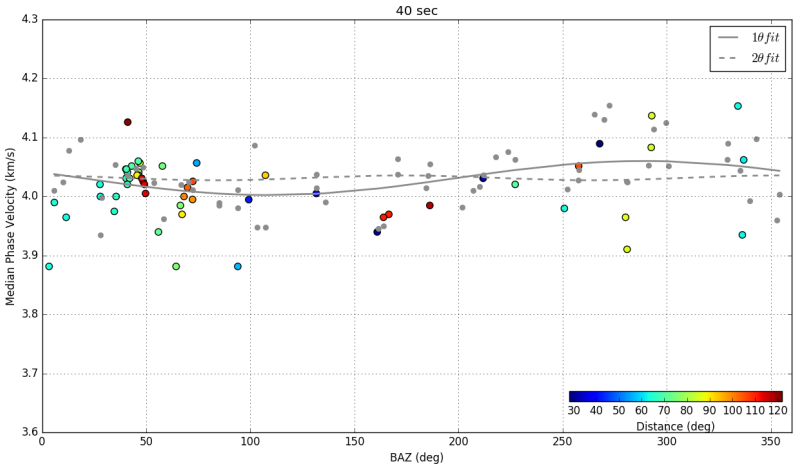

(a) Central sub-array

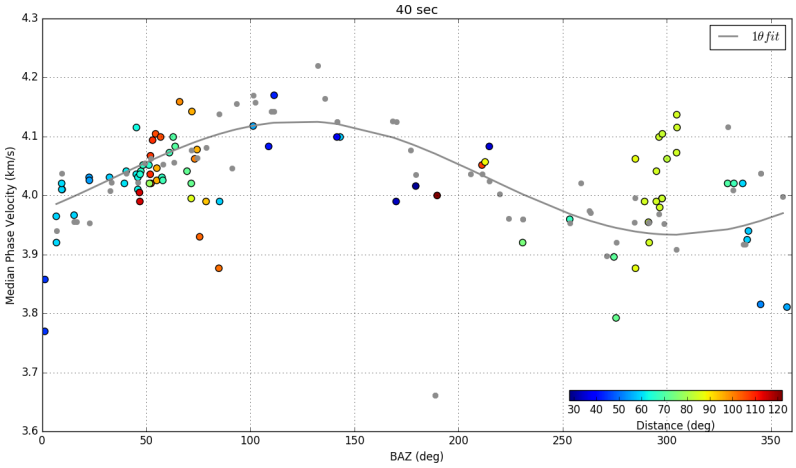

(b) North sub-array

Fig. B.5: Phase velocities as function of predicted backazimuth resulting from the beamforming processing after the Park method for the Central (a) and North (b) sub-arrays at a period of 40 s, respectively. The measurements for each event are shown, color-coded by the epicentral distance. Grey dots are the binned median phase velocities after the Maupin method and the grey lines show the corresponding 1θ and 2θ fits from Fig. 4.6 of chapter 4.

Appendix C

Supplementary for chapter 5

C.1 Supplementary material to paper II

Supplement to section 5.5.2: Ambient noise dispersion curve measurement

Inter-station phase-velocity measurements were obtained from the ZZ correlation traces using an automatic version of the software package *GSpecDisp* by Sadeghisorkhani et al. (2018). Their method follows Ekström et al. (2009) and converts the cross-correlations into the frequency-domain. Path average phase velocities are retrieved from matching the real part of the spectrum to the exact Bessel function at the respective zero crossings, where the zeroth-order Bessel function is used for the ZZ component. Since no far-field condition (inter-station distance > 3 wavelengths) is necessary, phase velocities can be measured up to a period corresponding to an inter-station distance of only one wavelength (Ekström et al., 2009). Both the acausal and causal noise signals are combined for the calculation in our study. The automatic picker uses a reference curve to pick the correct branch (to resolve the 2π ambiguity) at long periods and progresses to shorter periods for each of the single noise correlations. The reference curve is the average dispersion curve determined from the frequency and offset dependent coherency functions, following Prieto et al. (2009). The same method has been used by Sadeghisorkhani et al. (2021) in southern Sweden.

We used a subset of ∼15,800 cross-correlations (excluding some permanent stations in southern Norway) to estimate the reference dispersion curve used for all subsequent measurements. The automatic picker mainly relies on a gradient-based smoothness criterion with respect to the reference curve and other criteria to prevent picking of unrealistic dispersion values. In addition to the smoothness constraint, we chose to pick those dispersion points that (i) correspond to inter-station distances that are between 1.5 and 30 wavelengths, (ii) deviate less than 5% from the reference curve or less than 1.5 cycles, (iii) and where the amplitudes of the real-part spectrum are larger than 25% of the maximum amplitude at all other periods, which is analogous to an SNR constraint (see appendix of Sadeghisorkhani et al., 2018). Note that we set the minimum wavelength to 1.5 since shorter wavelength are likely to introduce complexities at the zero-crossings that cannot be resolved by the automatic picker. To avoid outlier picks, the algorithm predicts the next zero-crossing based on the previously picked dispersion point. If the deviation from the predicted value is too large, this dispersion point is skipped. If violation of this criterion occurs too often (e.g., more 15% of the total number of zero crossings) for a cross-correlation, all picked dispersion points for that cross-correlation are discarded. Furthermore, if less than 20% of all zero crossings are picked, the picks of that path are deleted. The thresholds have been selected based on experiences on our data set. Finally, we manually re-picked cross-correlations from the Lofoten region after initial 2D tomography tests indicated very low phase velocities at short periods in this area. such that the reference curve may not have been suitable for this region and these periods.

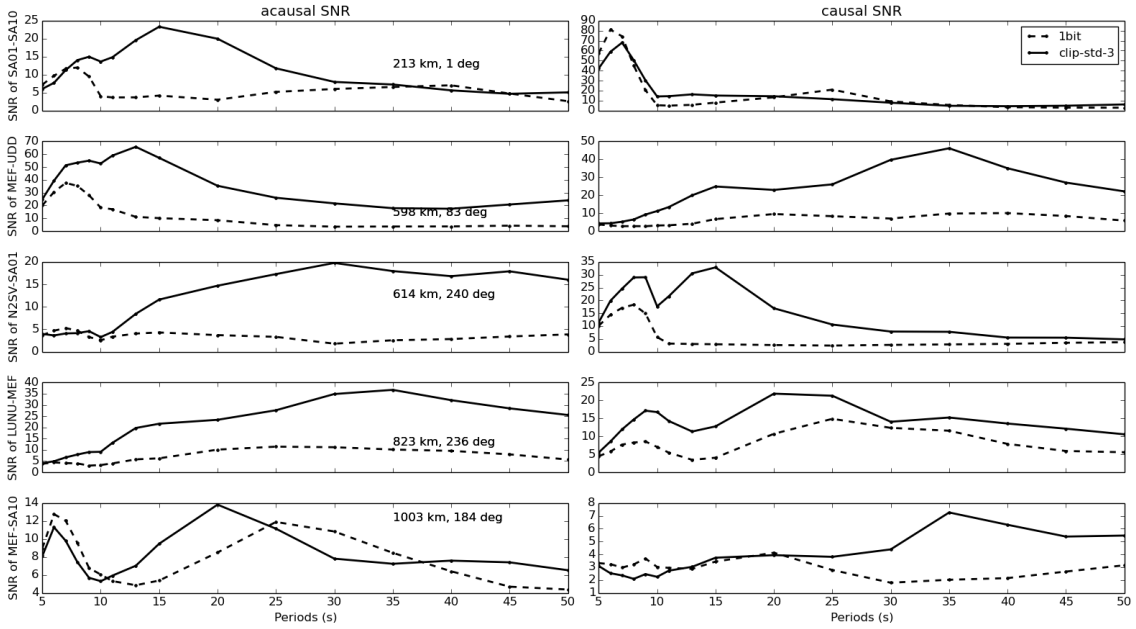

Fig. C.1: SNR vs period for 1-bit (dashed line) and clipping (solid line) time-domain normalizations for five represntative station pairs covering a range of inter-station distances. The SNR is calculated from time windows as shown in Fig. C.3. The acausal and causal part of the correlograms is shown on the left and right panels, respectively. Note the different y-axis scales.

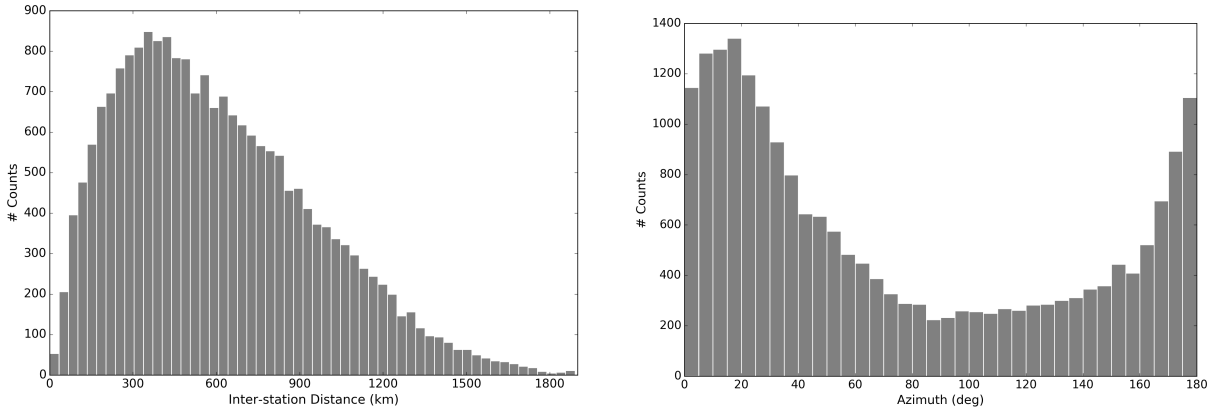

Fig. C.2: Histograms of the inter-station distance and azimuth distribution of the 20,847 correlated station pairs.

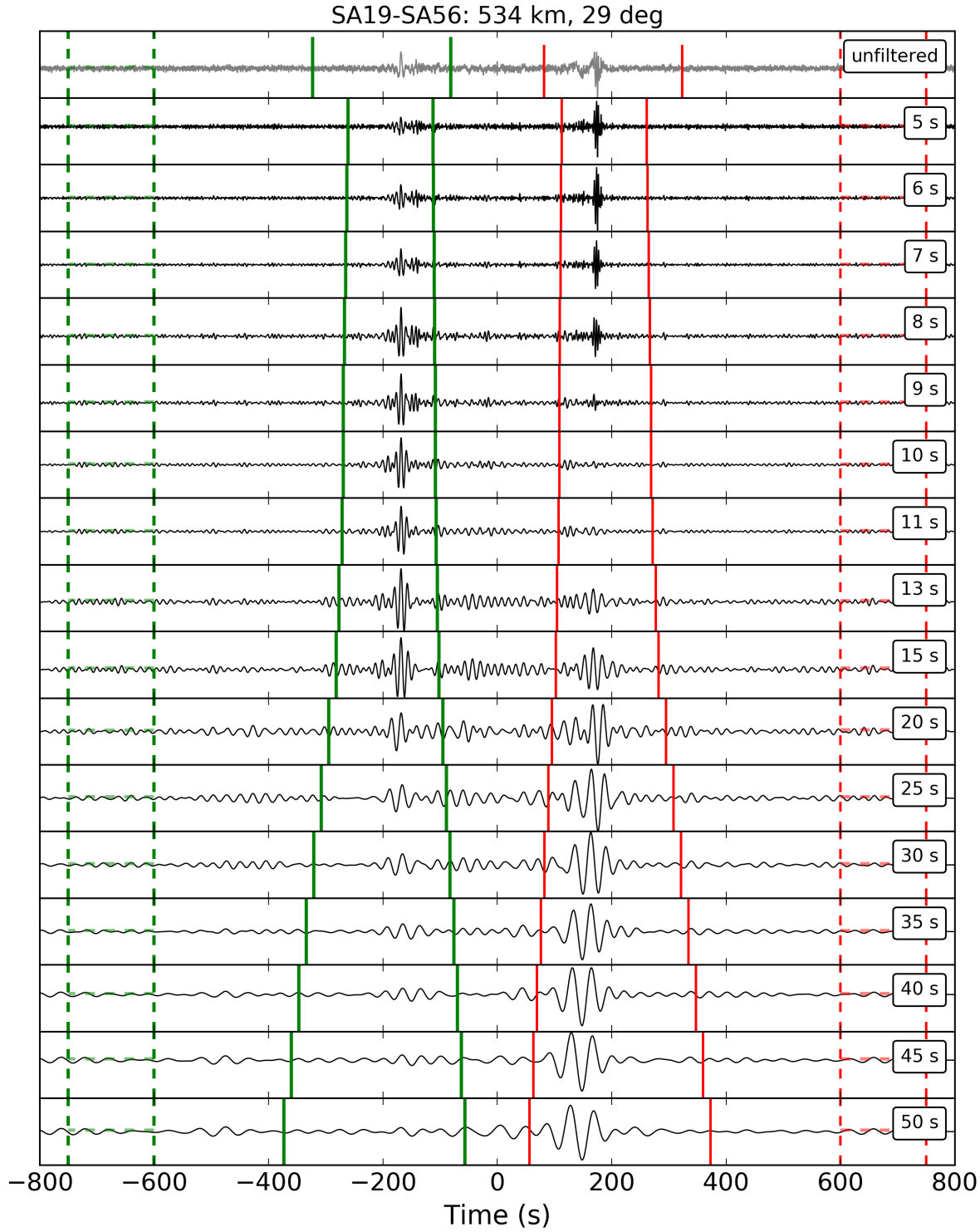

Fig. C.3: Correlogram of station pair SA19-SA56 which was filtered with a series of narrow band-pass filters around the center period labeled on the right side. Top panel shows the unfiltered signal. To account for the large inter-station distances, we used a total cut length of 1,600 s for both the causal and acausal leg. Time windows used for the calculation of the signal-to-noise ratio (SNR), after Bensen et al. (2007), are marked in green and red for the acausal and causal leg, respectively. Solid lines refer to the signal window and dashed lines to the noise window. In most of our station pairs the maximum signal amplitude changes from one time leg to the other at a period around 15 s and 20 s.

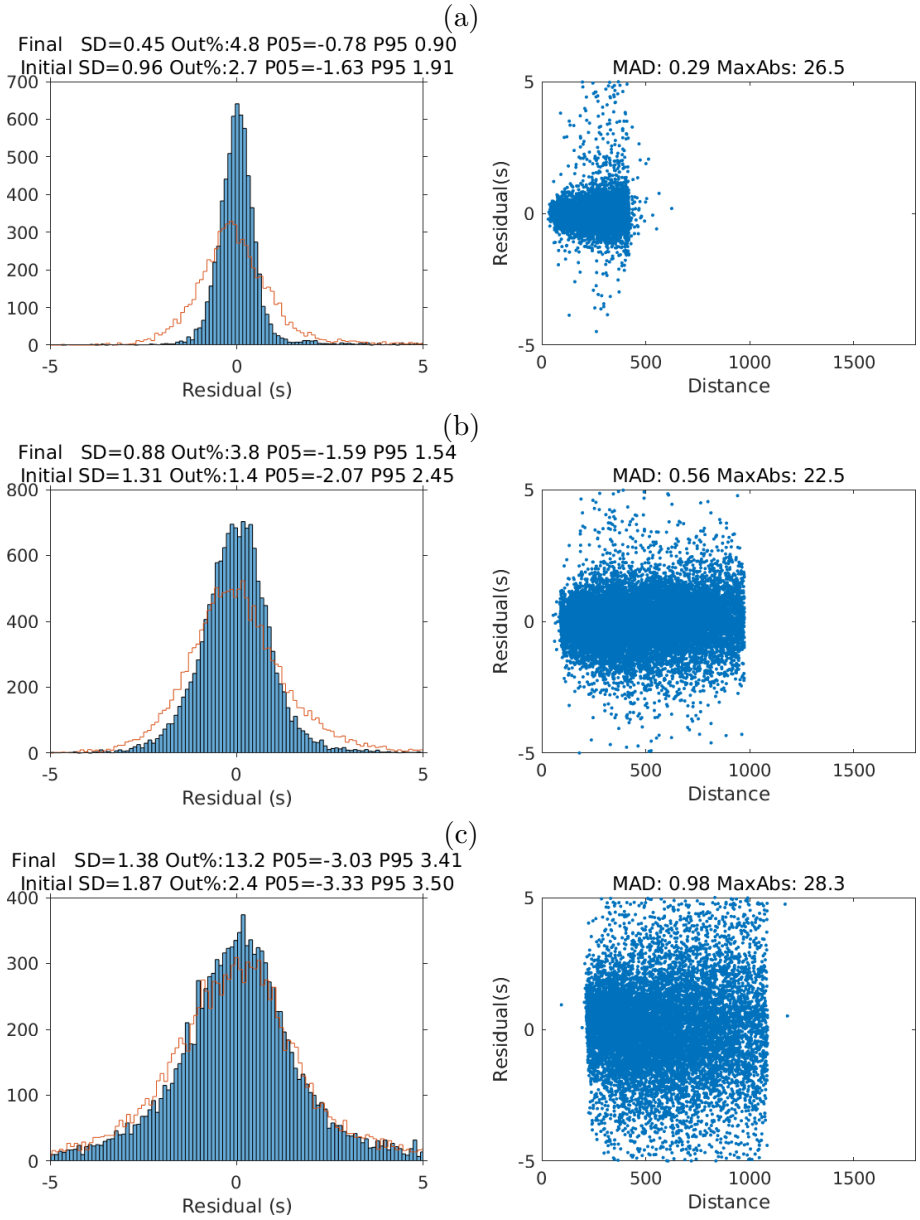

Fig. C.4: Residual histograms of the ambient noise phase arrival times at (a) 5 s, (b) 14 s and (c) 30 s, corresponding to the phase velocity maps shown in Fig. 5.5. The blue histogram gives the residuals relative to the 2D model and the red histogram shows the residuals relative to an uniform velocity background model. Out% denotes the outlier fraction, and P05 and P95 the 5% and 95% percentiles, respectively. On the right, the corresponding scatter plot of residuals vs. inter-station distance is shown. The median absolute deviation (MAD) and the largest absolute value (MaxAbs) are given.

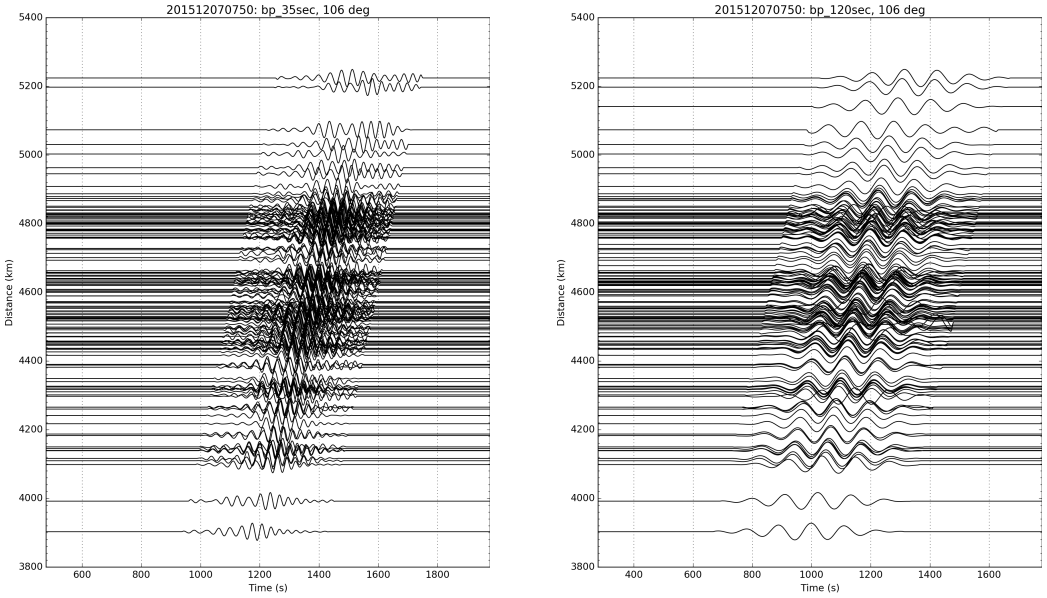

Fig. C.5: Record sections for an event in Tajikistan on 2015/12/07 07:50 UTC used for the surface wave phase velocity inversion with the TPW method. Traces shown here have been deconvolved and bandpass filtered around (a) 35 s and (b) 120 s. Outside the time window around the fundamental mode the data have been set to zero to avoid the influence of higher modes.

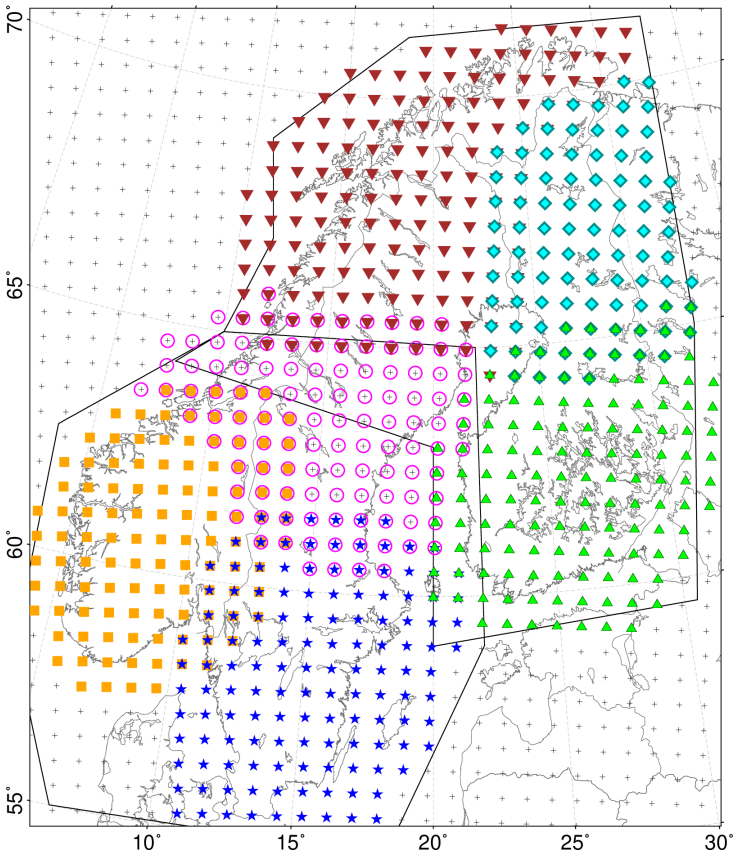

Fig. C.6: Map of grid nodes used for the phase velocity inversion. The different colored symbols refer to the six sub-regions used for the *a priori* starting velocities. The black polygons outline the northern and southern subset used for the inversion. In the overlapping area the phase velocity results have been averaged for the final phase velocity maps.

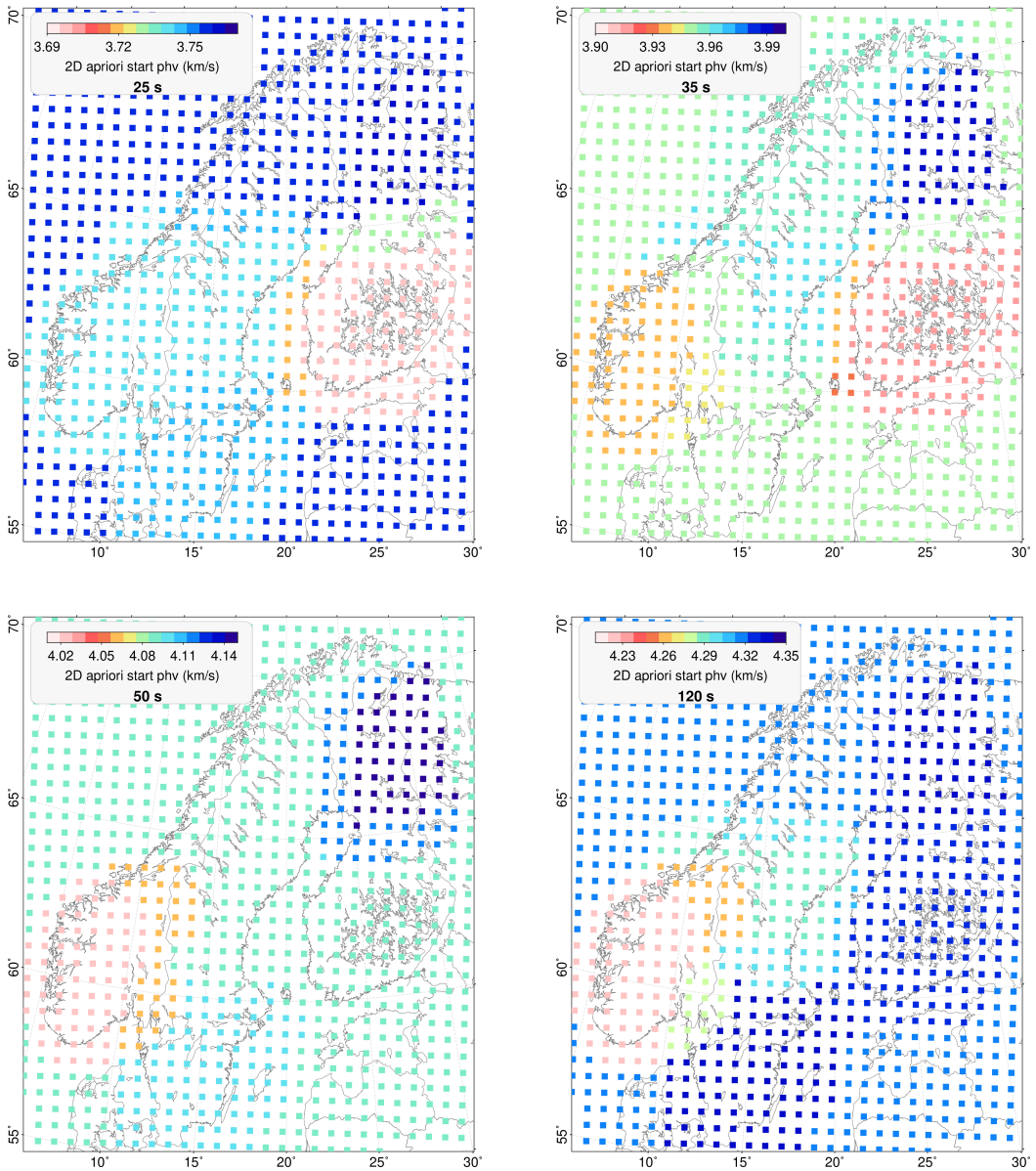

Fig. C.7: Map of the 2D *a priori* phase velocities at each grid node used as starting model for the phase velocity inversion. The different regions are outlined in Fig. C.6. Same periods as in Fig. 5.8 are shown. Our *a priori* phase velocities vary from 3.70 km/s (South Finland) at 25 s to 4.35 km/s (South Norway) or 4.48 km/s (North Finland) at 160 s.

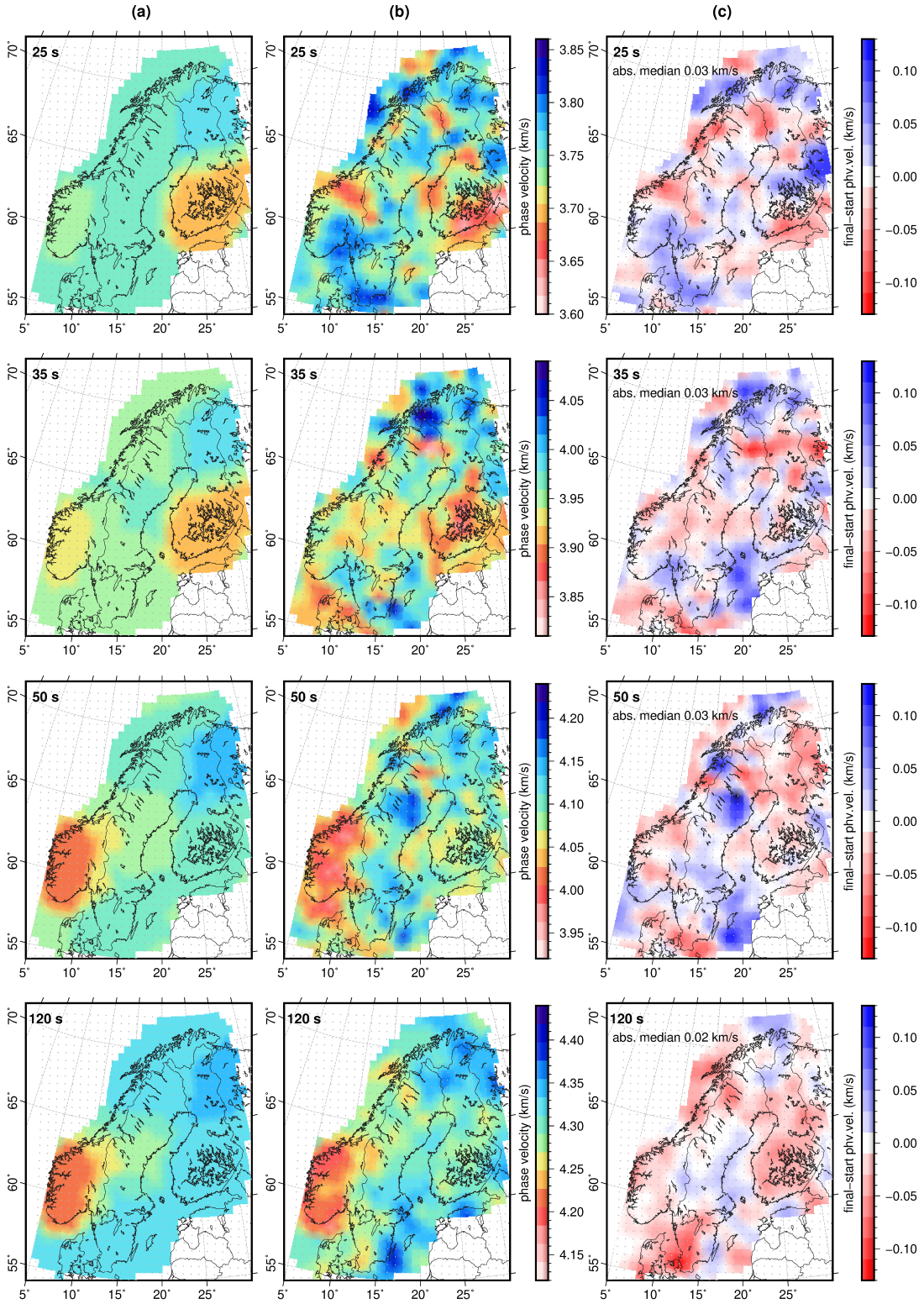

Fig. C.8: (a) 2D *a priori* models (cf. Fig. C.7). (b) Final phase velocity models. Same periods as in Fig. 5.8 and Fig. C.7 are shown. (c) Difference between (a) and (b). Blue colors mean that the final model is faster than the starting model. That comparison demonstrates that the modification of the final model is not constrained to the selected subregions of the 2D *a priori* model. Compared to the starting model, the high density of the ScanArray stations allows the inversion to recover structure at smaller spatial wavelength, resulting in additional detail in the phase velocity maps, but also an enhanced amplitude of larger scale anomalies. In southern Norway the low velocities are now more pronounced for longer periods, with a sharp transition to higher phase velocities towards the east, as expected from Medhus et al. (2012); Wawerzinek et al. (2013); Kolstrup et al. (2015); Hejrani et al. (2017). Southern and central Finland are slightly faster than before, but some low-velocity patches within the Nordland and Norrbotten provinces are consistent.

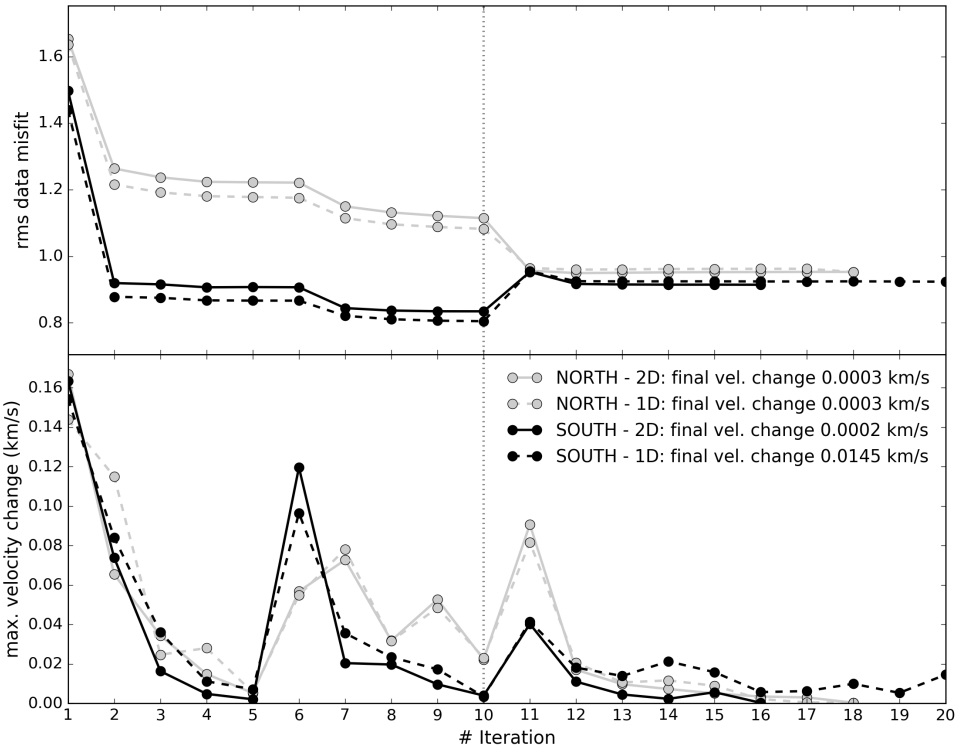

Fig. C.9: Convergence of the rms data misfit and the maximum velocity change for 50 s period. The comparison between the uniform (dashed lines) and 2D (solid lines) *a priori* models as well as between the northern (grey) and southern (black) inversion subsets are shown. The vertical dashed line marks the transition from the first to the second inversion stage (see main text for details).

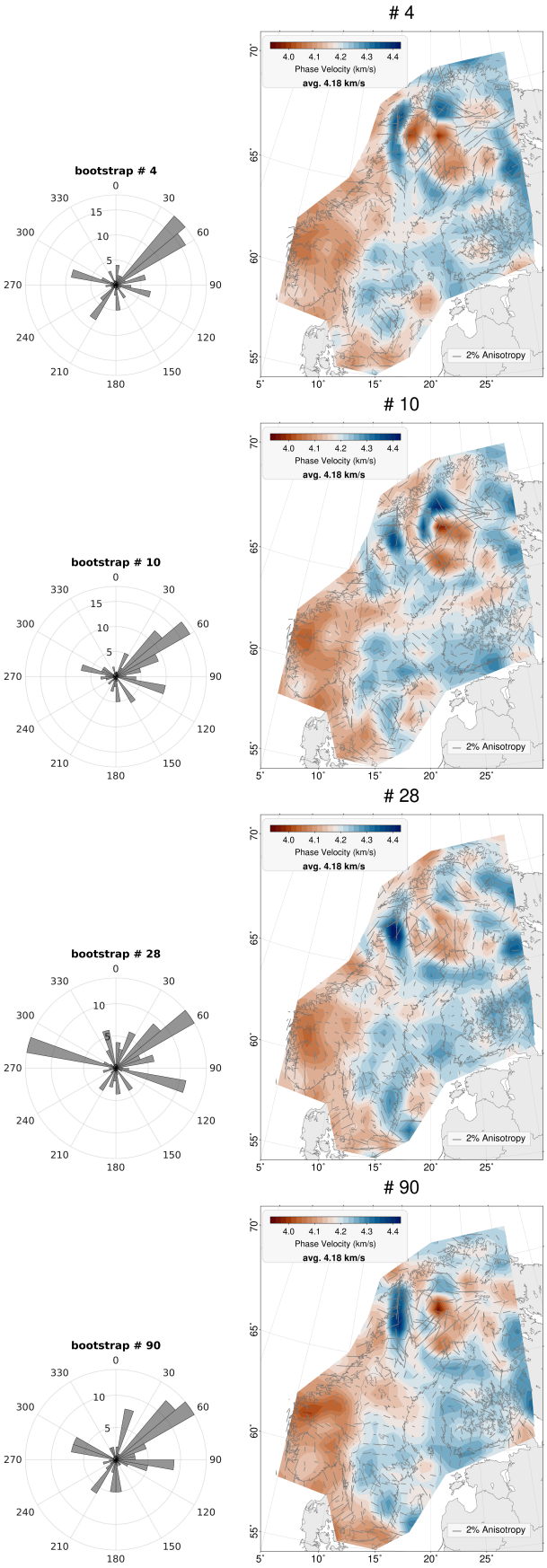

Fig. C.10: Additional bootstrap test examples (cf. Fig. 5.7) with different azimuthally unbalanced event distributions. Note the varying phase velocities in the north above 65°N.

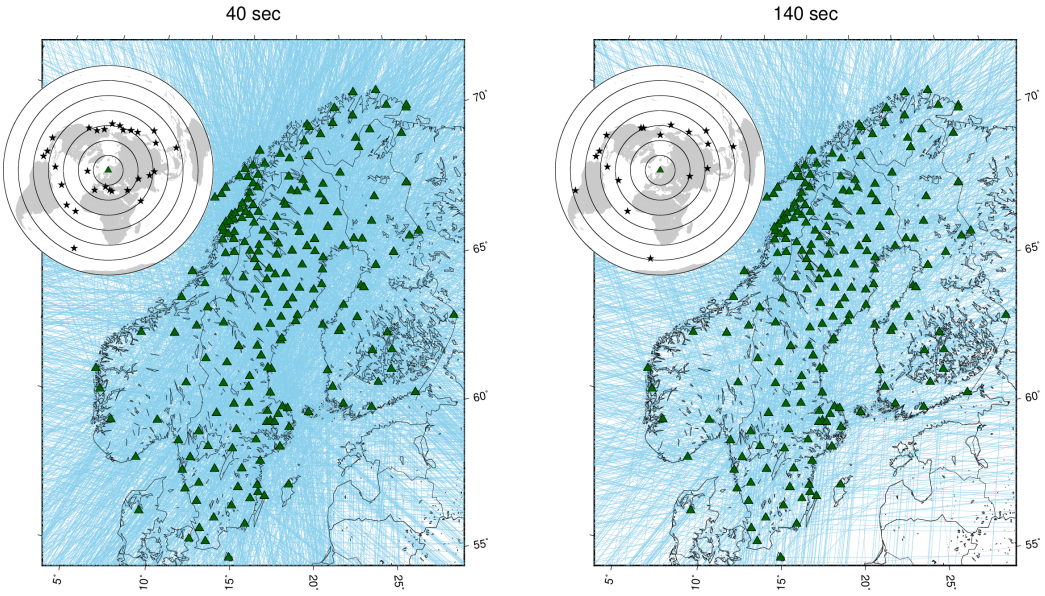

Fig. C.11: Ray coverage at 40 s and 140 s for the final phase velocity inversions with azimuthally balanced event distributions. Green triangles display the stations used for the inversion. Insets show the corresponding event distributions where black circles mark 20° epicentral distance intervals.

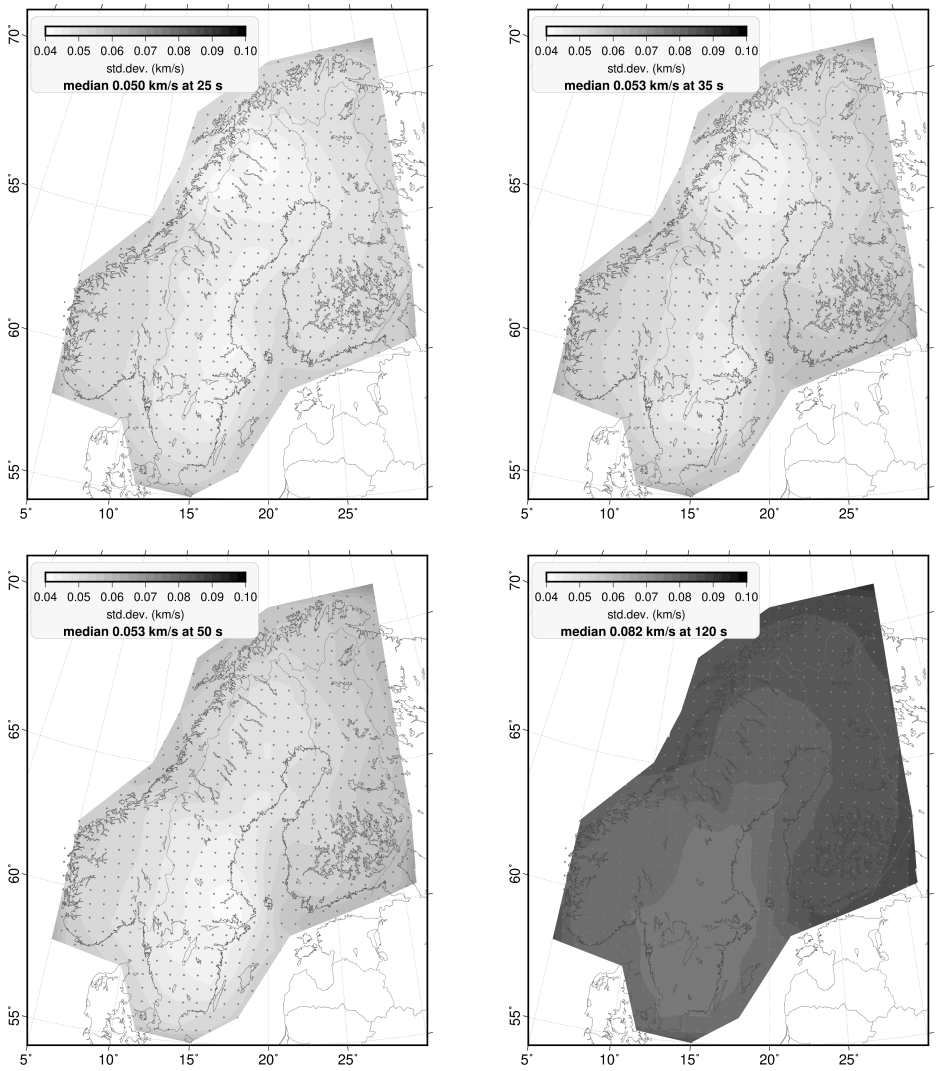

Fig. C.12: Maps of phase velocity standard deviations of the corresponding periods shown in Fig. 5.8.

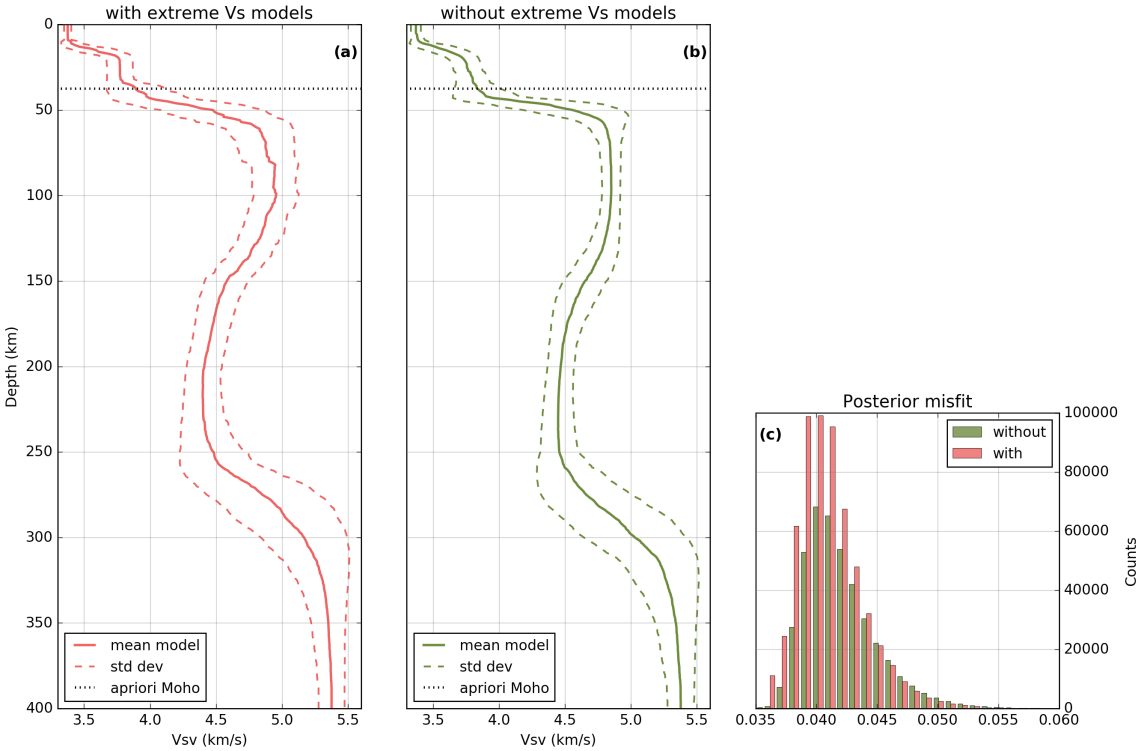

Fig. C.13: Posterior shear velocity models with and without extreme Vs models for the northern node marked as white cross in Fig. C.14.

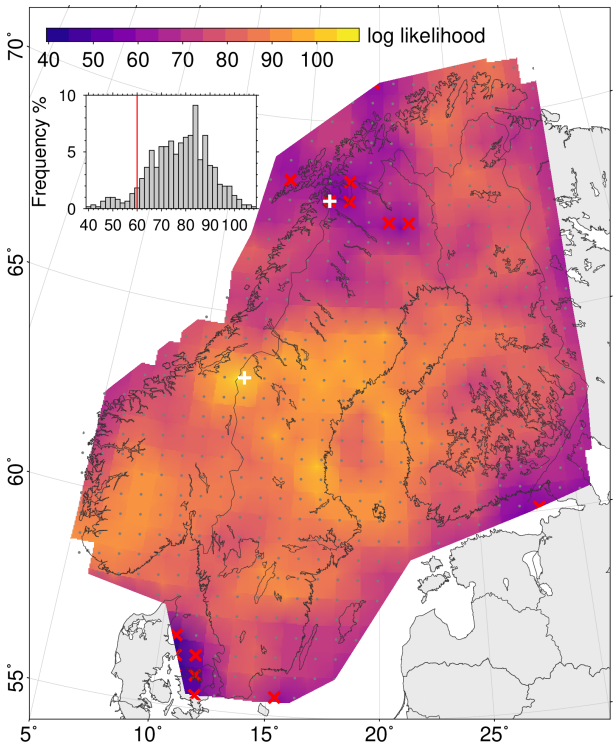

Fig. C.14: Median likelihood of the posterior distribution for each of the 605 1D inversions. The inversion results of two nodes (white crosses) are shown in Fig. 5.10. Red crosses mark nodes with poor misfit values which are omitted in the V_{SV} model interpretation.

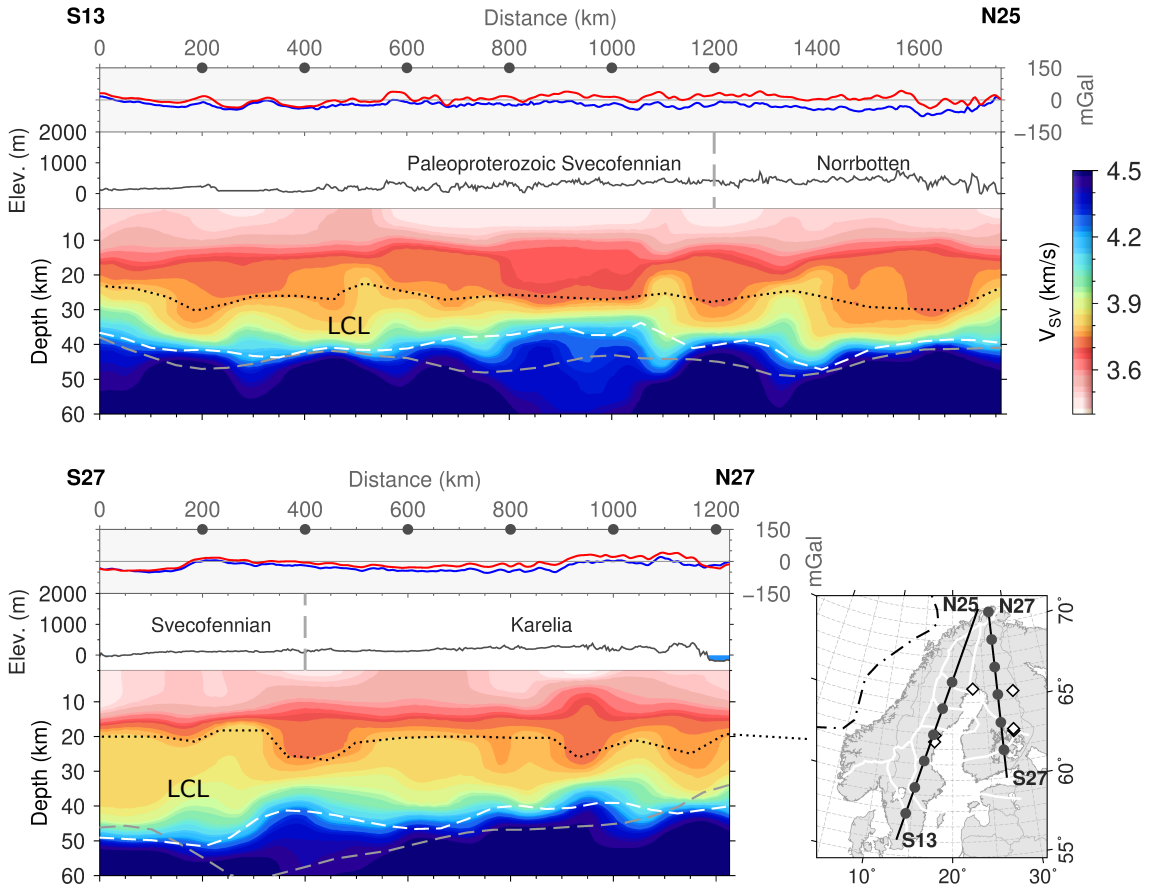

Fig. C.15: Cross sections for north-south profiles through the Svecofennian (profile S13-N25) and Archean (profile S27-N27) terranes in Sweden and Finland, respectively, showing crustal and sub-crustal structure down to 60 km depth. The topography profiles (grey lines) are shown on top of the V_{SV} models as well as the Free air gravity anomaly (red lines) and the Bouguer anomaly (blue lines) taken from EGM2008 (Pavlis et al., 2008). The grey, dashed lines are the Moho depths from *EUNAseis* (Artemieva & Thybo, 2013). The white, dashed lines are the obtained Moho depths from our inversion, calculated from the maximum gradient. LCL is the high-density lower crustal layer, indicated by the dotted lines.

C.2 Ambient noise data

Fig. C.16 shows the spectrograms of some coastal and inland stations after removal of instrument responses. The entire year 2015 is displayed where all stations reveal a similar noise energy pattern with peaks between 3–10 s period (0.1–0.35 Hz) corresponding to the secondary microseism. At around 14 s period (0.07 Hz) the primary microseism is seen as lower energy band. During the summer time the overall energy level of the two microseism bands significantly decreases. Similar noise pattern are obtained for the years 2014 and 2016 and for the other stations.

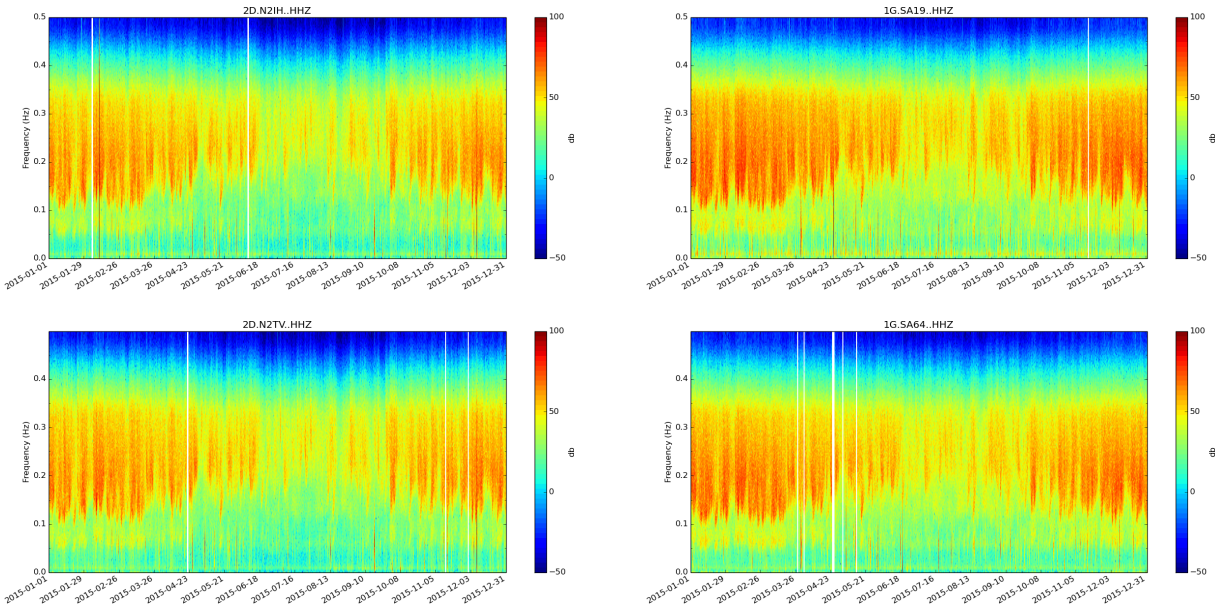

Fig. C.16: Spectrograms of the ScanArray stations SA19 (northern Sweden) and SA64 (southern Finland), and the NEONOR2D stations N2IH and N2TV (both Lofoten peninsula) for the time period Jan-Dec 2015.

The calculation of the cross-correlations requires a thorough pre-processing of the noise recordings. Fig. C.17 illustrates the difference between two time-domain normalizations, the 1-bit and clipping threshold, after Bensen et al. (2007), for noise and earthquake waveforms, respectively. For strong teleseismic or regional earthquakes (Fig. C.17c and d) the application of a clipping threshold equal to three times the standard deviation (or rms; clip-3-std) of the given day is insufficient to remove the entire surface wave amplitudes of strong earthquakes. However, the largest amount of the energy is eliminated and will not cause a bias in the cross-correlation functions. On the other side, a clip-3-std method preserves the ambient noise amplitude and phase information very well (b) and much better than a clip-1-std or 1-bit method. Since only 1% of the entire time period used for the cross-correlations is contaminated with teleseismic surface wave energy, it becomes clear that the clip-3-std method results in an overall higher signal-to-noise ratio (SNR) of the correlograms than the 1-bit normalization (see section C.1).

After the pre-processing the correlograms are stacked to increase the SNR (see chapter 5). Some stacked correlograms reveal interesting features. During the summer time, approximately between May and August, a dominant static noise signal around time zero occurs which is illustrated in Fig. C.18. The example station pair is located on the Lofoten peninsula (cf. Fig. C.16) and has been filtered between 2–10 s, i.e., the period range of the secondary

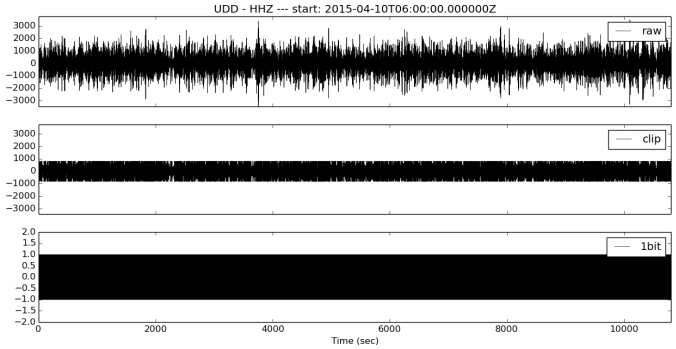

(a) noise - clipping with 1 stddev

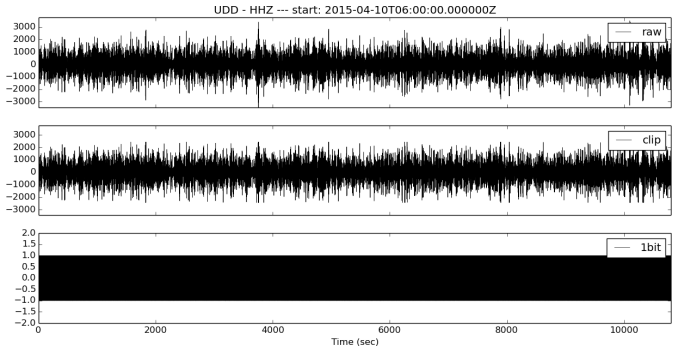

(b) noise - clipping with 3 stddev

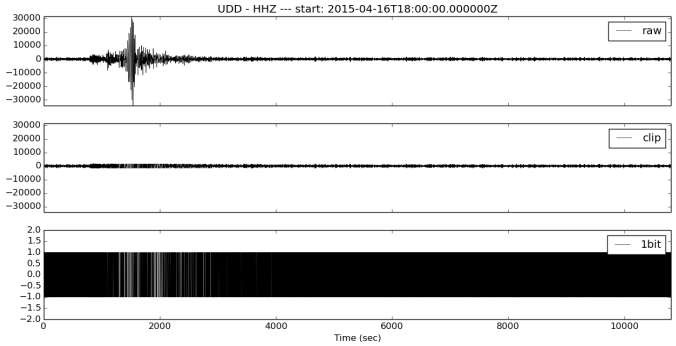

(c) Crete - clipping with 3 stddev

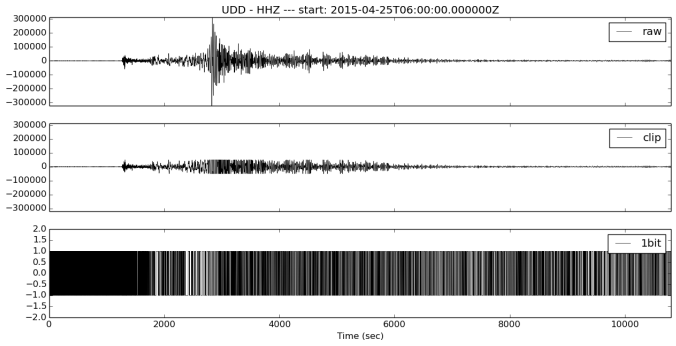

(d) Nepal - clipping with 3 stddev

Fig. C.17: Comparison of two different time-domain normalizations, 1-bit and clipping threshold, measured at station UDD in south-central Sweden. (a and b) For ambient noise and (c and d) for two teleseismic earthquakes. The top panels of each subfigure show the noise recordings after the deconvolution (labeled as raw). All middle panels illustrate the clipped recordings but with different thresholds. The bottom panels show the 1-bit normalization results. Top and bottom panels are identical in (a) and (b). The noise waveforms shown in the middle panel of (a) were clipped at a threshold of one times the standard deviation (or rms, clip-1-std) of the time window, whereas the noise in (b) was clipped at three times the standard deviation (clip-3-std). (c) shows an earthquake in Crete, Greece with magnitude M_S6.1 at 20 km depth. (d) shows the Nepal earthquake with M_S7.8. Both earthquake examples were clipped at three times the standard deviation.

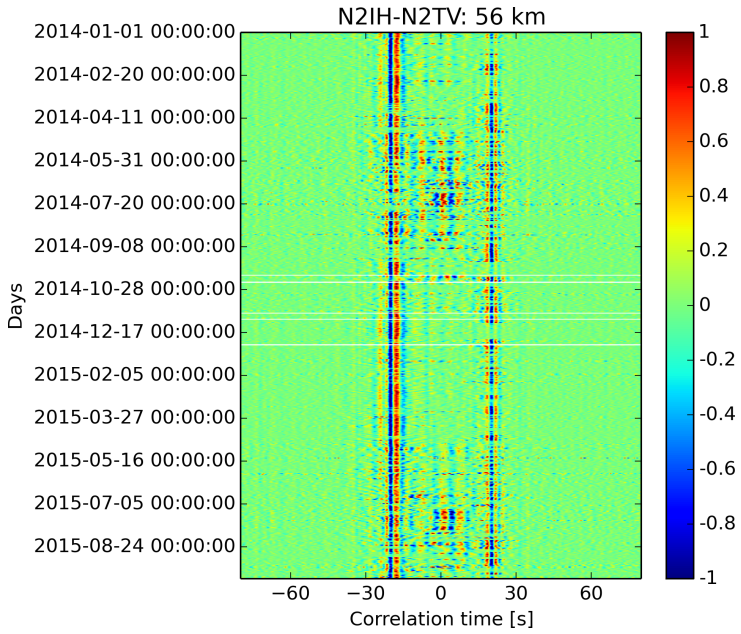

Fig. C.18: Daily cross-correlations from Jan 2014 to Aug 2015 of station pair N2IH-N2TV (cf. Fig. C.16), located on the Lofoten peninsula, in the normalized spectral domain filtered between 2 s and 10 s. The inter-station distance is 56 km. A coherent noise signal is seen on both time lags. The acausal lag has higher SNR but a significant reduction in amplitudes during the summer months. Additionally, during the summer months a pronounced static signal around time zero occurs.

microseism sources. A static time zero pulse indicates energy arriving from below the station pair. One origin might be the formation of winter storms at the antipodes of Scandinavia which lie in the South Pacific Ocean (Stehly et al., 2006). Stations where a time zero signal appears reveal also a slightly lower noise level between 3–5 s during the summer time compared to other stations as visible in Fig. C.16. The short-period time zero signal is most significant for coastal station pairs with a very short inter-stations distance. Since this correlation argues against a southern hemisphere origin, the time zero signal remains somewhat enigmatic.

Fig. C.19(a and b) show two cross-correlation functions filtered in multiple frequency bands after Bensen et al. (2007). Some correlograms reveal a move-out of a long-period time zero signal or a static time zero signal for periods >20 s (Fig. C.19a). This, however, is not a consistent feature as other station pairs with similar location and azimuth (Fig. C.19b) do not show such significant time zero energy. Neither is this spurious signal dependent on the season. These observations were made only on the ZZ components. The RR or TT components either show no time zero signal or the SNR is too poor for any analysis. The signal is irregularly seen on the record section of station SA29 (Fig. C.19c) indicating a local effect (cf. Fig. 5.3), but I can only speculate on its origin. Processing artifacts are unlikely due to the dependency on station pairs. In contrast to the short-period time zero pulse (Fig. C.18), this long-period signal cannot be related to microseism sources at the antipodes. Residual energy from insufficient removal of earthquake surface waves (Fig. C.17) is implausible because the signal indicates a velocity too high to be a teleseismic feature. Rather, the high velocities call for body waves. But surface waves that propagate from the west, i.e., perpendicular to the station pair, might also be possible as well as oblique propagating surface waves. Otherwise, the period range corresponds to the Earth's hum. In any case, the local SNR conditions might give rise to the absence of this signal at neighboring stations.

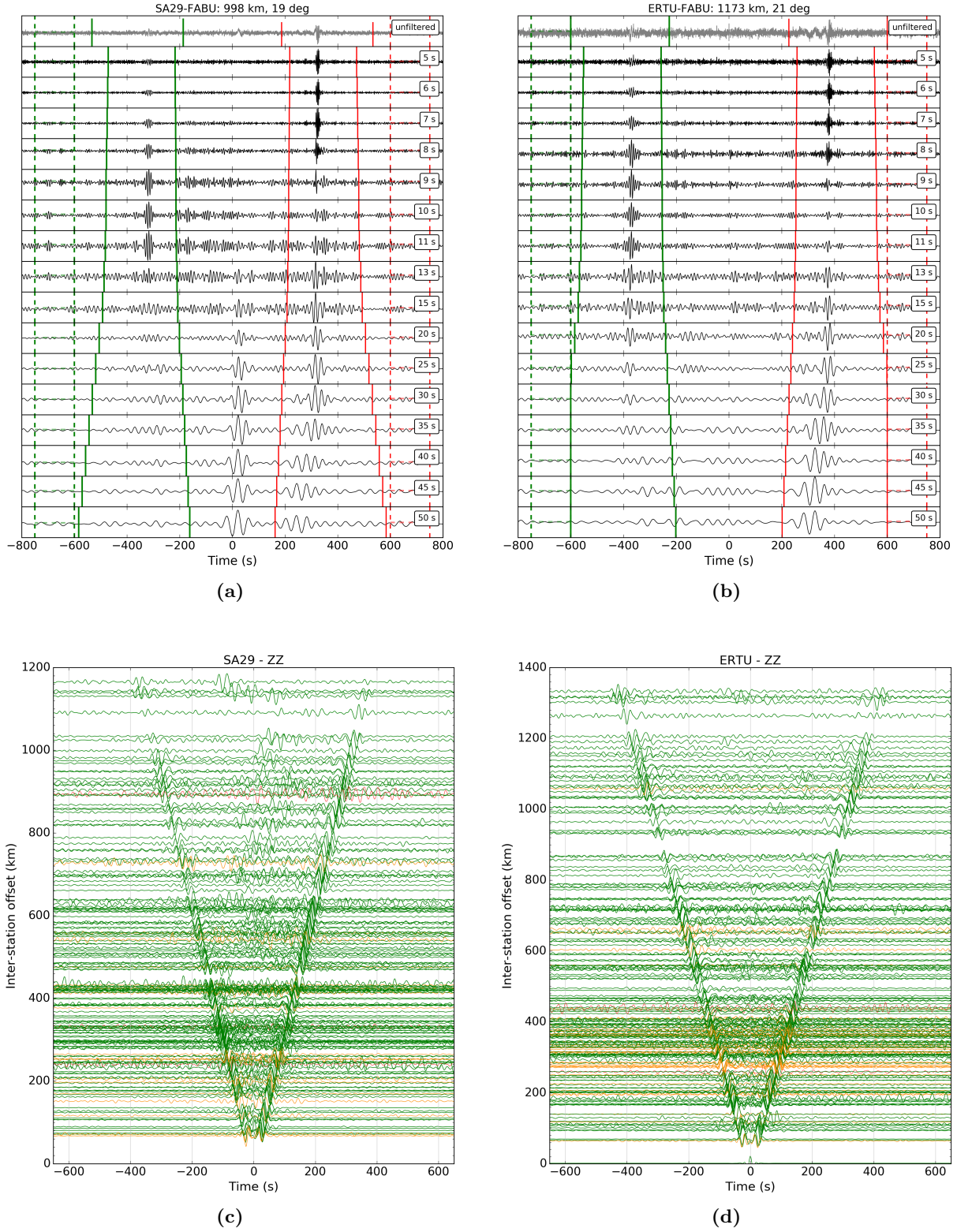

Fig. C.19: (a and b) Two examples of correlograms filtered with multiple band-pass filters. The central period is labeled on the right side of each trace. The green and red bars mark the time windows from which the signal and the noise were measured, respectively. Inter-station distance and azimuth are displayed in the title. (c and d) Vertical component stacked record sections with respect to stations SA29 (c) and ERTU (d), filtered between 15-50 s. Stacked traces based on more than 12 months of overlapping data are shown in green. Orange and red traces were stacked over less than 12 and 3 months, respectively. Many correlograms with SA29 show a long-period signal around time zero. Station ERTU is located ∼170 km north of SA29 and is not associated with any spurious signal.

C.3 Ambient noise phase velocity inversion

For comparison with the 2D McMC noise inversion technique (section 5.5.3), two other inversion schemes have been implemented by F. Tilmann (pers. comm.): a classic damped-least square (DLS) solution and a mixed, hybrid inversion of McMC and DLS. The latter is similar to the DLS inversion but uses the average McMC model as starting model instead of an uniform reference model. A DLS inversion involves a purely Gaussian error distribution and a post-inversion smoothing, equal for all periods, assuming straight ray paths. The frequency-independent smoothing coefficient and damping weight were determined from a cross-validation criterion. Here, the entire data set is randomly split into 10 equally sized subsets. One subset is chosen to be the validation data (not used for inversion) where the remaining 90% (training data set) are considered for the inversions with 20 different damping and smoothing parameters. For each of the 20 resultant models the misfit is calculated. This procedure is repeated by making each of the 10 data subsets the validation data and the remaining ones the training data set. Finally, damping and smoothing value were chosen as the 75th percentile of the best performing damping and smoothing values of the individual test data from the cross-validation trade-off curve. An optimum smoothing width of 1.5 times the grid-spacing was found for the DLS inversion. Whereas no smoothing yield the best results in case of the hybrid inversion. The phase velocity variations among the three noise inversion schemes with respect to the TPW Rayleigh wave inversion at 30 s period are illustrated in Fig. C.20 and C.21. This is the only period where we performed both the TPW and the noise inversions. I compared scatter plots of the phase velocities (Fig. C.20) and the individual dispersion curves at each TPW grid node and found an overall better fit of the McMC with TPW inversion than with the DLS or hybrid solutions.

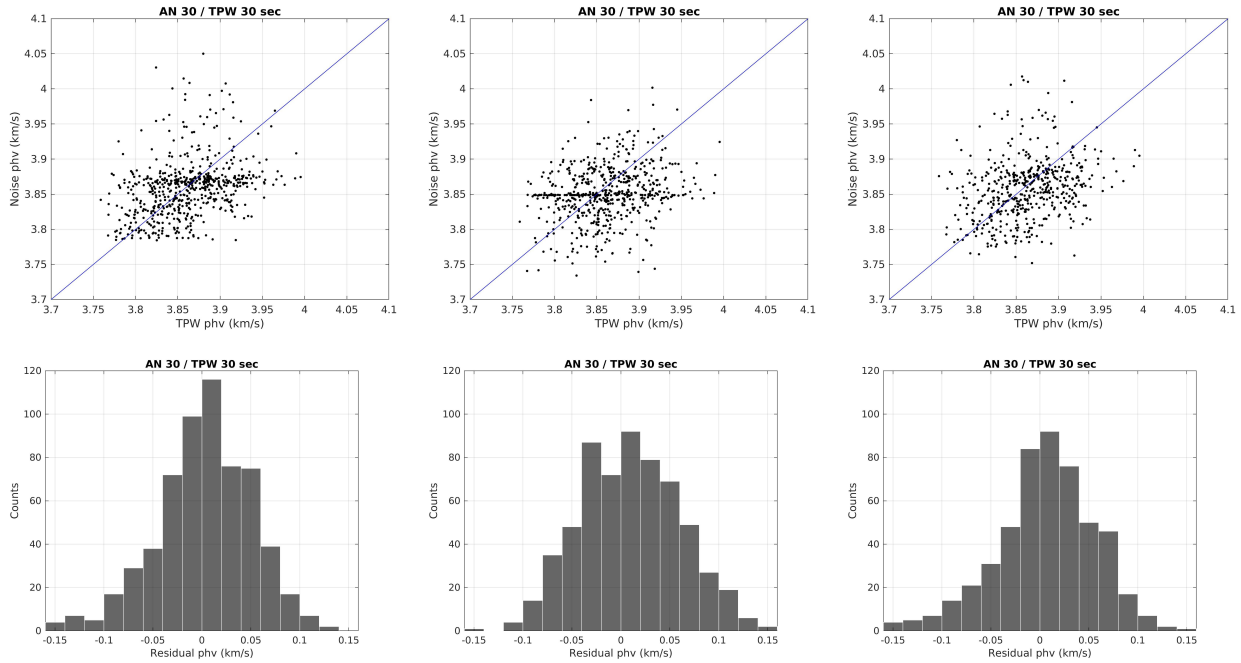

(a) McMC **(b)** DLS **(c)** Hybrid

Fig. C.20: Top: Scatter plot of the TPW phase velocity measurements at each grid node vs. the McMC, DLS and hybrid noise inversions at 30 s period. In case of the McMC and DLS inversions, a bias due to the uniform starting model can be seen. Bottom: Corresponding histogram of the phase velocity residuals between Rayleigh waves and noise.

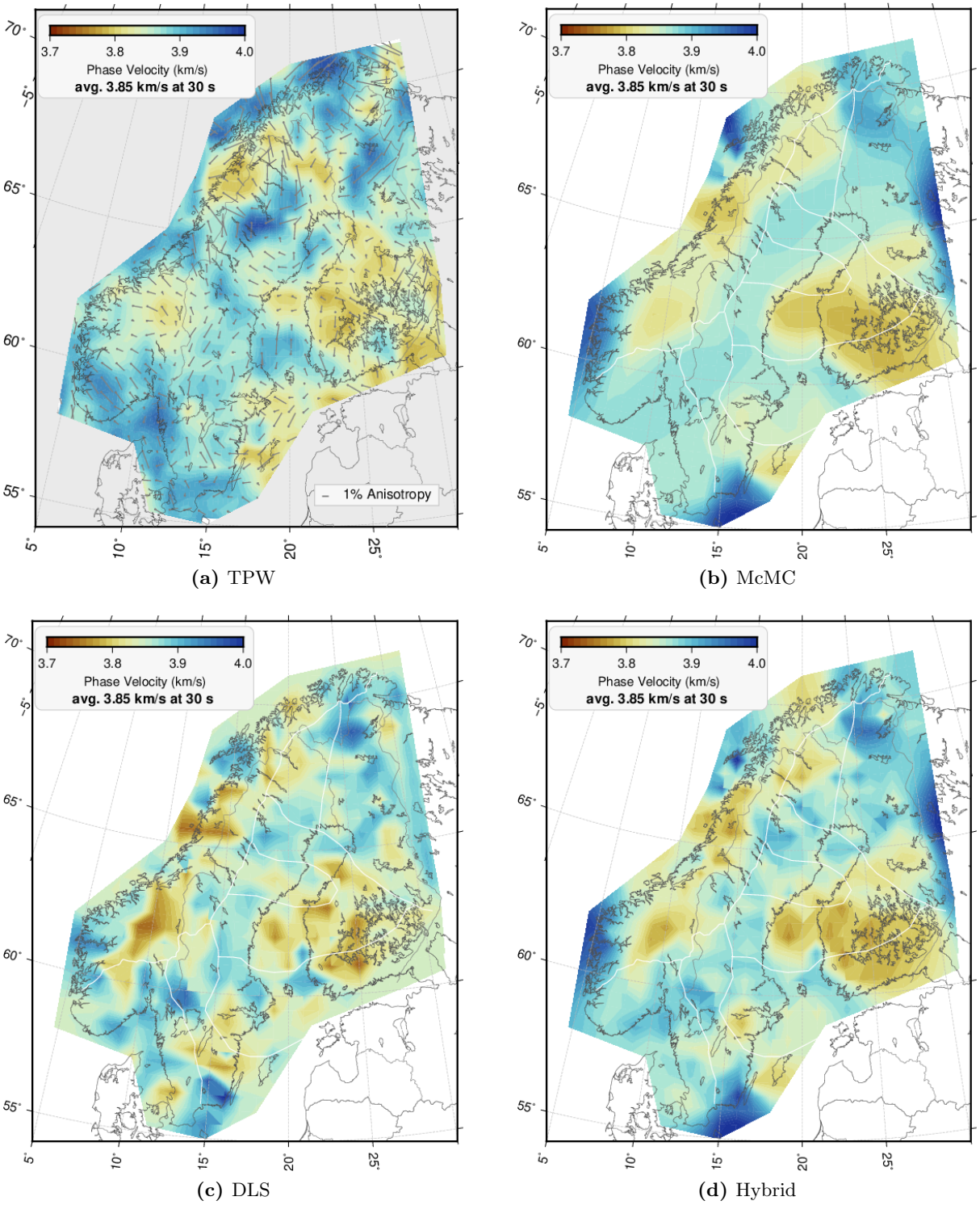

(a) TPW **(b)** McMC

(c) DLS **(d)** Hybrid

Fig. C.21: Comparison of the 2D phase velocity maps resultant from the TPW inversion and the three ambient noise inversion methods McMC, DLS and hybrid at 30 s period. Color scale is equal for all models with ±0.15 km/s around the labeled average velocity.

C.4 V_S-depth inversion with DLS noise results

For the subsequent 1D V_S-depth inversion with the DLS noise results, I used the same inversion parameters as for the McMC results (see section 5.7.2). I obtained higher inversion misfits in case of the DLS results than with the McMC noise values. The standard deviations of the posterior mean V_S models are similar for both noise inversion results. Fig. C.22 compares the depth inverted models for the McMC with DLS noise results. The low velocities in southern Norway (especially along the Oslo Graben) at 5 km and 10 km depth are visually more striking with the DLS solution and in better agreement with Köhler et al. (2012) (their Fig. 7). However, the largest difference is seen for the Karelia craton with ∼0.05 km/s higher velocities using the DLS values. But also the TIB low-velocity band at 15 km depth is more pronounced for the DLS results. Beside from that, the remaining crustal structure is similar to the McMC results, discussed in section 5.8. Minor small-scale variations that occur do not change the interpretation.

C.5 1D Airy isostasy modeling

I conducted a simple 1D isostasy modeling for the northern, central and southern Scandes assuming Airy isostasy and a complete compensation of the topography by the crust, following Stratford et al. (2009). The crustal thickness h_c is dependent on the topography h_t and the crustal thickness at sea level h_s which is about 30 km along the Scandes (Stratford & Thybo, 2011; Ben Mansour et al., 2018). ρ_m is the density of the sub-crustal mantle. The average densities for the crust ρ_c and topography ρ_t are taken from Ebbing et al. (2012).

$$h_c = h_s + h_t(1 + \frac{\rho_t}{\rho_m - \rho_c}) \tag{C.1}$$

I compare two types of models: a crust of average density of 2860 kg/m^3 ($\rho_c = \rho_t$) and a crust having a high-density lower crustal layer (LCL). For the central and northern Scandes I use for the LCL a density of 3200 kg/m^3 and for the southern Scandes 3050 kg/m^3. The topography is smoothed for the isostasy calculation with a filter width of 50 km. Short wavelengths undulations are negligible for the local compensation.

I note a lateral offset of the maximum Moho depth from the peak elevation, most pronounced for the northern and southern Scandes. Flexural support is likely present that supports load elastically. The calculations taking into account the LCL show that both along the northern profile and the southern profile, there is a change in compensation roughly along the CF, which points to changes in the nature of the underlying mantle. No notable change of compensation is seen along the central profile and the central Scandes are mainly compensated by the crustal thickness.

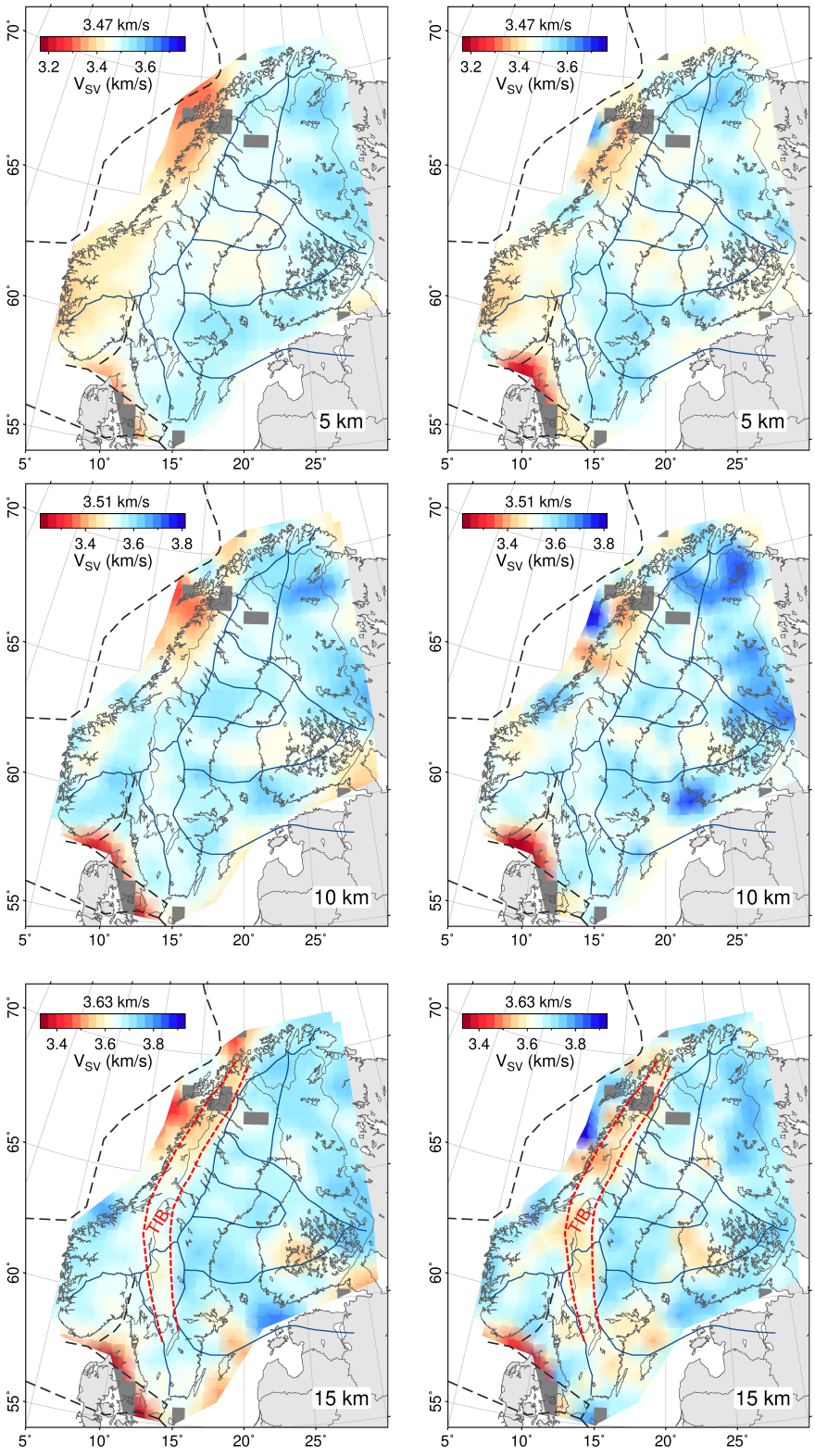

(a) McMC **(b)** DLS

Fig. C.22: Horizontal slices of absolute shear velocities through the 3D model using the McMC (a) and DLS (b) noise inversion results at 5, 10 and 15 km depths. Poor results are shaded in grey (cf. Fig. C.14). Blue lines mark the major Paleoproterozoic terranes simplified after Lahtinen et al. (2005) as well as the TIB and Sveconorwegian margins (Fig. 5.2). At 15 km depth the TIB, defined by the lower velocities and in congruence with magnetic data (Olesen et al., 2010), is outlined. The color scales are indicating absolute velocities but are adjusted for each depth slice, such that the range is ±0.3 km/s (ca. ±8.5%) around the average value denoted in the legend.

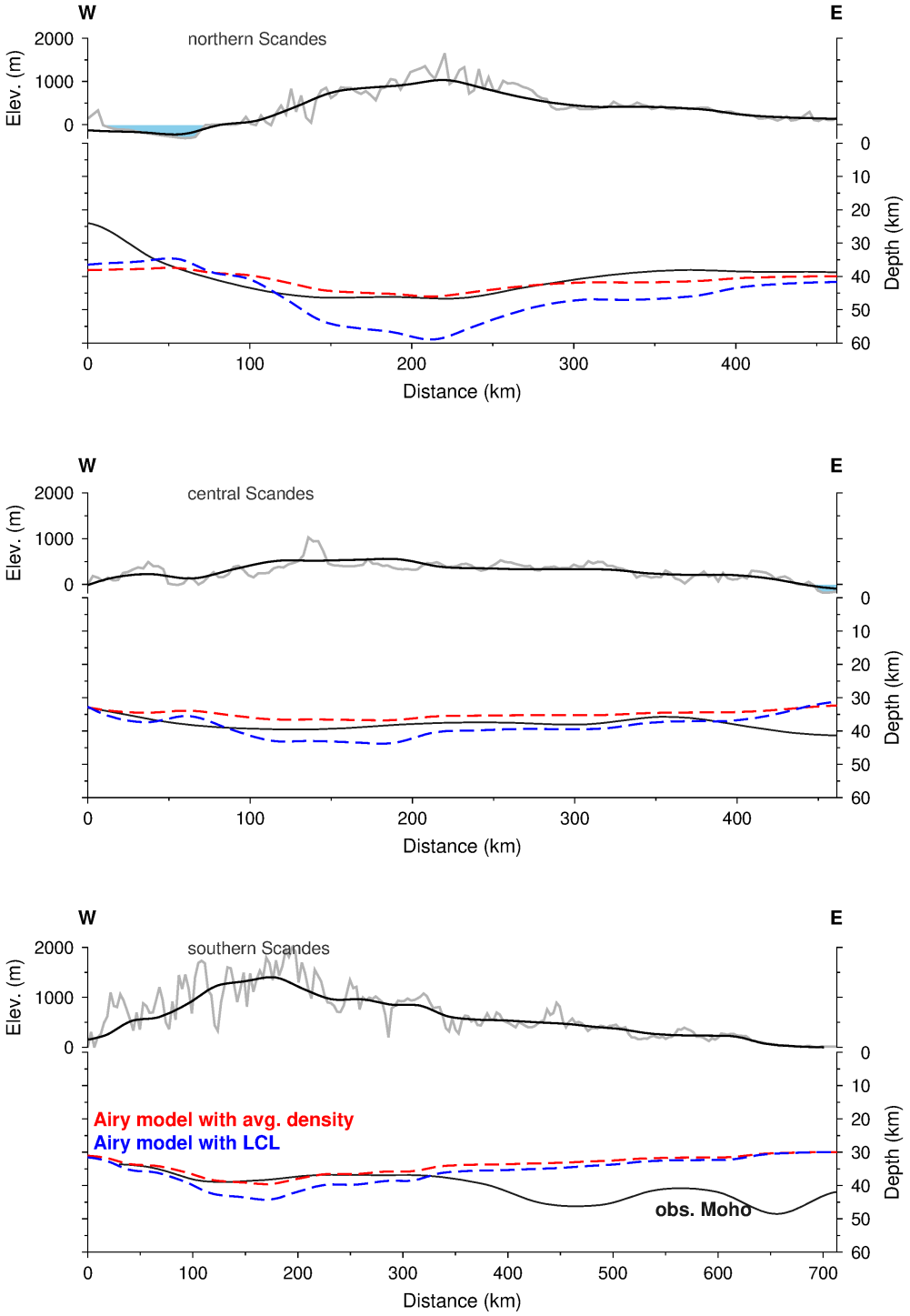

Fig. C.23: Isostatic balance 1D modeling of Airy-type compensation for the southern, central and northern Scandes. The topography is smoothed with a filter width of 50 km (thick, black line). The red and blue lines show the calculated location of the Moho in case of isostatically balanced topography with two types of models: a crust of average density (red lines) and a crust having a high-density lower crustal layer (LCL, blue lines) different for the northern and southern Scandes (see text). The black lines show the derived Moho depths from the V_S-depth model denoted as obs. Moho.

Appendix D

Impact of local inhomogeneities on Eikonal and Helmholtz tomography

D.1 Introduction

This chapter expands on the discussion of chapter 4 where the influence of strong local heterogeneities below the receivers on plane wave based methods as Eikonal tomography have been noted. The Eikonal equation is deduced from the ray theory which is a high-frequency approximation (i.e., a WKBJ assumption (Dahlen & Tromp, 1998)). This approximation requires a smoothly lateral varying medium with respect to the propagating characteristic wavelength to be valid. In such a regime, the surface wave phase delay can be expressed as linear path integral over the great-circle ray from the source to the receiver (Zhou et al., 2005):

$$\delta \mathbf{t_P} = -\frac{\omega}{c(\omega)} \int_0^\Delta \frac{\delta c(\omega, l)}{c(\omega)} \mathrm{d}l \tag{D.1}$$

where ω is the frequency and c(ω) and δc(ω) the unperturbed and perturbed surface wave phase velocities, respectively. The great-circle ray path length is l and Δ is the epicentral distance from the source to the receiver. This is a notation of the Eikonal equation.

A reformulation of this phase perturbation approach leads to the path average (PAVA) formalism in section 3.1.1 (cf. eq. 3.6). The important point is to draw the relation between the horizontal ray parameter p and the travel time equivalence of the frequency–phase velocity expression (Dahlen & Tromp, 1998; Liu & Gu, 2012).

$$\frac{\delta \omega_{local}}{\omega} = \frac{\Delta(p)/T(p)}{c} \frac{\delta c_{local}}{c} \tag{D.2}$$

$\Delta(p)$ and T(p) are hereby the distance and travel time dependent on the ray parameter, respectively, with c = 1/p. Accordingly, eq. D.2 is the travel time equivalence of eq. 3.7. The total travel time perturbation can be re-written in terms of local perturbations as

$$\delta T(p) = \frac{1}{\Delta} \int_0^\Delta \delta t_{local}(p, \theta, \Psi) \mathrm{d}\Delta \tag{D.3}$$

which is in turn the equivalence of eq. 3.9 with Ψ being the phase.

In terms of a travel time notation, one can define the travel time τ of a phase front (e.g., Wielandt, 1993) as

$$\frac{1}{c_a(\mathbf{r})} = |\nabla \tau(\mathbf{r})| \tag{D.4}$$

This is a common formalism of the Eikonal equation that forms the basis for the Eikonal tomography (e.g., Lin et al., 2009; Jin & Gaherty, 2015). Eq. D.4 describes the

frequency-dependent apparent (or dynamic) phase velocity c_a as the reciprocal of the surface gradient of the phase travel time $\tau(\mathbf{r})$ at location r relative to the source. The Eikonal equation is found as a high-frequency approximation of the 2D Helmholtz equation (Wielandt, 1993)

$$\frac{1}{c_s(\mathbf{r})} = |\nabla\tau(\mathbf{r})| - \frac{\nabla^2 A(\mathbf{r})}{A(\mathbf{r})\omega^2} \tag{D.5}$$

where c_s is referred to as the structural phase velocity and A describes the amplitude of the wavefield at location r. The amplitude term on the right hand side of eq. D.5 vanishes for high frequencies or smoothly varying amplitudes across the receiver site. In that case, the apparent and structural phase velocities would be the same. A correction of the Eikonal equation (or the apparent phase velocities) by this amplitude term might be necessary to account for non-planar propagation perturbations related to the structure outside the array, such as multipathing, backscattering and wavefront focusing (Lin et al., 2009).

In the following, I present the phase velocity inversion using a recently implemented Eikonal tomography algorithm which I applied in the very beginning of my PhD. The Eikonal equation implies a phase analysis of individual events, leading to separate phase velocity maps for each earthquake as distinct from the two plane wave approach in chapter 5 where all events are jointly inverted. The impact of local inhomogeneous structure below the receiver site on the ray theory is demonstrated in this chapter. Moreover, I discuss the advantage of the TPW method over an Eikonal tomography.

D.2 Method and data processing

The Automated Surface Wave Phase Velocity Measuring System (ASWMS) (IRIS DMS, 2014), implemented by Jin & Gaherty (2015), measures the surface wave phase delays and amplitudes by cross-correlations of nearby stations to generate Eikonal phase velocity maps. This approach differs from the Eikonal notation in eq. D.4 since the ASWMS algorithm measures differential phases instead of absolute phases at single stations (cf. TPW method in chapter 5) from which the travel time surface $\tau(\mathbf{r})$ needs to be derived first.
Instead, a slowness vector field is used to describe the propagating wavefield where the length of the slowness vector is the reciprocal of the apparent phase velocity in eq. D.4 and the direction of this vector corresponds to the wave propagation direction. The predicted phase delay time $\delta\tau_p$ between two stations is found from the integral over the slowness vector field with $\mathbf{S}(\mathbf{r})$ being the slowness vector and with $\mathbf{r_i}$ being the spherical inter-station path:

$$\delta\tau_{\mathbf{p}} = \int_{r_i} \mathbf{S}(\mathbf{r}) \cdot \mathrm{d}\mathbf{r} \tag{D.6}$$

A least-square inversion is then applied to invert for the slowness directly.

In contrast to the classical two-station method, which requires the cross-correlated station pair to be aligned with the great-circle path, all possible station pair combinations within a appropriate neighborhood can be used for the phase delay measurement. This multi-channel approach requires an upper distance threshold for nearby stations to avoid cycle-skipping of the phase delays (cf. section 3.1). An appropriate threshold is 3–4 times the wavelength of

the shortest period used. A lower inter-station distance limit is set to two times of the average station spacing to ensure a sufficient ray coverage for the tomography. As I used a minimum period of 22 s for the Eikonal tomography with an average phase velocity of ∼3.65 km/s (cf. chapter 4), the maximum inter-station distance was set to 350 km.

To make a comparison more convenient, I used the same events as for the beamforming of the Complete sub-array in chapter 4, in total 188 high-quality events (Fig 4.3). The phase delay measurements are performed at 12 different periods ranging from 22 s to 120 s. As a first step, the pre-filtered (10–200 s bandpass filter) and deconvolved Rayleigh surface waves, recorded on the vertical component, are roughly windowed based on an initial group velocity range between 2.7 km/s and 5.5 km/s to locate the fundamental mode energy. Fig. D.1 illustrates the tracing of the surface waves. The resultant time window is referred to as the window function W_S (Fig. D.2).

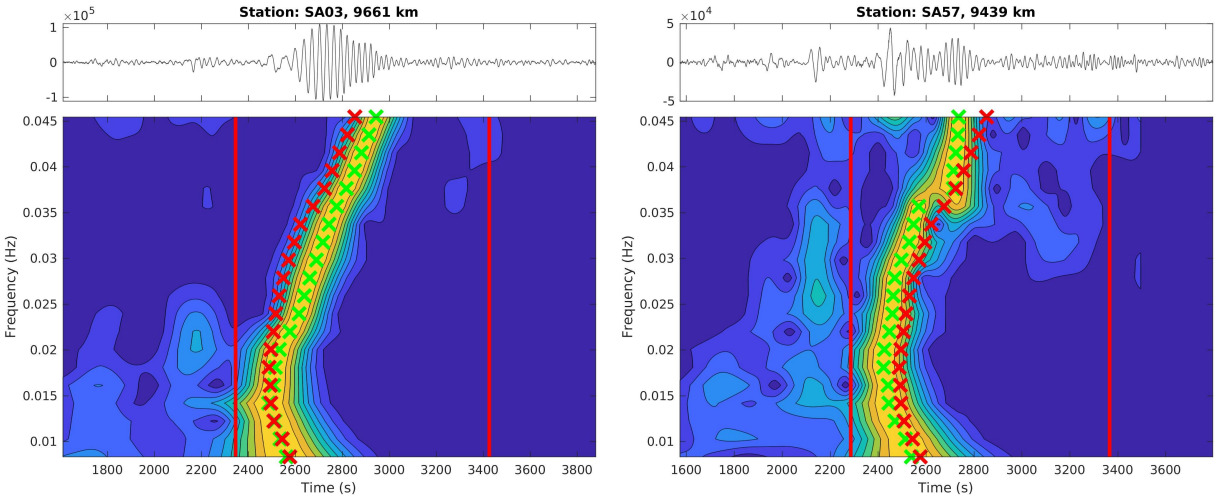

Fig. D.1: Illustration of the automatic time window selection to isolate the fundamental mode energy. The recordings at two different stations for an event from 14-10-2014 03:51 UTC in Central America (average baz is 288°) are shown where the time is relative to the origin. For each period of interest (see text) a narrow-band Gaussian filter has been applied to the recordings. The green crosses indicate the measured frequency-dependent group delays using the FTAN method (Levshin et al., 1992) based on the envelopes of the Gaussian filtered data. The group delays, averaged over all stations, are indicated by the red crosses which have been derived from the measured group delays by a polynomial fitting. Subsequently, these average group velocities are then used for the final time window estimation, displayed as red lines.

Some rejection criteria are applied during the time window calculation to control the data quality. Beside the obvious rejection of stations with data gaps or insufficient data length, also recordings with a group velocity deviation of >20% from the mean value are discarded as well as events with too many group velocities close to the initial group velocity limits. The minimum number of stations per event is 10. Additionally, I set a SNR threshold for the individual stations using an envelope ratio. A low SNR is detected if the ratio of the maximum peak of an individual envelope divided by the mean of the envelope peaks is less than 4, a value chosen by investigating the data. This should remove irregular waveforms with outlier peaks.

$$C(t) = S_1 * W_S S_2 \tag{D.7}$$

After isolating the surface wave energy in the time domain, the cross-correlation functions C(t) (eq. D.7) are calculated between station S_1 and a nearby windowed station S_2, as illustrated

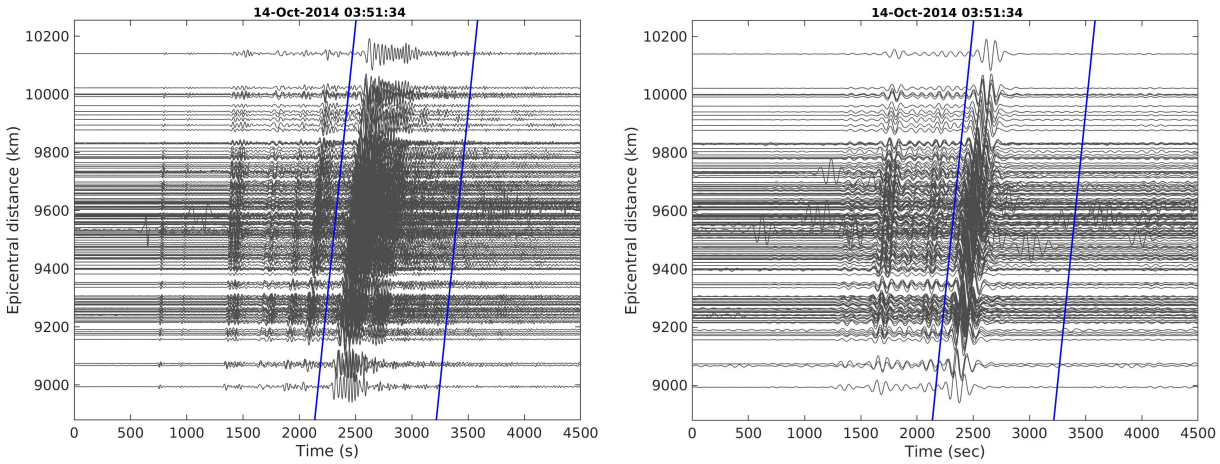

Fig. D.2: Bandpass filtered record sections as a function of the epicentral distance for the same event as in Fig. D.1. The blue lines show the automatically determined time window (window function W_S) used for extracting the fundamental Rayleigh mode. Left: Filtered between 20-120 s. Right: Filtered between 70-120 s.

in Fig. D.3. Additional windowing of C(t) using a Hanning taper is applied to further isolate the dominant energy which gives the windowed correlogram W_CC(t). Subsequently, a set of 12 Gaussian narrow-band filters (for the 12 periods of interest) are convolved with W_CC(t). The obtained filtered correlograms $F_i(\omega_i) * W_C C(t)$ are shown in Fig. D.4 with ω_i being the center frequency for filter F_i with a 10% band width. This is the essential processing step as the filtered correlograms contain the group and phase delays as well as the coherence between the two stations. A five-parameter Gaussian wavelet approximates the filtered correlograms (cf. red lines in Fig. D.4) from which the observed group and phase delays are derived. This wavelet is defined as the product of a Gaussian envelope and a cosine function

$$F_i * W_c\ C(t) \approx \underbrace{AGa[\sigma(t - \mathbf{t_G})]}_{\text{Gaussian envelope}} * \cos[\omega(t - \mathbf{t_P})] \tag{D.8}$$

where $\mathbf{t}_G$ and $\mathbf{t}_P$ are the observed frequency-dependent group and phase delays, respectively. Ga is the Gaussian function, multiplied by a factor A (which is an estimate of the amplitude), and σ is the half-bandwidth. A non-linear least-square inversion is used to fit the predicted wavelet to the data and to obtain $\mathbf{t}_G$ and $\mathbf{t}_P$. Along with the nearby cross-correlations also the auto-correlations of each station are calculated and fitted.

The quality of the phase delay measurements is subject to some criteria. First of all, the raw phase delays, retrieved from eq. D.8, are checked for a cycle-skipping bias. The necessity of such a correction is demonstrated in Fig. D.5 (left). Cycle-skipping is mainly related to the short period measurements and for stations pairs with large distances. In the latter case, the phase delay might be close to or even exceed a given period. Only phase delay measurements within a given range and relative to an estimated average phase delay are considered for the Eikonal inversion. Second, a potential bias introduced by the window function W_S at the edges of the window is corrected by using the cross-correlation of station $S_2 * W_S S_2$. This is nearly an auto-correlation and any non-zero group and phase delay is supposed to be a bias which is subtracted from the station pair phase delay.

Apart from the bias corrections, good measurements are further defined by a coherence

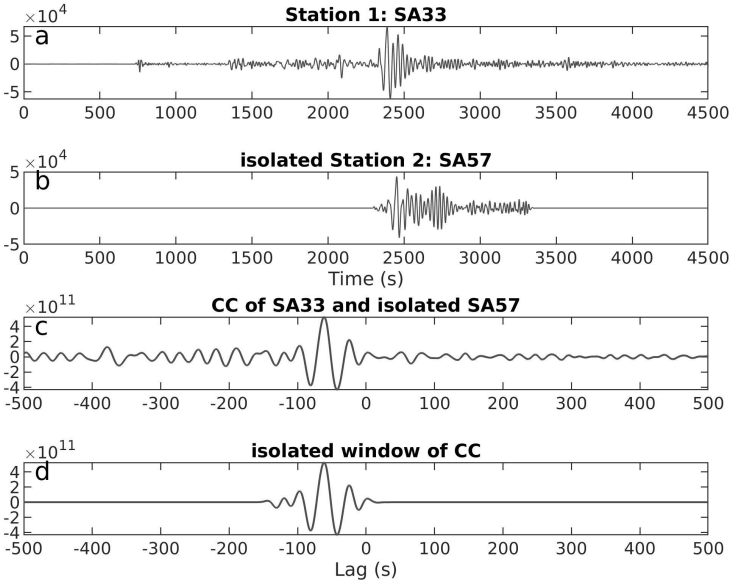

Fig. D.3: Cross-correlation procedure of nearby stations for the event shown in Fig. D.1. (a) Broadband and unwindowed station 1. (b) Windowed station 2 using the time window function W_S calculated before to extract the surface wave energy. (c) The cross-correlation function C(t) between the signals in (a) and (b) has been performed. (d) The correlogram in (c) is windowed again applying a Hanning taper which result in the windowed cross-correlation function $W_C C(t)$. This function contains the phase delay information that is necessary to invert for the phase velocity.

threshold of 0.5 where low-quality correlograms below that value are rejected. The coherence α is defined as the ratio of the amplitudes from the cross-correlation function, A_{12}, and the two auto-correlations, A_{11} and A_{22}.

$$\alpha = \frac{A_{12}}{\sqrt{A_{11} A_{22}}} \tag{D.9}$$

The amplitudes have been estimated in eq. D.8. Generally, the coherence does not depend on the inter-station distance or the azimuth, but only on the period. The varying degree of azimuthal scattering (Fig. D.6a) results only from the different number of station pairs due to the geographical shape (cf. Fig. C.2). Most reliable phase delay measurements are obtained if the coherence is around 1, i.e., in case of similar amplitudes. For short periods <32 s, most of the auto-correlation amplitudes are higher than the cross-correlation amplitudes, i.e., the coherence is <1 and many phase delay measurements are rejected. For longer periods >70 s and most of the events, coherence values significantly differ from 1.

Another decisive quality factor is given by the error estimation of the phase delay measurements of each cross-correlation function. The frequency-dependent average phase velocity over all measurements is estimated by polynomial linear fitting of the phase delay with the inter-station distance. An error threshold of 10 s relative to this linear fit has been set for the rejection of poor phase delay measurements. The number of outliers is increasing with the period (Fig. D.7 left): 15±12% of the phase delay measurements per event are discarded at 32 s but on average more than 40% for periods >80 s. It should be noted that the actual rejection ratio varies significantly between the individual events. A larger threshold of 15 s has been tested but this resulted in a generally larger standard deviation of the subsequent Eikonal tomography. Fig. D.5 (right) shows the measured phase delay vs. inter-station distance after all corrections and rejections.

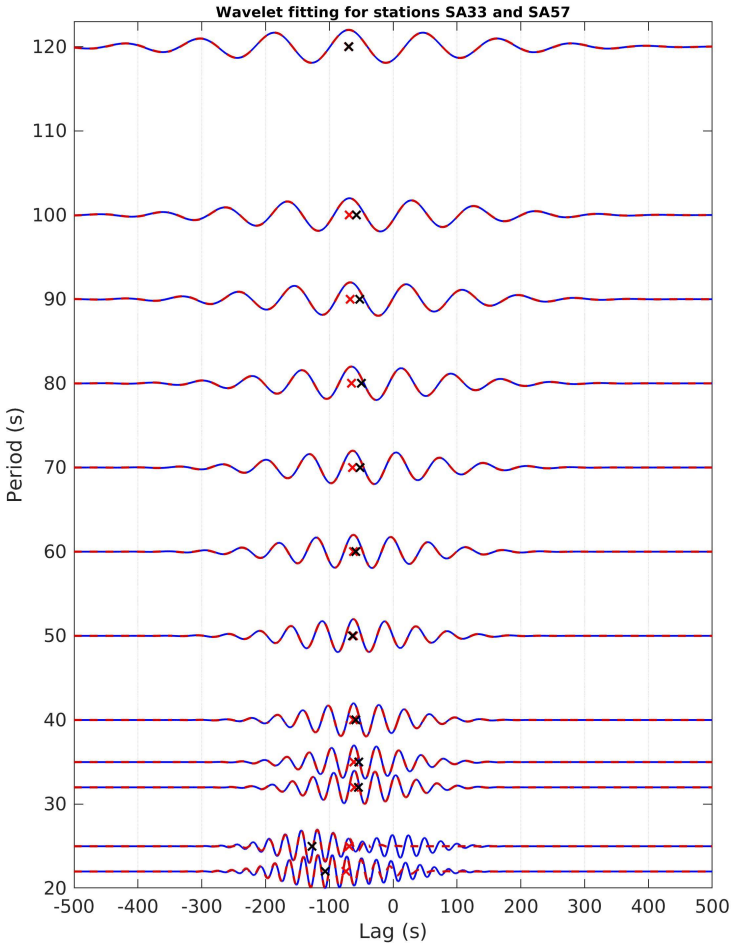

Fig. D.4: Windowed cross-correlation function $W_C C(t)$ of one station pair for the event shown in Fig. D.1. The signal has been filtered with a sequence of narrow-band Gaussian filters (solid blue lines) which are fitted by a five-parameter wavelet (dashed red lines). The inverted group and phase delay times are displayed as black and red crosses, respectively.

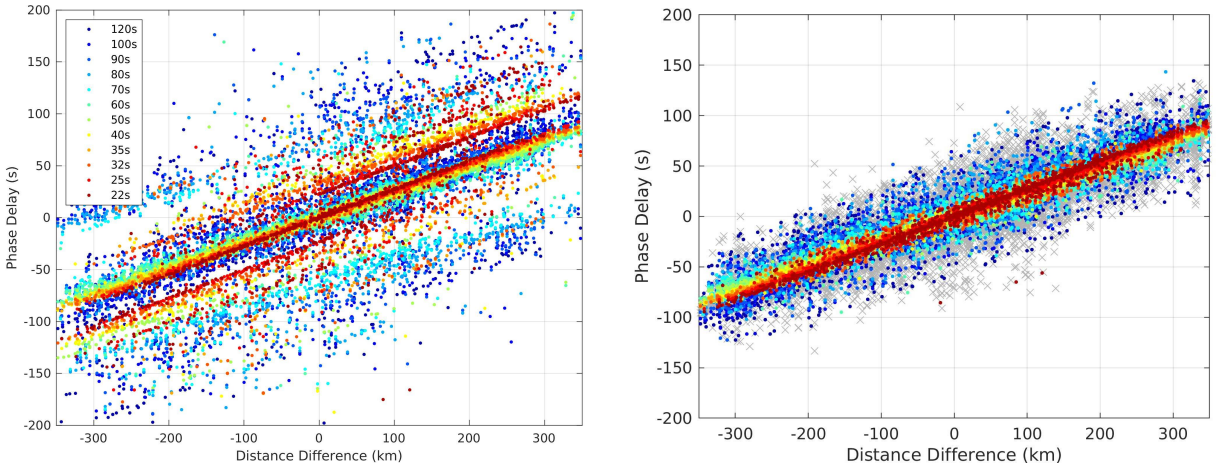

Fig. D.5: Relative phase delays as a function of the inter-station distance, color-coded by the period, for the event shown in Fig. D.1. Left: Before the cycle-skipping correction; Right: After the cycle-skipping and further corrections. See text for details. Grey crosses indicate the rejected measurements.

In summary, after the rejection of poor coherence and large phase delay misfits, the highest ratios of good phase delay measurements of all events were obtained for 35 s and 40 s period (Fig. D.7 right) with a mean value of 68±20% of the cross-correlations. With increasing period,

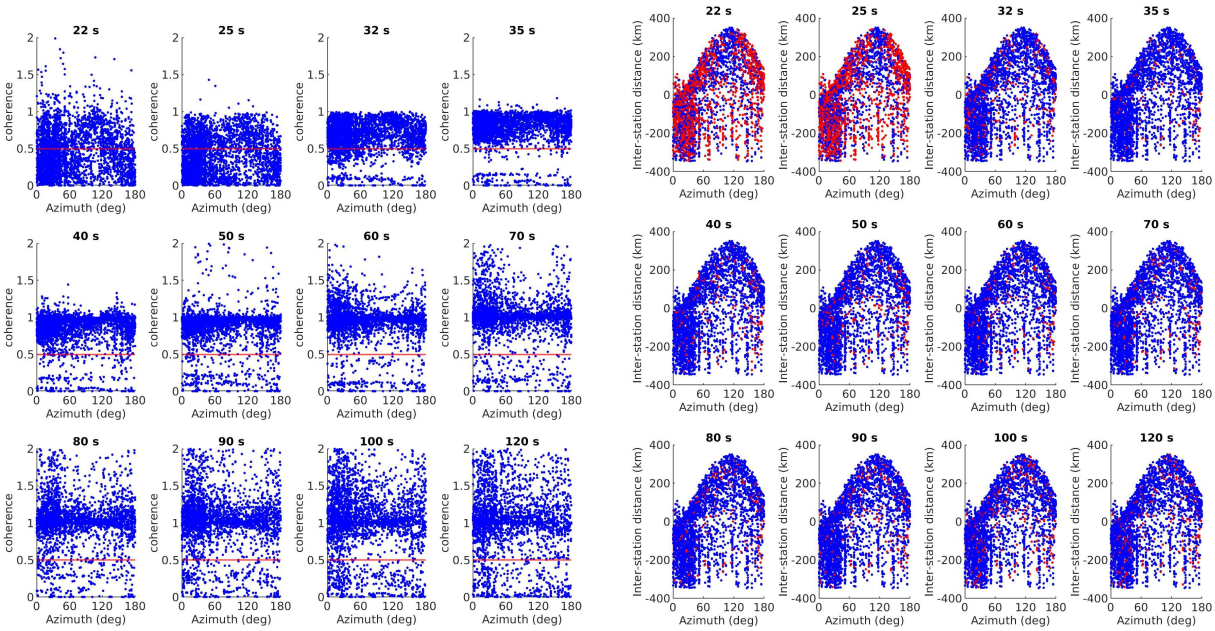

Fig. D.6: (a) Coherence of the cross-correlations vs. the inter-station azimuth for all periods and the event shown in Fig. D.1. The coherence threshold of 0.5 is indicated as red line. Note that coherence values >1 can occur due to the coherence definition (see text). (b) Inter-station distance vs. azimuth. The red points mark the low-coherence cross-correlations that are discarded.

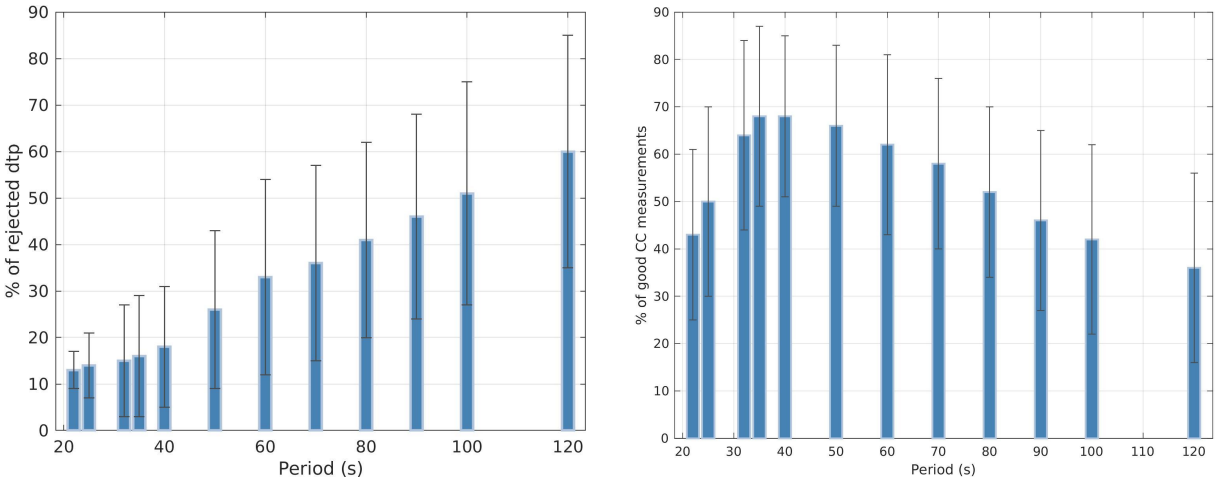

Fig. D.7: Left: Histogram of the fraction of discarded phase delay measurements per event for all events. Right: Histogram of the good cross-correlations of all events which passed the quality criteria (see text for details). The bars show the mean values and the error bars give the standard deviation.

the average ratio of good measurements is decreasing to less than 40%.

D.3 Eikonal tomography

The inversion of the slowness vector (eq. D.6) using the Eikonal equation (eq. D.4) results in 2D phase velocity maps for each event. I set the regular grid to a spacing of 0.3°× 0.3°. A minimum ray density of 50 within each grid is used to ensure the phase velocity inversion to be significant. The highest number of rays within each grid cell is obtained for the Nordland and Norrbotten area as well as along the Swedish coast, reflecting the dense station coverage. Different frequency-dependent smoothing parameters have been tested and evaluated against the

phase delay misfit, i.e., the difference between the predicted (eq. D.6) and observed (eq. D.8) phase delays. All phase velocity maps below were calculated with the smoothing weights found for the least phase delay misfits. The slowness inversion is performed twice where measurements with phase delay inversion misfits >2 s are rejected after the first inversion which affects mainly the longer periods.

Fig. D.8a shows the phase velocity maps at 40 s for three events with different propagation azimuths. Note that the eastern rim of Finland is not imaged with this cross-correlation technique due to the sparse station coverage. Especially in the Lofoten, Nordland and Norrbotten provinces the velocities differ significantly among the events whereas the central and southern areas are more coherent. The discrepancies in the north are also visible in the phase delay misfits (Fig. D.8b) where generally higher misfit values of >5 s than in the south or in Finland were obtained. Fig. D.8c displays the event-based dispersion curves. For most of the events up to 40 s period, the Eikonal dispersion curves are very similar to the median curves obtained from beamforming and the TPW inversion. For longer periods, the Eikonal phase velocities vary significantly among the different events and from the two reference curves. However, I do not recognize a systematic trend of increased phase velocities for events from eastern directions and lowered velocities from the west.

Fig. D.9 summarizes the median apparent phase velocities vs. the baz of all 188 events and for the complete study region. Here, it becomes clear that a systematic 1θ variation of the phase velocity with the baz is absent at all periods. This is in contrast to what was observed with the beamforming procedure in chapter 4 and appendix B.2. Rather, a combined 1θ and 2θ variation is visible, with the bulk having a 180° periodicity, similar to the examples shown by Lin & Ritzwoller (2011a). The fact that a pure 360° periodicity is not obtained here is likely related to the nature of the beamforming method. Coherent signals are stacked with respect to a fixed reference station and averaged over the study region which must unveil the (de)-focussing effects discussed in chapter 4.

The final apparent phase velocity maps were obtained by stacking the event-based phase velocities and then weighting the stack by the total number of events used for each period. Further quality criteria apply thereby to the stacking. A decisive parameter is the frequency-dependent ratio of good and bad cross-correlation measurements (Fig. D.7 right) where events are discarded when the ratios are below certain values. The stacking is performed twice where the difference between the single-event phase velocity and the stacked average value is calculated after the first stage. Events are discarded before the second stage if the differential value is above 2%. Moreover, deviations from the average phase velocity which are larger than 2% times the standard deviation within individual grid cells have been rejected. Individual grid cells with results from less than 5 events are not considered for the final stack. The number of events appropriate for the final stacking differs significantly with 57, 81, 81, 89, 101, 87, 82, 36 and 5 events at 22 s, 25 s, 32 s, 35 s, 40 s, 50 s, 60 s, 70 s and 80 s period, respectively. For longer periods, not enough events have been found to be appropriate. Note that in initial runs, I performed the Eikonal inversion using about 470 events, but this did not result in stacks for periods >80 s either. An alternative weight of the stacking has been tested by using the ray density which led to very similar final phase velocities and standard deviations.

Fig. D.10a shows the stacked phase velocity maps at 25 s, 40 s and 70 s period using all appropriate events. The stacked results using azimuthally balanced event distributions with 10° bin width, similar to the processing in chapter 5, are shown in Fig. D.10c. Highest uncertainties

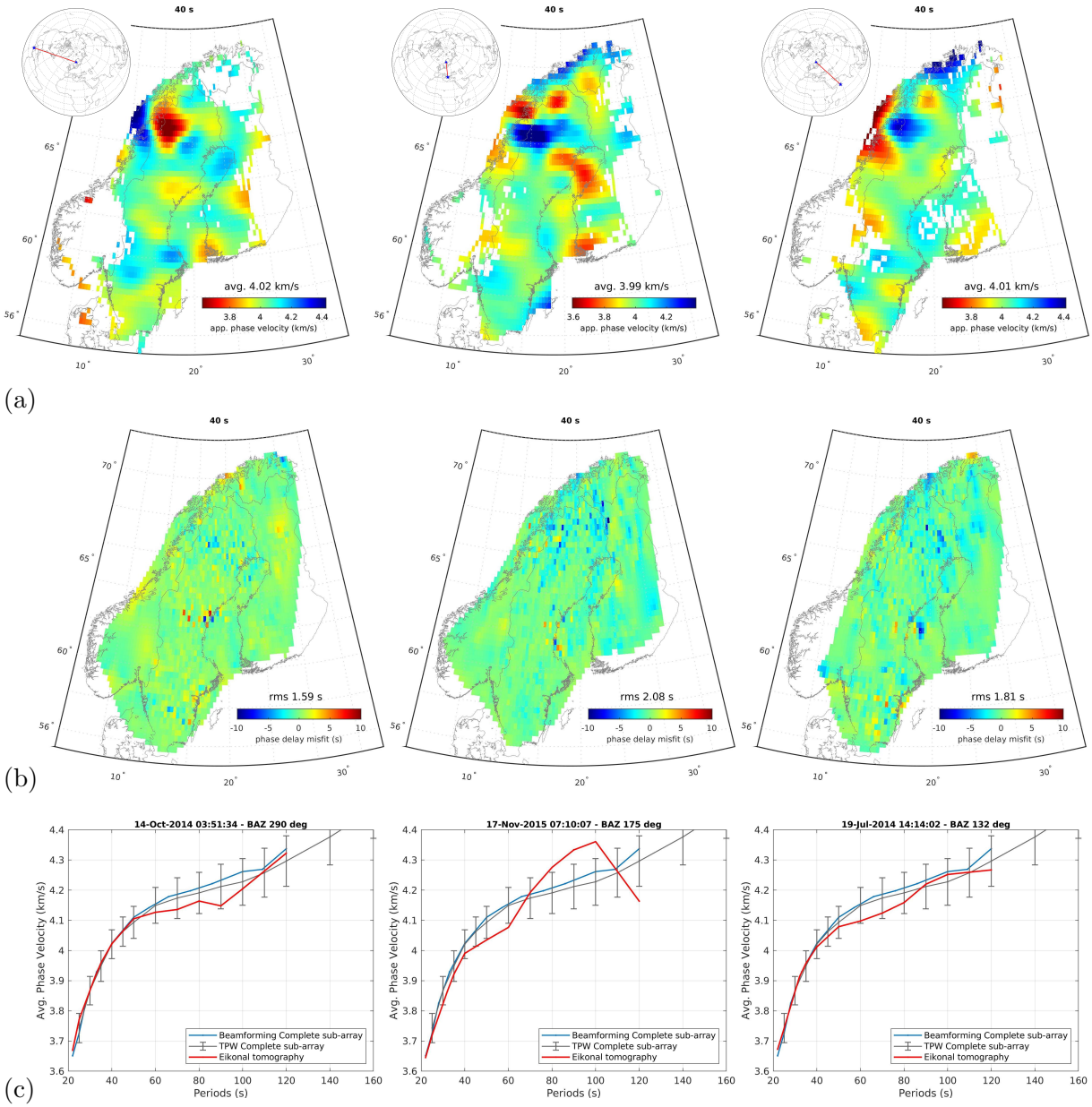

Fig. D.8: (a) Apparent phase velocity maps at 40 s obtained from the Eikonal tomography for three events with different propagation azimuths. The left event is the same as illustrated in Fig. D.2. (b) Corresponding maps of the phase delay misfits. Inter-station misfit values of each cross-correlation function have been interpolated to construct the maps. (c) Corresponding dispersion curves for the events (red lines). The median dispersion curves resultant from the complete beamforming sub-array (blue lines, cf. 4) and the TPW (grey lines,cf. 5) are also shown.

are obtained for the Lofoten and Nordland provinces (Fig. D.10b) and for periods >35 s reflecting again the problematic phase velocity calculation in that region. Unlike the event bootstrapping and balancing done with the TPW results in chapter 5, the improvement of the phase velocities for the Eikonal tomography is only little (Fig. D.10c and d). Potential bias is somehow removed from the results at the intermediate periods around 40 s, but for the longer periods no difference is seen. The standard deviations differ insignificantly between the full and the 10° bin width stack. I have tested also a 5° bin width distribution, as I did for the TPW bootstrapping. In contrast to the TPW results, no differences between 5° and 10° bin width are noticeable, neither in the phase velocity nor in the standard deviations maps.

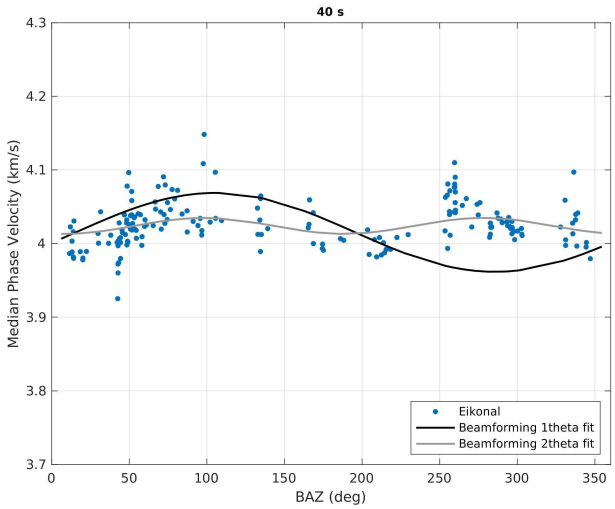

Fig. D.9: Apparent phase velocities as a function of the backazimuth, resultant from the Eikonal tomography of all 188 events. Shown are the median phase velocities over the entire study region at 40 s. The black and grey lines are the 1θ and 2θ fits, respectively, from the complete beamforming sub-array results in chapter 4.

To analyse southern Norway as well, I used the MAGNUS network (Weidle & Maupin, 2008) and about 500 events with $>M_S5.5$ originating between October 2006 and December 2008. Thereby I applied the same parameters as described above for the ScanArray data set. The merged phase velocity maps are illustrated in Fig. D.11. Highest uncertainty of the MAGNUS data set is obtained in northeast southern Norway with up to 0.2 km/s, a similar value as obtained in the northern part, however, mainly for shorter periods.

Fig. D.12 compares the dispersion curves obtained from the full and balanced Eikonal event stacks along with the results from TPW and beamforming analysis. In the period range 25–40 s, the median phase velocities of the study region (excluding the MAGNUS results) are nearly identical where the Eikonal standard deviations are larger compared to TPW or beamforming. For the longer periods, the Eikonal tomography seems to underestimate the phase velocities by about 0.5% with respect to TPW and beamforming, however, the values are still within the median standard deviations. The phase velocities of the Eikonal derived MAGNUS results show a huge variation for all periods. For periods <30 s, the velocities are on average faster than my Rayleigh wave and noise measurements and than the results by Maupin (2011). Moreover, the balanced event distributions with 5° and 10° bin widths do not deviate significantly from the results with full, unbalanced event distribution, neither do they improve the Eikonal tomography.

D.4 Helmholtz tomography

By applying the Helmholtz equation (eq. D.5), an amplitude correction on the apparent Eikonal phase velocities yield the structural phase velocity c_s. Estimations of the observed single station amplitudes are taken from the auto-correlations as described. The observed amplitude fields (Fig. D.13a and c) show a correlation with the direction of the propagating wavefields, at least for 25 s period. Whereas the calculated amplitude correction term (Fig. D.13b and d) results in significant short-wavelength variations with increasing period. This might point to a finite-frequency effect which is not taken into account by the Eikonal equation but should be simulated by the Helmholtz tomography. The largest amplitude

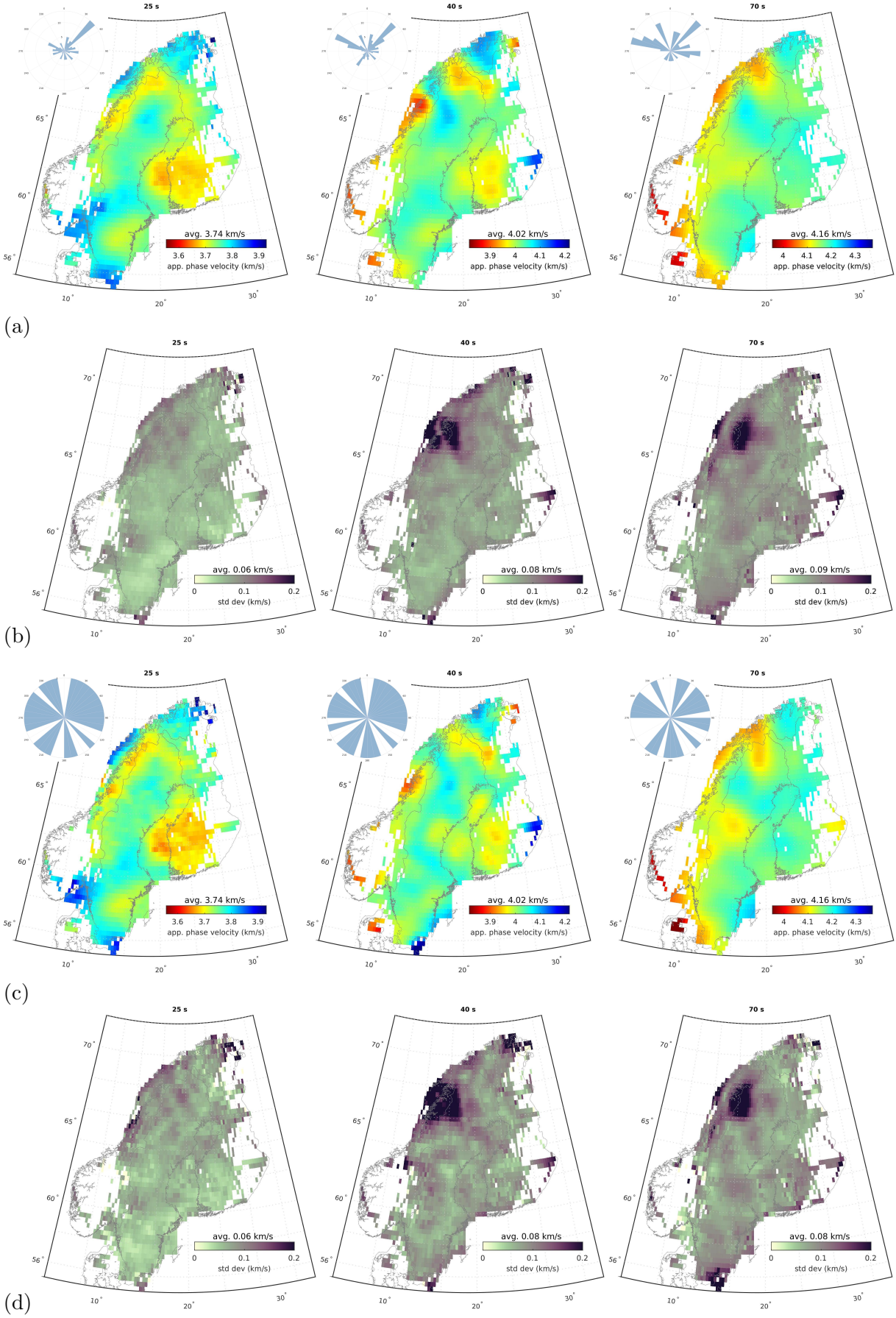

Fig. D.10: (a) Stacked apparent phase velocity maps at 25 s, 40 s and 70 s period for all 188 events and (b) the corresponding standard deviations. (c) and (d) Same as (a) and (b) but the stacking was done with azimuthally balanced event distributions with 10° bin width. The polar histograms in (a) and (c) show the event distributions with the propagation azimuth on the theta axis.

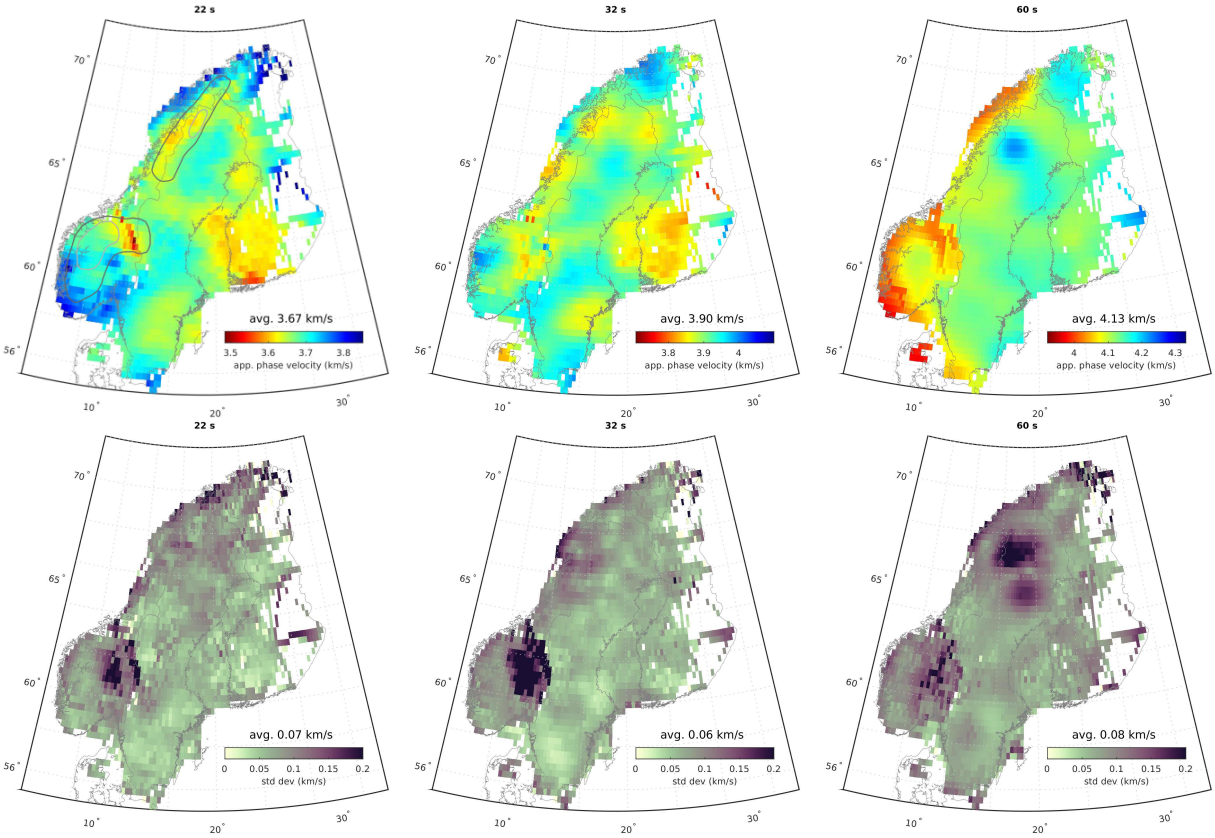

Fig. D.11: Final apparent phase velocity maps stacked with 10° bin width for the ScanArray and MAGNUS data. Additional periods as in Fig. D.10 are shown at 22 s, 32 s and 60 s. Overlapping phase velocities in southern Norway have been averaged. The grey lines mark the Scandes topography at 1000 m and 1500 m elevation, respectively.

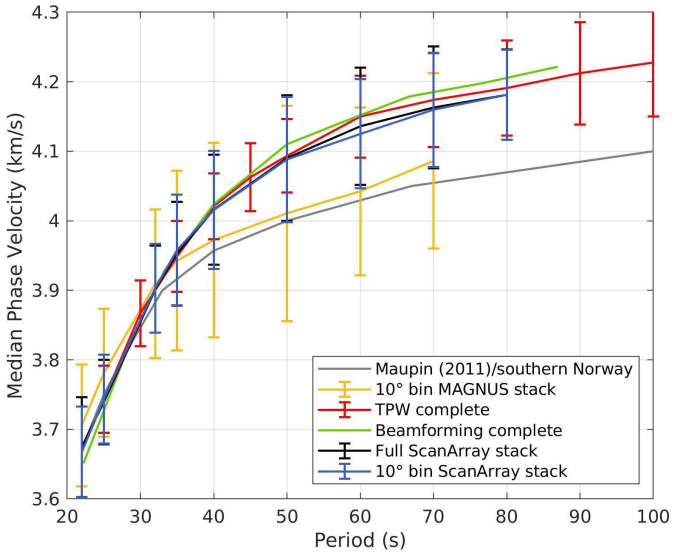

Fig. D.12: Median dispersion curves over the entire study region obtained from the methods applied in this thesis. The median phase velocities from all events used for the Eikonal stack (black) are shown as well as the median values over the balanced stacks with 10° bin widths (blue), respectively. For comparison the results from the beamforming (magenta) procedure (chapter 4) and TPW (red) method (chapter 5) are overlain. Error bars indicate the median of the corresponding standard deviations.

corrections take place in northern Norway/Sweden and southern Sweden but the central area shows rather smooth variations. To some extent, the largest amplitude corrections spatially match with the occurrence of the 1θ phase velocity variation.

The influence of any smoothing parameters is negligible as the short-wavelength variations of the amplitude correction term are introduced by taking the second gradient of the observed amplitude field. Jin & Gaherty (2015) recognized this problematic property and implemented a finite-difference calculation to estimate the second derivative numerically, but this procedure seems to fail with our data set. In general, the short-wavelength variations should correspond to the single amplitude measurements at the each station due to local heterogeneities, but this is clearly not the case here.

D.5 Discussion and conclusion

D.5.1 Comparison of the 2D phase velocity inversions

Although a detailed comparison cannot be made, there is a good qualitative agreement of the Eikonal tomography (Fig. D.11) with the ambient noise (Fig. 5.5) and TPW (Fig. 5.8) at short periods. The TPW tomography yielded, however, more short-wavelength variations due to the smoothing parameters chosen for the Eikonal tomography based on the least phase delay misfit (see above). Between 22–30 s, the crustal structure below the Lofoten peninsula is considerably faster than the average (up to +3%), most noticeable from the noise and Eikonal results. In contrast, the onshore regions of the Nordland and Norrbotten provinces have much lower than average velocities (∼-1.5%), trending NNE-SSW in a narrow branch right below the northern Scandes. This probably indicates the thicker crust due to the crustal root as discussed in section 5.8. Also the faster structure along the coast in southernmost Norway and Sweden as well as the decreasing velocities further inland, respectively, can be imaged with all three methods and corresponds to the varying crustal thickness in the southern parts of Norway and Sweden (Fig. 5.13). Lower than average velocities (∼-2%) below southern Finland are observed for periods <50 s which represents the deep Moho in that area.

At periods between 40–70 s, the low-velocity Norrbotten craton can be clearly separated in the Eikonal and TPW phase velocity maps from the high-velocity structure of the adjacent Svecofennian domain. As imaged previously (e.g., Wawerzinek et al., 2013; Kolstrup et al., 2015; Hejrani et al., 2017), southern Norway and southernmost Sweden (corresponding to the STZ) reveal very low velocity with -4% respect to the average for periods >40 s. The eastward transition from low to high velocities across the Oslo Graben is likewise well resolved with the Eikonal tomography.

D.5.2 Difficulties with the Eikonal and Helmholtz tomography

Although, the TPW method comes also with some difficulties (chapter 5), the Eikonal tomography seems to have serious disadvantages which emphasizes the preferable usage of the TPW approach. The strongly varying phase velocities with propagation direction (Fig. D.8) shown here are in contrast to the observations made by Lin & Ritzwoller (2011a) where a lateral shift of the phase velocities might occur but otherwise the velocity structure seems to be robust. A stabilization of the phase velocity variation in the north would be mandatory as the lateral velocity perturbation among the different events is severely (Fig. D.8). The

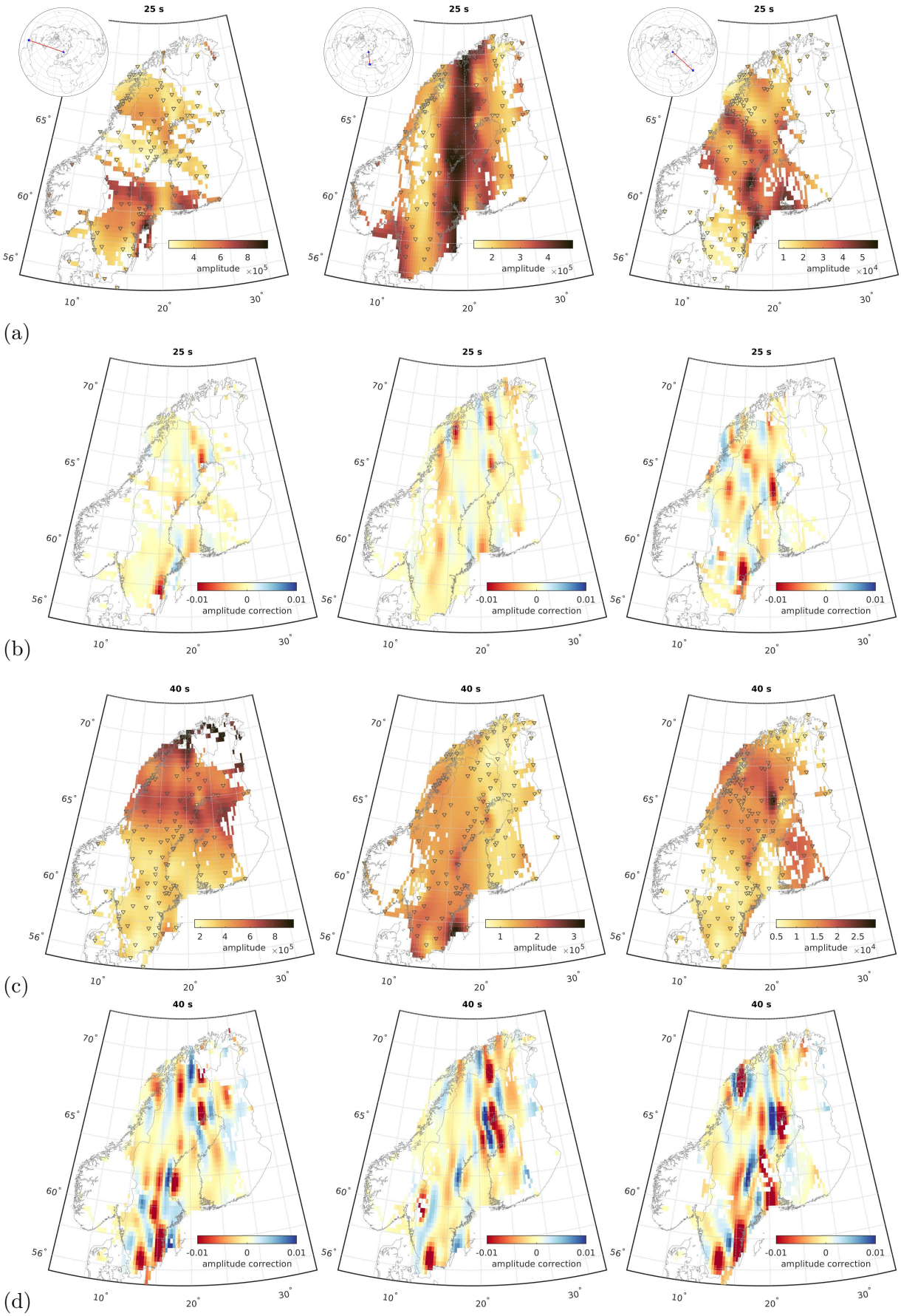

Fig. D.13: Amplitude maps as measured from the auto-correlations of each station for the three events shown in Fig. D.8 at 25 s (a) and 40 s (c) period, respectively. The single measurements have been projected on a 2D grid using a minimum curvature surface interpolation. Grey triangles denote the used stations. Note the different color scales. The insets show the source location and propagation direction. (b) and (d) Corresponding maps resultant from the amplitude correction term in eq. D.5.

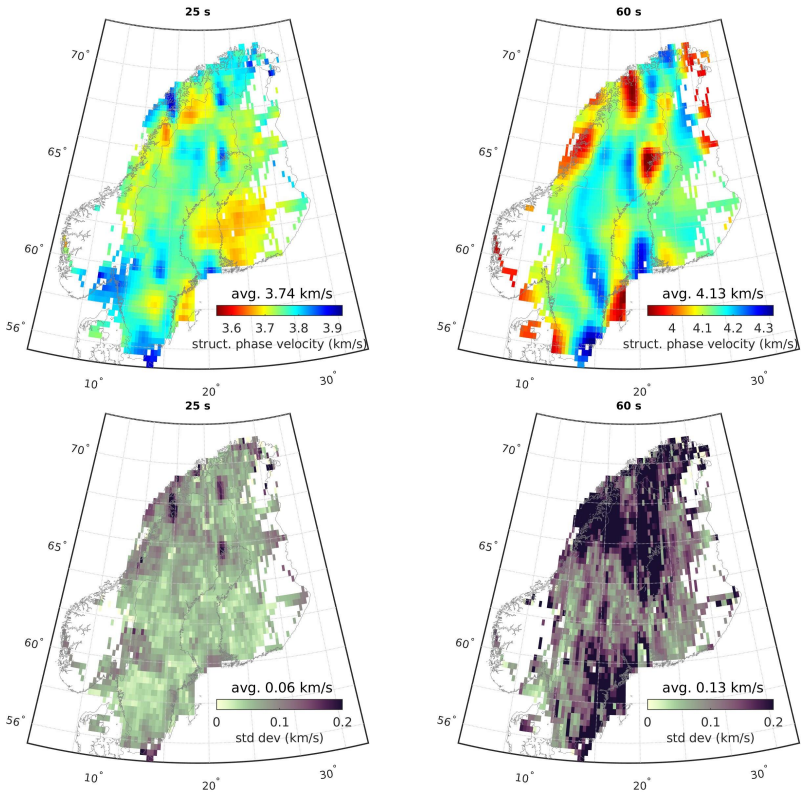

Fig. D.14: Top row: Corrected, structural phase velocity maps obtained via Helmholtz tomography and stacked with 10° bin width at 25 s and 60 s period. Bottom row: Corresponding standard deviations.

azimuthal balancing of the events used for the stacking did not significantly differ from the full stack with unbalanced event distribution. From that point of view, the Eikonal phase velocity results are highly uncertain and structural bias is probably still present (Fig. D.11).

It is questionable insufficient phase velocity results were obtained for periods >80 s (or >70 s in case of the MAGNUS data), independent from the number of used events. This also hints at a lower reliability of the short and intermediate period measurements as for longer periods robust results were obtained with the TPW method and for the complete sub-array beamforming. A reason for the failure of the long-period measurements might be the cross-correlation approach although Jin & Gaherty (2015) calculated phase velocity maps up to 100 s period for the entire U.S. Another difficulty might be the fitting with the five-parameter Gaussian wavelet to derive the observed phase delay as indicated by an increasing rms misfit with period. A wavelet fitting seems to be problematic for regions with strong lateral and vertical heterogeneities.

The application of the Helmholtz tomography does not correct the structural variation as seen in Fig. D.8. Due to the extreme amplitude correction terms (Fig. D.13b and d), implausible small-scale features are introduced into the structural phase velocity maps (Fig. D.14). The azimuthal balanced stack with 10° bin width cannot reduce these artifacts (Fig. D.14). Neither the application of the Helmholtz tomography reduced the phase velocity standard deviations. Therefore, the Helmholtz tomography results are not suitable for any interpretation. Unlike in the study by Lin & Ritzwoller (2011b), finite-frequency effects cannot be corrected for in our study region using the Helmholtz equation. Rather, the usage of true finite-frequency kernels (e.g., Zhou et al., 2004) should be preferred in our study region to reduce the structural bias. On the other hand, a numerical problem with the derivation of the amplitude term within the

ASWMS algorithm cannot be ruled out as Jin & Gaherty (2015) modified the original amplitude measurement technique by Lin et al. (2009). Moreover, multipathing effects likely introduce bias on the phase velocities in the direction of the propagating wavefield as seen in Jin & Gaherty (2015)(Fig. 17 and 18). Since the apparent phase velocities retrieved in this study (Fig. D.8) do not reveal any systematic distortion in alignment with the propagation direction, I assume the bias by non-planar multipathing effects is negligible compared to the structural bias introduced by the strong lithosphere heterogeneities below the receivers.

Acknowledgements

This thesis arose from the funding by the DFG project grants LITHOS-CAPP DFG Gz TI 316/3-1 and -2. I wrote this thesis while I was working at GFZ Potsdam and enrolled at the Freie Universität Berlin.

As almost everything in life, special achievements as a dissertation are not possible without the support of many people.
First of all, I would like to thank my principal supervisor Frederik Tilmann with whom I was working at GFZ. His critical feedbacks and instructions improved my work deeply.

I am grateful for the support by my second supervisor Valérie Maupin. It was always a pleasure to meet with her to finally disclose the scientific puzzles. Beyond that, her advices and encouragements for my future work and (scientific) career were always helpful.

I thank Anya Makushkina, another PhD in the ScanArray project, for our constructive discussions and friendly meetings during the project.

A special thank goes to my working group at the GFZ which provided me a pleasant and cooperative setting. Many thanks to the GFZ GEOFON team - especially Susanne Hemmleb, for their help and advise in archiving the ScanArray data.
I want to thank Elisa Rindraharisaona, Jennifer Dreiling, Felix Schneider, Hamzeh Sadeghisorkhani, Michael Grund, Werner Scherer, Thomas Zieke, Karl-Heinz Jäckl, Martin Haxter, Ben Heit and Christoph Sens-Schönfelder.

Finally, I would like to thank my family who has been growing during my PhD. I would like to give special thanks to my husband, Stefan, for his love and support throughout this journey. Without him that would not have been possible. He gave me strength and also reminded me that there is a world beyond work - but often enough I did not listen to.

Usually, the acknowledgement ends at this point. But I want to tell the truth. Often enough I thought this period will never end. And often enough I doubt that it is worth keep going on or if it will be worth at any time in the future. It is not helpful for your health, your friendships or even for a harmonic marriage. Or happy children. Is it worth to continue if your family tells that you have changed negatively or you doesn't care about your children anymore. Most likely, one needs to be on obsessed egomaniac to overcome that moments and those long, dark nights of doubts and guilt. And to stand up again every morning, hunting a childhood dream to be a scientist. And to continue, even no one will ever acknowledge what it has cost. Maybe my words are too dramatic for natural sciences. Maybe they are not. Maybe I wrote down these words in a quite depressing mood.
Against all odds.